

**SYNTHESIS AND REACTIVITY OF Rh AND Ir
IMINO AND AZIDOPHOSPHONAMIDO COMPLEXES**

DAISY ELIZABETH CRUZ-MILETTE
Bachelor of Science (Honours), University of Lethbridge, 2020

A thesis submitted in partial fulfillment of the
requirements for the degree of

MASTER OF SCIENCE

in

CHEMISTRY

Department of Chemistry and Biochemistry
University of Lethbridge
LETHBRIDGE, ALBERTA, CANADA

SYNTHESIS AND REACTIVITY OF Rh^I AND Ir^I
IMINO AND AZIDOPHOSPHONAMIDO COMPLEXES

DAISY ELIZABETH CRUZ-MILETTE

Date of Defense: December 09, 2022

Dr. P. Hayes Thesis Supervisor	Professor	Ph.D.
Dr. M. Gerken Thesis Examination Committee Member	Professor	Ph.D.
Dr. J.D. Hamel Thesis Examination Committee Member	Assistant Professor	Ph.D.
Dr. R. Roesler External Examiner University of Calgary Calgary, Alberta	Associate Professor	Ph.D.
Dr. N. Thakor Chair, Thesis Examination Committee	Associate Professor	Ph.D.

ABSTRACT

This work reports a family of iminophosphonamido Rh and Ir cyclooctadiene (COD) complexes, $[\text{Ph}_2\text{P}(\text{NR})_2]\text{M}(\text{COD})$, where the substituents on nitrogen vary, R = 2,4,6-trimethylphenyl (Mes) or adamantyl (Ad). The reaction chemistry of the iminophosphonamido Rh and Ir COD complexes was probed. This work also demonstrates the synthetic route to and of a family of azidophosphonamide Rh and Ir phosphazide containing ligand cyclooctadiene (COD) complexes, $[\text{Ph}_2\text{P}(\text{N}_3\text{R})(\text{NR})]\text{M}(\text{COD})$. The unusual ligand linkage isomerism of said species is discussed. Preliminary results pertaining to bis(cyclooctene) (COE) complexes bearing both ligand types are also reported.

ACKNOWLEDGEMENTS

To my parents, Luisa and Benoit, you have always supported me and been my biggest cheerleaders and would always listen to my rambles over the phone, regardless of the hour. Thank you so much for your patience, love, support, and belief that one day I would finish this thesis (even when I did not).

To my sister Ashley, it is in the time we have spent apart that I have learned to appreciate the time we did get to spend together. Your constant bombardment of hugs never failed to cheer me up and eliminate all sense of home sickness whenever I came to visit.

To my grandparents, Fabia and Joao: thank you for always being so supportive, you kept me fed with your fresh and frozen goodies and always had kind words of support and wisdom whenever I came to visit.

To my close friends, Sam N., Dylan, Ed, Sam D., Bryana, Ramiro and Shauné, thank you for the joy you brought, the random Friday conversations, weekend adventures, Dungeons and Dragons sessions, impromptu afternoon drinks and all the memories I will not forget.

To my fellow lab mates, Dylan, Ed, Sam, Jackson, Desmond, Tara, Connor, Ash and Corey, as well as my chemistry department friends, Craig, Felix, Shauné, Nolan, Nathan, Janelle and Taylor; thank you for supporting me by listening to my research rambles and putting up with my stresses and moans for the past few years of study!

A special thank you to my supervisor, Professor Paul Hayes, for letting a third-year undergraduate he had never met into his lab and eventually for taking me on as a graduate student. You sparked my love of ligand design and shaped me into the scientist I am today. I also thank you for having suffered through numerous revisions and helping make some sense of the confusion that is my writing.

Thank you to Dr. René Boéré for teaching me X-ray crystallography and how to use the instrument, it was my absolute joy to use the instrument as often as I did. To Michael Opyr and Tony Montana, thank you for aiding me whenever I ran into trouble on the NMR instruments, which seemed to happen ever other week.

Many thanks to my committee members, Dr. Michael Gerken, Dr. Jean-Denys Hamel, who offered guidance and support throughout my past years of study. Thank you to my external examiner Dr. Roland Roesler for having to endure through my thesis.

TABLE OF CONTENTS

Abstract.....	iii
Acknowledgements.....	iv
List of Tables	xiv
List of Figures.....	xvi
List of Schemes.....	xix
List of Symbols and Abbreviations.....	xxii
List of New Compounds	xxv
Chapter 1: Introduction.....	1
1.1 General Introduction.....	1
1.2 Introduction to Metals and Ligands.....	2
1.3 Noble Metal Catalysts.....	2
1.4 Importance of Rhodium and Iridium in Catalysis	3
1.5 Principles of Ligand Design: A Historical Perspective	6
1.5.1 Metal Carbonyls and Other π -Acceptor Ligands	7
1.5.2 Monodentate and Bidentate Phosphines: Controlling Ligand Properties	8
1.5.3 Cp Ligands and Their Derivatives: The Start of Ancillary Ligand Design ...	12
1.6 Principles in Ligand Design: Current Trends in Ligand Design	15
1.6.1 β -Diketiminato 'NacNac' Ligands	17
1.6.2 Amidinate and Guanidinate Ligands.....	18
1.6.3 Pincer Ligands.....	20
1.6.4 N-Heterocyclic Carbenes	21

1.7 Applications of Ligand Design: Phosphorus–Nitrogen Units	22
1.7.1 Imines (C=N) Versus Phosphinimines (P=N).....	23
1.7.2 The Syntheses of Phosphinimines.....	24
1.7.3 [CH(Ph ₂ P=NR) ₂] [−] and [C(Ph ₂ P=NR) ₂] ^{2−} Ligands	26
1.7.4 Metal-Ligand Cooperation of Phosphinimine Ligands.....	27
1.7.5 Phosphazides (R ₃ P=N ₃ –R ¹).....	27
1.8 Iminophosponamide Ligands.....	29
1.9 Project Aims	32
1.9.1 Chapter 2 Goals and Accomplishments	32
1.9.2 Chapter 3 Goals and Accomplishments	33
1.9.3 Chapter 4 Goals and Accomplishments	37
Chapter 2: Investigations into Iminophosponamide Rh and Ir Complexes	38
2.1 Overview: Iminophosponamide Ligands.....	38
2.1.1 Group 1 and 2 Metal Iminophosponamido Complexes	39
2.1.2 Early Transition Metal and Lanthanide Iminophosponamido Complexes ..	40
2.1.3 First Row Transition Metal Iminophosponamido Complexes	41
2.1.4 Late Transition Metal Iminophosponamido Complexes.....	41
2.2 Synthetic Routes to [Ph ₂ P(NR) ₂] [−] Ligands.....	43
2.2.1 Synthesis of Ph ₂ P(NHAd)(NAd), (1).....	45
2.2.2 Synthesis of Li[Ph ₂ P(NAd) ₂], (2).....	46
2.3 Synthesis of Iminophosponamido Rh ^I Complexes	47

2.3.1 Characterization of $[\text{Ph}_2\text{P}(\text{NR})_2]\text{Rh}(\text{COD})$ where R = Mes (3) and R = Ad (4)	48
2.3.1.1 X-ray Crystal Structure of $[\text{Ph}_2\text{P}(\text{NMe}_3)_2]\text{Rh}(\text{COD})$, (3)	48
2.3.1.2 X-ray Crystal Structure of $[\text{Ph}_2\text{P}(\text{NAd})_2]\text{Rh}(\text{COD}) \cdot 1.5\text{C}_6\text{H}_6$ (4).....	50
2.4 Reactivity of Rh^{I} Iminophosphonamido Complexes Toward Small Molecules ..	52
2.4.1 Reactions of Rh^{I} Iminophosphonamido Complexes with CO	53
2.4.1.1 X-ray Crystal Structure of $[\text{Ph}_2\text{P}(\text{NMe}_3)_2]\text{Rh}(\text{CO})_2$, (5).....	54
2.4.1.2 X-ray Crystal Structure of $[\text{Ph}_2\text{P}(\text{NAd})_2]\text{Rh}(\text{CO})_2$, (6).....	56
2.4.2 Reactions of Rh^{I} Iminophosphonamido COD Complexes with Silanes and H_2	61
2.4.3 Attempted Reaction of Rh^{I} Iminophosphonamido complexes with Phosphines	63
2.4.4 Reactivity of Rh^{I} Iminophosphonamido Complexes with 2,6- $\text{Me}_2\text{C}_6\text{H}_3\text{N}\equiv\text{C}$	64
2.4.4.1 X-ray Crystal Structure of $[\text{Ph}_2\text{P}(\text{NMe}_3)_2]\text{Rh}[\text{C}\equiv\text{N}(2,6\text{-Me}_2\text{C}_6\text{H}_3)]_2$, (7)...	66
2.4.5 Synthesis of $[\text{N},\text{C}\text{-Ph}_2\text{P}(\text{NMe}_3)(\text{Me}_3\text{NC}=\text{N}(2,6\text{-Me}_2\text{C}_6\text{H}_3))]\text{Rh}[\text{C}\equiv\text{N}(2,6\text{-Me}_2\text{C}_6\text{H}_3)]_2$ (8)	68
2.4.5.1 X-ray Crystal Structure of $[\text{N},\text{C}\text{-Ph}_2\text{P}(\text{NMe}_3)(\text{Me}_3\text{NC}=\text{N}(2,6\text{-Me}_2\text{C}_6\text{H}_3))]\text{Rh}[\text{C}\equiv\text{N}(2,6\text{-Me}_2\text{C}_6\text{H}_3)]_2 \cdot 1.5\text{C}_6\text{H}_6$ (8).....	69
2.4.6 Attempted Reactivity of Isocyano Complexes (7) and (8).....	72
2.5 Synthesis of Iminophosphonamido Ir^{I} Complexes	72

2.5.1 Characterization of $[\text{Ph}_2\text{P}(\text{NR})_2]\text{Ir}(\text{COD})$ where $\text{R} = \text{Mes}$ (9) and $\text{R} = \text{Ad}$ (10)	73
2.5.1.1 X-ray Crystal Structure of $[\text{Ph}_2\text{P}(\text{NMes})_2]\text{Ir}(\text{COD})$, (9)	74
2.5.1.2 X-ray Crystal Structure of $[\text{Ph}_2\text{P}(\text{NAd})_2]\text{Ir}(\text{COD}) \cdot 1.5\text{C}_6\text{H}_6$ (10)	76
2.6 Reactivity of Ir^{I} Iminophosponamido Complexes Toward Small Molecules	78
2.6.1 Reactions of Ir^{I} Iminophosponamido COD Complexes with CO and H_2	78
2.6.2 Reactivity of Ir^{I} Iminophosponamido Complexes Towards 2,6- $\text{Me}_2\text{C}_6\text{H}_3\text{N}\equiv\text{C}$	80
2.6.3 Reactions of Ir^{I} Iminophosponamido COD Complexes with Silanes	82
2.7 Towards a More Active Rh^{I} Iminophosponamido Species	83
2.7.1 Synthesis of $[\text{Ph}_2\text{P}(\text{NMes})_2]\text{Rh}(\text{COE})_2$, (13)	83
2.7.1.1 X-ray Crystal Structure of $[\text{Ph}_2\text{P}(\text{NMes})_2]\text{Rh}(\text{COE})_2 \cdot 1.5\text{C}_6\text{H}_6$ (13)	86
2.7.2 Future Directions for $[\text{Ph}_2\text{P}(\text{NMes})_2]\text{Rh}(\text{COE})_2$, (13)	87
2.8 Concluding Remarks	88
Chapter 3: Synthesis of Azidophosponamide Rh and Ir Complexes	89
3.1 Overview	89
3.1.1 Phosphazides and Stabilization Methods	89
3.1.2 Binding Modes	90
3.1.3 Potential Catalytic Applications of Phosphazides	91
3.1.4 Synthetic Routes to Phosphazide Ligands and Complexes	93
3.1.5 Synthesis of Phosphazide Ligand Salts	93
3.1.6 Towards Rh^{I} and Ir^{I} Phosphazide complexes	95

3.1.7 Literature Precedents for an “Azido”phosphonamide.....	96
3.2 Synthesis of Azidophosphonamide Ligands.....	100
3.2.1 From Iminophosphonamides to Azidophosphonamides.....	100
3.2.2 Synthesis of $K[{}^iPr_2P(NMes)(N_3Mes)]$ (14).....	101
3.2.3 Synthesis of Adamantyl-Substituted Azidophosphonamido Ligands.....	104
3.2.4 Synthesis of ${}^iPr_2P(NAd)$ (15).....	105
3.2.5 Synthesis of ${}^iPr_2P(N_3Ad)(NHAd)$ (16).....	105
3.2.6 Synthesis of $Li_2[{}^iPr_2P(N_3Ad)(NAd)]_2$ (17).....	107
3.2.6.1 X-ray Crystal Structure of $Li_2[{}^iPr_2P(N_3Ad)(NAd)]_2 \cdot C_2Cl_2$ (17).....	108
3.3 Towards Rh^I and Ir^I Azidophosphonamido Complexes.....	111
3.3.1 Synthesis of Rh^I and Ir^I Adamantyl-Substituted Azidophosphonamido Species.....	111
3.3.1.1 X-ray Crystal structure of $[{}^iPr_2P(N_3Ad)(NAd)-\kappa^2-N,N^a]Rh(COD)$ (18)	112
3.3.2 Synthesis of Rh^I and Ir^I Mesityl-Substituted Azidophosphonamido Complexes.....	115
3.3.2.1 X-ray Crystal Structure of $[{}^iPr_2P(N_3Mes)(NMes)-\kappa^2-N,N^a]Rh(COD)$ (20)	116
3.3.2.2 X-ray Crystal Structure of $[{}^iPr_2P(N_3Mes)(NMes)-\kappa^2-N,N^a]Ir(COD)$ (21)	118
3.4 Concluding Remarks.....	121
Chapter 4: Reactivity of Azidophosphonamide Rh and Ir Complexes.....	122
4.1 Overview.....	122

4.1.1 Phosphazides.....	122
4.1.2 Phosphazide Linkage Isomerism	122
4.1.3 Photochemically Induced Phosphazide Linkage Isomerism.....	123
4.1.4 Thermally-Induced Linkage Isomerism of Phosphazides.....	125
4.2 Linkage Isomerism of Rh ^I and Ir ^I Azidophosponamido Complexes.....	126
4.2.1 Linkage Isomerism of Mesityl-Substituted Rh ^I and Ir ^I Complexes (20 and 21)	126
4.2.3 Lack of Thermally- or Photochemically-Induced Coordinative Isomerism	135
4.3 Reaction Chemistry of Rh ^I and Ir ^I Azidophosponamido Complexes.....	136
4.3.1 Reactions of [ⁱ Pr ₂ P(N ₃ Ad)(NAd)-κ ² -N,N ^α]M(COD)], M = Rh (18), Ir (19), with CO	136
4.3.2 X-ray Crystal structure of [ⁱ Pr ₂ P(N ₃ Ad)(NAd)-κ ² -N,N ^α]Ir(CO) ₂ (25)	141
4.3.3 Reactions of [ⁱ Pr ₂ P(N ₃ Mes)(NMes)-κ ² -N,N ^α]M(COD)], M = Rh (20), Ir (21), with CO	142
4.3.4 Comparison of Carbonyl-Azidophosponamido complexes (24-27)	144
4.3.5 Reactivity of Rh ^I and Ir ^I Azidophosponamido Complexes Toward Small Molecules	148
4.4 Towards a More Reactive Azidophosponamido Rh ^I Complex.....	150
4.4.1 Substituting COD with COE.....	150
4.4.2 Synthetic Challenges that Arise from COE Groups.....	157
4.5 Concluding Remarks	157
Chapter 5: Summary, Conclusion and Future Work Avenues.....	159

5.1 Summary of Chapter 2.....	159
5.2 Summary of Chapter 3.....	160
5.3 Summary of Chapter 4.....	161
5.4 Future Work Stemming from Chapter 4: Azidophosponamide Isomerization.	162
5.5 Conclusions from Chapters 2 and 4.....	164
5.6 Towards Substituting COD for COE Chapters 2 and 4.....	165
5.7 Conclusions from Preliminary Work Substituting COD with Two COE Ligands in Chapter 4.....	167
5.8 Future Work Stemming from Chapters 2 and 4: COE Complexes and Catalysis	167
Chapter 6: Experimental Methods	171
6.1 General Laboratory Equipment	171
6.2 Solvents.....	171
6.3 Chemical Materials	172
6.4 Instrumentation Details for NMR Experiments.....	173
6.5 X-ray Crystallographic Details	174
6.6 Elemental Analysis Details.....	174
6.7 Additional Instrumentation.....	175
6.8 Naming Conventions of Adamantyl Groups	175
6.9 Synthetic Experimental Procedures Pertaining to Chapter 2.....	175
6.10 Synthetic Experimental Procedures Pertaining to Chapter 3.....	189
6.11 Synthetic Experimental Procedures Pertaining to Chapter 4.....	200

Chapter 7: References	212
Appendix 1– Crystallographic Data Tables	223

LIST OF TABLES

Table 2.1 Selected bond distances (Å) and angles (°) for compound 1	46
Table 2.2 Selected bond distances (Å) and angles (°) for compound 3	50
Table 2.3 Selected bond distances (Å) and angles (°) for compound 4	52
Table 2.4 Selected bond distances (Å) and angles (°) for compound 5	56
Table 2.5 Selected bond distances (Å) and angles (°) for compound 6	58
Table 2.6 TEP values for known NHC complexes and compound 5-6	61
Table 2.7 Selected bond distances (Å) and angles (°) for compound 7	67
Table 2.8 Selected bond distances (Å) and angles (°) for complex 8	71
Table 2.9 Selected bond distances (Å) and angles (°) for complex 9	75
Table 2.10 Selected bond distances (Å) and angles (°) for compound 10	77
Table 2.11 Selected bond distances (Å) and angles (°) for complex 13	87
Table 3.1 Selected bond distances (Å) and angles (°) for compound 16	107
Table 3.2 Selected bond distances (Å) and angles (°) for compound 17	110
Table 3.3 Selected bond distances (Å) and angles (°) for compound 18	114
Table 3.4 Selected bond distances (Å) and angles (°) for complex 20	118
Table 3.5 Selected bond distances (Å) and angles (°) for compound 21	120
Table 4.1 Selected bond distances (Å) and angles (°) for compound 22	131
Table 4.2 Selected bond distances (Å) and angles (°) for complex 23	134
Table 4.3 Selected bond distances (Å) and angles (°) for compound 24	140
Table 4.4 Selected bond distances (Å) and angles (°) for compound 25	142
Table 4.5 TEP _{Rh} values (cm ⁻¹) for known κ ² - <i>N,N'</i> monoanionic complexes and complexes 5, 6, and 24-27	146
Table 4.6 Selected bond distances (Å) and angles (°) for compound 28	152
Table 4.7 Selected bond distances (Å) and angles (°) for compound 29	156
Table A1.1 X-ray crystallography data of compounds Ph ₂ P(NAd)(NHAd) (2) and Ph ₂ P(NMes) ₂ Rh(COD) (3).....	223
Table A1.2 X-ray crystallography data of compounds Ph ₂ P(NAd) ₂ Rh(COD)•1.5C ₆ H ₆ (4) and Ph ₂ P(NMes) ₂ Rh(CO) ₂ (5)	224
Table A1.3 X-ray crystallography data of compounds Ph ₂ P(NAd) ₂ Rh(CO) ₂ (6) and Ph ₂ P(NMes) ₂ Rh(CN(2,6-Me ₂ C ₆ H ₃)) ₂ (7)	225
Table A1.4 X-ray crystallography data of compounds and Ph ₂ P(NMes) ₂ Rh(CN(2,6- Me ₂ C ₆ H ₃)) ₃ (8) and Ph ₂ P(NMes) ₂ Ir(COD) (9)	226
Table A1.5 X-ray crystallography data of compounds Ph ₂ P(NAd) ₂ Ir(COD)•1.5C ₆ H ₆ (10) and Ph ₂ P(NMes) ₂ Rh(COE) ₂ •0.5C ₆ H ₆ (13)	227
Table A1.6 X-ray crystallography data of compounds ⁱ Pr ₂ P(N ₃ Ad)(NHAd) (15) and [ⁱ Pr ₂ P(N ₃ Ad)(NAd)]Li•0.5CH ₂ Cl ₂ (16).....	228
Table A1.7 X-ray crystallography data of compounds [ⁱ Pr ₂ P(N ₃ Ad)(NAd)-κ ² - <i>N,N'</i>] Rh(COD) (18) and [ⁱ Pr ₂ P(N ₃ Mes)(NMes)-κ ² - <i>N,N'</i>] Rh(COD) (20)	229
Table A1.8 X-ray crystallography data of compounds [ⁱ Pr ₂ P(N ₃ Mes)(NMes)-κ ² - <i>N,N'</i>] Ir(COD) (21) and [ⁱ Pr ₂ P(N ₃ Mes)(NMes)-κ ² - <i>N,N'</i>] Rh(COD) (22)	230

Table A1.9 X-ray crystallography data of compounds [$i\text{Pr}_2\text{P}(\text{N}_3\text{Mes})(\text{NMes})-\kappa^2-N,N^\beta$]Ir(COD) (23) and [$i\text{Pr}_2\text{P}(\text{N}_3\text{Ad})(\text{NAd})-\kappa^2-N,N^\alpha$]Rh(CO) ₂ (24).....	231
Table A1.10 X-ray crystallography data of compounds [$i\text{Pr}_2\text{P}(\text{N}_3\text{Ad})(\text{NAd})-\kappa^2-N,N^\alpha$]Ir(CO) ₂ (25) and [$i\text{Pr}_2\text{P}(\text{NMes})(\text{N}_3\text{Mes})-\kappa^2-N,N^\alpha$]Rh(COE) ₂ (28).....	232
Table A1.11 X-ray crystallography data of compounds [$i\text{Pr}_2\text{P}(\text{NMes})_2$]Rh(COE) ₂ (29)...	233

LIST OF FIGURES

Figure 1.1 Metal-to-ligand orbital interaction of CO ligands, σ -donation (left) and π -backdonation (right). Note, only one of the two degenerate CO LUMO π^* -antibonding orbitals is depicted	8
Figure 1.2 Influence of a σ -donating phosphine on π -backbonding	10
Figure 1.3 Visual representation of the definition of cone angle.....	10
Figure 1.4 Visual representation of the definition of bite angle	11
Figure 1.5 Visual representation of non-bent (left) and bent (right) metallocenes.....	12
Figure 1.6 Example of an activated Ziegler-Natta catalyst.....	13
Figure 1.7 Three examples of activated <i>ansa</i> -zirconocene catalysts directing the polymerization of propene to isotactic, syndiotactic, and atactic polypropylene ..	14
Figure 1.8 An example of a constrained geometry catalyst (CGC).....	16
Figure 1.9 Diversity of coordination modes of NacNac ligands in mononuclear coordination compounds ⁶⁹	17
Figure 1.10 General structures of amidinate (left) and guanidinate (right) ligands.....	18
Figure 1.11 Coordination modes of amidinate and guanidinate ligands	19
Figure 1.12 General structures of hybrid amidinate and guanidinate ligands	19
Figure 1.13 General representation of a pincer ligand.....	21
Figure 1.14 Structure of an NHC (left) and bonding diagram (right) to explain the stabilizing effect of the adjacent nitrogen atoms	21
Figure 1.15 Comparison of the resonance structure(s) of imine and phosphinimines.....	23
Figure 1.16 General structural examples of <i>endo</i> (left) and <i>exo</i> (right) phosphinimines ..	25
Figure 1.17 Primary coordination modes of $[\text{CH}(\text{Ph}_2\text{P}=\text{NR})_2]^-$ (left), and $[\text{C}(\text{Ph}_2\text{P}=\text{NR})_2]^{2-}$ (right) to a metal centre	26
Figure 1.18 Structure of amidinates and iminophosponamides and their resonance forms	30
Figure 1.19 Schematic drawing of the HOMO orbitals of iminophosponamides (top), β -diketiminato (middle), and amidinate (bottom) ligands π -bonding with a metal d_{xz} orbital	31
Figure 1.20 Structure of co-crystallized azidophosponamido and iminophosponamido lithium salt ¹²⁷	34
Figure 2.1 Resonance forms of amidinate and iminophosponamide ligands	38
Figure 2.2 Salt metathesis reaction using an alkali metal iminophosponamide species ¹³⁰ (left); an enantiopure calcium complex ¹³¹ (right)	40
Figure 2.3 Group 3 and 4 iminophosponamide polymerization catalysts ^{120,124}	40
Figure 2.4 First-row transition metal iminophosponamide catalysts ¹²¹⁻¹²³	41
Figure 2.5 Late transition metal iminophosponamido complexes reported by Kalsin <i>et al.</i> ^{125,132,134}	42
Figure 2.6 X-ray crystal structure of 1 depicted as 50% displacement ellipsoids. Hydrogen atoms (except H1) are omitted for clarity	45

Figure 2.7 X-ray crystal structure of 3 depicted as 50% displacement ellipsoids. Hydrogen atoms are omitted for clarity	49
Figure 2.8 X-ray crystal structure of 4 •1.5C ₆ H ₆ depicted as 50% displacement ellipsoids. Hydrogen atoms and solvent molecules are omitted for clarity	51
Figure 2.9 X-ray crystal structure of 5 depicted as 50% displacement ellipsoids. Hydrogen atoms and one of the two independent molecules of 5 in the unit cell are omitted for clarity.....	55
Figure 2.10 X-ray crystal structure of 6 depicted as 50% displacement ellipsoids. Hydrogen atoms are omitted for clarity	57
Figure 2.11 ³¹ P{ ¹ H} NMR spectrum of the 2 (2,6-Me ₂ C ₆ H ₃ N≡C) + 3 reaction mixture: δ 25.1 (d, ² J _{RhP} = 13.7 Hz, 68%, 7), 15.2 (32%, 8).....	65
Figure 2.12 X-ray crystal structure of 7 , depicted as 50% displacement ellipsoids. Hydrogen atoms are omitted for clarity	66
Figure 2.13 X-ray crystal structure of 8 •C ₆ H ₆ depicted as 50% displacement ellipsoids. Hydrogen atoms and the solvent molecule are omitted for clarity	69
Figure 2.14 X-ray crystal structure of 9 depicted as 50% displacement ellipsoids. Hydrogen atoms are omitted for clarity	74
Figure 2.15 X-ray crystal structure of 10 •1.5C ₆ H ₆ depicted as 50% displacement ellipsoids. Hydrogen atoms and solvent molecules are omitted for clarity	76
Figure 2.16 Proposed structures of 2,6-Me ₂ C ₆ H ₃ N≡C iridium complexes 11 and 12	80
Figure 2.17 ³¹ P{ ¹ H} NMR spectrum of the 2:1 2,6-Me ₂ C ₆ H ₃ N≡C to 9 reaction mixture: δ 40.9 (17%, 9), 37.7 (21%, 11), 23.0 (26%, 12), -15.4 (6%, I).....	81
Figure 2.18 Aromatic and aliphatic regions of the ¹ H NMR spectrum of complex 13	85
Figure 2.19 X-ray crystal structure of 13 •1.5C ₆ H ₆ depicted as 50% displacement ellipsoids. Hydrogen atoms and solvent molecules are omitted for clarity	86
Figure 3.1 The phosphazide N atom naming convention used throughout this work and coordination modes displayed by metal-coordinated phosphazides ¹⁵¹	91
Figure 3.2 Proposed structure of the first transition metal phosphazide complex ¹⁵⁸	95
Figure 3.3 Structure of co-crystallized azidophosponamido lithium salts ¹²⁷	97
Figure 3.4 Resonance forms of amidinate and iminophosponamide ligands	100
Figure 3.5 X-ray crystal structure of 16 depicted as 50% displacement ellipsoids. Hydrogen atoms (except H1) are omitted for clarity	106
Figure 3.6 X-ray crystal structure of 17 •CH ₂ Cl ₂ depicted as 50% displacement ellipsoids. Hydrogen atoms and the solvent molecule (CH ₂ Cl ₂) are omitted for clarity	109
Figure 3.7 Two possible azidophosponamide resonance structures placing the anionic charge of the ligand on the N ^α (left) or the phosphonamido nitrogen (right)	110
Figure 3.8 X-ray crystal structure of 18 depicted as 50% displacement ellipsoids. Hydrogen atoms are omitted for clarity	112
Figure 3.9 X-ray crystal structure of 20 depicted as 50% displacement ellipsoids. Hydrogen atoms are omitted for clarity	117
Figure 3.10 X-ray crystal structure of 20 depicted as 50% displacement ellipsoids. Hydrogen atoms are omitted for clarity	119

Figure 4.1 X-ray crystal structure of 22 depicted as 50% displacement ellipsoids. Hydrogen atoms are omitted for clarity. Only one of the two independent molecules of 22 in the unit cell is shown.....	128
Figure 4.2 X-ray crystal structure of 23 depicted as 50% displacement ellipsoids. Hydrogen atoms are omitted for clarity. Only one of the two independent molecules of 23 in the unit cell is shown.....	133
Figure 4.3 X-ray crystal structure of 24 depicted as 50% displacement ellipsoids. Hydrogen atoms are omitted for clarity	139
Figure 4.4 X-ray crystal structure of 25 depicted as 50% displacement ellipsoids. Hydrogen atoms are omitted for clarity	141
Figure 4.5 X-ray crystal structure of 28 depicted as 50% displacement ellipsoids. Hydrogen atoms are omitted for clarity	151
Figure 4.6 X-ray crystal structure of 29 depicted as 50% displacement ellipsoids. Hydrogen atoms are omitted for clarity	155

LIST OF SCHEMES

Scheme 1.1 Oxidative addition (forward reaction) and reductive elimination (reverse reaction) of X–Y bond toward a metal complex ML_n	3
Scheme 1.2 General reaction schemes for most common Rh or Ir catalyzed processes ¹⁸ ...	4
Scheme 1.3 Example of Rh-catalyzed Heck coupling, the initial mechanism proposed by Hartwig and Ishiyama. ²¹	5
Scheme 1.4 Pd^{II} and Rh^I -catalysed conjugate addition model proposed by Wu <i>et al</i> ²²	6
Scheme 1.5 An example of a Kirsanov reaction that generates a phosphinimine	24
Scheme 1.6 An example of a Staudinger reaction that generates a phosphinimine	25
Scheme 1.7 Formation of rhodium ^I silylenes by a dehydrogenative process	27
Scheme 1.8 An example Staudinger reaction showing the two conformers of a phosphazide.....	28
Scheme 1.9 Proposed general synthesis for iminophosphonamido bearing Rh^I and Ir^I COD complexes	32
Scheme 1.10 Stepwise functionalization of CO_2 mediated by a diphosphazide-supported thorium complex ¹¹⁷	34
Scheme 1.11 Proposed synthetic route to alkyl-substituted azido- and imino-phosphonamide ligands.....	36
Scheme 1.12 Proposed general synthesis for alkyl-substituted azido- and imino-phosphonamido Rh^I and Ir^I COD complexes.....	36
Scheme 1.13 Thermally or photochemically induced linkage isomerism of the phosphazide moiety exhibited by the mesityl-substituted azidophosphonamido complexes	37
Scheme 2.1 Synthesis of Mes-Substituted iminophosphonamido lithium salt $Li[Ph_2P(NMes)_2]^{127}$	43
Scheme 2.2 Synthesis of 1 and 2	44
Scheme 2.3 Synthesis of iminophosphonamido-rhodium COD complexes 3 and 4	47
Scheme 2.4 Synthesis of Rh^I carbonyl complexes 5 and 6	53
Scheme 2.5 Attempted synthesis of Rh^{III} silyl iminophosphonamido complexes.....	62
Scheme 2.6 Attempted synthesis of Rh^{III} dihydride iminophosphonamido complexes	63
Scheme 2.7 Attempted synthesis of Rh^I phosphine iminophosphonamido complexes	64
Scheme 2.8 Synthesis of 7 and 8	69
Scheme 2.9 Synthesis of iminophosphonamido- Ir^I COD complexes 9 and 10	73
Scheme 2.10 Attempted synthesis of Ir^I carbonyl and Ir^{III} dihydride iminophosphonamido complexes	79
Scheme 2.11 Attempted synthesis of Ir^{III} silyl iminophosphonamido complexes	83
Scheme 2.12 Synthesis of the Rh^I COE complex 13	84
Scheme 3.1 The Staudinger reaction	89
Scheme 3.2 Stepwise functionalization of CO_2 mediated by a diphosphazide-supported thorium complex ¹¹⁷	92
Scheme 3.3 Two synthetic routes to metal phosphazide complexes ¹⁵²⁻¹⁵⁴	93

Scheme 3.4 Synthesis of the first K-stabilized phosphazide and subsequent salt metathesis reaction to afford κ^2 - <i>N,N'</i> -[(2,6- ⁱ Pr ₂ C ₆ H ₄ N=C ₅ H ₆) ⁱ Pr ₂ PN ₃ (2,6-Me ₂ C ₆ H ₄)]FeBr•THF ¹⁵⁵	94
Scheme 3.5 Synthesis of phosphazide-containing ligands ^{115,156}	95
Scheme 3.6 Complete Staudinger reaction forming an iminophosphonamide (top, green box) and the azidophosphonamide isomers VIII , IX , and X (middle, purple box), which eventually form the azidophosphonamido impurities VI and VIII ¹²⁷	98
Scheme 3.7 Attempted synthesis of K[ⁱ Pr ₂ P(NMes)(N ₃ Mes)], 14	102
Scheme 3.8 Synthesis of K[ⁱ Pr ₂ P(NMes)(N ₃ Mes)], 14	103
Scheme 3.9 Synthesis of ⁱ Pr ₂ P(NHAd)(N ₃ Ad), 16	104
Scheme 3.10 Synthesis of [ⁱ Pr ₂ P(N ₃ Ad)(NAd)- κ^2 - <i>N,N'</i>]M(COD), M = Rh (18) and Ir (19)	111
Scheme 3.11 Synthesis of [ⁱ Pr ₂ P(N ₃ Mes)(NMes)- κ^2 - <i>N,N'</i>]M(COD)], where M = Rh (20), Ir (21)	115
Scheme 4.1 Photochemically induced linkage isomerism of a phosphazidoborane ¹⁶⁴	123
Scheme 4.2 Photochemically induced linkage isomerism of a phosphazinoborane ¹⁶⁴	124
Scheme 4.3 Formation of various phosphazide-containing FLPs ¹¹⁶	125
Scheme 4.4 Possible structures of the minor impurities observed during the synthesis of complexes 20 and 21	127
Scheme 4.5 Phosphazide linkage isomerism of the N ^{α} →B to the N ^{β} →B coordination mode; as reported by Bourissou (top left), ¹⁶⁴ Slootweg (top right) ¹¹⁶ and exhibited by Rh ^I and Ir ^I azidophosphonamido complexes 20 and 21	130
Scheme 4.6 Thermally or photochemically induced linkage isomerism of complexes 20 and 21	133
Scheme 4.7 Synthesis of [ⁱ Pr ₂ P(N ₃ Ad)(NAd)- κ^2 - <i>N,N'</i>]M(CO) ₂ , M = Rh (24), Ir (25) ...	137
Scheme 4.8 Synthesis of [ⁱ Pr ₂ P(N ₃ Mes)(NMes)- κ^2 - <i>N,N'</i>]M(CO) ₂ , M = Rh (26), Ir (27)	143
Scheme 4.9 Synthesis of [ⁱ Pr ₂ P(N ₃ Mes)(NMes)]Rh(COE) ₂ 28	150
Scheme 4.10 Synthesis of [ⁱ Pr ₂ P(NMes) ₂]Rh(COE) ₂ 29	154
Scheme 5.1 General synthetic route to generate Rh ^I and Ir ^I imino- and azidophosphonamido complexes 3 , 4 , 9 , and 10	159
Scheme 5.2 Reaction of Rh ^I iminophosphonamido complexes 3 and 4 towards strong π -accepting ligands	160
Scheme 5.3 Synthetic route to azidophosphonamide ligand salts 14 , 17	160
Scheme 5.4 General synthetic route to generate Rh ^I and Ir ^I azidophosphonamido complexes 18-22	161
Scheme 5.5 Reaction of Rh ^I iminophosphonamido complexes 18-20 towards CO	161
Scheme 5.6 Linkage isomerism of mesityl-substituted azidophosphonamido complexes 22 and 23	162
Scheme 5.7 Phosphazide-containing FLP linkage isomers reported by Slootweg <i>et al.</i> ¹¹⁶	163
Scheme 5.8 Proposed synthesis and linkage isomerism of Pipp and Dipp substituted azidophosphonamido complexes	164
Scheme 5.9 Complexes that are inert to an atmosphere of CO	165

Scheme 5.10 Synthesis of $[\text{Ph}_2\text{P}(\text{NMe}_s)_2]\text{Rh}(\text{COE})_2$ 13 , and $[\text{Pr}_2\text{P}(\text{N}_3\text{Me}_s)(\text{NMe}_s)]\text{Rh}(\text{COE})_2$ 28	166
Scheme 5.11 Synthesis of $[\text{Pr}_2\text{P}(\text{NMe}_s)_2]\text{Rh}(\text{COE})_2$ 29	167
Scheme 5.12 Proposed synthetic route to COE imino- and azidophosponamido species	168
Scheme 5.13 Example of proposed substitution reactions, replacing COD to generate dihydride and silyl complexes, expanding the family of imino- and azidophosponamido complexes	169

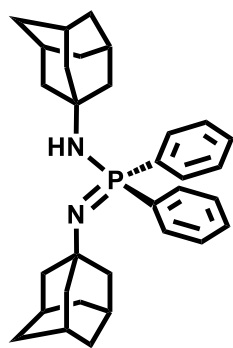
LIST OF SYMBOLS AND ABBREVIATIONS

%	percent
{ ¹ H}	proton decoupled
{ ³¹ P}	phosphorus decoupled
°	degree
Å	Angstrom
<i>a, b, c, α, β, γ</i>	crystallographic unit cell parameters
Ad	adamantyl (C ₁₀ H ₁₅)
AdN ₃	adamantyl-1-azide
Anal. Calcd.	analysis calculated
APT	attached proton test
Ar	aryl
br	broad
C	Celsius
CNAr	isocyanide with aryl group bound to N
CNR	isocyanide with aryl or alkyl group bound to N
COD	cyclooctadiene (C ₈ H ₁₂)
COE	cyclooctene (C ₈ H ₁₄)
COSY	correlated spectroscopy
Cp	η ⁵ -cyclopentadienyl (C ₅ H ₅)
Cp*	η ⁵ -pentamethylcyclopentadienyl (C ₅ Me ₅)
Cy	cyclohexyl (C ₆ H ₁₁)
d	doublet
D, X	donor atom
DCM	dichloromethane (CH ₂ Cl ₂)
dd	doublet of doublets
DEPT	distortionless enhancement by polarization transfer
Dipp	2,6-diisopropylphenyl (2,6-iPr ₂ C ₆ H ₃)
DippN ₃	2,6-diisopropyl-1-azidophenyl
dppe	bis(diphenylphosphino)ethane (Ph ₂ PCH ₂ CH ₂ PPh ₂)
dppm	bis(diphenylphosphino)methane (Ph ₂ PCH ₂ PPh ₂)
<i>E</i>	entgegen, opposite arrangement of higher priority groups on a double bond
EA	elemental analysis
Et	ethyl (CH ₂ CH ₃)
Et ₂ O	diethylether (CH ₃ CH ₂) ₂ O
FLP	frustrated Lewis pair
Flu	fluorenyl (C ₆ H ₄) ₂ CH ₂
FWHM	full width half maximum
GooF	goodness of fit

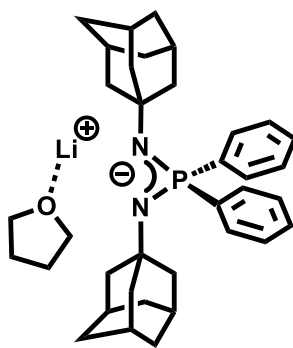
HMBC	heteronuclear multiple bond coupling
HMDS	bis(trimethylsilyl)amine, or hexamethyldisilazane ((Me ₃ Si) ₂ NH)
HOMO	highest occupied molecular orbital
HSQC	heteronuclear single quantum coherence
<i>hν</i>	light, nm not specified
Ind	indenyl (C ₆ H ₄)C ₃ H ₃
iPr	isopropyl (CH(CH ₃) ₂)
IR	infrared
KHMDS	potassium bis(trimethylsilyl)amide
L	ligand
Li[HMDS]	lithium bis(trimethylsilyl)amine
LUMO	lowest unoccupied molecular orbital
M	metal
Me	methyl, or a CH ₃ group
Mes	2,4,6-trimethylphenyl (2,4,6-Me ₃ C ₆ H ₂)
MesN ₃	2,4,6-trimethyl-1-azidophenyl
MW	molecular weight
m	multiplet
ⁿ J _{X-Y}	coupling constant between nuclei X and Y, separated by n bonds
NacNac	1,3-diketimine or β-diketiminato ligand system
nBu	<i>n</i> -butyl
nBuLi	<i>n</i> -butyllithium
NaHMDS	sodium bis(trimethylsilyl)amide
NHC	N-heterocyclic carbene
NHSi	N-heterocyclic silylene
NMR	nuclear magnetic resonance
NPN ligand	iminophosphonamide ligand [R ₂ P(NR) ₂] ⁻
N ^α , N ^β , N ^γ	nitrogen naming system of phosphazides, where P–N ^α –N ^β –N ^γ
ov	overlapping
pTol	<i>para</i> -toluene (4-MeC ₆ H ₄)
Ph	phenyl
Pipp	4-isopropylphenyl (4- ⁱ PrC ₆ H ₄)
ppm	parts per million
Py	pyridine
R, R ¹ , R ²	defined organic group
s	singlet
t	triplet
tBu	<i>tert</i> -butyl
tBuLi	<i>tert</i> -butyllithium
TEP	Tolman electronic parameter
THF	tetrahydrofuran (C ₄ H ₈ O)
TM	transition metal

TMS	trimethylsilyl (SiMe_3)
Tol	toluene (MeC_6H_5)
UV	ultraviolet
Z	zusammen, opposite arrangement of higher priority groups on a double bond
Δ	change in heat
δ	chemical shift in parts per million
η^x	hapticity of order x
θ	ligand cone angle
κ^x	denticity of order x
μ^x	bridging of order x
τ_4	four-coordinate geometry index, used to help distinguish between tetrahedral or square planar geometries
τ'_4	alternate four-coordinate geometry index, used to help distinguish a seesaw geometry
ω	ligand bite angle

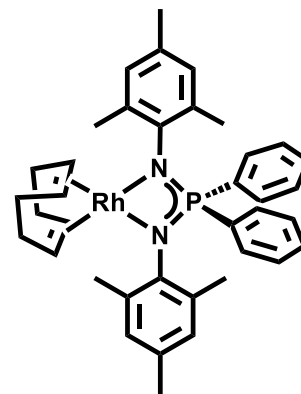
LIST OF NEW COMPOUNDS



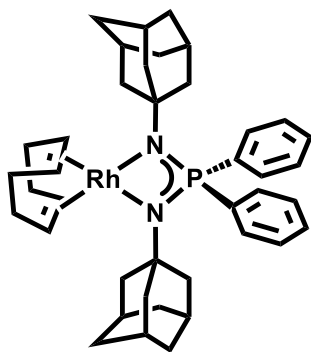
1



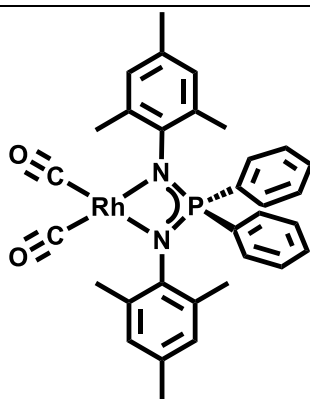
2



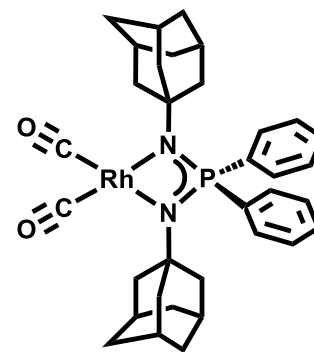
3



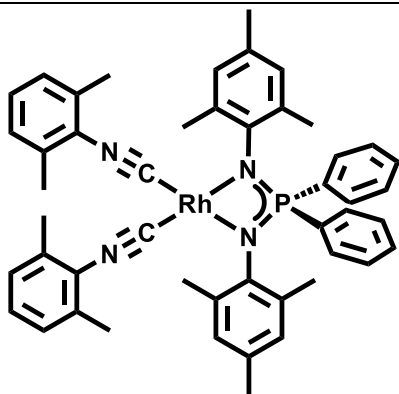
4



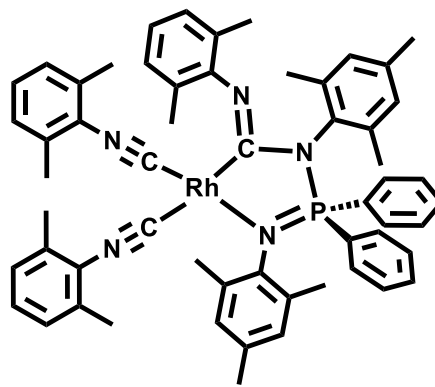
5



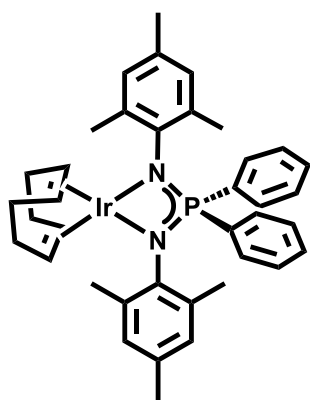
6



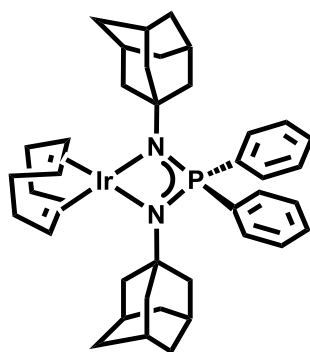
7



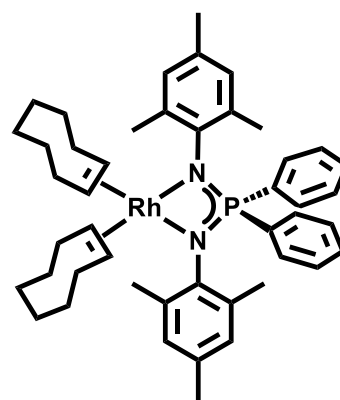
8



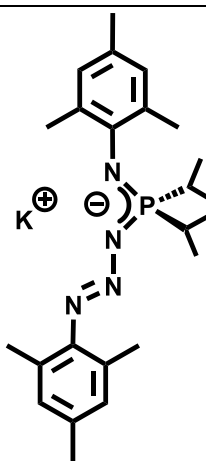
9



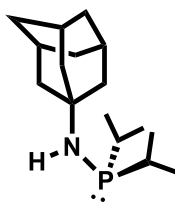
10



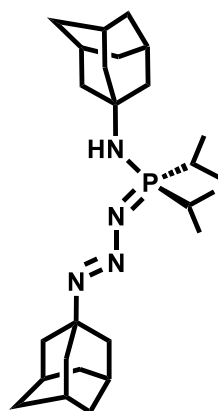
13



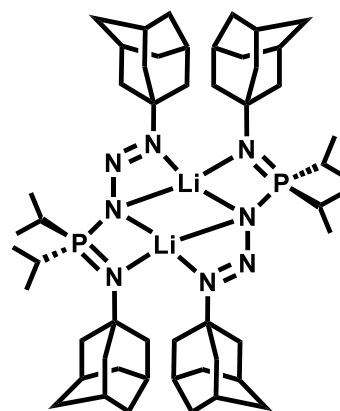
14



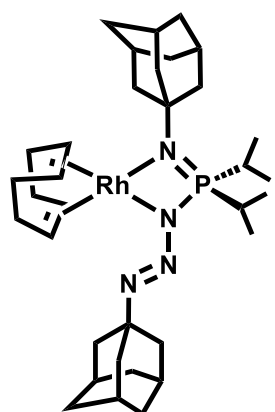
15



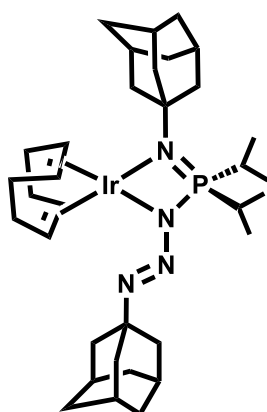
16



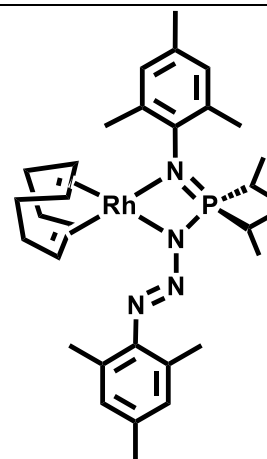
17



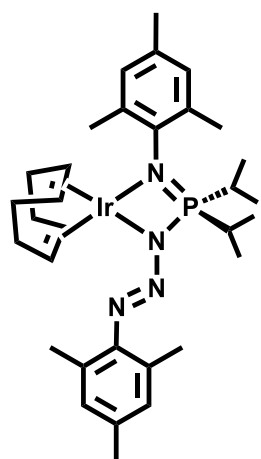
18



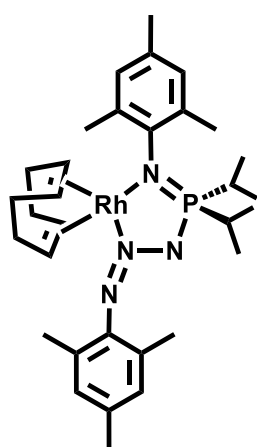
19



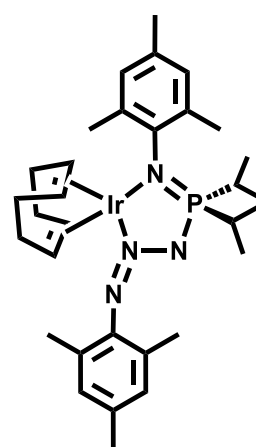
20



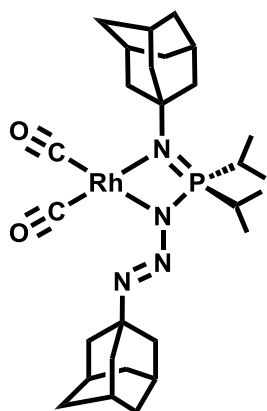
21



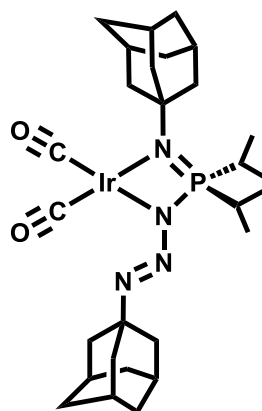
22



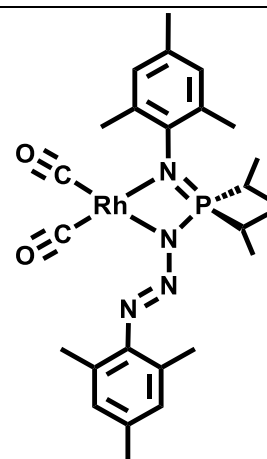
23



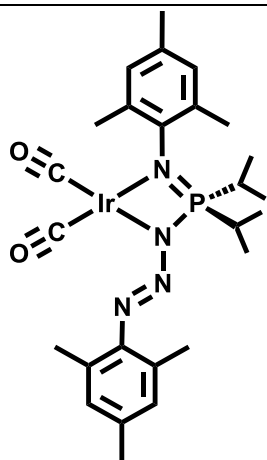
24



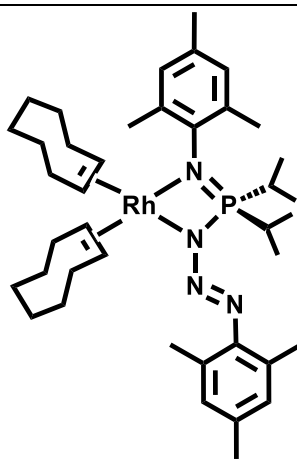
25



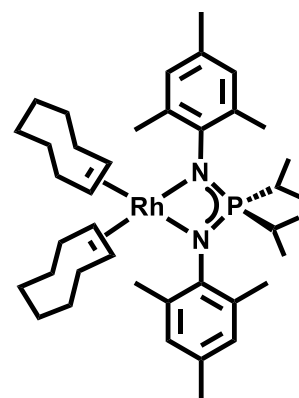
26



27



28



29

CHAPTER 1: INTRODUCTION

1.1 General Introduction

One of the greatest challenges in synthetic chemistry still consists of inventing new reactions to construct and modify carbon molecular architectures. Accordingly, synthetic chemistry has evolved to a state where it is commonly believed that a large amount of molecules can be synthetically produced, albeit given enough time and resources. Remarkable work done by several synthetic research groups in the 1990s led to the completion of the total synthesis of several natural products of great complexity; however, the synthetic routes were typically lengthy (30 to 60 steps).¹ For example, akuammiline alkaloid (\pm)-vincorine (part of the indole alkaloid family and used in a variety of biological applications) was originally generated *via* a 31-step process with an overall yield of 1%.²

Parallel to total synthesis advances, the field of transition metal catalysis has undergone remarkable developments, particularly over the last 40 years.¹ Employing transition metals as catalysts expedites the reaction *via* lowering the energy barrier between products and reagents, facilitating chemical transformations that would not normally occur, at least at an appreciable rate, when mixing said reagents together without the catalyst. The addition of a metal catalyst can yield pure or enantiopure products, instead of a difficult-to-separate mixture. Implementing catalytic steps in a synthesis may reduce the number of total reactions, as one catalyst can impart several formal transformations in a single operation. A modern total synthetic route to akuammiline alkaloid (\pm)-vincorine has employed several catalytic steps including intramolecular oxidative coupling, Pd-catalyzed

direct C–H functionalization and an organocatalyzed asymmetric Michael addition, thereby, reducing the number of steps from 31 to 18 and increasing the overall yield (5%).³ Similarly, employing asymmetric catalysis in the total synthesis of various indole alkaloids (\pm) has yielded enantiopure products while increasing overall yields (ranging from 13-45%) and decreasing the number of steps (ranging from 7-12 steps).⁴

1.2 Introduction to Metals and Ligands

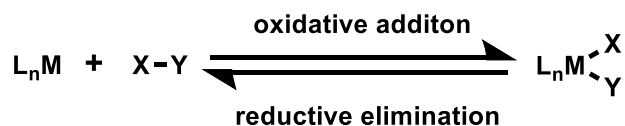
A metal complex is a species in which a metal atom is bound to one or more ligands (a molecule or ion that binds to a central atom).⁵ The binding ligands can affect the geometric environment and electronic properties at the metal center, thereby influencing its reactivity. A subset of metal complexes that contain, at minimum, one C–M bond are given the moniker organometallic and the prefix organo- (*e.g.* organorhodium is used to describe an organometallic rhodium species).

1.3 Noble Metal Catalysts

Homogeneous catalysis, featuring ligand-supported transition metal complexes, is now an indispensable tool for modern chemical transformations. Materials such as plastics and pharmaceuticals, which are essential to our standard of living, are generated by carbon-heteroatom and carbon-carbon bond-forming reactions, often catalyzed by noble transition metal (Ru, Os, Rh, Ir, Pd, Pt, and Au) complexes.⁶⁻⁹

Two-electron reactions are common steps within a catalytic cycle; specific reactions, namely, reductive elimination and oxidative addition, are often the rate-determining step of a catalytic process. Oxidative addition to a metal complex most

frequently raises the coordination number and oxidation state of the transition metal centre by 2, and reductive elimination is the reverse (Scheme 1.1). Noble transition metal complexes (Ru, Os, Rh, Ir, Pd, Pt, and Au) exhibit increased stability under various reaction conditions and tend to perform two-electron transformations, unlike first-row transition metals.⁶ Thus, noble transition metals have been employed in various catalytic processes; well-known examples of such catalytic transformations include ruthenium-catalyzed alkene cross-metathesis,⁷ rhodium-catalyzed asymmetric hydrogenations,⁸ and palladium-catalyzed cross-coupling reactions.⁹

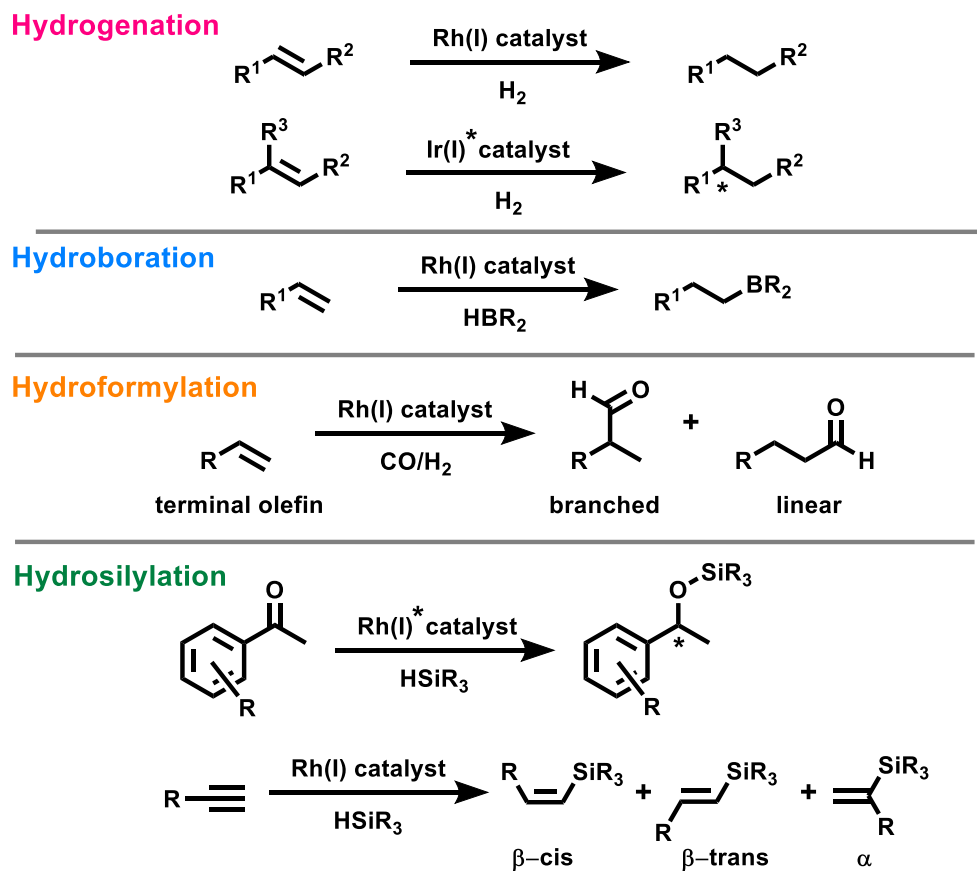


Scheme 1.1 Oxidative addition (forward reaction) and reductive elimination (reverse reaction) of X–Y bond toward a metal complex ML_n

1.4 Importance of Rhodium and Iridium in Catalysis

Group 9 metal rhodium has been employed for a broad range of chemical transformations, making it one of the more essential metals for catalysis.¹⁰ The origin of homogeneous rhodium catalysis can be traced back to Wilkinson's chloridotris(triphenylphosphine)rhodium(I), $[\text{RhCl}(\text{PPh}_3)_3]$, in the mid-60s:¹¹ wherein the complex was employed for the hydrogenation of olefins (Scheme 1.2).¹² Vaska's complex $\text{IrCl}(\text{CO})(\text{PPh}_3)_2$ provided the conceptual framework for homogenous catalysis in reversibly activating O_2 ;¹³ however, it is Crabtree's organoiridium hydrogenation catalyst $[(\text{COD})\text{Ir}(\text{PCy}_3)(\text{Py})]\text{PF}_6$ that is attributed to sparking modern iridium homogeneous

catalysis.¹⁴ Since then, numerous rhodium, and heavier group 9 element iridium, complexes have been prepared and applied to several catalytic hydrofunctionalization reactions such as alkene hydroformylation,¹⁵ hydroboration,¹⁶ and hydrosilylation¹⁷ (Scheme 1.2).^{10,18}

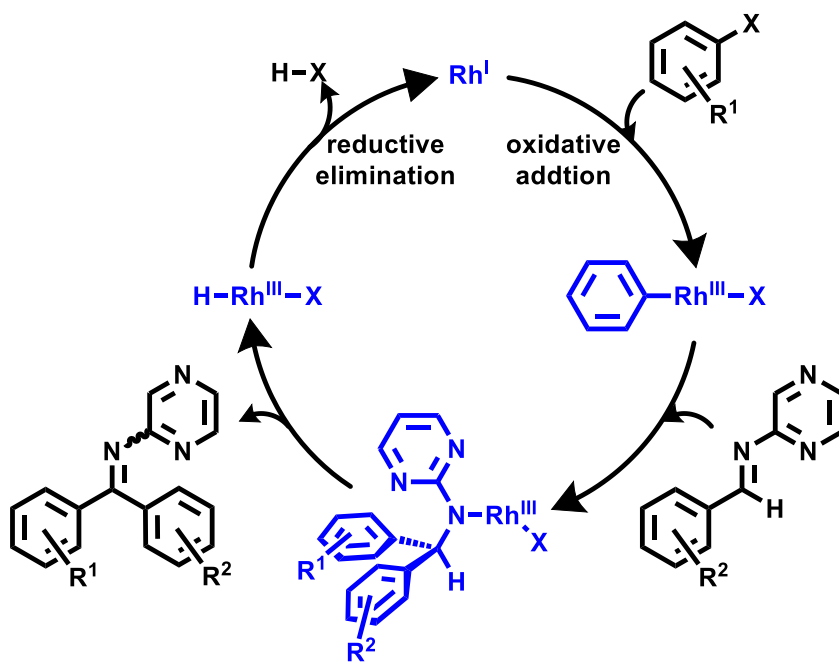


* = formation of a stereocenter (*R* or *S*) which is controlled *via* a stereoselective catalyst

Scheme 1.2 General reaction schemes for most common Rh or Ir catalyzed processes¹⁸

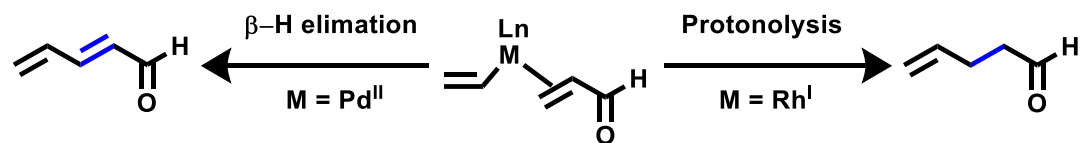
Rhodium, and to a lesser extent iridium, provide unmatched levels of chemo-, regio-, and stereoselectivity for cycloaddition, alkene addition, C–H insertion, and hydrofunctionalization reactions. Rhodium and iridium generally operate between the M^I

and M^{III} oxidation states within catalytic cycles, while other metals (Pt, Pd, Ni, or Ru) shuttle between the M^0 and M^{II} states.¹⁹ Fundamentally M^{II} ($M = Pt, Pd, Ni$ or Ru) and Rh^I -catalysed reactions share some similarities as most elementary steps in various catalytic processes follow two-electron transfer mechanisms. For example, Heck coupling (Scheme 1.3) can employ either Pd^{II} or Rh^I catalysts.²⁰



Scheme 1.3 Example of Rh-catalyzed Heck coupling, the initial mechanism proposed by Hartwig and Ishiyama.²¹

In 2012, Wu *et al.* found that the termination of Heck coupling of α,β -unsaturated carbonyls involved two competitive steps; β -hydride elimination and protonolysis.²² The Pd^{II} -catalyzed process generated Heck-type products (Scheme 1.4, right), while an isoelectronic Rh^I catalyst yielded unsaturated β -hydride elimination products (Scheme 1.4, left).²²



Scheme 1.4 Pd^{II} and Rh^I-catalysed conjugate addition model proposed by Wu *et al*²²

Further investigations into C–H bond functionalization of the analogous Rh^I and Pd^{II} complexes suggested that formyl C–H bond cleavage is more facile for rhodium species due to lower energy pathways, leading to milder reaction conditions.²³ A similar Rh^{III} complex was also shown to perform C–H transformations while maintaining redox neutrality, as internal oxidants are involved as reactants, which has yet to be demonstrated for any Pd^{II} species.²³

1.5 Principles of Ligand Design: A Historical Perspective

Enormous numbers of reported transition metal catalysis have examined various ligands and donor atoms to discover the optimal catalyst for any given reaction, or niche substrate in terms of selectivity, and activity. The bound ligands strongly affect the electronic and geometric environment at, or around the metal centre; therefore, systematic modification of a ligand's steric or electronic properties necessarily influences the catalytic intermediates, products, and rates of reactions. For example, sterically bulky ligands prevent substrates above a specific size from coordinating to the metal centre. Excessively stable metal-to-substrate bonding interactions can retard or prohibit further reactivity of the complex

1.5.1 Metal Carbonyls and Other π -Acceptor Ligands

An essential and versatile ligand throughout transition metal chemistry has been carbon monoxide (CO).²⁴ Historically, metal complexes bearing CO ligands, metal carbonyls, have played a vital role in the chemical industry. The homoleptic nickel tetracarbonyl complex $\text{Ni}(\text{CO})_4$ ²⁵ was applied to the preparation of ultrapure nickel in 1890.²⁶ Numerous industrial processes also employ carbon monoxide as a reactant, and various metal catalysts involve metal carbonyl intermediates.^{13,27,28} Other π -acceptor ligands, such as cyanide, ethylene, and isocyanides also have historical significance. The earliest known synthetic complexes Prussian blue $\text{Fe}_4[\text{Fe}(\text{CN})_6]_3$,²⁹ and Turnbull's blue, $\text{Fe}_3[\text{Fe}(\text{CN})_6]_2$,³⁰ features cyano ligands.³¹ The first organometallic complex, discovered in 1827, $\text{K}[\text{PtCl}_3(\text{C}_2\text{H}_4)]$, better known as Zeise's salt,³² features an ethylene ligand. However, the exact bonding mode of the olefin was not confirmed until 1969.³³ More recent developments in the chemistry of metal carbonyls include highly-reduced metal carbonyl anions,^{34,35} and the first *f*-block carbonyl complexes $[(\text{C}_5\text{Me}_4\text{H})\text{U}(\text{CO})]$.³⁶ Notably, alkaline earth metal³⁷ and metalloidal³⁸ carbonyl complexes demonstrate that CO can bind to a central atom incapable of π -backdonation interactions (due to the lack of d-electrons); however, these complexes employ sterically bulky and stabilizing pentamethylcyclopentadienyl (Cp^*) ligands.

The binding mode of carbon monoxide is typically terminal; however, CO can bridge between multiple metal centres as exhibited in numerous metal complexes and clusters. Metal-to-carbonyl bonding involves synergistic σ -donor and π -backbonding interactions. The HOMO of CO donates a lone pair to an empty metal orbital;

simultaneously, electron density from a filled d -metal orbital is backdonated into the LUMO of CO (Figure 1.2). The backdonation into the two degenerate CO π^* -antibonding orbitals weakens the C \equiv O triple bond, while increasing the M=C double bond character. This weaker C \equiv O bond exhibits less C \equiv O triple bond character with increased backdonation, a phenomenon which can be directly observed *via* the decreasing ν_{CO} stretch in a complex's IR spectrum.³⁹

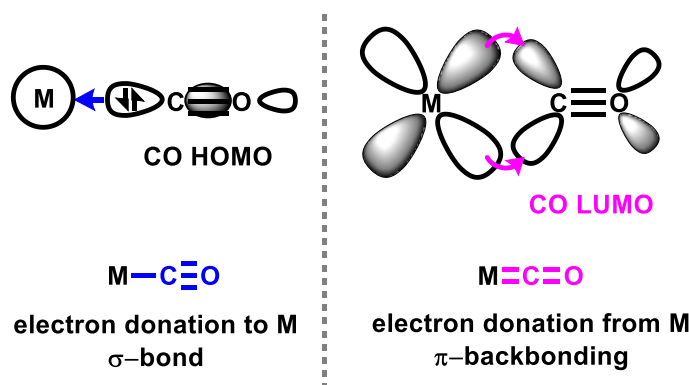


Figure 1.1 Metal-to-ligand orbital interaction of CO ligands, σ -donation (left) and π -backdonation (right). Note, only one of the two degenerate CO LUMO π^* -antibonding orbitals is depicted

1.5.2 Monodentate and Bidentate Phosphines: Controlling Ligand Properties

Phosphine ligands are ubiquitous throughout coordination chemistry and catalysis.⁴⁰ Metal-phosphine coordination complexes such as the Grubbs' catalyst $[(\text{PCy}_3)_2\text{RuCl}_2(\text{CHC}_6\text{H}_5)]$,⁷ Crabtree's catalyst $[(\text{COD})\text{Ir}(\text{PCy}_3)\text{Py}][\text{PF}_6]$,¹⁴ Vaska's complex $[\text{IrCl}(\text{CO})(\text{PPh}_3)_2]$,¹³ and Wilkinson's complex $[\text{RhCl}(\text{PPh}_3)_3]$,¹¹ underpin modern-day transition metal catalysis. The propensity for phosphines to adopt the role of spectator ligand boosts their catalytic applications; however, on rare occasions, phosphines can also act as reactive ligands to give cyclometallation⁴¹ or P-R bond cleavage products.⁴²

Like any ligand, the substituents of a phosphine govern the ligand's reactivity and behaviour, wherein a substituent is defined as a particular feature of a ligand that can be exchanged for alternate groups (*e.g.* R groups in the general phosphine PR_3). The relative ease by which one can fine-tune a phosphine's steric and electronic properties through alteration of its substituents is a critical factor in the prevalence of phosphines throughout homogeneous catalysts.⁴³

Initially, the effect of phosphine substituents was primarily rationalized in terms of electronic effects *via* the Tolman electronic parameter (TEP).⁴⁴ TEP directly measures the decrease in the infrared-stretching frequencies of CO ligands in the metal complex $[\text{LNi}(\text{CO})_3]$, thereby indirectly evaluating the donor abilities of a given ligand (L). The stronger the σ -donating abilities of L, the greater the electron density at the metal centre, which amplifies π -backdonation to CO, thereby lowering the frequency of the $\text{C}\equiv\text{O}$ stretch (ν_{CO}) in the IR spectrum (Figure 1.2).^{44,45} In contrast, if L is a poor σ -donor and a strong π -acceptor, then the phosphine competes with CO for π -backdonation, resulting in less lowering of the ν_{CO} stretching frequencies.^{44,45} For example, alkyl groups on phosphorus lead to a strongly σ -donating ligand,^{44,45} while aryl groups on P generate a stronger π -accepting phosphine.^{44,45} Controlling electron density about the metal centre directly influences catalysis, as oxidative addition is facilitated best by electron-rich metal centres possessing low oxidation states due to the increased electron density at the metal centre.

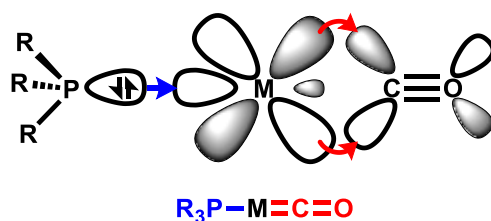


Figure 1.2 Influence of a σ -donating phosphine on π -backbonding

The term cone angle was introduced in 1977 to quantify the steric impact of a given ligand in a metal complex.⁴⁴ A cone angle encloses the van der Waals surfaces of all ligand's atoms and is measured at a set metal-to-phosphorus distance of 2.28 Å (Figure 1.3).⁴⁴ A larger cone angle is a consequence of more sterically bulky substituents. The tunability of the steric bulk is critical; larger ligands favour processes like reductive elimination, but sterically encumbering substituents inhibit substrate coordination. In cross-coupling reactions, phosphine ligands must be both sufficiently sterically encumbered and electron-rich.⁴⁴

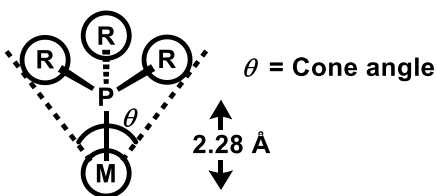


Figure 1.3 Visual representation of the definition of cone angle

The propensity of monodentate phosphines to dissociate yields a vacant coordination site which is often essential for stoichiometric or catalytic reactions; however, unwanted side reactions, such as β -hydride elimination, can also occur upon phosphine

dissociation.⁴⁴ Bidentate phosphines have been extensively explored as a potential solution to maintain the benefits of partial phosphine dissociation (*e.g.* one of the phosphine groups decoordinates) while mitigating unwanted side reactions as the dissociated phosphine can readily re-coordinate to the metal centre due to the chelate effect.⁴⁶ The chelate effect is the greater affinity of chelating ligands for a metal center than that of similar nonchelating (monodentate) ligands for the same metal; it is driven by entropy.⁴⁷

Electronic and steric modifications of bidentate phosphines can be extended to include the backbone; in particular, altering the bite angle can have powerful implications for catalysis.⁴⁸ The bite angle of a bidentate, chelating ligand is defined at the ligand-metal-ligand angle (Figure 1.4).⁴⁸ Many catalytic processes have reported optimal bite angles, which correlate with improved regio- or stereo-selectivity.⁴⁸

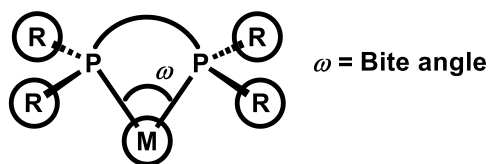


Figure 1.4 Visual representation of the definition of bite angle

The main drawback of most phosphine ligands is their sensitivity towards oxidation and, therefore, the requirement that they are handled under an inert atmosphere. In fact, many trialkylphosphines are pyrophoric. Accordingly, the generation of new phosphines *via* traditional synthetic routes can be fraught with toxic and highly reactive reagents; however, some synthetic approaches to new phosphines have been reported.⁴⁹ In contrast, PPh_3 does not readily oxidize when stored under ambient conditions and thus has been

utilized in various catalysts, for example, Vaska's $[\text{IrCl}(\text{CO})(\text{PPh}_3)_2]$,¹³ and Wilkinson's $[\text{RhCl}(\text{PPh}_3)_3]$ ¹¹ complexes.

1.5.3 Cp Ligands and Their Derivatives: The Start of Ancillary Ligand Design

A metallocene $[\text{M}^{\text{II}}(\text{C}_5\text{H}_5)_2]$ is an organometallic complex typically consisting of two parallel η^5 -monoanionic cyclopentadienyl ligands (C_5H_5^- , abbreviated to Cp) bound to a metal centre (Figure 1.5, left). A subset of metallocenes, wherein the rings bound to the metal are tilted at an angle instead of parallel, are denoted as bent metallocenes, and often feature additional ligands coordinated to the metal centre (Figure 1.5 right).

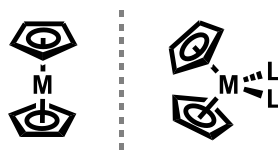


Figure 1.5 Visual representation of non-bent (left) and bent (right) metallocenes

Simultaneously discovered in 1951 by Kealy and Pauson,⁵⁰ and Miller et al.⁵¹, ferrocene $[\text{FeCp}_2]$, the first metallocene, expanded the idea of ligands involving more intricate chemical structures.^{52,53} Three years later, in 1954, Wilkinson and Birmingham synthesized $[\text{Cp}_2\text{TiCl}_2]$,⁵⁴ the first bent metallocene applied to the catalytic polymerization of α -olefins. In 1960, high-activity homogenous Ziegler-Natta catalysts (Figure 1.6)

produced polyethylene and polypropylene inexpensively and efficiently, later earning Ziegler and Natta the 1963 Nobel prize for their work.⁵⁵

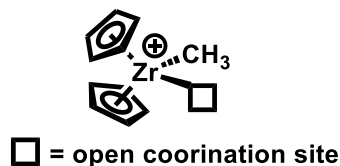


Figure 1.6 Example of an activated Ziegler-Natta catalyst

The Ziegler-Natta system sparked investigations into ancillary ligand design *via* tuning the substituents of cyclopentadienyls and observing the influence each modification had on olefin polymerization, *e.g.* tacticity (stereochemical control) and activity.⁵⁶ The success of Cp ligands in catalysis can be traced to several key factors; the large M–Cp bond dissociation energy, the ligand’s ability to occupy several coordination sites, the ligand’s tendency to adopt the role of ancillary ligand,⁵⁷ and their electronic and steric tunability. Pentamethylcyclopentadienyl ligand, $C_5(CH_3)_5^-$ designated as Cp^{*-} , is a Cp's common and more sterically demanding analogue of Cp.⁵⁸ An unintended advantage of methyl substituents on the Cp is their use to form catalytic intermediates wherein a methyl group is deprotonated and the resulting methylene binds to the metal forming a tuck-in complex.⁵⁸ The increased steric bulk of methyl substituents on Cp^* has allowed for the isolation of metallocene complexes for which the analogous Cp species was kinetically unstable or unknown. An equivalent to the Tolman method of ligand classification has yet to be adopted for Cp ligands, as trends in substituent alteration are less predictable. Exchanging cyclopentadienyl with indenyl or fluorenyl group further modifies the ligand’s architecture

with the additional fused benzo rings; this modification both increases the steric bulk around the metal centre and had yielded complexes with multiple accessible binding modes (η^5 , η^3 and η^1) achieved *via* ring slippage.⁵⁹ *ansa*-Metallocenes contain a one or multi-atom linker (*ansa*-bridge) between the two Cp, indenyl or fluorenyl ligands forcing a bent geometry about the metal centre (Figure 1.7). Group 4 *ansa*-bridged complexes have proved beneficial in olefin polymerization, namely due to their ability to impart direct control over the generated polymer properties (Figure 1.7).^{60,61} Disadvantages of Group 4 metallocene systems is the high oxophilicity of said metals and significant consumption of expensive activators, as the neutral bent metallocenes require activation to form the open coordination site on the activated catalyst (Figure 1.7) which is required for olefin polymerization.⁶²

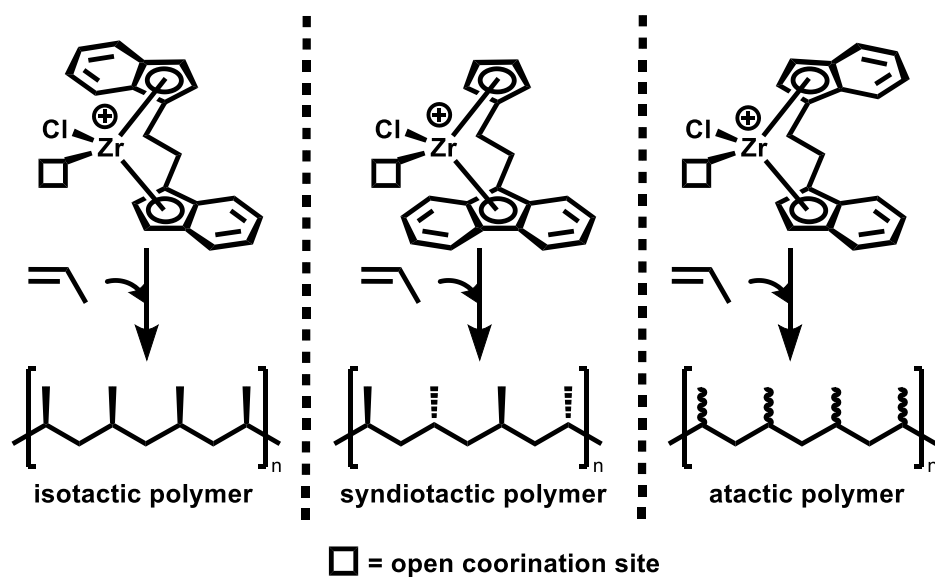


Figure 1.7 Three examples of activated *ansa*-zirconocene catalysts directing the polymerization of propene to isotactic, syndiotactic, and atactic polypropylene

The limitation of cyclopentadienyl ligands lie in their synthesis as cyclopentadiene readily dimerizes to dicyclopentadiene, typically necessitating cracking of the dimer at approximately 180 °C to form the monomer, which must be used soon thereafter. The steric bulk of pentamethylcyclopentadiene prevents rapid dimerization but requires a more complex and costly synthesis.⁶³ An exhaustive multitude of functionalized cyclopentadienyl complexes have been reported,⁶³ prompting the search for more effective catalysts using other ligand scaffolds and applications beyond olefin polymerization.

1.6 Principles in Ligand Design: Current Trends in Ligand Design

Classical ligands, such as phosphines, Cp, and Cp* derivatives, have been used extensively in the brief history of metal-catalyzed reactions and are still much used today. As previously stated, ancillary ligand design aims to control the metal centre's formal oxidation state, geometry, and coordination number, while influencing steric bulk about the active site to modulate selectivity. Over the last 20–30 years, a wide assortment of other tuneable ligand systems has been published and demonstrated to form selective and efficient transition metal species for various catalytic processes. The bridged Cp-containing ligands were first explored in the search for a new generation of olefin polymerization catalysts, often referred to as constrained geometry catalysts (CGC, Figure 1.8).⁶⁴

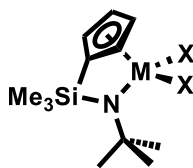


Figure 1.8 An example of a constrained geometry catalyst (CGC)

More recently, in the last 15–20 years, the metal–nitrogen bond, as opposed to the metal–carbon bond, has been utilized in various chelating ligand systems. The reactivity of the resultant transition metal complexes can be modified towards specific applications in areas such as organic synthesis,⁶⁵ homogeneous catalysis⁶⁶ or small molecule activation.⁶⁷ Similarly, the novel class of N-heterocyclic carbenes (NHC, see section 1.6.4) developed in the '90s and early 2000s, also referred to as “phosphine mimics”, were investigated to improve upon traditional phosphines. NHCs have since become a pervasive new class of compounds in both metal and non-metal catalysts.

Apart from early transition metals utilized throughout olefin polymerization and other catalytic processes, late transition metal catalysts (Ni, Pd, Fe, Ru, Co, Rh, and Cu) have gained popularity due to their higher oxidation resistance. Although general trends in the reactivity of specific metal complexes are identifiable, no metal nor ligand has universal catalytic application. Discovering the optimal combination of reaction conditions, substrate, metal centre and ligand is often a matter of exhaustive efforts in systematic alterations.

1.6.1 β -Diketiminato ‘NacNac’ Ligands

The ‘NacNac’ ligand class, better known as monoanionic β -diketiminates (BDI), has the general form $RC(R^1C=NR^2)_2^-$, where R, R^1 , and R^2 are H or aryl or alkyl groups. The bonding mode of NacNac ligands typically affords a six-membered metallacyclic ring *via* κ^2 - N,N' bidentate coordination (Figure 1.9, top left); however, many other less common coordination modes are known (Figure 1.9). These N,N' -chelating ligands have supported various transition metals across the periodic table.⁶⁸

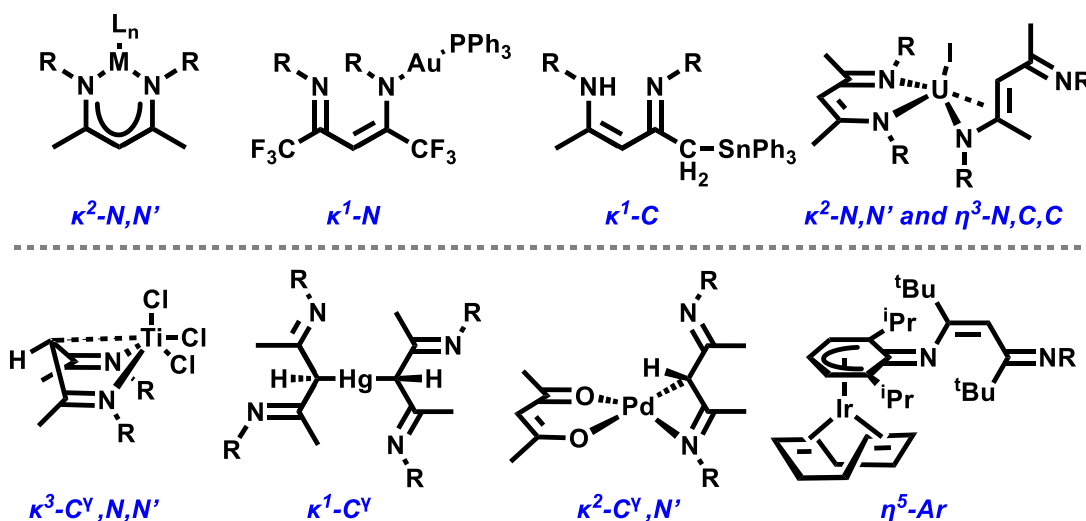


Figure 1.9 Diversity of coordination modes of NacNac ligands in mononuclear coordination compounds⁶⁹

NacNac ligands offer a vast range of possible electronic and steric modifications compared to Cp ligands. Most commonly, the $N-R$ substituents are altered, affecting both electronic and steric properties of the ligand;⁷⁰ however, modifying the ligand backbone has also been reported.⁷¹⁻⁷³ Due to the versatility of the β -diketiminates, several s-, p-, d, and f-block compounds bearing NacNac ligands have been reported.^{68,73} However, much

work has focused on ligand modification and stoichiometric transformations, while their catalytic applications are limited.⁷⁴ The NacNac motif has been employed in first-row transition metals for hydrofunctionalization and ring-opening polymerization reactions.⁷⁴

1.6.2 Amidinate and Guanidinate Ligands

Amidates and guanidinate ligands (Figure 1.10) are highly accessible and versatile. These ligands can formally be regarded as the combination of an amido, and an imine donor with the general formula $RC(NR^1)_2$ and $R_2NC(NR^1)_2$, where R is alkyl or aryl (Figure 1.10). However, the general ligand systems can be modified in many ways; for example, the imine moiety of the amidinate ligand can also be part of an aromatic system, such as a pyridine resulting in the well-established aminopyridinate anions.⁷⁵

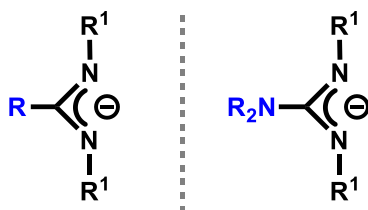


Figure 1.10 General structures of amidinate (left) and guanidinate (right) ligands

Both amidinate and guanidinate ligands display three coordination modes. The chelating binding mode κ^2-N,N' is the most common, typically exhibiting small bite angles around 64° (Figure 1.11, left). Rare examples of κ^1-N coordination are known in the literature, typically resulting from steric crowding of bulky nitrogen substituents (Figure 1.11, middle). Amidinate and guanidinate ligands have a propensity for the bridging coordination mode when bound to group 11 and divalent metals (Figure 1.11, right).⁷⁶

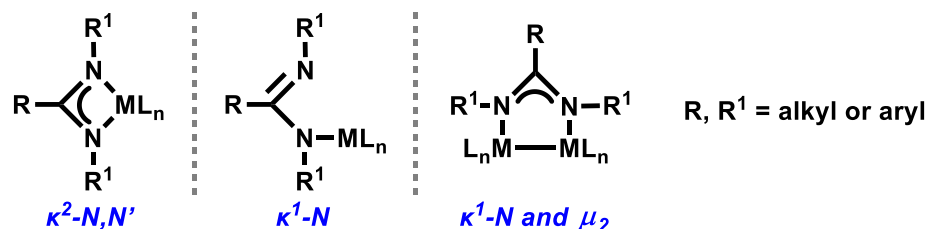


Figure 1.11 Coordination modes of amidinate and guanidinate ligands

The readily manipulable substituents at carbon and nitrogen allow for tuning of steric hindrance and electron density about the metal centre, akin to NacNac ligands. However, the impact of a bulky group on the central carbon atom can directly affect the metal atoms' coordination sphere *via* smaller N–C–N bond angles. Structural modification of the carbon and nitrogen substituents to include additional chelating donors has led to diverse coordination of the resultant chelating arm, called hybrid amidinate and guanidinate (Figure 1.12).⁷⁷ Metal complexes bearing hybrid amidinate or guanidinate ligands have been applied to various catalytic transformations.⁷⁷

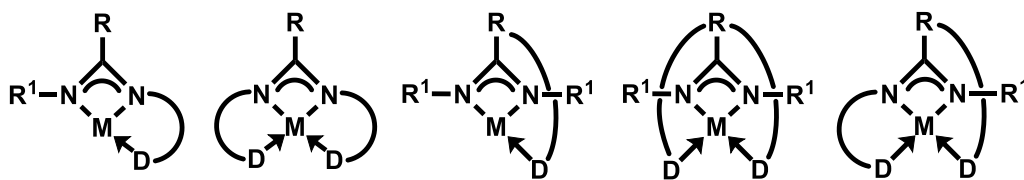


Figure 1.12 General structures of hybrid amidinate and guanidinate ligands

Due to their accessibility and versatility, amidinate and guanidinate ligands have been employed in combination with most periodic table metals. These ligands have been commonly used to stabilize higher oxidation states exhibited by early transition metals⁷⁸

and lanthanides.^{78,79} The most prominent application of amidinates and, to a lesser extent, guanidates, has been to support various group 3 polymerization catalysts.^{80,81} Amidinate ligands have been used to prepare remarkable examples of group 1–2 and main group (group 13–15) complexes, typically in the +1 oxidation state. More recently, a large body of fascinating research has evolved around amidinate-based cyclic silylenes and interconnected bis-silylenes.⁸²

1.6.3 Pincer Ligands

Chelating ligands that bind to three coplanar sites on a metal centre meridionally are given the moniker “pincer” (Figure 1.13). Pincer ligands can be given the abbreviation ECE, where E is the flanking two-electron donor atom, and C is the central anchoring donor atom, historically an *ipso*-carbon atom hence the C notation. However, the ECE notation can vary depending on the identity of the central and donor atoms (*e.g.* CCP, NCN, NNN, or CPC).⁸³ The ECE pincer platform provides ample variation of the ligand architecture *via* modification of the E and C donors and the organic linkers between donor atoms.⁸⁴ Therefore, systematic manipulation of the electronic and steric properties of the pincer ligand architecture can impart a degree of control over the metal centre in the resultant complex.⁸³ In homogenous catalysis, pincer ligands have aided in understanding numerous catalytic processes,⁸⁴ yielded complexes with enhanced chemical and thermal stability, as well as minimized metal leaching during catalytic transformations.^{84–86}

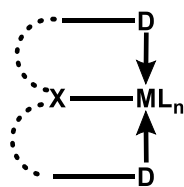


Figure 1.13 General representation of a pincer ligand

1.6.4 N-Heterocyclic Carbenes

N-Heterocyclic carbenes (NHCs) have been thoroughly investigated over the last two decades due to their strong σ -donating abilities, surpassing phosphine ligands.⁴³ The structure of NHCs, most commonly a 5-membered diazaheterocyclic system (Figure 1.14), yields numerous structural modification possibilities, thereby allowing for precision control of the ligand's properties towards the metal centre. The nitrogen atoms adjacent to the central carbenic atom stabilize this structure by donating electron density into the vacant orbital on the carbenic atom (Figure 1.14), a phenomena that is enhanced *via* the use of electron-withdrawing nitrogen substituents.^{45,87} When the backbone of an NHC features an alkene, the carbene is also stabilized *via* aromatic electron stabilization (6π -electron delocalization) and favours the singlet state as it is forced into a planar, more sp^2 -like arrangement.^{45,87}

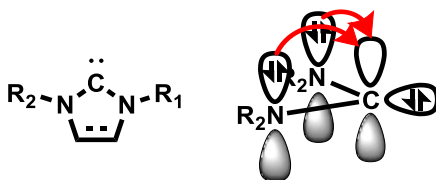


Figure 1.14 Structure of an NHC (left) and bonding diagram (right) to explain the stabilizing effect of the adjacent nitrogen atoms

Originally NHCs were referred to as phosphine mimics, but they have since outmatched phosphines in numerous key areas beyond σ -donation, such as steric bulk and tunability. The wedge-shaped steric demand of NHCs minimizes clashing with other bulky ligands and provides more shielding around the metal centre, unlike the cone-shaped bulk of phosphine ligands.^{43,45} The steric and electronic properties of NHCs are independently varied through modification of the nitrogen substituents, backbone functionality or heterocycle class (5, 6, 7 or 8 membered ring) *via* numerous well-established synthetic routes, whereas varying the substituents on a phosphine ligand inevitably affects both the steric and electronic parameters.^{43,45} For example, numerous substituted, chelating, pincer NHC complexes have been reported and employed as ancillary ligands for a variety of late and heavy transition metals for multiple chiral and non-chiral catalytic transformations such as cycloisomerization, hydrosilylation, cyclopropanation, enol-ester synthesis, C–C alkyne coupling, allylation and desilylation.⁸⁸

1.7 Applications of Ligand Design: Phosphorus–Nitrogen Units

Research in the last 30 years has heavily focused on the design and application of amido-based ligands and complexes thereof.^{64,89,90} In the last 15 years, the incorporation of phosphorus into ancillary ligands *via* phosphinimine moieties ($R_2P=NR^1$) has grown substantially, yielding diverse coordination modes and reactivity.⁹¹ Examples of such ligands are phosphoraneiminates $[R_3P=N]^-$,⁹² phosphinimines $(R_2P=NR^1)$,⁹³ bis(phosphinimino)methanides $[CH(Ph_2P=NR)_2]^-$,⁹⁴ bis(phosphinimino)methanediides $[C(Ph_2P=NR)_2]^{2-}$,⁹⁴ and iminophosponamides $[(R_2P(NR^1)_2]^-$.⁹⁵

1.7.1 Imines (C=N) Versus Phosphinimines (P=N)

Although structurally analogous to imines ($R_2C=NR^1$), phosphinimines, also known as iminophosphoranes ($R_3P=NR^1$, see Figure 1.15), are much stronger electron donors⁹⁶ due to enhanced ylidic character. These functional groups can be depicted as lacking a formal P=N double bond, where instead, formal charges are placed on the P and N atoms (Figure 1.15). Within this thesis, however, phosphinimines will be portrayed akin to imines (Figure 1.15, middle structure), since P=N multiple bond character has been shown to exist.⁹⁶

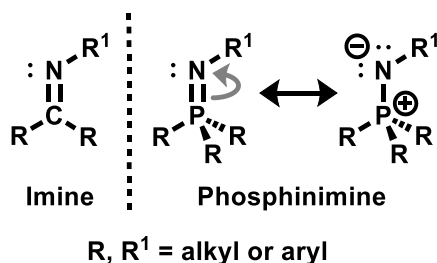


Figure 1.15 Comparison of the resonance structure(s) of imine and phosphinimines

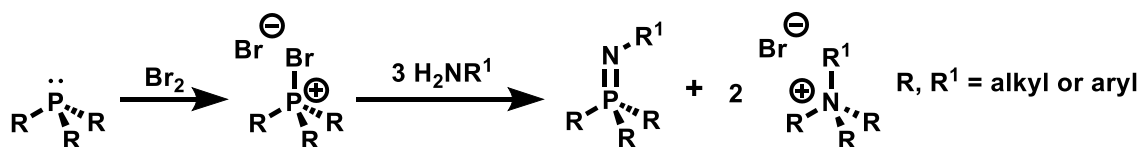
Generally, phosphinimines are not π -accepting, unlike their imine analogous. Instead, they act as both σ and π donors *via* the lone pair(s) on nitrogen.⁹⁷ Compared to imines, phosphinimines are typically stable under strongly reducing conditions and less prone to nucleophilic attack.⁹⁷ The phosphorus atom in a phosphinimine moiety is sensitive to changes within its chemical environment, akin to phosphine ligands, meaning that ^{31}P NMR spectroscopy (spin $\frac{1}{2}$, 100% abundant nucleus) is a vital tool to determine when the phosphinimine is coordinated to a metal centre, *via* significant shifts observed in the ^{31}P

NMR spectrum. ^{31}P NMR spectroscopy can also be used to gain insights into catalytic mechanisms *via* spectroscopically observable catalytic intermediates.⁹¹

1.7.2 The Syntheses of Phosphinimines

1.7.2.1.1 Kirsanov Synthesis

One synthetic route to a phosphinimine is the Kirsanov reaction,⁹⁸ which involves the addition of a phosphine to elemental bromine, forming a bromide salt ($[\text{R}_3\text{PBr}][\text{Br}]$). Excess primary amine is added to the bromide salt, forming the target phosphinimine and ammonium salt byproduct (Scheme 1.5). Isolation of the phosphinimine is achieved through standard filtration techniques.

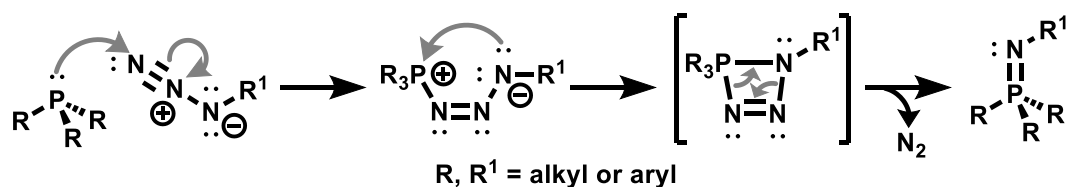


Scheme 1.5 An example of a Kirsanov reaction that generates a phosphinimine

1.7.2.1.2 Staudinger Synthesis

The Staudinger reaction⁹⁹ employs an organic azide and phosphine to generate the desired phosphinimine (Scheme 1.6).^{100,101} The phosphazide ($\text{R}_3\text{P}-\text{N}_3-\text{R}^1$) intermediate is generated in the first step of the Staudinger reaction in the absence of water. The phosphazide then rapidly cyclizes to extrude dinitrogen (N_2) gas to form a phosphinimine (Scheme 1.6). This highly selective process requires minimal to no purification, as the only byproduct is N_2 gas. Since organic azides are continuously becoming more synthetically

viable with more cost-effective reagents and increasingly safer reaction conditions, the Staudinger reaction has become the more favoured of the two synthetic routes. However, the Kirsanov reaction is employed when no organic azide is on hand, or the phosphine is too sterically hindered to form the 4-membered cyclic phosphazide intermediate required to extrude N₂ (Scheme 1.6).



Scheme 1.6 An example of a Staudinger reaction that generates a phosphinimine

Phosphinimine moieties can also be attached to larger ligand scaffolds by substituting one R group on phosphorus or nitrogen with an organic linker, thus having the phosphinimine employed as a chelating donor arm. If the phosphinimine is bound to the linker at the phosphorus atom, the ligand is given the moniker *endo*; otherwise, the linking fragment is bound to the nitrogen and classified as *exo* (Figure 1.16). However, most literature publications have focused on *endo*-phosphinimines.⁹¹

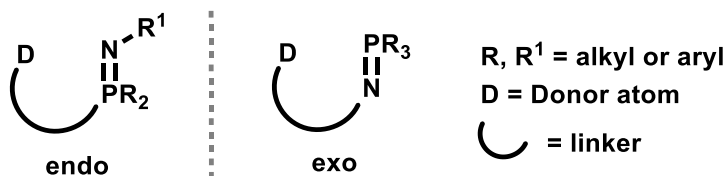


Figure 1.16 General structural examples of *endo* (left) and *exo* (right) phosphinimines

1.7.3 $[\text{CH}(\text{Ph}_2\text{P}=\text{NR})_2]^-$ and $[\text{C}(\text{Ph}_2\text{P}=\text{NR})_2]^{2-}$ Ligands

The deprotonated derivatives of the common class of bisphosphinimines, $\text{CH}_2(\text{PPh}_2\text{NR}_2)_2$, the monoanionic bis(phosphinimine)methanides $[\text{CH}(\text{Ph}_2\text{P}=\text{NR})_2]^-$ and the dianionic bis(phosphinimine)methanediides $[\text{C}(\text{Ph}_2\text{P}=\text{NR})_2]^{2-}$ have drawn the attention of several research groups due to their unusual coordination modes (Figure 1.17).^{102,103}

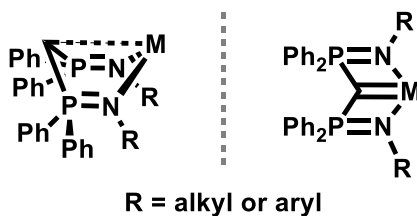


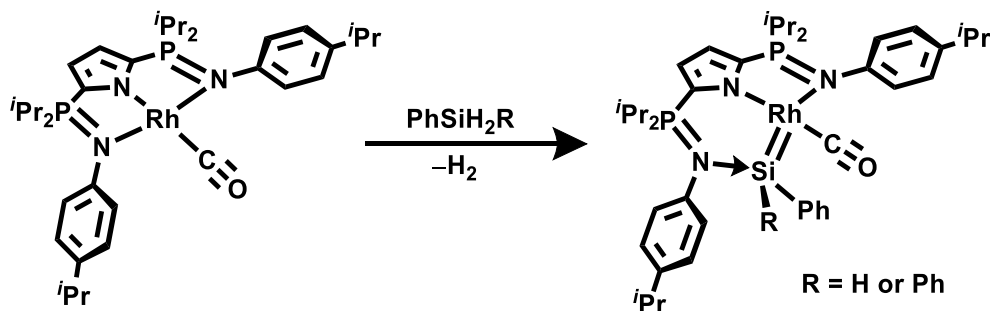
Figure 1.17 Primary coordination modes of $[\text{CH}(\text{Ph}_2\text{P}=\text{NR})_2]^-$ (left), and $[\text{C}(\text{Ph}_2\text{P}=\text{NR})_2]^{2-}$ (right) to a metal centre

The monoanionic methanide species has been employed as a ligand with various transition and main group metals.¹⁰⁴ The implementation of these ligands in catalysis is sparse, with examples of lanthanide complexes acting as precatalysts for intramolecular hydroamination reactions.¹⁰² However, direct comparison to the carbon analogue, NacNac $[\text{H}_2\text{C}(\text{RCNR}^1)_2]^-$, is difficult due to the coordination mode of bis(phosphinimino)methanides having increased metal-to-central carbon atom interactions (Figure 1.17, left). The central carbon atom is deprotonated to generate the bis(phosphinimine)methanide ligand salt, thereby leading to stronger carbon-to-metal interactions. In contrast, the NH of a neutral NacNac ($\text{H}_2\text{C}(\text{RC}=\text{NR}^1)(\text{RC}-\text{NHR}^1)$) undergoes deprotonation to generate the ligand salt, resulting in minimal to no carbon-to-metal interaction. The dianionic methanediides have the propensity to form stable carbene-

like complexes with numerous transition metals and actinides (Figure 1.17, right).¹⁰⁵ Methanediides complexes are known to undergo stoichiometric 1,2-addition or [2+2] cycloadditions across the M=C carbene-like bond, thereby reducing the M–C bond order. Notably, there are no reports of any methanediides species applied to a catalytic process.⁹⁴

1.7.4 Metal-Ligand Cooperation of Phosphinimine Ligands

Work from the Hayes group has employed tridentate *NNN*-pincer ligands bearing multiple phosphinimine groups, where the phosphinimine nitrogen atoms aid the metal centre through metal-ligand cooperation. The strongly donating phosphinimine ligands help dehydrogenate primary and secondary silanes at rhodium, generating an isolable base-stabilized rhodium silylene (Scheme 1.7).¹⁰⁶ Further studies by the group revealed similar reactivity prevails with MesBH_2 .¹⁰⁷

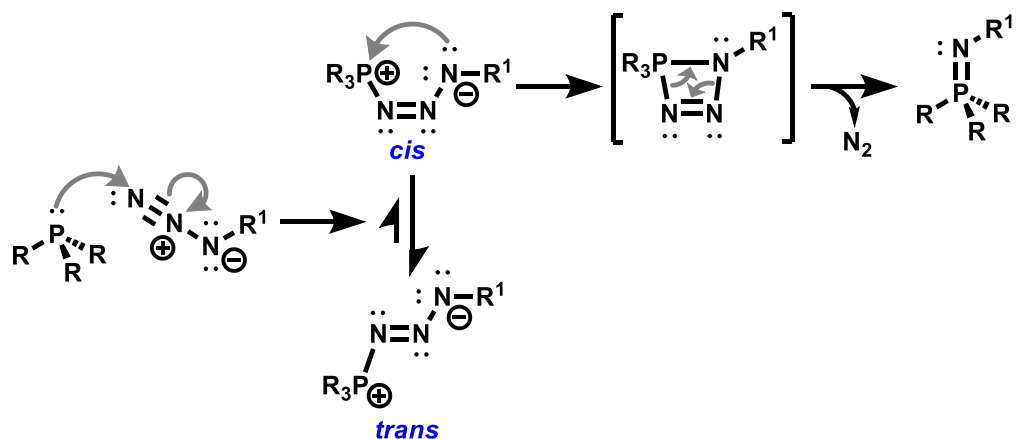


Scheme 1.7 Formation of rhodium^I silylenes by a dehydrogenative process

1.7.5 Phosphazides ($\text{R}_3\text{P}=\text{N}_3\text{-R}^1$)

The intermediate phosphazide ($\text{R}_3\text{P}=\text{N}_3\text{-R}^1$) generated in the Staudinger reaction is prone to eliminating dinitrogen (N_2) gas. As a result, phosphazides are often thought of as transient species.¹⁰⁸ The extrusion of N_2 is a highly favoured process requiring the

phosphazide to adopt a *cis* conformation, which then cyclizes, generating a four-membered transition state that can release N₂ (Scheme 1.8). Most reported phosphazides in the literature adopt the *trans* conformation, as the energy barrier to dinitrogen elimination is substantially higher.¹⁰⁹⁻¹¹²



Scheme 1.8 An example Staudinger reaction showing the two conformers of a phosphazide

Reported cases of stabilized phosphazides have utilized sterically bulky substituents on both phosphorus and nitrogen to hinder cyclization (Scheme 1.8).¹¹¹ Additional methods of phosphazide stabilization have sought to favour the *trans* isomer over the *cis* by including electron-donors on P and electron-withdrawing groups on N.¹¹¹ However, a more common method of stabilization is coordination of the phosphazide nitrogen atom(s) to a metal centre or Lewis acid.¹¹³ Phosphazide ligands are quite scarce in the literature, only gaining some popularity in the past ten years.¹¹⁴⁻¹¹⁶ The ability of these ligands to adopt one of several coordination modes, due to the three different coordinating nitrogen atoms, could lead to diverse and intriguing reactivity in transition

metal chemistry and catalysis. There has yet to be a reported case of phosphazide ligands applied to a catalytic process. Recently, the Hayes group demonstrated the ability of a phosphazide-supported thorium complex to capture and functionalize CO₂ *via* a stepwise process,¹¹⁷ thereby exhibiting the promising applications of phosphazide ligands.

1.8 Iminophosphonamide Ligands

Iminophosphonamide ligands are the phosphorus analogue of amidinate ligands described in section 1.6.2. These ligands can formally be regarded as a combination of an amido and a phosphinimine donor with the general formula R¹₂P(NR)₂, R¹ is almost exclusively aryl, and R is alkyl or aryl (Figure 1.18). Akin to phosphinimines, the phosphorus atom in iminophosphonamides serves as a spectroscopic marker, allowing for convenient monitoring of reactions. At a glance, the coordination of these iminophosphonamides can be expected to be similar to amidinates. However, the respective E–N bond lengths and N–E–N bite angles where E = C or P differ substantially, impacting the chemical behaviour of the corresponding coordination compounds. The iminophosphonamide ligand system has two resonance forms. The negative charge of the ligand can be delocalized between the N atoms, similar to amidinate ligands (Figure 1.18, middle). Iminophosphonamides are also known to exhibit formal amido and phosphinimine behaviour (Figure 1.18, right).¹¹⁸

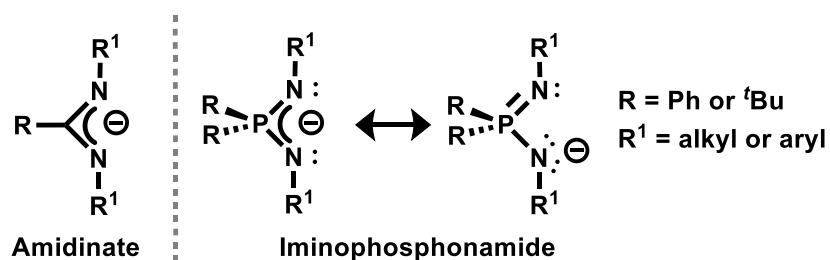


Figure 1.18 Structure of amidinates and iminophosphonamides and their resonance forms

Iminophosphonamides exhibit two degenerate HOMO orbitals with either C_2 or C_s symmetry (Figure 1.19, top).¹¹⁹ Akin to β -diketiminate complexes; the C_s HOMO of iminophosphonamides can effectively donate π -electron density from N towards the d_{xz} -orbital on the metal (Figure 1.19, top and middle). In contrast, the C_2 symmetric orbitals only allow for lateral metal coordination, as observed with amidinate ligands (Figure 1.19, bottom). The lateral coordination of amidinate ligands weakens the M–N σ -bond and thus inefficiently stabilizes $16e^-$, M^{II} divalent complexes, explaining the ligand's propensity to form stable bimetallic bridging-amidinate complexes wherein one ligand binds κ^1-N to each metal centre (Figure 1.11, right).¹¹⁹

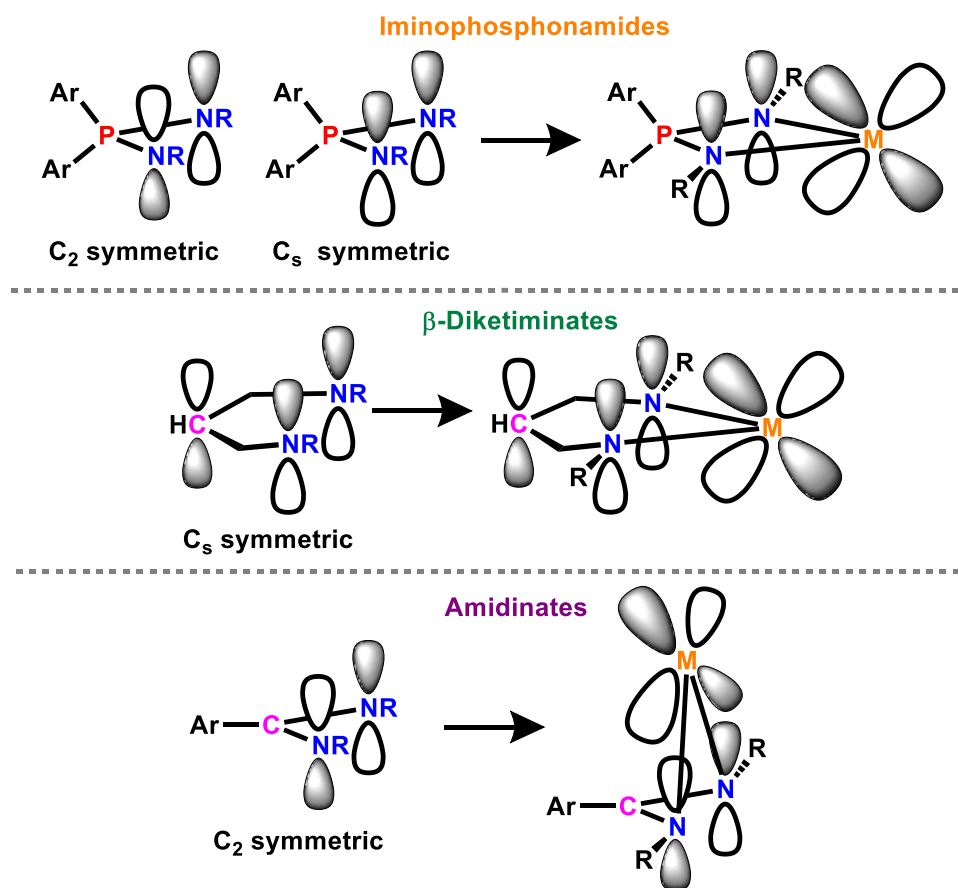


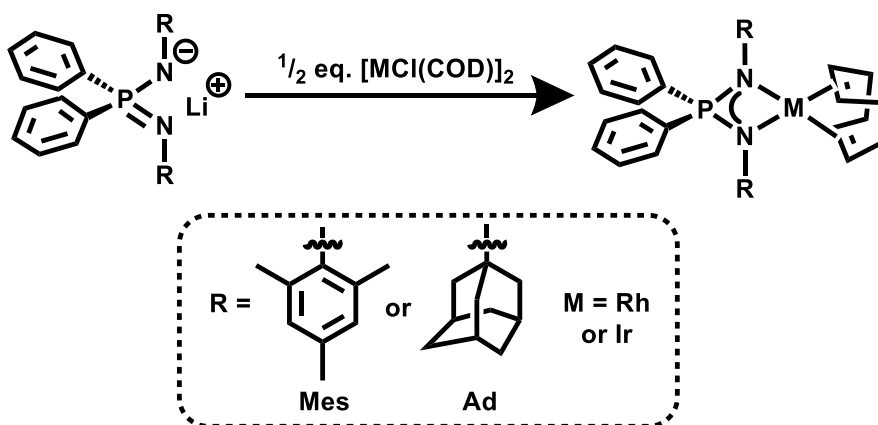
Figure 1.19 Schematic drawing of the HOMO orbitals of iminophosphonamides (top), β -diketiminates (middle), and amidinate (bottom) ligands π -bonding with a metal d_{xz} orbital

The iminophosphonamide ligand framework has been utilized to generate various transition metal and main group element compounds. Catalytic investigations of iminophosphonamido complexes have been mainly limited to the polymerization of various olefins with lanthanide, group 3–4 metals and select first-row transition metals.¹²⁰⁻
¹²⁴ The Kalsin group has begun to investigate half-sandwich Ru^{II} iminophosphonamido complexes for transfer hydrogenation.¹²⁵

1.9 Project Aims

1.9.1 Chapter 2 Goals and Accomplishments

No reports of a rhodium or iridium complex bearing an iminophosphonamido ligand are known; despite the heavier group 9 metals forming important complexes used in various catalytic processes. This chapter aimed to generate Ir^I, and Rh^I complexes bearing iminophosphonamide ligands (Scheme 1.9), and scope their reactivity towards the activation of small molecules. The common Mes and the yet-to-be-reported adamantyl (Ad or C₁₀H₁₅) substituted iminophosphonamide ligands were chosen to generate the target Ir^I, and Rh^I complexes; thereby, allowing for some insight into the electron impact of the ligand's nitrogen substituents on the resultant Ir^I, and Rh^I complexes reactivity. The metal dimer [MCl(COD)]₂ was utilized as it was both readily available in the lab and is commonly used as a starting metal source for *in situ* preparation of many Rh^I catalysts.¹⁸



Scheme 1.9 Proposed general synthesis for iminophosphonamido bearing Rh^I and Ir^I COD complexes

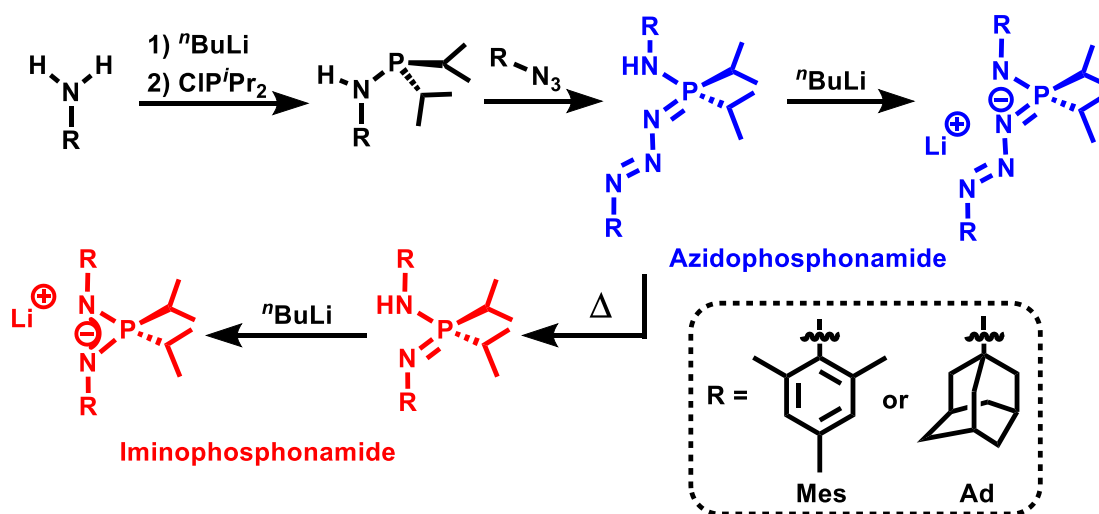
The resultant Rh^I and Ir^I complexes, with the general formula [Ph₂P(NR)₂]M(COD), were then reacted stoichiometrically to exchange the COD group on the metal centre for various other ligands. Initially carbon monoxide was chosen to probe the viability of replacing the COD ligand, and to scope the electron-donor properties of the iminophosphonamide *via* measuring and comparing the Tolman electronic parameter (TEP) of the resultant dicarbonyl species [Ph₂P(NR)₂]M(CO)₂. The reaction chemistry of the Rh^I and Ir^I iminophosphonamido complexes was then probed *via* stoichiometric reactions with H₂ in an attempt to generate a corresponding dihydride [Ph₂P(NR)₂]M(H)₂, an intermediate of hydrogenation. The iminophosphonamido complexes were also reacted with various silanes in attempts to form a silyl hydride species [Ph₂P(NR)₂]MH(SiR₃), an intermediate in Chalk-Harrod hydrosilylation.

1.9.2 Chapter 3 Goals and Accomplishments

Recent work by Hayes *et al.* demonstrated a stepwise synthetic cycle of CO₂ functionalization mediated by a diphosphazide-supported thorium complex. Partial dissociation of the phosphazide moieties within the trialkyl Th^{IV} complex, from a κ^2 -N ^{α} ,N ^{β} to a κ^1 -N ^{α} coordination mode, is vital to the insertion of CO₂ (Scheme 1.10).¹¹⁷ Despite this recent insight from the Hayes group, phosphazide ligands have yet to be applied to any catalytic processes. It is postulated that the unique coordinative versatility of phosphazides, and their ability to access a variety of coordination modes, due to the three donor nitrogen atoms, could prove beneficial in catalytic transformations where dissociation or association of a ligand (an N atom in this case) is important in the catalytic cycle.¹¹⁷

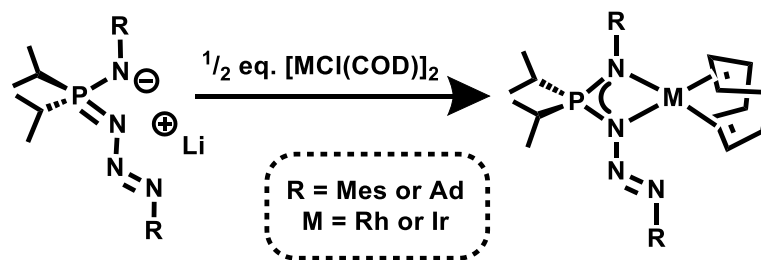
This chapter aimed to generate Ir^I, and Rh^I complexes bearing azidophosponamido ligands [Ph₂P(N₃R)(NR)]M(COD) (M = Rh or Ir), analogous to the iminophosphonamido species [Ph₂P(NR)₂]M(COD) isolated in chapter 2. The effect of the phosphazide functional group on the reaction chemistry of the resultant azidophosponamido complex was then examined.

Electronic factors, such as strong electron donors on phosphorus or electron-withdrawing groups on nitrogen have been shown to destabilize the cyclization of a phosphazide, thereby preventing N₂ extrusion to the phosphinimine while increasing the likelihood of stabilizing a phosphazide in the *trans* conformation.¹¹¹ Therefore, relatively more electron-donating isopropyl phosphorus substituents (instead of phenyl groups) were chosen to generate this new family of azidophosponamide ligands. The proposed synthetic route to azidophosponamide ligands is analogous to the synthesis of aryl-substituted iminophosponamides, where the R-substituted phosphonamide is reacted with an organic azide *via* an arrested Staudinger reaction (Scheme 1.11). It was postulated that access to an iminophosponamide would be readily achieved *via* extrusion of N₂ upon heating of the azidophosponamide (Scheme 1.11). Both the neutral iminophosponamide and azidophosponamide would then undergo deprotonation with ⁿBuLi to yield lithium salts of said ligands (Scheme 1.11).



Scheme 1.11 Proposed synthetic route to alkyl-substituted azido- and imino-phosphonamide ligands

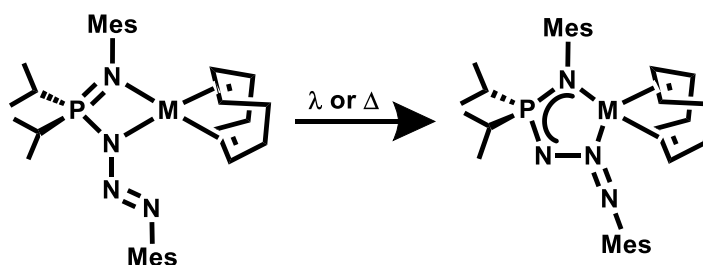
The resultant azidophosphonamides or azidophosphonamido-metal salts, however, were proven to be remarkably thermally robust, showing no sign of N_2 loss when heated to $100\text{ }^\circ\text{C}$ for numerous days. Thus, only the azidophosphonamide Rh^{I} and Ir^{I} complexes $[\text{ } ^i\text{Pr}_2\text{P(N}_3\text{R)(NR)]M(COD)}$ were generated *via* salt metathesis reactions (Scheme 1.12).



Scheme 1.12 Proposed general synthesis for alkyl-substituted azido- and imino-phosphonamido Rh^{I} and Ir^{I} COD complexes

1.9.3 Chapter 4 Goals and Accomplishments

The mesityl-substituted azidophosphonamide Rh^I and Ir^I species $[^iPr_2P(N_3Mes)(NMe_3)]M(COD)$ obtained in chapter 3 demonstrated interesting thermally or photochemically-induced linkage isomerization of the phosphazide functionality (Scheme 1.13), a remarkably rare phenomenon in the literature.



Scheme 1.13 Thermally or photochemically induced linkage isomerism of the phosphazide moiety exhibited by the mesityl-substituted azidophosphonamido complexes

The substitution of the COD ligands within the azidophosphonamido Rh^I and Ir^I complexes $[^iPr_2P(N_3R)(NR)]M(COD)$ was demonstrated *via* generation of the dicarbonyl species $[^iPr_2P(N_3R)(NR)]M(CO)_2$, allowing for direct comparison with the iminophosphonamido species in chapter 2 $[Ph_2P(NR)]M(CO)_2$ to the azidophosphonamido *via* the change in the infrared $C\equiv O$ stretching frequency. The azidophosphonamido complexes were then reacted with H_2 and various silanes in an attempt to generate dihydride $[^iPr_2P(N_3R)(NR)]M(H)_2$ and silyl hydride species $[^iPr_2P(N_3R)(NR)]MH(SiR_3)$, respectively.

CHAPTER 2: INVESTIGATIONS INTO IMINOPHOSPHONAMIDE Rh AND Ir COMPLEXES

2.1 Overview: Iminophosphonamide Ligands

Iminophosphonamides are the phosphorus analogous of the well-known amidinate ligand family (Figure 2.1, left).¹²⁸ Also referred to as NPN ligands, iminophosphonamides have the general formula $R_2P(NR^1)_2$, where R is almost exclusively aryl, and R^1 can be an alkyl or aryl group. These ligands formally contain both an amido and phosphinimine donor, exhibiting two key resonance structures due to the polarizable P=N moiety (Figure 2.1, right).¹¹⁸ The substitution of carbon (in amidinates) for phosphorus (in iminophosphonamides) yields considerably longer bond lengths and larger bite angles. However, iminophosphonamido ligands have only been studied sporadically, and catalytic investigations have been limited to lanthanide, group 3-4 metals and select first-row transition metals.^{120-124,129}

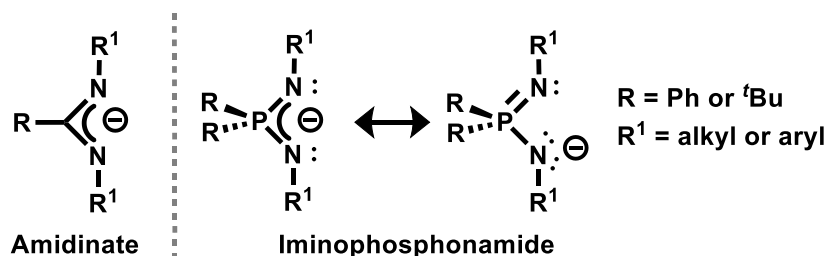


Figure 2.1 Resonance forms of amidinate and iminophosphonamide ligands

The phosphorus atom in iminophosphonamides also serves as a spectroscopic “marker” due to the spin $\frac{1}{2}$, 100% abundant ^{31}P nucleus. The ^{31}P nucleus is sensitive to

changes in its environment, exhibiting large changes in chemical shifts upon coordination of the nitrogen atom to a metal centre.⁹¹ Therefore, ³¹P NMR spectroscopy can be conveniently used to monitor chemical transformations and is helpful when identifying reaction intermediates and products.

2.1.1 Group 1 and 2 Metal Iminophosphonamido Complexes

Treatment of a neutral iminophosphonamide with an alkali metal base, such as ⁿBuLi, NaH, NaHMDS, KH, or KHMDS, leads to the corresponding alkali metal complex. Structural investigation of reported group 1 iminophosphonamido complexes demonstrates that the aggregation state of said metal species depends on the N-substituents and ionic radius of the central metal atom. For example, the potassium salt [K(Ph₂P(NDipp)₂)]_n is polymeric while the lithium analogue (THF)Li[(Ph₂P(NDipp)₂)] is monomeric.¹²⁷ Alkali metal iminophosphonamide species are useful precursors for salt metathesis reactions, which transfer the ligand to another central atom (Figure 2.2, left).¹³⁰ However, the group 2 species themselves, for example, the enantiopure calcium iminophosphonamido complexes [Ph₂P(N-*R*-CHMe(naphthyl))₂]₂Ca, have exhibited rich photoluminescence properties and have been employed as hydroboration catalysts (Figure 2.2, right).¹³¹

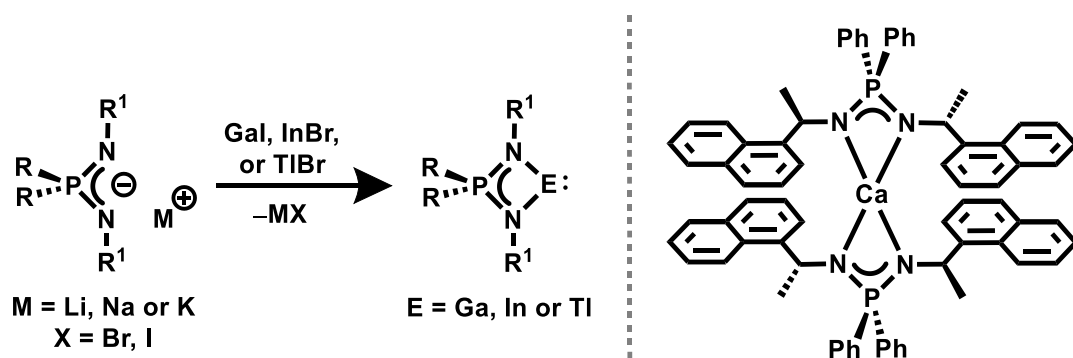


Figure 2.2 Salt metathesis reaction using an alkali metal iminophosphonamide species¹³⁰ (left); an enantiopure calcium complex¹³¹ (right)

2.1.2 Early Transition Metal and Lanthanide Iminophosphonamido Complexes

Iminophosphonamido lanthanide and group 3-4 metals complexes are more scarce in the literature than analogous amidinate species.¹¹⁸ Lanthanide iminophosphonamido complexes, where $\text{M} = \text{Y, Sm, Ho, Yb}$ and Lu , have mainly been investigated as catalysts in olefin polymerization (Figure 2.3, left).¹²⁰ These complexes, due to their different and sterically demanding nitrogen substituents, favour high 3,4-regio- and stereoselectivity and *trans*-selective isoprene polymerization.¹²⁰ Group 4 half-sandwich complexes bearing iminophosphonamide ligands have also been employed for ethylene polymerization (Figure 2.3, right).¹²⁴

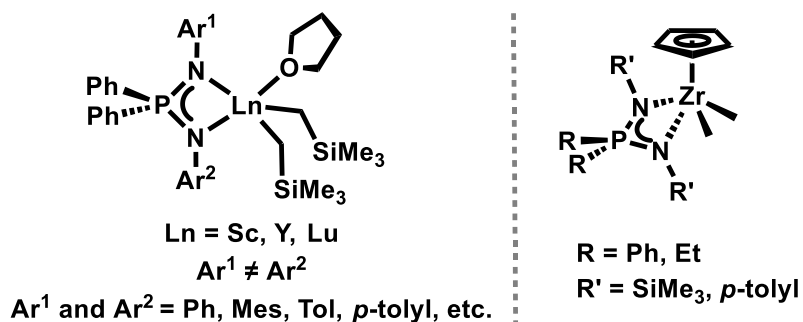


Figure 2.3 Group 3 and 4 iminophosphonamide polymerization catalysts^{120,124}

2.1.3 First Row Transition Metal Iminophosphonamido Complexes

Investigations into the catalytic activity of iminophosphonamido complexes have been mostly limited to first-row transition metals, including chromium (Figure 2.3, left),¹²¹ nickel (Figure 2.3, top right),¹²² and copper (Figure 2.3, bottom right).¹²³ Such species have found application in olefin oligomerization,¹²¹ polymerization¹²² and cyclopropanation.¹²³

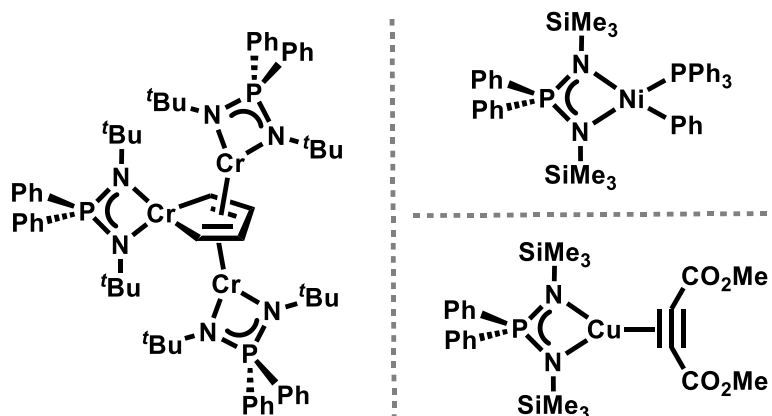


Figure 2.4 First-row transition metal iminophosphonamido catalysts¹²¹⁻¹²³

2.1.4 Late Transition Metal Iminophosphonamido Complexes

A few iminophosphonamido complexes featuring heavier metals, such as palladium^{132,133} and ruthenium,¹¹⁹ have been reported by the Kalsin group. Initially, in 2014, their investigations focused on the palladium complex $[(\text{Ph}_2\text{P}(N\text{-}4\text{-COOEtC}_6\text{H}_4)_2)\text{PdC}_3\text{H}_5]$, shown to be active for Tsuji-Trost and Suzuki-Miyaura reactions (Figure 2.5, left).¹³³ Later, in 2016, Kalsin *et al.* changed tactics, reporting the half-sandwich $16e^- \text{Ru}^{\text{II}}$ complex $[(\text{Ph}_2\text{P}(\text{NTol})_2)\text{RhCpCl}]$ (Figure 2.5, right). The ruthenium complex was employed as a catalyst for ring-opening polymerization,¹¹⁹ and later for transfer hydrogenation.¹²⁵ Further computational mechanistic studies of the transfer

hydrogenation catalytic cycle suggested two distinct pathways; the route the Ru^{II} catalyst employs depends on the basicity of the nitrogen atoms, controlled by altering the N-substituents (R = Tol or Me).¹³⁴ Despite the recent insights provided by the Kalsin group into late transition metal iminophosphonamido complexes, the literature reveals a distinct lack of Rh and Ir complexes bearing said ligands.

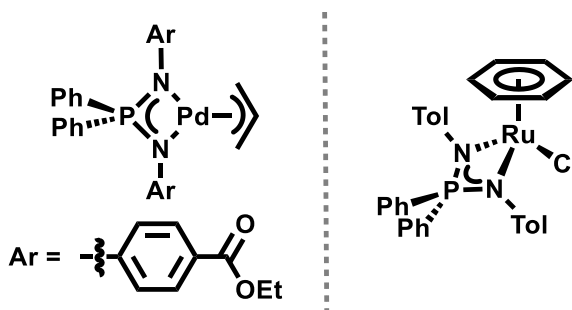


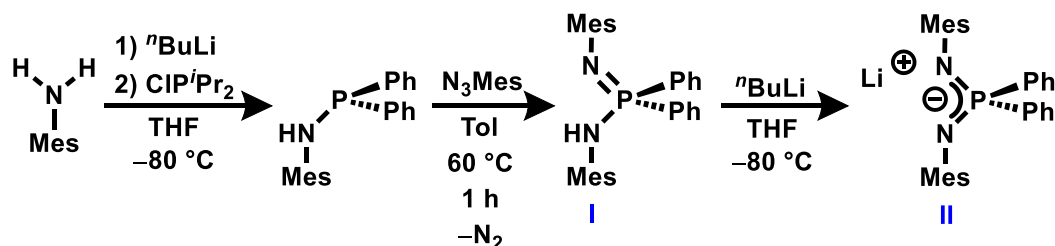
Figure 2.5 Late transition metal iminophosphonamido complexes reported by Kalsin *et al.*^{125,132,134}

The lack of heavy group 9 iminophosphonamido complexes is surprising given the ubiquity of rhodium and, to a lesser extent, iridium, in various catalytic processes, namely, cycloaddition, C–H insertion, hydrogenation and hydrofunctionalization reactions.¹⁹ Access to a low-coordinate 14-electron metal species is key to many catalytic processes, including hydrosilylation and hydrogenation. In olefin metathesis, alkene dissociation is a key step in generating the reactive 14-electron catalytic intermediate. Therefore, a square planar Rh^I or Ir^I complex bearing an alkene ligand was targeted, as the alkene was predicted to be labile. The metal dimers [MCl(COD)]₂ (COD = cyclooctadiene, M = Rh, Ir) are commonly used starting materials and are readily available.¹⁸ The COD ligand can often be replaced by other donors.

2.2 Synthetic Routes to $[\text{Ph}_2\text{P}(\text{NR})_2]^-$ Ligands

Much like phosphinimines, iminophosphonamides can be generated by Kirsanov and Staudinger protocols.¹¹⁸ The latter route is more prevalent in the literature, as it allows for greater versatility in altering the substituents on nitrogen.

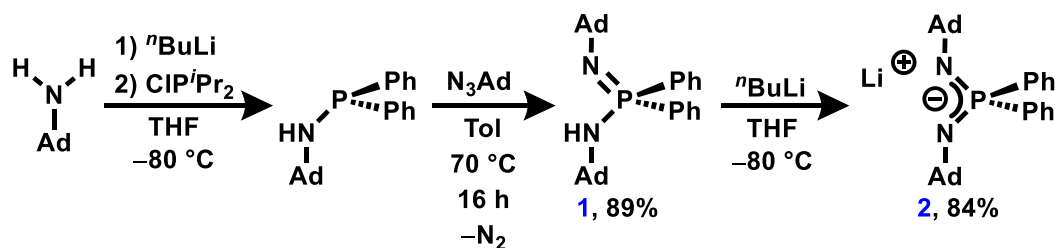
The 2,4,6-trimethylphenyl (Mes) substituted iminophosphonamide ligand **I** $\text{Ph}_2\text{P}(\text{NHMes})(\text{NMe}_3)$ was chosen as the only reported group 9 iminophosphonamido complex, $\text{Co}[\text{Ph}_2\text{P}(\text{NMe}_3)_2]_2$,¹²⁶ bears the same Mes-substituted ligand and therefore allows for some comparison of metal-to-ligand metrical parameters. The route to generate the Mes-substituted neutral ligand **I** $[\text{Ph}_2\text{P}(\text{NMe}_3)(\text{NHMe}_3)]$ and the lithium salt **II** $\text{Li}[\text{Ph}_2\text{P}(\text{NMe}_3)_2]$,¹²⁷ have been reported by Stasch *et al.*¹²⁷ (Scheme 2.1).



Scheme 2.1 Synthesis of Mes-Substituted iminophosphonamido lithium salt $\text{Li}[\text{Ph}_2\text{P}(\text{NMe}_3)_2]$ ¹²⁷

In line with the principles of ligand design, alkyl substituents on nitrogen were also targeted to vary the electronic properties of the metal centre and observe any impacts this change may have on the reactivity of the resultant iminophosphonamido complexes. However, using ubiquitous groups, such as ^tBu and SiMe₃, requires the organic azides ^tBuN₃ and Me₃SiN₃ (also known as TMSN₃).¹¹⁸ Organic azides are especially sensitive to violent, potentially explosive decomposition caused by external energy sources, including

light, heat, friction, and pressure.^{135,136} These two organic azides (^tBuN₃ and Me₃SiN₃) have low C:N ratios (see note in section 6.1.3) that render them potentially hazardous and impractical for large-scale synthesis.¹³⁵ Instead, adamantyl (Ad, C₁₀H₁₅) azide was chosen because of its higher C:N ratio of 3.4. Adamantyl groups exhibit similar steric bulk and electronic influence to ^tBu, as demonstrated through model phosphine ligands PR₃ where R = Ad or ^tBu.¹³⁷ An analogous synthetic route to Scheme 2.1 was therefore proposed to generate the yet-to-be-reported Ad-substituted iminophosphonamide **1**, Ph₂P(NHAd)(NAd), and the corresponding iminophosphonamide lithium salt **2**, Li[Ph₂P(NAd)₂] (Scheme 2.2).



Scheme 2.2 Synthesis of **1** and **2**

*Note: The roman numerals **I** and **II** are used to describe the known mesityl-substituted iminophosphonamide compounds **I** [Ph₂P(NMes)(NHMes)] and **II** Li[Ph₂P(NMes)₂] which were prepared according to literature procedures,¹²⁷ while the analogous adamantyl-substituted ligands **1**, Ph₂P(NHAd)(NAd), and **2**, Li[Ph₂P(NAd)₂] are denoted with Arabic numerals as their isolation and characterization are discussed within this work.*

2.2.1 Synthesis of Ph₂P(NHAd)(NAd), (**1**)

The Staudinger reaction, to generate the neutral iminophosphonamide **1**, Ph₂P(NHAd)(NAd)), required heating for 16 h at 70 °C to reach completion, presumably due to the steric bulk and electronic impacts of the Ad groups, compared to the planar, electron-withdrawing Mes substituents in **I**, Ph₂P(NHMes)(NMes), which only required 1 h at 60 °C.¹²⁷ The ³¹P{¹H} NMR chemical shift of **1**, Ph₂P(NHAd)(NAd), at δ -22.4, is lower in frequency than that observed for **I**, Ph₂P(NHMes)(NMes), δ -16.7.¹²⁷ This difference is attributed to the electron-donating adamantyl substituents on the nitrogen atoms. In the ¹H NMR spectrum of **1**, Ph₂P(NHAd)(NAd), the Ad-CH and Ad-CH₂ protons are magnetically inequivalent, displaying several overlapping resonances ranging from δ 2.16 to δ 1.45. Light yellow crystalline needles of **1** were grown over 3 days from a saturated benzene solution at ambient temperature. The iminophosphonamide neutral ligand was found to crystallize within the common P-1 space group (Figure 2.6).

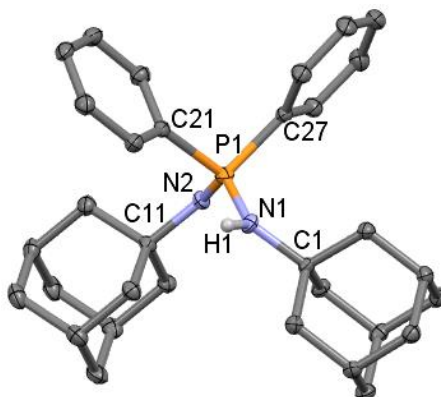


Figure 2.6 X-ray crystal structure of **1** depicted as 50% displacement ellipsoids. Hydrogen atoms (except H1) are omitted for clarity

The bulk of the Ad groups pushes the two phenyl substituents on phosphorus together as indicated by the Ph–P–Ph bond angle of **1**, 102.58(9)° in Table 2.1, which is much smaller than that in **I**, 108.19(3)°. ¹²⁷ However, the N1–P–N2 bond angle is mainly unaffected (**1**, 121.926(9)° vs **I**, 120.87(2)). ¹²⁷

Table 2.1 Selected bond distances (Å) and angles (°) for compound **1**

Atoms	Distance (Å)	Atoms	Angle (°)
P–N1	1.6158(17)	P–N1–C1	126.16(13)
P–N2	1.6064(17)	C1–N1–H1	116.9(2)
N–C1	1.479(2)	H1–N1–P	116.9(2)
N–C11	1.479(2)	C11–N2–P	127.57(13)
P–C21	1.819(2)	N1–P–N2	121.96(9)
P–C27	1.8199(19)	C21–P–C27	102.58(9)

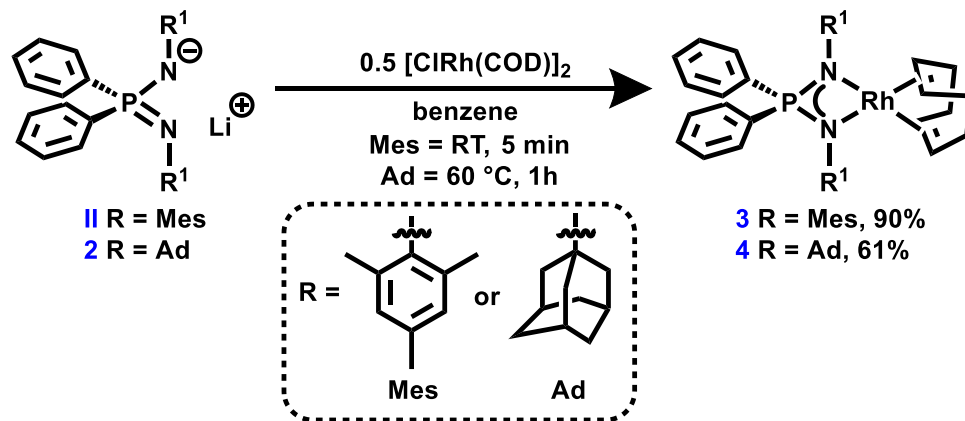
2.2.2 Synthesis of Li[Ph₂P(NAd)₂], (**2**)

The conversion of **1**, Ph₂P(NHAd)(NAd), to the lithium salt **2**, Li[Ph₂P(NAd)₂], required the use of ^tBuLi to deprotonate the N–H bond. Complex **2** exhibits chemical inequivalence of the adamantyl methylene and methine protons on the ¹H NMR timescale. The lithium salt **2** exhibits a similar chemical shift to Mes-substituted **II**, Li[Ph₂P(NMes)₂], ¹²⁷ in both the ³¹P{¹H} (**2** δ –2.3 and **II** δ –3.0) ¹²⁷ and ⁷Li NMR spectra (**2** δ 0.9 and **II** δ 2.9) ¹²⁷. Complex **2**, Li[Ph₂P(NAd)₂], is only isolable as a THF adduct;

coordinated THF is observed in the ^1H and $^{13}\text{C}\{^1\text{H}\}$ NMR spectrum. Numerous attempts to crystallize the salt **2** have proven unsuccessful.

2.3 Synthesis of Iminophosphonamido Rh^I Complexes

The desired Rh^I cyclooctadiene (COD) complexes **3**, $[\text{Ph}_2\text{P}(\text{NMes})_2]\text{Rh}(\text{COD})$, and **4**, $[\text{Ph}_2\text{P}(\text{NAd})_2]\text{Rh}(\text{COD})$, were generated *via* a salt metathesis reaction between the lithium iminophosphonamide salts **II**, $\text{Li}[\text{Ph}_2\text{P}(\text{NMes})_2]^{127}$ and **2**, $\text{Li}[\text{Ph}_2\text{P}(\text{NAd})_2]$ and half an equivalent of $[\text{ClRh}(\text{COD})]_2$ (Scheme 2.3). The mesityl-substituted complex **3**, $[\text{Ph}_2\text{P}(\text{NMes})_2]\text{Rh}(\text{COD})$, can be readily generated in aromatic solvent within 5 min. The adamantyl complex **4**, $[\text{Ph}_2\text{P}(\text{NAd})_2]\text{Rh}(\text{COD})$, requires heating at 60 °C for 1 h; further heating results in a slow decomposition to Rh black and the degradation product **1**, $\text{Ph}_2\text{P}(\text{NHAd})(\text{NAd})$ as indicated *via* $^{31}\text{P}\{^1\text{H}\}$ NMR spectroscopy. Removing benzene *in vacuo* affords the target complexes as bright yellow powders in 90% (**3**) and 61% (**4**) yield.



Scheme 2.3 Synthesis of iminophosphonamido-rhodium COD complexes **3** and **4**

2.3.1 Characterization of $[\text{Ph}_2\text{P}(\text{NR})_2]\text{Rh}(\text{COD})$ where $\text{R} = \text{Mes}$ (**3**) and $\text{R} = \text{Ad}$ (**4**)

The Mes complex **3**, $[\text{Ph}_2\text{P}(\text{NMes})_2]\text{Rh}(\text{COD})$ exhibits a notably more upfield signal in the $^{31}\text{P}\{^1\text{H}\}$ NMR spectrum (δ 24.5) than the Ad analogue **4**, $[\text{Ph}_2\text{P}(\text{NAd})_2]\text{Rh}(\text{COD})$, (δ 50.0). As expected, all ^{31}P resonances display coupling to ^{103}Rh , $^2J_{\text{RhP}} = 13.8$ Hz (**3**) and $^2J_{\text{RhP}} = 11.8$ Hz (**4**). In the ^1H NMR spectra of both complexes, the substituents on nitrogen display one set of resonances. Similarly, the COD ligand exhibits a single methine (CH) resonance (δ 3.52 (**3**) and 4.95 (**4**)) in the ^1H NMR spectrum, and two distinct methylene (CH_2) signals at δ 2.38 and 1.63 for complex **3**, and at 2.59 and 1.73 for complex **4**.

2.3.1.1 X-ray Crystal Structure of $[\text{Ph}_2\text{P}(\text{NMes})_2]\text{Rh}(\text{COD})$, (**3**)

Yellow plates of **3**, $[\text{Ph}_2\text{P}(\text{NMes})_2]\text{Rh}(\text{COD})$, were grown over 16 h from a saturated pentane solution stored at -30 °C. The structure of **3** was confirmed *via* single-crystal X-ray diffraction analysis (Figure 2.7).

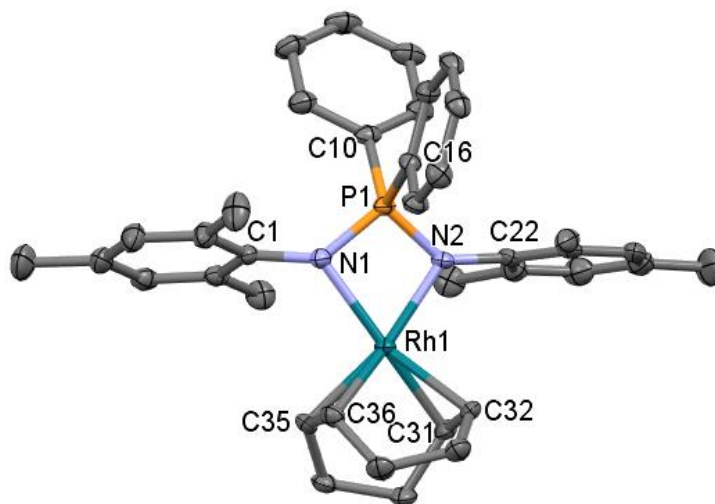


Figure 2.7 X-ray crystal structure of **3** depicted as 50% displacement ellipsoids. Hydrogen atoms are omitted for clarity

The coordination environment about Rh is predictably distorted square planar, $\tau_4 = 0.27$, attributed to the small N–Rh–N bite angle of $71.72(8)^\circ$. By comparison, the aforementioned Co^{II} complex, $\text{Co}[\text{Ph}_2\text{P}(\text{NMes})_2]_2$,¹²⁶ adopts a distorted tetrahedral geometry ($\tau_4 = 0.76$). The two P–N bond distances in **3**, $[\text{Ph}_2\text{P}(\text{NMes})_2]\text{Rh}(\text{COD})$ are similar to each other, $1.606(2)$ and $1.603(2)$ Å (Table 2.2), indicating delocalization of the ligand’s anionic charge (left resonance structure in Figure 2.1). By contrast, the P–N bond lengths in $\text{Co}[\text{Ph}_2\text{P}(\text{NMes})_2]_2$ are distinctly different ($1.657(1)$ and $1.536(1)$ Å),¹²⁶ suggesting localization of the ligands charge on one nitrogen atom (right resonance structure in Figure 2.1). Expectedly, the Rh–N bond distances ($2.106(2)$ and $2.0814(19)$ Å) are longer in **3** by 0.5 Å than the Co–N bonds ($2.015(4)$ – $2.038(3)$ Å) in $\text{Co}[\text{Ph}_2\text{P}(\text{NMes})_2]_2$,¹²⁶ due to the larger atomic radius of Rh (1.83 Å) compared to Co (1.67 Å).

Table 2.2 Selected bond distances (Å) and angles (°) for compound **3**

Atoms	Distance (Å)	Atoms	Angle (°)
Rh–N1	2.106(2)	N1–Rh–N2	71.72(8)
Rh–N2	2.0814(19)	C32–Rh–N2	96.79(9)
N1–C1	1.415(3)	C35–Rh–N1	97.91(9)
N2–C22	1.412(3)	C31–Rh–N2	101.88(9)
P–C10	1.821(2)	C32–Rh–N1	101.88(9)
P–C16	1.807(3)	C36–Rh–C31	82.19(10)
P–N1	1.606(2)	C35–Rh–C32	82.60(10)
P–N2	1.603(2)	N1–P–N2	99.72(11)
Rh–C31	2.120(2)	C10–P–C16	103.89(12)
Rh–C32	2.106(3)		
Rh–C35	2.122(2)		
Rh–C36	2.114(2)		

2.3.1.2 X-ray Crystal Structure of [Ph₂P(NAd)₂]Rh(COD)•1.5C₆H₆ (**4**)

Crystals of **4**, [Ph₂P(NAd)₂]Rh(COD)•1.5C₆H₆, suitable for X-ray diffraction analysis, were grown over one week from a saturated 1:1 solution of benzene and pentane at ambient temperature. The asymmetric unit contains one and a half solvent molecules of benzene and one molecule of **4** (Figure 2.8). Akin to **3**, [Ph₂P(NMes)₂]Rh(COD), complex **4** exhibits distorted square planar geometry (τ_4

= 0.25) and a small bite angle ($71.71(6)^\circ$). The box-like steric impact of the adamantyl groups was observed through larger R–N bond distances in **4** where R = Ad ($1.478(2)$ and $1.482(2)$ Å, Table 2.3) compared to **3** where R = Mes in ($1.415(3)$, $1.412(3)$ Å, Table 2.2), a difference of ~ 0.06 Å. As a result, the adamantyl substituents in **4** are held further away from the nitrogen they are directly bound to, which allows for an increase in the Ph–P–Ph angle in **4**, $[\text{Ph}_2\text{P}(\text{NAd})_2]\text{Rh}(\text{COD})$, ($108.51(8)^\circ$) compared to **3**, $[\text{Ph}_2\text{P}(\text{NMes})_2]\text{Rh}(\text{COD})$, ($103.89(12)^\circ$).

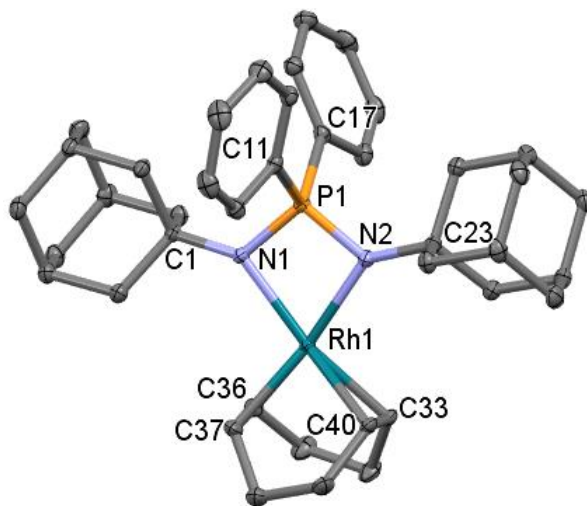


Figure 2.8 X-ray crystal structure of **4**·1.5C₆H₆ depicted as 50% displacement ellipsoids. Hydrogen atoms and solvent molecules are omitted for clarity

Table 2.3 Selected bond distances (Å) and angles (°) for compound **4**

Atoms	Distance (Å)	Atoms	Angle (°)
Rh–N1	2.1273(14)	N1–Rh–N2	71.71(6)
Rh–N2	2.1176(15)	C40–Rh–N2	99.44(6)
N1–C1	1.478(2)	C36–Rh–N1	97.93(6)
N2–C23	1.482(2)	C33–Rh–N2	101.53(6)
P–C11	1.8220(18)	C37–Rh–N1	102.02(6)
P–C17	1.8259(18)	C36–Rh–C33	80.35(7)
P–N1	1.6157(15)	C37–Rh–C40	81.17(7)
P–N2	1.6103(15)	N1–P–N2	100.69(8)
Rh–C33	2.1256(17)	C11–P–C17	108.51(8)
Rh–C36	2.1104(18)		
Rh–C37	2.1219(18)		
Rh–C40	2.1084(17)		

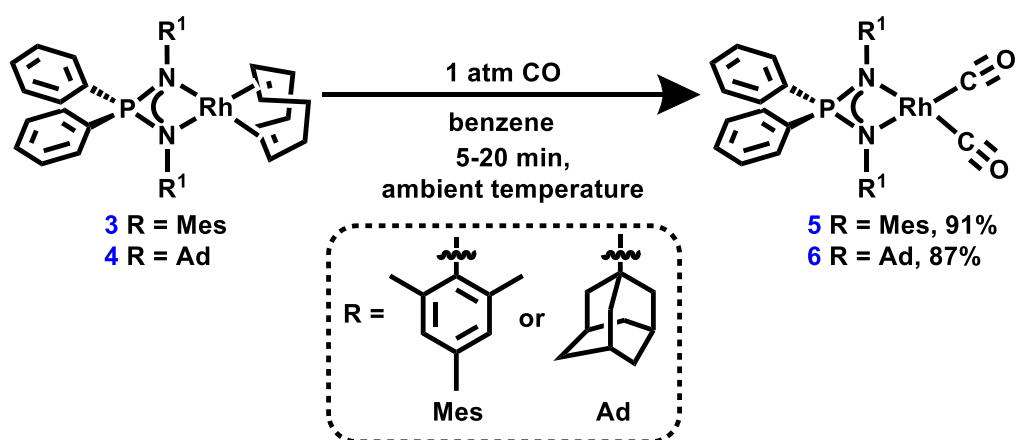
2.4 Reactivity of Rh^I Iminophosphonamido Complexes Toward Small Molecules

As complexes **3**, [Ph₂P(NMes)₂]Rh(COD), and **4**, [Ph₂P(NAd)₂]Rh(COD), represent a new class of organorhodium iminophosphonamide species, their reactivity toward small molecules was investigated.

2.4.1 Reactions of Rh^I Iminophosphonamido Complexes with CO

Incorporating a CO ligand into a metal complex can help gauge the electronic impact of ligand variation on the metal centre, *e.g.* different N-substituents on the iminophosphonamide. A change in the ν_{CO} frequency in the IR spectrum of a complex paints a picture of the electronic environment around the metal, where an electronic-rich metal centre yields more π backdonation to CO and, consequently, a lower ν_{CO} frequency stretch.

Complexes **5** $[\text{Ph}_2\text{P}(\text{NMe}_3)_2]\text{Rh}(\text{CO})_2$ and **6** $[\text{Ph}_2\text{P}(\text{NAd})_2]\text{Rh}(\text{CO})_2$ were generated *via* the addition of one atmosphere of CO to a J. Young NMR tube containing the Rh(COD) precursor **3** or **4** in benzene-*d*₆ (Scheme 2.4). While the mesityl complex **5** was readily generated at ambient temperature within 2 minutes, the adamantyl complex required 20 minutes to achieve complete conversion. The solutions were then filtered to remove insoluble particles, and the residual solvent was removed *in vacuo* to afford the products as brown powders in 91% (**5**) and 87% (**6**) yield.



Scheme 2.4 Synthesis of Rh^I carbonyl complexes **5** and **6**

The Mes complex **5**, $[\text{Ph}_2\text{P}(\text{NMes})_2]\text{Rh}(\text{CO})_2$, exhibits a significantly more upfield signal in the $^{31}\text{P}\{^1\text{H}\}$ NMR spectrum (δ 39.8) than the adamantyl analogue **6**, $[\text{Ph}_2\text{P}(\text{NAd})_2]\text{Rh}(\text{CO})_2$, δ 49.8. All resonances exhibit coupling to ^{103}Rh , $^2J_{\text{RhP}} = 15.1$ Hz (**5**) and $^2J_{\text{RhP}} = 10.0$ Hz (**6**). Expectedly, the mesityl-substituted iminophosphonamido dicarbonyl complex **5** is shifted further downfield by 15 ppm (δ 39.8) than its COD precursor **3**, $[\text{Ph}_2\text{P}(\text{NMes})_2]\text{Rh}(\text{COD})$, (δ 24.5). The adamantyl carbonyl complex **6** exhibits a minimal downfield chemical shift of 0.2 ppm (δ 49.8) compared to the $^{31}\text{P}\{^1\text{H}\}$ resonance of the COD precursor **5**, $[\text{Ph}_2\text{P}(\text{NAd})_2]\text{Rh}(\text{COD})$, at δ 50.0. In the ^1H NMR spectrum, the substituents on nitrogen are magnetically equivalent, displaying a single set of resonances. In the $^{13}\text{C}\{^1\text{H}\}$ NMR spectra, a doublet ($^1J_{\text{RhC}} = 69.8$ Hz for **5** and $^1J_{\text{RhC}} = 67.4$ Hz for **6**) attributed to $\text{C}\equiv\text{O}$ was observed for each complex (δ 187 (**5**) and δ 189 (**6**)). Both complexes exhibit two ν_{CO} stretches in their respective IR spectra; 2053, 1996 cm^{-1} for **5**, $[\text{Ph}_2\text{P}(\text{NMes})_2]\text{Rh}(\text{CO})_2$ and 2033, 1957 cm^{-1} for **6**, $[\text{Ph}_2\text{P}(\text{NAd})_2]\text{Rh}(\text{CO})_2$. The lower ν_{CO} stretching frequency exhibited by **6** indicates that the Rh centre is more electron-rich due to Ad being more electron-donating than Mes.

2.4.1.1 X-ray Crystal Structure of $[\text{Ph}_2\text{P}(\text{NMes})_2]\text{Rh}(\text{CO})_2$, (**5**)

Light yellow rectangular crystals of **5** suitable for X-ray diffraction were grown over one week from a saturated benzene solution stored at ambient temperature. Two independent molecules of **5** are contained within the asymmetric unit; however, only one is depicted in Figure 2.9.

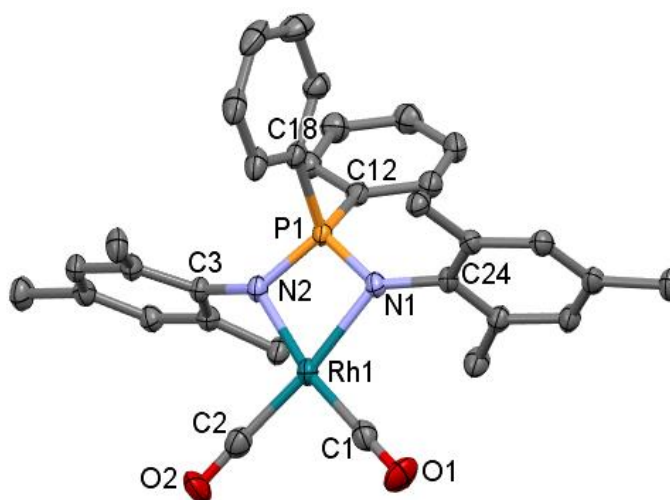


Figure 2.9 X-ray crystal structure of **5** depicted as 50% displacement ellipsoids. Hydrogen atoms and one of the two independent molecules of **5** in the unit cell are omitted for clarity

The geometry at Rh is approximately square planar ($\tau_4 = 0.13$) and, notably, less distorted than its COD precursor **5**, $[\text{Ph}_2\text{P}(\text{NMe}_2)_2]\text{Rh}(\text{CO})_2$. All P–N bond lengths exhibit less phosphinimine-like character, with similar bond distances (1.609(2)-1.614(2) Å), indicative of delocalized anionic charge (Figure 2.1). The short carbonyl bond distances (1.135(4) and 1.143(4) Å) are diagnostic of a formal $\text{C}\equiv\text{O}$ triple bond. Additional bond lengths and angles are similar between **5** (see Table 2.4) and the COD complex **3**, $[\text{Ph}_2\text{P}(\text{NMe}_2)_2]\text{Rh}(\text{COD})$ (see Table 2.2).

Table 2.4 Selected bond distances (Å) and angles (°) for compound **5**

Atoms	Distance (Å)	Atoms	Angle (°)
Rh–N1	2.085(2)	N1–Rh–N2	71.50(9)
Rh–N2	2.082(2)	C1–Rh–N1	98.80(11)
Rh–C1	1.852(3)	C2–Rh–N2	100.76(11)
Rh–C2	1.863(3)	C1–Rh–C2	88.94(13)
C1≡O1	1.143(4)	N1–P–N2	97.12(12)
C2≡O2	1.138(4)	C12–P–C18	101.26(12)
P–C12	1.811(3)		
P–C18	1.809(3)		
P–N1	1.609(2)		
P–N2	1.614(2)		
N2–C3	1.425(3)		
N1–C24	1.418(3)		

2.4.1.2 X-ray Crystal Structure of [Ph₂P(NAd)₂]Rh(CO)₂, (**6**)

Crystals of **6**, [Ph₂P(NAd)₂]Rh(CO)₂ suitable for X-ray diffraction analysis were grown from a saturated benzene solution at ambient temperature. Complex **6** crystallizes in the orthorhombic space group Pbc_a (Figure 2.10), whereas the previous complexes **3-5** crystallize in the P-1 space group.

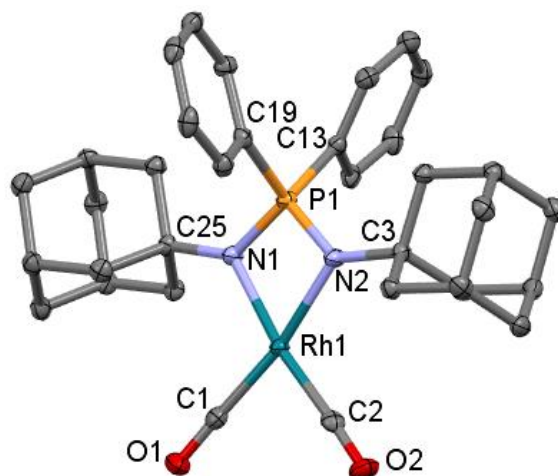


Figure 2.10 X-ray crystal structure of **6** depicted as 50% displacement ellipsoids. Hydrogen atoms are omitted for clarity

Complex **6** exhibits the least distorted square planar geometry about Rh ($\tau_4 = 0.12$) of all the iminophosphonamido rhodium structures discussed thus far. Akin to **5**, $[\text{Ph}_2\text{P}(\text{NMe}_s)_2]\text{Rh}(\text{CO})_2$, the similar P–N bond lengths (1.6090(16)-1.6102(16) Å) lie somewhere between a single and double bond, suggesting delocalization of the ligand's anionic charge (Figure 2.1). Key bond distances, such as C≡O, and bond angles, such as N–P–N, are nearly identical between the adamantyl complex **6** $[\text{Ph}_2\text{P}(\text{NAd})_2]\text{Rh}(\text{CO})_2$ (see Table 2.5) and **5** $[\text{Ph}_2\text{P}(\text{NMe}_s)_2]\text{Rh}(\text{CO})_2$, (see Table 2.4).

Table 2.5 Selected bond distances (Å) and angles (°) for compound **6**

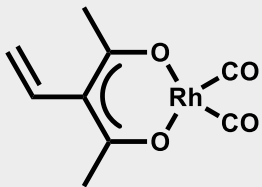
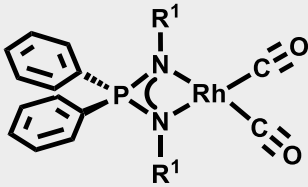
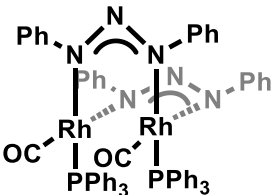
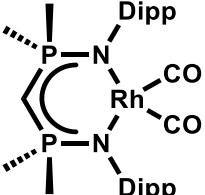
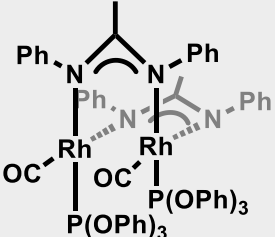
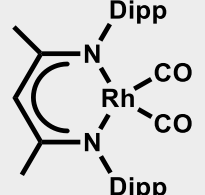
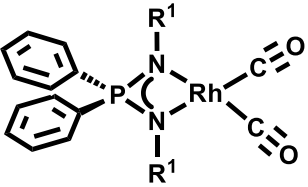
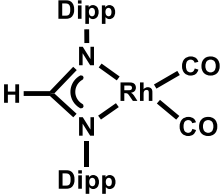
Atoms	Distance (Å)	Atoms	Angle (°)
Rh–N1	2.0780(15)	N1–Rh–N2	71.21(6)
Rh–N2	2.0716(16)	C1–Rh–N1	102.12(7)
Rh–C1	1.847(2)	C2–Rh–N2	101.66(7)
Rh–C2	1.847(2)	C1–Rh–C2	85.39(9)
C1≡O1	1.144(3)	N1–P–N2	97.27(8)
C2≡O2	1.146(2)	C13–P–C19	106.58(9)
P–C13	1.823(2)		
P–C15	1.8212(19)		
P–N1	1.6090(16)		
P–N2	1.6102(16)		
N1–C19	1.473(2)		
N2–C3	1.472(3)		

The Tolman electronic parameter (TEP)⁴⁴ employs the model complexes [Ni(CO)₃(L)] or *cis*-[RhCl(CO)₂(L)]. The average of the ν_{CO} stretches is used to compare the electron-donating ability of various ligands (L).^{138,139} TEP directly measures the decrease in the IR stretching frequencies of CO ligands in the metal complex; meaning that the stronger the σ -donating abilities of neutral donor ligand L, the greater the electron density at the metal centre which amplifies π -backdonation to CO, thereby lowering the frequency of the C≡O stretch (ν_{CO}) in the IR spectrum.^{44,45} In contrast, if L is a poor σ -donor, the ligand competes with CO for π -backdonation (only if L can participate in such bonding), which results in less lowering of the ν_{CO} stretching frequency.^{44,45} In the IR

spectrum of **5**, $[\text{Ph}_2\text{P}(\text{NMe}_s)_2]\text{Rh}(\text{CO})_2$, the ν_{CO} stretching frequencies 2053, 1996 cm^{-1} exhibit a TEP of 2025 cm^{-1} , similar to the eight-membered-ring NHCs (2025 cm^{-1})¹⁴⁰ and 1,2,3-triazolylidene-based NHCs (2015 cm^{-1}).¹⁴⁰ However, the TEP is designed for neutral monodentate ligands (L) in the model system, *cis*- $[\text{RhCl}(\text{CO})_2(\text{L})]$; thus, comparison between bidentate anionic ligands (iminophosphonamide) and neutral monodentate ligands (NHCs) is not necessarily appropriate. Evaluating a more precise picture of the ligand electronic influence is best done with analogous literature complexes. The lack of reported carbonyl iminophosphonamido complexes is disappointing; however, there are several known rhodium dicarbonyl compounds supported by other bidentate monoanionic ligands, namely, *disubstituted* acetylacetonato (acac) (Table 2.6, 1st row, left),¹⁴¹ bridging diaryltriazenido (Table 2.6, 2nd row, left),¹⁴² and bridging amidinate (Table 2.6, 3rd row, left) ligands,¹⁴³ which all have reported TEP values for comparison with **5**, $[\text{Ph}_2\text{P}(\text{NMe}_s)_2]\text{Rh}(\text{CO})_2$, and **6**, $[\text{Ph}_2\text{P}(\text{NAd})_2]\text{Rh}(\text{CO})_2$. However, there are also several calculated TEP values for ligands similar to iminophosphonamides $[\text{R}_2\text{P}(\text{NR}^1)_2]$, such as NacNacs (Table 2.6, 3rd row, right), bis(phosphinimine)methanides (Table 2.6, 2nd row, right), and most importantly, a rhodium amidinate complex $[\text{HC}(\text{NDipp})_2]\text{Rh}(\text{CO})_2$ (Table 2.6, 4th row, right).¹⁴⁴ The adamantyl-substituted ligand in **6** is predictably less electron-donating than both the electron-rich acac complex $[\text{H}_2\text{C}=\text{CHC}(\text{COMe})_2]\text{Rh}(\text{CO})_2$ and the bridging amidinate species $[\text{MeC}(\text{NPh})_2]\text{Rh}(\text{P}(\text{OPh})_3)_2(\text{CO})_2$. This difference is attributed to the additional phosphine donors in the bridging amidinate complex, as the phosphinimine containing bis(phosphinimine)methanide species $[\text{CH}_2(\text{Me}_2\text{P}=\text{NDipp})]\text{Rh}(\text{CO})_2$ exhibits a lower TEP value than the imine (NacNac)

analogue $[\text{CH}_2(\text{MeC}=\text{NDipp})\text{Rh}(\text{CO})_2]$ (Table 2.6), presumably due to the more donating P=N moiety.⁹⁷ As expected, both complexes **5**, $[\text{Ph}_2\text{P}(\text{NMes})_2]\text{Rh}(\text{CO})_2$ (TEP value 2025 cm^{-1}) and **6**, $[\text{Ph}_2\text{P}(\text{NAd})_2]\text{Rh}(\text{CO})_2$ (TEP value 1995 cm^{-1}) display lower TEP values than the rhodium amidinate complex $[\text{HC}(\text{NDipp})_2]\text{Rh}(\text{CO})_2$.¹⁴⁴

Table 2.6 TEP values for known NHC complexes and compound 5-6

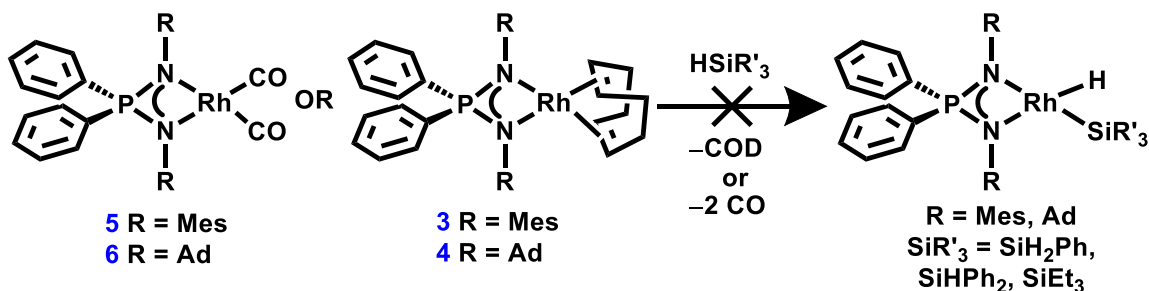
Complex	TEP (cm ⁻¹)	Complex	TEP (cm ⁻¹)
	1713 ¹⁴¹	 5 R = Mes	2025
	1973 ¹⁴²		*2097 ¹⁴⁴
	1993 ¹⁴³		*2104 ¹⁴⁴
 6 R = Ad	1995		*2109 ¹⁴⁴
* Indicates calculated CO stretching frequencies of L bound to a Rh(CO) ₂ fragment at the b3-lyp/def-TZVP level of theory, ¹⁴⁴ as no experimental values have been measured			

2.4.2 Reactions of Rh^I Iminophosphonamido COD Complexes with Silanes and H₂

Hydrosilylation and hydrogenation of alkenes are mechanistically similar, commercially relevant processes, and given the prevalence of Rh species as effective

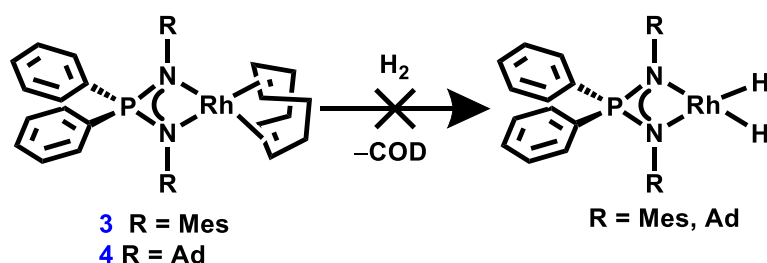
hydrosilylation and hydrogenation catalysts,¹⁴⁵ it seemed a natural choice to scope the capabilities of the newly prepared Rh^I iminophosponamido species. Complexes **3** [Ph₂P(NMes)₂]Rh(COD), **4** [Ph₂P(NAd)₂]Rh(COD), **5** [Ph₂P(NMes)₂]Rh(CO)₂, and **6** [Ph₂P(NAd)₂]Rh(CO)₂.

Before catalytic scoping reactions were conducted, the Rh^I complexes (**3-6**) were reacted with one equivalent of either a primary, secondary, or tertiary silane (H₃SiPh, H₂SiPh₂, and HSiEt₃) in benzene-*d*₆ in an attempt to isolate the corresponding silyl hydride complex (Scheme 2.5), an intermediate in Chalk-Harrod hydrosilylation. At ambient temperature in benzene-*d*₆, no reactions occurred within 16 h. Heating the reaction mixture to 70 °C or using THF-*d*₈ or CDCl₃ also yielded no reaction. Attempts to induce loss of the COD ligand by placing the reaction vessel under a static vacuum, wherein the reaction mixture was degassed by two freeze-pump-thaw cycles, resulted in no reaction. Given that stoichiometric reactions were unsuccessful, it was expected that catalytic scoping reactions would be unsuccessful, and indeed, reacting the COD complexes (**3** [Ph₂P(NMes)₂]Rh(COD), and **4** [Ph₂P(NAd)₂]Rh(COD)) with excess silane and dimethylacetylene (2-butyne) yielded no conversion.



Scheme 2.5 Attempted synthesis of Rh^{III} silyl iminophosponamido complexes

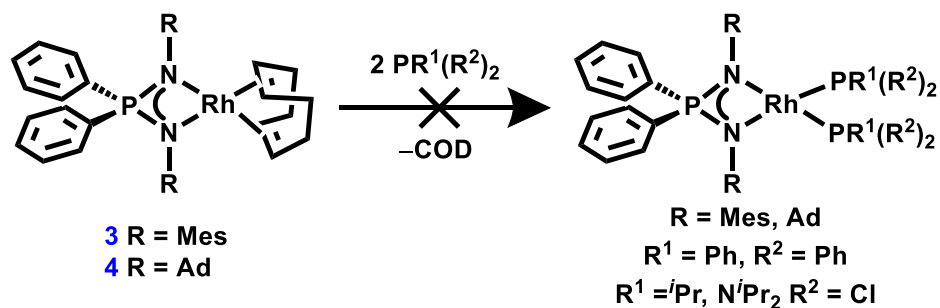
Alternatively, in an attempt to generate the Rh hydrides $[\text{Ph}_2\text{P}(\text{NMes})_2]\text{Rh}(\text{H})_2$, and $[\text{Ph}_2\text{P}(\text{NAd})_2]\text{Rh}(\text{H})_2$, an intermediate in hydrogenation processes, the COD complexes (**3** and **4**) were placed under an atmosphere of H_2 (Scheme 2.6). No reaction was observed after 16 h in benzene- d_6 at ambient temperatures. Variation of reaction conditions *via* elevated temperatures (70 °C), longer reaction times (2 weeks) and solvent (THF- d_8 or CDCl_3) did not lead to consumption of the starting Rh COD complex (**3** or **4**).



Scheme 2.6 Attempted synthesis of Rh^{III} dihydride iminophosphonamido complexes

2.4.3 Attempted Reaction of Rh^{I} Iminophosphonamido complexes with Phosphines

It was postulated that the COD group of **3** $[\text{Ph}_2\text{P}(\text{NMes})_2]\text{Rh}(\text{COD})$, **4** $[\text{Ph}_2\text{P}(\text{NAd})_2]\text{Rh}(\text{COD})$ could be replaced with two phosphine ligands, thus generating *bis*phosphine iminophosphonamido complexes $[\text{Ph}_2\text{P}(\text{NR})_2]\text{Rh}(\text{PR}^1_3)_2$ (Scheme 2.7); which, could then react with various silanes and H_2 after dissociation of the phosphine ligands. However, 2:1 stoichiometric additions of numerous phosphines (PPh_3 , $^i\text{Pr}_2\text{PCl}$, $(^i\text{Pr}_2\text{N})_2\text{PCl}$) to the COD complexes (**3** and **4**) yielded no reaction at ambient or elevated temperatures (70 °C), regardless of solvent (benzene- d_6 , THF- d_8 or CDCl_3).



Scheme 2.7 Attempted synthesis of Rh^I phosphine iminophosphonamido complexes

2.4.4 Reactivity of Rh^I Iminophosphonamido Complexes with 2,6-Me₂C₆H₃N≡C

The COD group in the complexes **3** [Ph₂P(NMes)₂]Rh(COD), and **4** [Ph₂P(NAd)₂]Rh(COD), can be readily substituted by CO but is inert towards displacement by silanes, phosphines and H₂. Hence, it was deemed likely that a COD group could be easily substituted by a ligand isolobal with CO, such as the isocyanide 2,6-dimethylphenylisocyanide (CN(2,6-Me₂C₆H₃)). Two and a third equivalents of 2,6-dimethylphenylisocyanide were required to fully consume **3**, [Ph₂P(NMes)₂]Rh(COD) at ambient temperature in benzene-*d*₆. Two product signals were observed in the ³¹P{¹H} NMR spectrum (Figure 2.11) at δ 15.2 (s) and δ 25.1 (²J_{RhP} = 13.7 Hz). The latter doublet (δ 25.1) was attributed to the target bis(2,6-dimethylphenylisocyano) complex **7**, [(Ph₂P(NMes)₂]Rh[C≡N(2,6-Me₂C₆H₃)]₂, while the former singlet (δ 15.2) was later found to correspond to the bis(2,6-dimethylphenylisocyano)2,6-dimethylphenylimine species **8**, [*N,C*-Ph₂P(NMes)(MesNC=N(2,6-Me₂C₆H₃))]Rh[C≡N(2,6-Me₂C₆H₃)]₂ (see section 2.4.5).

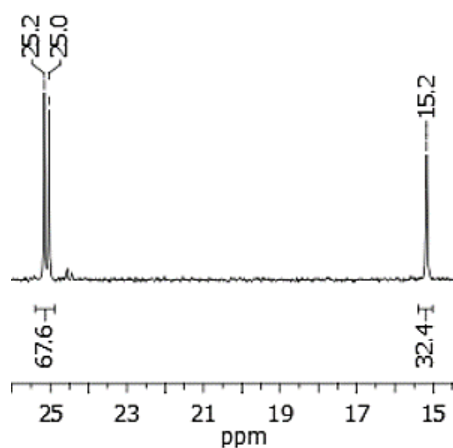


Figure 2.11 $^{31}\text{P}\{^1\text{H}\}$ NMR spectrum of the **2** (2,6-Me₂C₆H₃N≡C) + **3** reaction mixture:
 δ 25.1 (d, $^2J_{\text{RhP}} = 13.7$ Hz, 68%, **7**), 15.2 (32%, **8**)

Cold pentane (-35 °C) was added to a mixture of 2,6-dimethylphenylisocyanide and complex **3**; after which, the solution was kept at -35 °C to minimize the formation of the *tris*-isocyano side product **8**. After 16 h, benzene was added to the reaction mixture, the solution filtered, and left to crystallize for 3 days at ambient temperature, resulting in yellow cube-shaped crystals of **7** (Figure 2.12).

2.4.4.1 X-ray Crystal Structure of $[\text{Ph}_2\text{P}(\text{NMe}_3)_2]\text{Rh}[\text{C}\equiv\text{N}(2,6\text{-Me}_2\text{C}_6\text{H}_3)]_2$, (**7**)

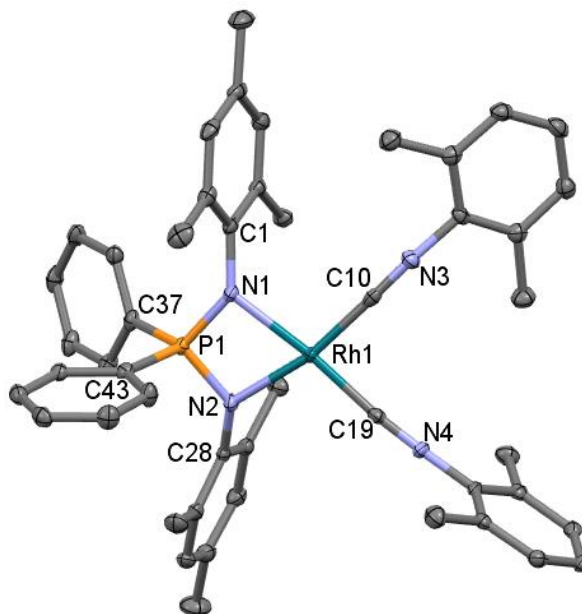


Figure 2.12 X-ray crystal structure of **7**, depicted as 50% displacement ellipsoids. Hydrogen atoms are omitted for clarity

The complex **7**, $[\text{Ph}_2\text{P}(\text{NMe}_3)_2]\text{Rh}[\text{C}\equiv\text{N}(2,6\text{-Me}_2\text{C}_6\text{H}_3)]_2$ crystallized in the $P-1$ space group, with distorted square planar geometry around rhodium ($\tau_4 = 0.12$), akin to the dicarbonyl complex **5**, $[\text{Ph}_2\text{P}(\text{NMe}_3)_2]\text{Rh}(\text{CO})_2$ ($\tau_4 = 0.13$). The $\text{C}\equiv\text{N}$ bond distances in **7** (1.173(2) and 1.169(2) Å) are diagnostic for a triple bond and comparable to the $\text{C}\equiv\text{O}$ lengths in the dicarbonyl complex **5** (1.135(4) and 1.143(4) Å). The P–N lengths are similar to each other (1.6086(14) and 1.627(14) Å) and indicative of charge delocalization. Other metrical parameters (see Table 2.7) are similar to those in complexes **3** $[\text{Ph}_2\text{P}(\text{NMe}_3)_2]\text{Rh}(\text{COD})$, **4** $[\text{Ph}_2\text{P}(\text{NAd})_2]\text{Rh}(\text{COD})$, **5** $[\text{Ph}_2\text{P}(\text{NMe}_3)_2]\text{Rh}(\text{CO})_2$, and **6** $[\text{Ph}_2\text{P}(\text{NAd})_2]\text{Rh}(\text{CO})_2$.

Table 2.7 Selected bond distances (Å) and angles (°) for compound **7**

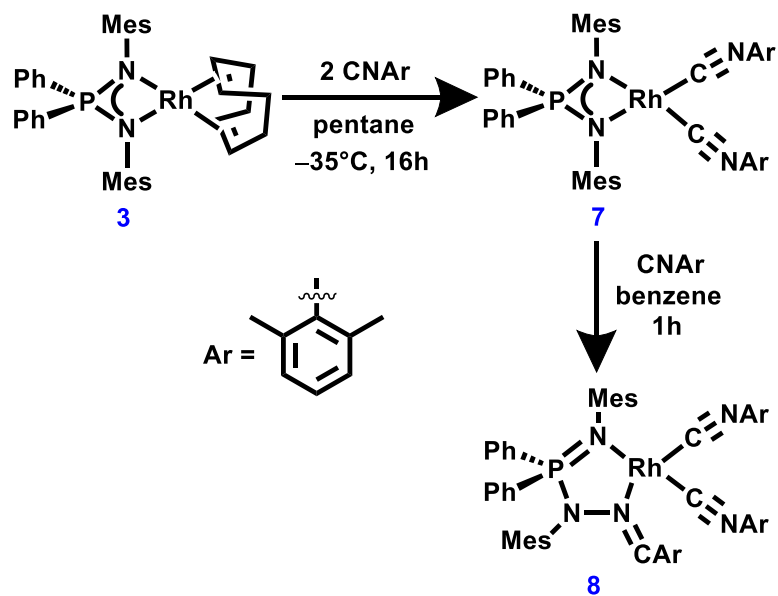
Atoms	Distance (Å)	Atoms	Angle (°)
Rh–N1	2.1140(14)	N1–Rh–N2	71.04(5)
Rh–N2	2.1146(14)	C10–Rh–N1	98.20(6)
Rh–C10NAr	1.8817(18)	C19–Rh–N2	104.47(6)
Rh–C19NAr	1.862(18)	C10–Rh–C19	86.51(7)
C10≡N3	1.169(2)	N1–P–N2	99.82(7)
C19≡N4	1.173(2)	C37–P–C43	103.34(8)
P–C37	1.8186(17)		
P–C43	1.8166(17)		
P–N1	1.6086(14)		
P–N2	1.6027(14)		
N–C1	1.418(2)		
N–C28	1.418(2)		

In the ^1H NMR spectrum of **7**, $[\text{Ph}_2\text{P}(\text{NMe}_s)_2]\text{Rh}[\text{C}\equiv\text{N}(2,6\text{-Me}_2\text{C}_6\text{H}_3)]_2$, one set of resonances was observed for each of the isocyano, phosphorus and nitrogen alkyl and phenyl substituents. Similarly, in the $^{13}\text{C}\{^1\text{H}\}$ NMR spectrum, a single $\text{C}\equiv\text{N}$ resonance was observed at δ 161.97. The $^{31}\text{P}\{^1\text{H}\}$ resonance, at δ 25.1, displays coupling to ^{103}Rh ($^2J_{\text{RhP}} = 13.7$ Hz), is barely shifted from the COD precursor **3**, $[\text{Ph}_2\text{P}(\text{NMe}_s)_2]\text{Rh}(\text{COD})$, which resonates at δ 24.5. Complex **7**, $[\text{Ph}_2\text{P}(\text{NMe}_s)_2]\text{Rh}[\text{C}\equiv\text{N}(2,6\text{-Me}_2\text{C}_6\text{H}_3)]_2$, and exhibits a

substantially more upfield $^{31}\text{P}\{^1\text{H}\}$ NMR signal than the carbonyl complex **5** $[\text{Ph}_2\text{P}(\text{NMe}_s)_2]\text{Rh}(\text{CO})_2$, which resonates at δ 39.8. The bis(2,6-dimethylphenylisocyano) complex **7** exhibits two ν_{CN} stretches in the IR spectrum at 2035 and 1964 cm^{-1} ($\nu_{\text{average}} = 2000 \text{ cm}^{-1}$) that are, as expected, lower in frequency than that of uncoordinated 2,6-dimethylphenylisocyanide (2119 cm^{-1}), suggesting π -backdonation into the LUMO of the isocyano ligand. For reference, **5** $[\text{Ph}_2\text{P}(\text{NMe}_s)_2]\text{Rh}(\text{CO})_2$ displays two ν_{CO} triple bonding stretching frequencies of 2053, 1996 cm^{-1} .

2.4.5 Synthesis of $[\text{N},\text{C}\text{-Ph}_2\text{P}(\text{NMe}_s)(\text{MesNC}=\text{N}(2,6\text{-Me}_2\text{C}_6\text{H}_3))]\text{Rh}[\text{C}\equiv\text{N}(2,6\text{-Me}_2\text{C}_6\text{H}_3)]_2$ (**8**)

The addition of another equivalent of 2,6-dimethylphenylisocyanide to $[\text{Ph}_2\text{P}(\text{NMe}_s)_2]\text{Rh}[\text{C}\equiv\text{N}(2,6\text{-Me}_2\text{C}_6\text{H}_3)]_2$ led to complete consumption of **7**; however, neutral iminophosphonamide ligand **I**, $\text{Ph}_2\text{P}(\text{NHMe}_s)(\text{NMe}_s)$ is observed as a decomposition product in the $^{31}\text{P}\{^1\text{H}\}$ NMR spectrum (δ -16.7, 10%), presumably due to excess isocyanide sequestering the Rh centre. The major product in the $^{31}\text{P}\{^1\text{H}\}$ NMR spectrum (δ 15.2, 90%) is attributed to the complex **8**, $[\text{N},\text{C}\text{-Ph}_2\text{P}(\text{NMe}_s)(\text{MesNC}=\text{N}(2,6\text{-Me}_2\text{C}_6\text{H}_3))]\text{Rh}[\text{C}\equiv\text{N}(2,6\text{-Me}_2\text{C}_6\text{H}_3)]_2$ (Scheme 2.8), which was later found to contain a 5-membered metallocycle wherein an isocyanide is inserted (1,1 insertion) into the iminophosphonamide Rh–N bond, confirmed by X-ray diffraction (Figure 2.13).



Scheme 2.8 Synthesis of **7** and **8**

2.4.5.1 X-ray Crystal Structure of $[N,C\text{-Ph}_2\text{P}(\text{NMe}_s)(\text{MesNC}=\text{N}(2,6\text{-Me}_2\text{C}_6\text{H}_3))\text{Rh}[\text{C}\equiv\text{N}(2,6\text{-Me}_2\text{C}_6\text{H}_3)]_2 \cdot 1.5\text{C}_6\text{H}_6$ (**8**)

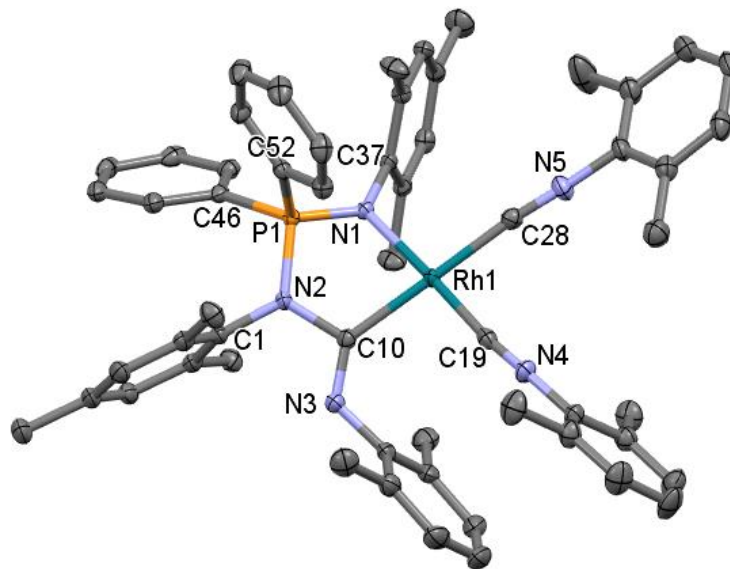


Figure 2.13 X-ray crystal structure of **8**·C₆H₆ depicted as 50% displacement ellipsoids. Hydrogen atoms and the solvent molecule are omitted for clarity

Yellow rectangular crystals of complex **8**, [*N,C*-Ph₂P(NMes)(MesNC=N(2,6-Me₂C₆H₃))]Rh[C≡N(2,6-Me₂C₆H₃)₂], were grown from a saturated benzene solution stored in a sealed 20 mL scintillation vial at ambient temperature over 3 days. The 5-membered metallocycle in **8** increased the iminophosphonamide bite angle from 71.04(5)° in **7**, [Ph₂P(NAd)₂]Rh[C≡N(2,6-Me₂C₆H₃)₂] to 83.63(5)° in **8**, [*N,C*-Ph₂P(NMes)(MesNC=N(2,6-Me₂C₆H₃))]Rh[C≡N(2,6-Me₂C₆H₃)₂]. The geometry at rhodium is square planar ($\tau_4 = 0.03$) and far less distorted than all other iminophosphonamido complexes discussed thus far. The two C≡N bond distances are consistent with C≡N triple bonds (1.166(2) and 1.172(2) Å). In contrast, the C=N bond distance of the inserted 2,6-dimethylphenylimine [*N,C*-Ph₂P(NMes)(MesNC=N(2,6-Me₂C₆H₃))]Rh[C≡N(2,6-Me₂C₆H₃)₂], resembles a typical C=N double bond (1.276 Å). The Rh–C28 and Rh–C19 bond distances of the isocyano moieties (1.989(16) and 1.8689(16) Å, Table 2.8) are shorter than Rh–C≡O in **5** (1.135(4) and 1.143(4) Å) due to π -backdonation into the C≡N antibonding π^* orbitals. The C10–N2 distance (1.4575(18) Å) is indicative of a single bond.

Table 2.8 Selected bond distances (Å) and angles (°) for complex **8**

Atoms	Distance (Å)	Atoms	Angle (°)
Rh–N1	2.1269(12)	N3–C10–N2	111.54(13)
C19≡N4	1.172(2)	N2–C10–Rh	112.19(10)
C28≡N5	1.166(2)	Rh–C10–N3	136.22(11)
C10=N3	1.276(2)	C10–N2–P	116.84(10)
Rh–C28	1.9589(16)	N2–P–N1	104.80(6)
Rh–C19	1.8689(16)	C28–Rh–N1	86.19(6)
Rh–C10	2.0666(15)	N1–Rh–C10	83.63(5)
C10–N3	1.4575(18)	C10–Rh–C19	94.07(6)
P–C46	1.8142(16)	C19–Rh–C28	86.19(6)
P–C52	1.8159(15)	C28–Rh–N1	96.08(5)
P–N1	1.5902(12)	C46–P–C52	105.26(7)
P–N2	1.6679(13)		
N2–C1	1.4479(18)		
N1–C37	1.4248(18)		

The ^1H NMR spectrum of **8** contains several overlapping aromatic resonances, ranging from δ 8.21–6.40, attributed to two magnetically equivalent phosphorus substituents, two magnetically inequivalent mesityl groups and three magnetically inequivalent 2,6-dimethylphenyl moieties. The IR spectrum exhibits three distinct CN

stretches, two in the predicted $\nu_{\text{C}\equiv\text{N}}$ stretching frequency range at 2106 and 2044 cm^{-1} , and a lower frequency signal (1566 cm^{-1}) attributed to the C=N of the inserted “isocyano” group *N,C*-Ph₂P(NMes)(MesNC=N(2,6-Me₂C₆H₃))Rh[C≡N(2,6-Me₂C₆H₃)]₂.

2.4.6 Attempted Reactivity of Isocyano Complexes (7) and (8)

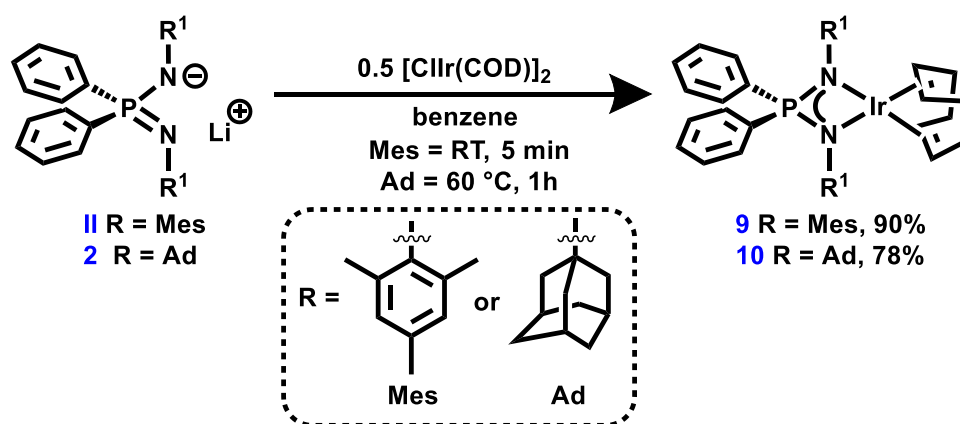
Much like the Rh^I iminophosphonamido complexes (**3** [Ph₂P(NMes)₂]Rh(COD), **4** [Ph₂P(NAd)₂]Rh(COD), **5** [Ph₂P(NMes)₂]Rh(CO)₂, and **6** [Ph₂P(NAd)₂]Rh(CO)₂), the isocyano Rh^I species (**7** [Ph₂P(NAd)₂]Rh[C≡N(2,6-Me₂C₆H₃)]₂, and **8** *N,C*-Ph₂P(NMes)(MesNC=N(2,6-Me₂C₆H₃))Rh[C≡N(2,6-Me₂C₆H₃)]₂) were found to be inert toward both silanes and H₂. Interestingly, the isocyano groups could not be exchanged for carbon monoxide upon exposure to an atmosphere of CO.

2.5 Synthesis of Iminophosphonamido Ir^I Complexes

Given the limited reactivity of the Rh^I complexes (**3** [Ph₂P(NMes)₂]Rh(COD), **4** [Ph₂P(NAd)₂]Rh(COD), **5** [Ph₂P(NMes)₂]Rh(CO)₂, and **6** [Ph₂P(NAd)₂]Rh(CO)₂), **7** [Ph₂P(NAd)₂]Rh[C≡N(2,6-Me₂C₆H₃)]₂, and **8** *N,C*-Ph₂P(NMes)(MesNC=N(2,6-Me₂C₆H₃))Rh[C≡N(2,6-Me₂C₆H₃)]₂), it was postulated that the heavier metal Ir^I might exhibit increased activity towards H₂ as iridium is the more prevalent of the two metals in hydrogenation processes.¹⁴⁶

The generation of the Ir^I species **9**, [Ph₂P(NMes)₂]Ir(COD) and **10**, [Ph₂P(NAd)₂]Ir(COD) was readily achieved *via* a salt metathesis reaction, wherein a benzene solution of the iminophosphonamido lithium salts (**II**, Li[Ph₂P(NMes)₂] and **2**, Li[Ph₂P(NAd)₂]) were added to the iridium dimer [ClIr(COD)]₂ to generate the desired Ir^I

COD complexes **9** and **10** (Scheme 2.9). The mesityl-substituted species **9**, $[\text{Ph}_2\text{P}(\text{NMes})_2]\text{Ir}(\text{COD})$, can be prepared at ambient temperature, while the adamantyl derivative **10**, $[\text{Ph}_2\text{P}(\text{NAd})_2]\text{Ir}(\text{COD})$, requires heating at 60 °C for 1 h in benzene. Further heating of the reaction mixture results in slow decomposition to the neutral iminophosphonamide ligand **1**, $\text{Ph}_2\text{P}(\text{NHAd})(\text{NAd})$, indicated by $^{31}\text{P}\{^1\text{H}\}$ NMR spectroscopy.



Scheme 2.9 Synthesis of iminophosphonamido-Ir^I COD complexes **9** and **10**

2.5.1 Characterization of $[\text{Ph}_2\text{P}(\text{NR})_2]\text{Ir}(\text{COD})$ where R = Mes (**9**) and R = Ad (**10**)

The substitution of rhodium by the heavier metal iridium in complexes **9**, $[\text{Ph}_2\text{P}(\text{NMes})_2]\text{Ir}(\text{COD})$, and **10** $[\text{Ph}_2\text{P}(\text{NAd})_2]\text{Ir}(\text{COD})$, yields significantly higher frequency $^{31}\text{P}\{^1\text{H}\}$ NMR signals. Complex **9** is shifted by 26 ppm (δ 40.9) from the analogous Rh complex **5** $[\text{Ph}_2\text{P}(\text{NMes})_2]\text{Rh}(\text{COD})$ (δ 24.5), while **10** is further downfield (δ 66.7) than the Rh species **6** $[\text{Ph}_2\text{P}(\text{NAd})_2]\text{Rh}(\text{COD})$ (δ 50.0). Both iridium complexes **9** and **10** contain broad resonances throughout the ^1H NMR spectra, unlike the analogous Rh complexes (**3** $[\text{Ph}_2\text{P}(\text{NMes})_2]\text{Rh}(\text{COD})$ and **4** $[\text{Ph}_2\text{P}(\text{NAd})_2]\text{Rh}(\text{COD})$), attributed to some

dynamic process occurring in in the solution state. Notably, the adamantyl substituted iridium complex **10**, $[\text{Ph}_2\text{P}(\text{NAd})_2]\text{Ir}(\text{COD})$, contains a more deshielded COD methine resonance (CH) (δ 4.72) than the corresponding mesityl complex **9**, $[\text{Ph}_2\text{P}(\text{NMes})_2]\text{Ir}(\text{COD})$ (δ 3.42), attributed to the more electron-donating nature of the adamantyl substituents on nitrogen, as demonstrated in Section 2.4.1.

2.5.1.1 X-ray Crystal Structure of $[\text{Ph}_2\text{P}(\text{NMes})_2]\text{Ir}(\text{COD})$, (**9**)

From a saturated pentane solution of **9**, $[\text{Ph}_2\text{P}(\text{NMes})_2]\text{Ir}(\text{COD})$, stored at ambient temperature, yellow plate-shaped crystals were grown. The structure of **9**, depicted in Figure 2.14, contains slightly distorted square planar geometry about the metal centre ($\tau_4 = 0.28$), akin to the analogous mesityl-substituted Rh complex **3**, $[\text{Ph}_2\text{P}(\text{NMes})_2]\text{Rh}(\text{COD})$ ($\tau_4 = 0.27$).

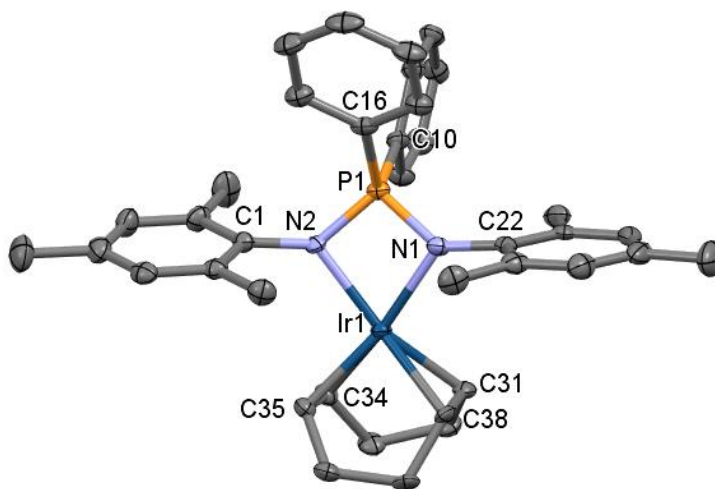


Figure 2.14 X-ray crystal structure of **9** depicted as 50% displacement ellipsoids. Hydrogen atoms are omitted for clarity

The Ir–COD and Ir–N bond distances (~2.11 and ~2.08 Å, respectively) in **9**, [Ph₂P(NMes)₂]Ir(COD) are comparable to the Rh–COD and Rh–N bond lengths (~2.10 and ~2.09 Å, respectively) in the analogous Rh complex **3**, [Ph₂P(NMes)₂]Rh(COD), attributed to the nearly identical atomic radii of iridium and rhodium.¹⁴⁷ Similarly, other key bond distances and angles, such as the P–N bond distances and the N–M–N bite angle, in complex **9** (Table 2.9), are also unchanged when compared to the Rh^I analogue **3**, [Ph₂P(NMes)₂]Rh(COD) (Table 2.2).

Table 2.9 Selected bond distances (Å) and angles (°) for complex **9**

Atoms	Distance (Å)	Atoms	Angle (°)
Ir–N1/N2	2.074(2), 2.095(2)	N1–Ir–N2	71.55(9)
N1–C1	1.413(3)	C31–Ir–N1	97.31(10)
N2–C22	1.414(3)	C35–Ir–N2	98.01(10)
P–C10	1.813(3)	C38–Ir–N1	101.70(10)
P–C16	1.802(3)	C34–Ir–N2	101.34(10)
P–N1	1.614(2)	C34–Ir–C31	81.45(11)
P–N2	1.614(2)	C35–Ir–C38	82.29(10)
Ir–C31	2.102(2)	N1–P–N2	98.01(10)
Ir–C34	2.114(3)	C10–P–C16	104.28(12)
Ir–C35	2.103(2)		
Ir–C38	2.124(2)		

2.5.1.2 X-ray Crystal Structure of [Ph₂P(NAd)₂]Ir(COD) · 1.5C₆H₆ (**10**)

Colourless blocks of **10**, [Ph₂P(NAd)₂]Ir(COD), were grown from a saturated benzene solution stored in a sealed 20 mL scintillation vial at ambient temperature for 3 days. One and a half benzene molecules were found in the asymmetric unit but are not depicted in Figure 2.15.

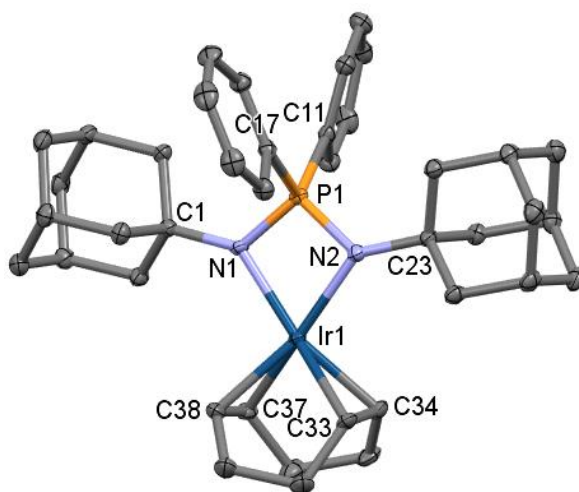


Figure 2.15 X-ray crystal structure of **10**·1.5C₆H₆ depicted as 50% displacement ellipsoids. Hydrogen atoms and solvent molecules are omitted for clarity

The square planar geometry at Ir is distorted ($\tau_4 = 0.26$) in a manner similar to other structures described in this chapter. All key bond distances and angles in **10** (Table 2.10) are unaffected by the change in ligand or metal centre when compared to the mesityl Ir^I species **9**, [Ph₂P(NMes)₂]Ir(COD) (Table 2.9), or the adamantyl Rh^I complex **4**, [Ph₂P(NAd)₂]Rh(COD) (Table 2.2).

Table 2.10 Selected bond distances (Å) and angles (°) for compound **10**

Atoms	Distance (Å)	Atoms	Angle (°)
Ir–N1	2.1082(18)	N1–Ir–N2	71.62(7)
Ir–N2	2.1047(17)	C38–Ir–N1	99.40(8)
N1–C1	1.481(3)	C33–Ir–N2	98.09(8)
N2–C23	1.483(3)	C37–Ir–N1	102.16(8)
P–C11	1.819(2)	C34–Ir–N2	101.87(8)
P–C17	1.821(2)	N1–P–N2	99.15(9)
P–N1	1.6243(18)	C11–P–C17	109.37(10)
P–N2	1.6135(19)		
Ir–C33	2.119(2)		
Ir–C34	2.113(2)		
Ir–C37	2.120(2)		
Ir–C38	2.112(2)		

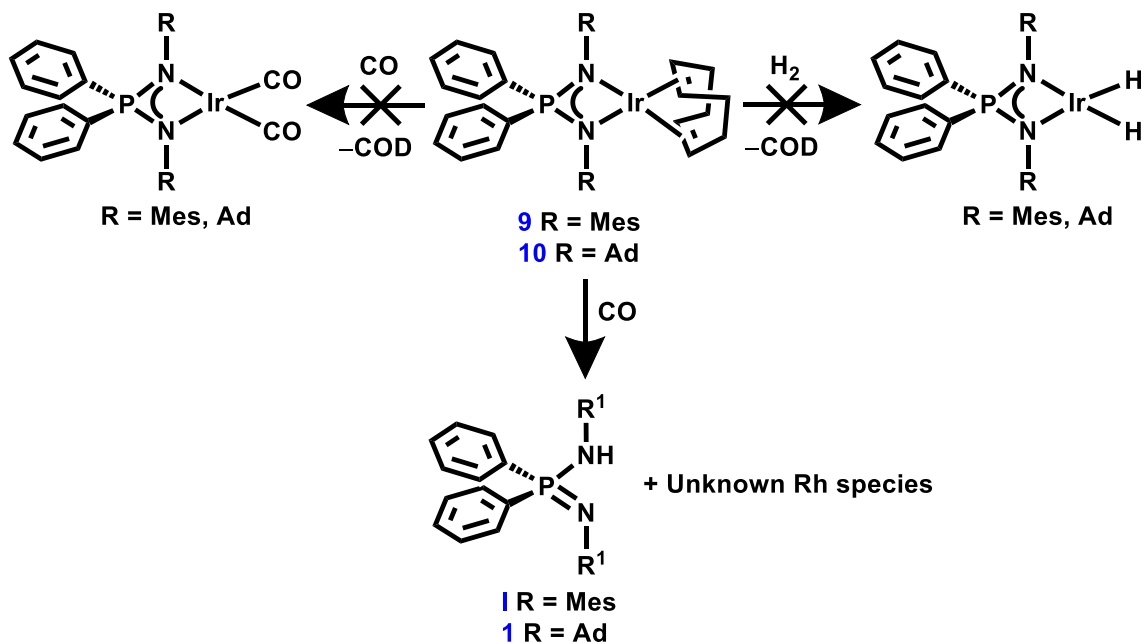
2.6 Reactivity of Ir^I Iminophosphonamido Complexes Toward Small Molecules

2.6.1 Reactions of Ir^I Iminophosphonamido COD Complexes with CO and H₂

Like the previously discussed rhodium species, iridium carbonyl complexes of the general form *cisoid*-[IrCl(CO)₂(L)] have also been employed to evaluate the donor/acceptor properties of a given ligand L *via* the Tolman electronic parameter (TEP). In 2003, Crabtree *et al.* first employed the model iridium complex to measure the TEP of NHC ligands and proposed an interconversion equation between Ir^I and Rh^I values: $TEP_{Rh} = 0.8475[\nu_{av} (Ir)] + 336.2 \text{ cm}^{-1}$.¹⁴⁸ Thus, measuring the ν_{CO} stretching frequencies of the same ligand in two model complexes is not necessary, but for comparison sake, the TEP values of **9**, [Ph₂P(NMes)₂]Ir(COD) (2052 cm⁻¹) and **10**, [Ph₂P(NAd)₂]Ir(COD) (2027 cm⁻¹) were easily calculated from the measured Rh TEP values in section 2.4.1. Generation of an iridium carbonyl target complex would allow an Ir TEP value to be measured and one to compare and contrast the reaction chemistry of these iminophosphonamido complexes with strong π -acceptor ligands within group 9.

When placed under an atmosphere of CO and warmed to ambient temperature in benzene-*d*₆, the iridium COD complexes **9** [Ph₂P(NMes)₂]Ir(COD) and **10** [Ph₂P(NAd)₂]Ir(COD) were predicted to form the dicarbonyl species [Ph₂P(NMes)₂]Ir(CO)₂ and [Ph₂P(NAd)₂]Ir(CO)₂ (Scheme 2.10). Instead, there is evidence in the ³¹P NMR spectra that suggest decomposition of **9** and **10** in the presence of 1 CO atm, as the only peaks observed can be attributed to neutral iminophosphonamide ligands Ph₂P(NHMes)(NMes) and Ph₂P(NHAd)(NAd). In addition, free COD was observed in the ¹H NMR spectrum. Exchanging the aromatic benzene-*d*₆ solvent for THF-*d*₈, thereby

allowing the reaction to proceed at cooler temperatures of $-35\text{ }^{\circ}\text{C}$, did not prevent decomposition. The exact decomposition pathway is unknown.



Scheme 2.10 Attempted synthesis of Ir^{I} carbonyl and Ir^{III} dihydride iminophosponamido complexes

In an attempt to generate $[\text{Ph}_2\text{P}(\text{NMe}_s)_2]\text{IrH}_2$ and $[\text{Ph}_2\text{P}(\text{NAd})_2]\text{IrH}_2$ (Scheme 2.10), the COD complexes **9** and **10** were placed under an atmosphere of H_2 in benzene- d_6 at ambient temperature; however, no new resonances were observed in the ^{31}P NMR spectrum over 72 h. Elevating the reaction temperature to $60\text{ }^{\circ}\text{C}$ for 16 h or attempting the reaction in THF- d_8 only afforded unchanged COD complexes **9** and **10**. Attempted catalytic scoping reactions, wherein 10 equivalents of 2-butyne were added to 1 equivalent of an iridium complex (**9** or **10**) in benzene- d_6 and an atmosphere of H_2 , also failed to lead to any reactions.

2.6.2 Reactivity of Ir^I Iminophosphonamido Complexes Towards 2,6-Me₂C₆H₃N≡C

Preliminary scoping reactions between two equivalents of 2,6-dimethylphenylisocyanide and the iridium complex **9** [Ph₂P(NMes)₂]Ir(COD) indicate generation of complexes **11** [Ph₂P(NAd)₂]Ir[C≡N(2,6-Me₂C₆H₃)₂] (Figure 2.16 left) and **12** *N,C*-Ph₂P(NMes)(MesNC=N(2,6-Me₂C₆H₃))Ir[C≡N(2,6-Me₂C₆H₃)₂] (Figure 2.16 right); the iridium analogous of the Rh complexes **7**, [Ph₂P(NAd)₂]Rh[C≡N(2,6-Me₂C₆H₃)₂], and **8**, *N,C*-Ph₂P(NMes)(MesNC=N(2,6-Me₂C₆H₃))Rh[C≡N(2,6-Me₂C₆H₃)₂], see section 2.4.4.

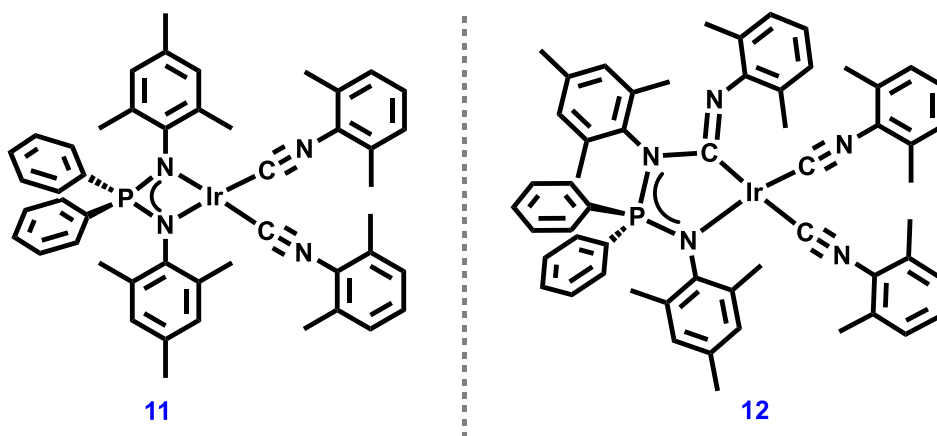


Figure 2.16 Proposed structures of 2,6-Me₂C₆H₃N≡C iridium complexes **11** and **12**

The ³¹P{¹H} NMR spectrum of the reaction mixture of two 2,6-Me₂C₆H₃N≡C + **9** (Figure 2.17) contains a resonance at δ 37.7 (21%) which is attributed to the desired bis(2,6-dimethylphenylisocyanato) iridium species **11**, [Ph₂P(NAd)₂]Ir[C≡N(2,6-Me₂C₆H₃)₂]. The chemical shift of **11** is downfield compared to the analogous Rh complex **7**, [Ph₂P(NAd)₂]Rh[CN(2,6-Me₂C₆H₃)₂] (δ 25.1). However, **11** is not the major product in the mixture's ³¹P{¹H} NMR spectrum (Figure 2.17). Another signal (δ 23.0)

equates to 56%, and is attributed to the bis(2,6-dimethylphenylisocyano)2,6-dimethylphenylimine complex **12**, *N,C*-Ph₂P(NMes)(MesNC=N(2,6-Me₂C₆H₃))Ir[C≡N(2,6-Me₂C₆H₃)]₂ (Figure 2.16 right). The ³¹P{¹H} NMR signal of **12** (δ 23.0) is 16 ppm upfield of bis(2,6-dimethylphenylisocyano) iridium complex **11** (δ 37.7) which correlates well with the difference in chemical shift observed between the analogous Rh complexes **7** ([Ph₂P(NAd)₂]Rh[C≡N(2,6-Me₂C₆H₃)]₂, δ 25.1) and **8** (*N,C*-Ph₂P(NMes)(MesNC=N(2,6-Me₂C₆H₃))Rh[C≡N(2,6-Me₂C₆H₃)]₂, δ 15.2). Hence, **12** is anticipated to be isostructural with **8**, with an isocyanide inserted into the Ir–N iminophosphonamide bond. The ¹H NMR spectrum of the mixture contains several distinct CH₃ signals attributed to the mesityl and dimethylphenyl groups present in both **11** and **12**.

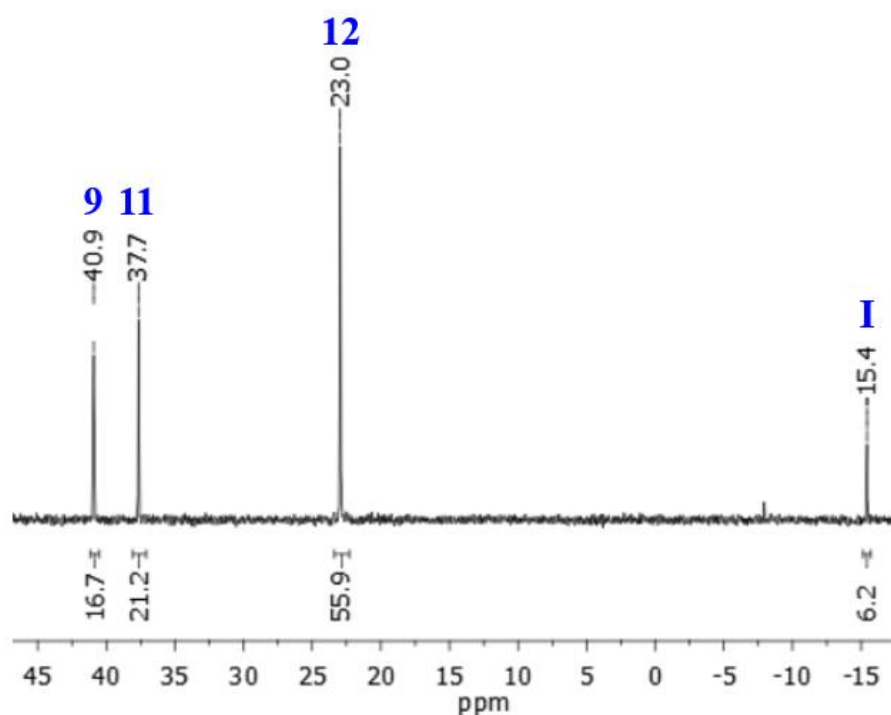
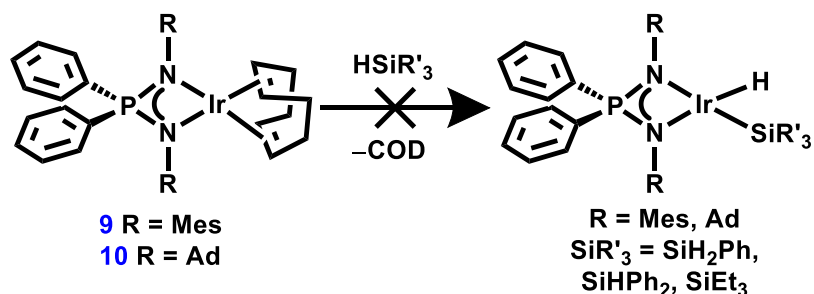


Figure 2.17 ³¹P{¹H} NMR spectrum of the 2:1 2,6-Me₂C₆H₃N≡C to **9** reaction mixture: δ 40.9 (17%, **9**), 37.7 (21%, **11**), 23.0 (26%, **12**), -15.4 (6%, **I**)

The $^{31}\text{P}\{^1\text{H}\}$ NMR spectrum of the reaction mixture of two 2,6-Me₂C₆H₃N≡C + **9** (Figure 2.17) also exhibits a peak at δ -15.4 (6%) indicative of neutral iminophosphonamide ligand **I** (Ph₂P(NHMes)(NMes)), and a signal at δ 40.9 (17%) attributed to unreacted COD complex **9**, [Ph₂P(NMes)₂]Ir(COD). The presence of unreacted COD precursor **9** suggests that 2,6-Me₂C₆H₃N≡C reacts preferentially with **11**, [Ph₂P(NAd)₂]Ir[C≡N(2,6-Me₂C₆H₃)]₂ over **9**. Variation of reaction conditions, for example, temperature and rate of addition, had little impact on product distribution. Attempts to isolate pure **11** or **12** *via* crystallization have proven fruitless.

2.6.3 Reactions of Ir^I Iminophosphonamido COD Complexes with Silanes

Addition of stoichiometric quantities of silanes (H₃SiPh, H₂SiPh₂, and HSiEt₃) to the COD complexes **9** [Ph₂P(NMes)₂]Ir(COD), and **10** [Ph₂P(NAd)₂]Ir(COD), in benzene-*d*₆ at ambient temperature was anticipated to generate the iridium silyl complexes [Ph₂P(NR)₂]Ir(H)(SiR₃) (Scheme 2.11). Unfortunately, no reaction was indicated by either the $^{31}\text{P}\{^1\text{H}\}$ or ^1H NMR spectra. Elevated temperatures (60 °C and 100 °C) and the use of polar solvent CDCl₃ did not lead to consumption of **9** or **10**. Similarly, scoping reactions with 10 equivalents of a silane, 2-butyne, and **9** or **10** in benzene-*d*₆ at ambient temperature for 60 °C did not result in a discernable reaction.



Scheme 2.11 Attempted synthesis of Ir^{III} silyl iminophosponamido complexes

2.7 Towards a More Active Rh^I Iminophosponamido Species

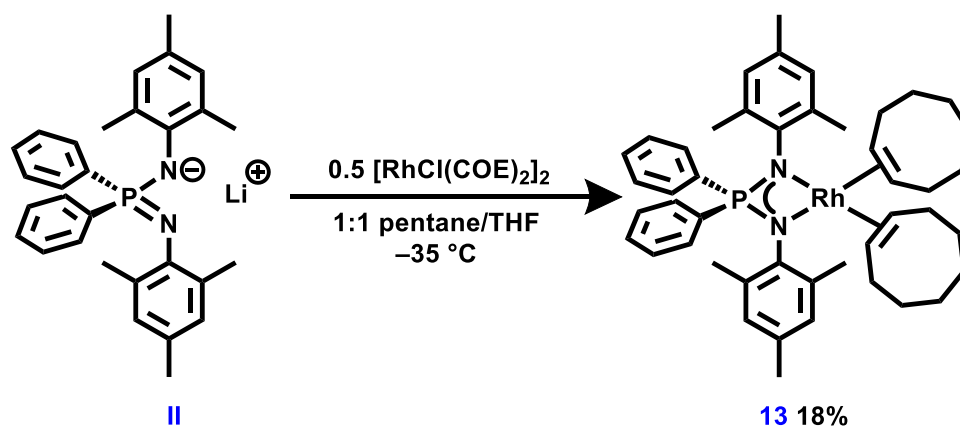
The COD complexes developed throughout this chapter, [Ph₂P(NMes)₂]M(COD) where M = Rh (**3**) or Ir (**9**) and [Ph₂P(NAd)₂]Rh(COD) where M = Rh (**4**) or Ir (**10**), are more inert than hoped. Since it is difficult to displace COD, related COE complexes, which were expected to be more reactive, were targeted.

2.7.1 Synthesis of [Ph₂P(NMes)₂]Rh(COE)₂, (**13**)

Cyclooctadiene (COD) is a bidentate, κ² ligand meaning any possible dissociation of an alkene could be counteracted by the chelate effect. As COE is not tethered to another coordinating ligand (no chelate effect), the likelihood of rapid re-coordination after dissociation decreases compared to COD.

The COE analogue [RhCl(COE)₂]₂ of the dimer [RhCl(COD)]₂, which contains two equivalents of COE per metal, was prepared according to literature methods.¹⁴⁹ This material was then allowed to react with the lithium salt **II**, Li[Ph₂P(NMes)₂], to generate the desired Rh^I COE complex **13**, [Ph₂P(NMes)₂]Rh(COE)₂ (Scheme 2.12). However, when the reaction was conducted at ambient temperature in benzene-*d*₆, rapid

decomposition of the target complex **13** to neutral iminophosphonamide ligand **I**, $\text{Ph}_2\text{P}(\text{NHMe})_2$, was observed within 5 minutes in the $^{31}\text{P}\{^1\text{H}\}$ NMR spectrum. A chilled ($-35\text{ }^\circ\text{C}$) 1:1 pentane:THF solution (to ensure solubility of **II**) was added to a vial containing a 1:1 ratio of **II**, $\text{Li}[\text{Ph}_2\text{P}(\text{NMe})_2]$, and $[\text{RhCl}(\text{COE})_2]_2$. The mixture was stirred for one minute and stored at $-35\text{ }^\circ\text{C}$ for one week, during which yellow-orange blocks of **13** formed. The crystals, much like **13**, are sensitive to reduced pressure, rapidly decomposing to **I** $\text{Ph}_2\text{P}(\text{NHMe})_2$. Accordingly, crystals of **13** were dried by flowing argon over the material for 5 minutes.



Scheme 2.12 Synthesis of the Rh^{I} COE complex **13**

The two broad peaks observed at δ 3.28 and 2.97 in the ^1H NMR spectrum, assigned as the COE methine (CH) protons, as well as the myriad of COE methylene (CH_2) resonances in the alkyl region, suggest chemical inequivalence of the two COE ligands (Figure 2.18 right). It is postulated that the COE groups restrict the free rotation of the mesityl groups, hence the observed chemical inequivalence for both the *ortho* and *para* mesityl-methyl groups and the COE ligand's protons in the ^1H NMR spectrum (Figure

2.18). In contrast, the aryl phenyl substituents in the iminophosphonamide ligand only exhibit a single set of signals (Figure 2.18).

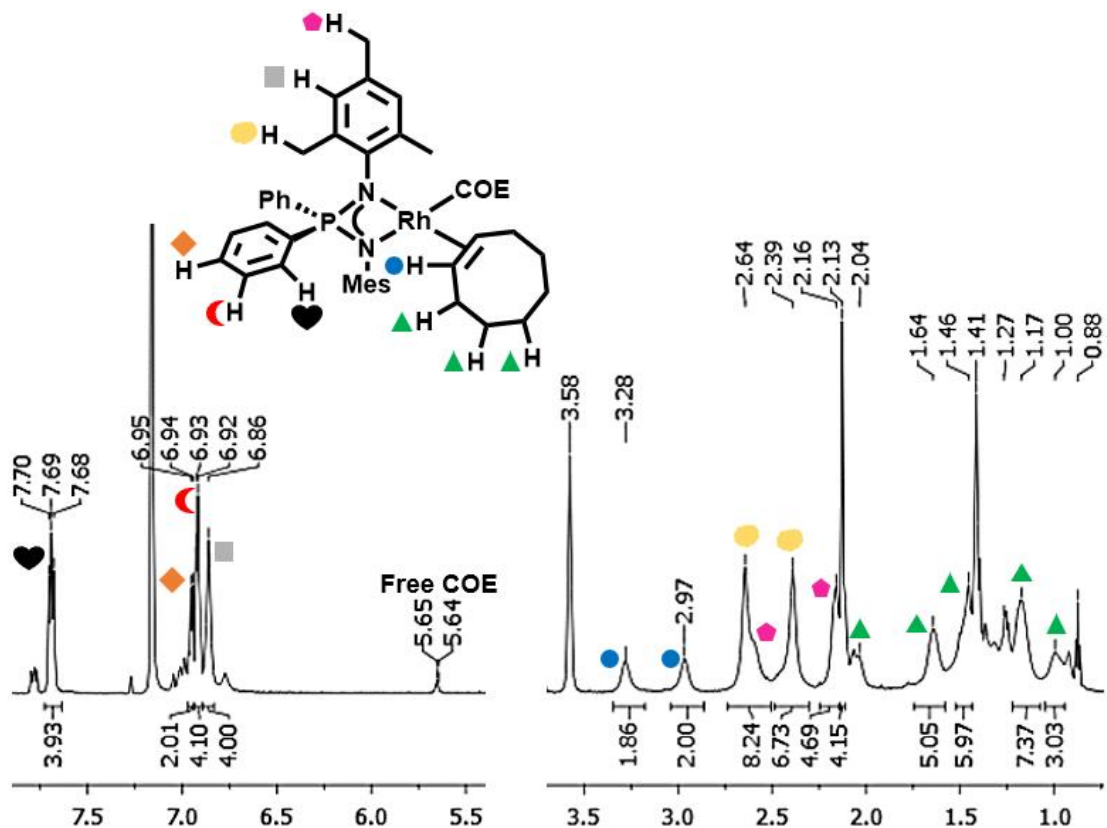


Figure 2.18 Aromatic and aliphatic regions of the ^1H NMR spectrum of complex **13**

The $^{31}\text{P}\{^1\text{H}\}$ NMR resonance attributed to **13**, $[\text{Ph}_2\text{P}(\text{NMes})_2]\text{Rh}(\text{COE})_2$, is a doublet with coupling to ^{103}Rh ($^2J_{\text{RhP}} = 9.6$ Hz). At δ 27.5, the ^{31}P chemical shift of **13** is slightly more downfield than its COD analogue **3**, $[\text{Ph}_2\text{P}(\text{NMes})_2]\text{Rh}(\text{COD})$, which resonates at δ 24.5. Complex **13** is unstable in solution at ambient temperature, decomposing to the neutral ligand **I** and Rh black within 6 h. Accordingly, ^{13}C NMR experiments of **13** were not attempted. However, a high-quality $^{13}\text{C}\{^1\text{H}\}$ NMR spectrum of **13** could likely be obtained from a concentrated sample of **13** at low temperatures,

thereby decreasing the rate of decomposition; however, due to time constraints this was not pursued.

2.7.1.1 X-ray Crystal Structure of $[\text{Ph}_2\text{P}(\text{NMe}_s)_2]\text{Rh}(\text{COE})_2 \cdot 1.5\text{C}_6\text{H}_6$ (**13**)

X-ray diffraction experiments confirmed the structure of **13**, $[\text{Ph}_2\text{P}(\text{NMe}_s)_2]\text{Rh}(\text{COE})_2 \cdot 1.5\text{C}_6\text{H}_6$ depicted in Figure 2.19. Crystals of **13** were grown over one week from a solution of **II**, $\text{Li}[\text{Ph}_2\text{P}(\text{NMe}_s)_2]$, and $[\text{RhCl}(\text{COE})_2]_2$ in a 1:1 pentane/THF mixture stored at -35°C .

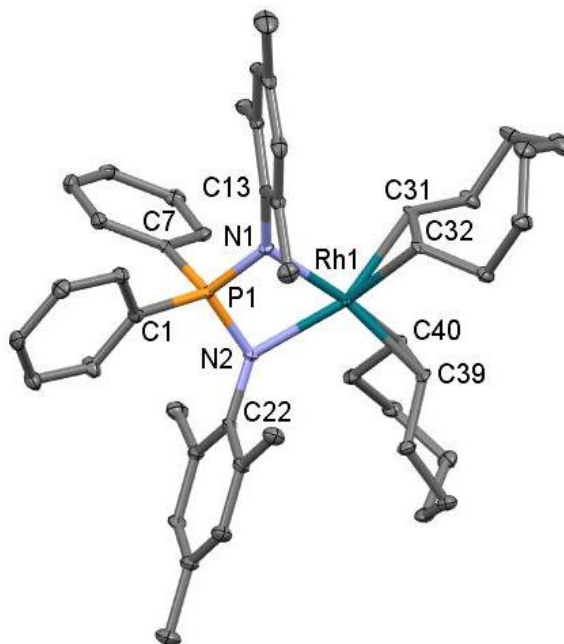


Figure 2.19 X-ray crystal structure of **13**· $1.5\text{C}_6\text{H}_6$ depicted as 50% displacement ellipsoids. Hydrogen atoms and solvent molecules are omitted for clarity

The L–Rh–L angles range from $89.67(7)^\circ$ to $103.57(7)^\circ$ (Table 2.11) and are larger than in the analogous organorhodium COD complex **3** $[\text{Ph}_2\text{P}(\text{NMe}_s)_2]\text{Rh}(\text{COD})$ (C–Rh–C = $82.19(1)$ and $82.61(10)^\circ$). The N–Rh–N bite angle ($69.99(6)^\circ$), however, is attributed as the cause of the distorted square planar geometry around Rh ($\tau_4 = 0.20$), akin to **3**.

Additional bond lengths and angles in **13** remain unchanged relative to complex **3** (Table 2.2).

Table 2.11 Selected bond distances (Å) and angles (°) for complex **13**

Atoms	Distance (Å)	Atoms	Angle (°)
Rh–N1	2.1199(15)	N1–Rh–N2	69.99(6)
Rh–N2	2.1198(16)	C31–Rh–N1	92.73(7)
N1–C13	1.421(2)	C32–Rh–N1	89.67(7)
N2–C23	1.423(3)	C39–Rh–N2	96.84(7)
P–C1	1.814(2)	C40–Rh–N2	103.57(7)
P–C7	1.827(2)	C31–Rh–C40	91.09(7)
P–N1	1.6015(16)	C32–Rh–C39	91.04(7)
P–N2	1.6073(16)	N1–P–N2	100.47(8)
Rh–C31	2.1594(19)	C1–P–C7	101.87(9)
Rh–C32	2.1425(18)		
Rh–C39	2.1691(18)		
Rh–C40	2.1433(18)		

2.7.2 Future Directions for [Ph₂P(NMes)₂]Rh(COE)₂, (**13**)

Exchanging COD for two COE moieties generated complex **13**, [Ph₂P(NMes)₂]Rh(COE)₂, which is prone to decomposition during isolation. *In situ*

generation of **13** for subsequent reactions with a range of small molecules, such as H₂, PR₃, and HSiR₃, was not examined due to time constraints; however, it is postulated to be a viable avenue for further investigation.

2.8 Concluding Remarks

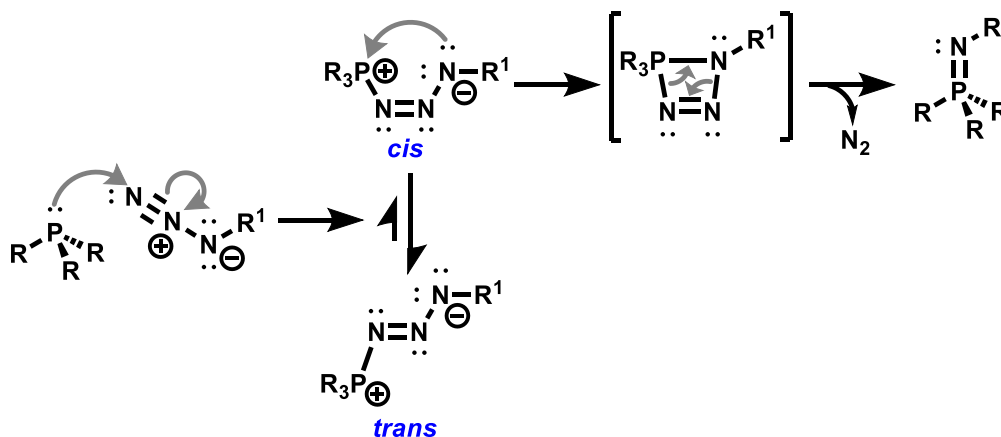
A new family of organorhodium and iridium iminophosphonamido complexes has been prepared and characterized by multinuclear NMR spectroscopy and X-ray crystallography. The COD ligand has proven convenient for facile generation, isolation and characterization. However, these species are relatively inert complexes, with the exception that COD can be substituted by strong π -acceptor ligands (*e.g.* carbon monoxide and isocyanides). Preliminary work substituting COD for COE has demonstrated that the resultant species is inherently unstable and prone to rapid decomposition. Future work investigating *in situ* generation of the COE-containing species may render it easier to probe the potentially rich reactivity of this new class of complex.

CHAPTER 3: SYNTHESIS OF AZIDOPHOSPHONAMIDE RH AND IR COMPLEXES

3.1 Overview

3.1.1 Phosphazides and Stabilization Methods

Initially considered transient in nature until the 1980's,¹⁰⁸ phosphazides ($R_3P=N_3-R^1$) (the intermediate of the Staudinger reaction) are prone to the rapid elimination of N_2 to form the corresponding phosphinimine (Scheme 3.1).



Scheme 3.1 The Staudinger reaction

Most known phosphazides assume the *trans* form, which must first isomerize to the *cis*-conformation to eliminate dinitrogen (Scheme 3.1).¹¹² Steric factors, namely bulky groups on both N and P atoms, hinder cyclization of the *cis* conformer. Electronic factors, such as strong electron donors on phosphorus or electron-withdrawing groups on nitrogen, have been shown to help stabilize the *trans* isomer.¹¹¹ The most common stabilization method, however, is coordination to a Lewis acid or metal.¹¹³ Despite advances in

phosphazide stabilization reported in the early 2000's,¹⁰⁸ it has been only in the past decade that they have garnered substantial interest. Phosphazides have been used as transient protecting groups for organic azides in click reactions, applicable to various organic and biochemical applications,¹⁵⁰ though only a limited number of main group, transition metal, and *f*-block complexes which contain a phosphazide ligands are known.¹¹⁴⁻¹¹⁶

3.1.2 Binding Modes

Phosphazides exhibit a unique ability to access eight different coordination modes *via* three potential donor nitrogens, the N^α, N^β and N^γ, where the N^α is directly bound to P (Figure 3.1). Sporadic reports of phosphazides as ligands yield no insight into predicting which coordination mode any given complex will adopt. Phosphazides, have been shown to change coordination modes, namely from $\kappa^2\text{-N}^\alpha, \text{N}^\gamma$ to $\kappa^1\text{-N}^\alpha$ (Figure 3.1) induced by steric crowding around the metal centre, thereby allowing for additional ligands to coordinate to a metal centre.¹¹⁷

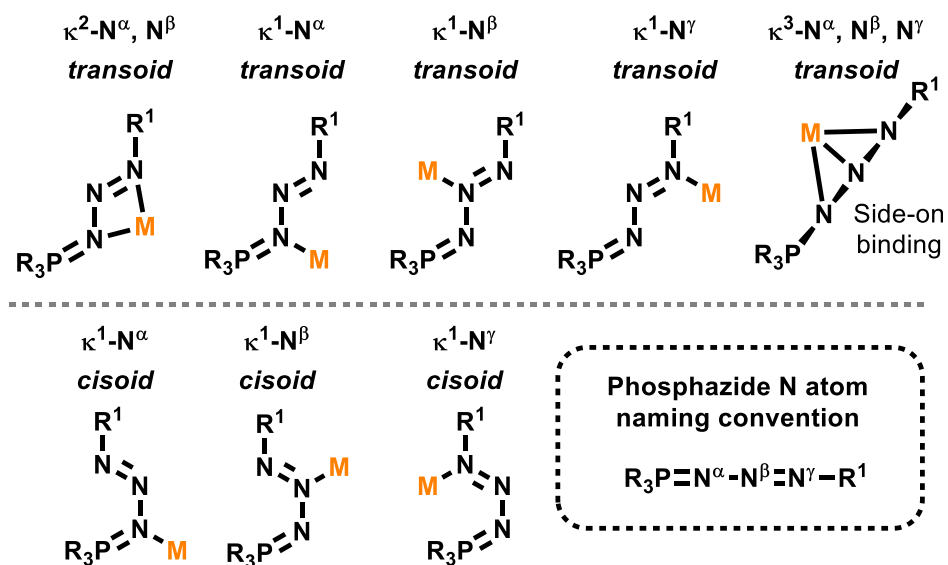
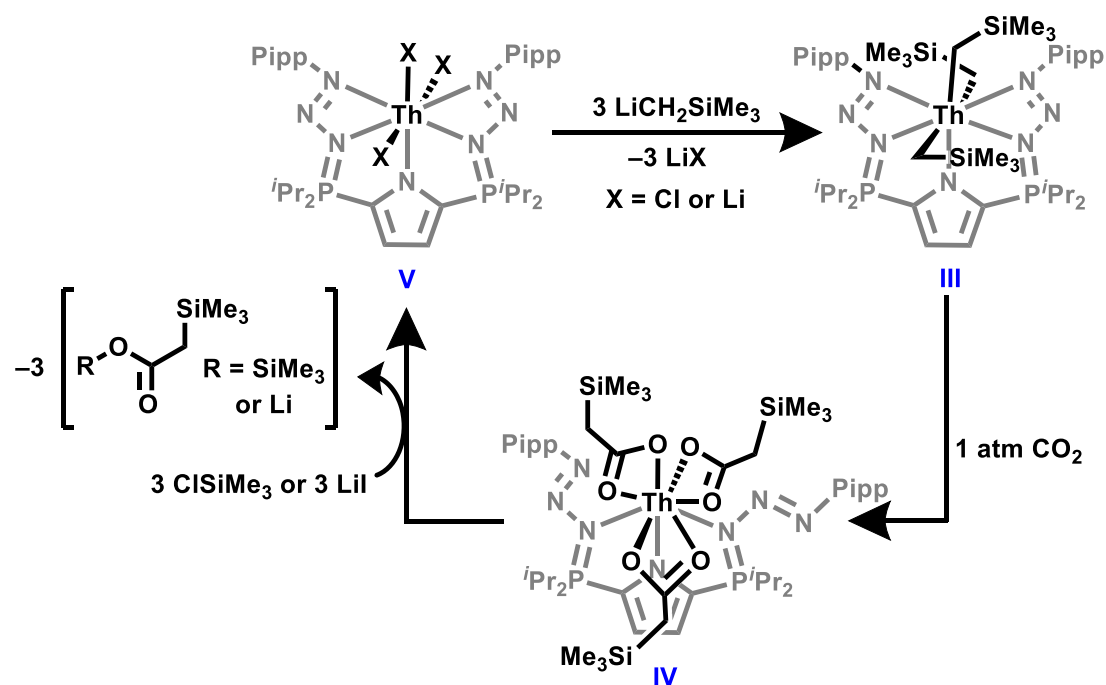


Figure 3.1 The phosphazide N atom naming convention used throughout this work and coordination modes displayed by metal-coordinated phosphazides¹⁵¹

3.1.3 Potential Catalytic Applications of Phosphazides

In January 2022, Hayes *et al.* demonstrated a stepwise synthetic cycle of CO₂ functionalization mediated by a diphosphazide-supported thorium complex (Scheme 3.2).¹¹⁷



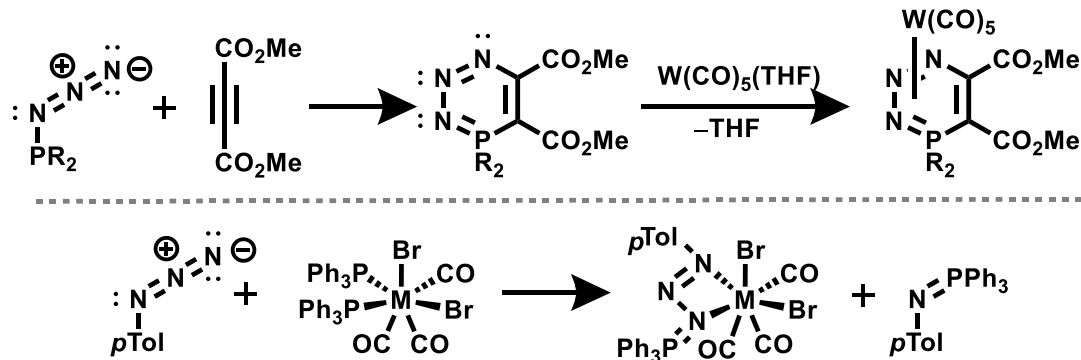
Scheme 3.2 Stepwise functionalization of CO₂ mediated by a diphosphazide-supported thorium complex¹¹⁷

The complex **III**, κ^5 -[(*para*-^{*i*}PrC₆H₄)N₃P^{*i*}Pr₂NC₄H₂]^{*i*}Th(CH₂SiMe₃)₃, was shown to capture and insert CO₂ into the three Th–C bonds to afford the tricarboxylate species **IV**, κ^3 -[(*para*-^{*i*}PrC₆H₄)N₃P^{*i*}Pr₂NC₄H₂]^{*i*}Th(CO₂CSiMe₃)₃.¹¹⁷ The phosphazide moieties within the ligand partially dissociate, from a κ^2 -*N*^{*α*},*N*^{*β*} coordination mode in **III** to a κ^1 -*N*^{*α*} coordination mode in **IV**, which is vital to the insertion of CO₂ to form the tricarboxylate species **IV**.¹¹⁷ Complex **IV** was then reacted with either ClSiMe₃ or LiI to form the ester products Me₃SiO₂CCH₂SiMe₃ and LiO₂CCHSiMe₃, regenerating the trihalide complex **V**, κ^5 -[(*para*-^{*i*}PrC₆H₄)N₃P^{*i*}Pr₂NC₄H₂]^{*i*}ThX₃, X = Cl or I.¹¹⁷ The addition of LiCH₂SiMe₃ to the trihalide species **III** completes the synthetic cycle; however, this process has yet to be made catalytic.¹¹⁷ Despite this recent insight from the Hayes group, phosphazide ligands have yet to be applied to any catalytic processes. The unique coordinative

versatility of phosphazides could prove beneficial, as the three donor nitrogen atoms allow for many accessible coordination modes (Figure 3.1), which may play a key role in catalytic transformations where dissociation or association of an N atom is a critical step in the catalytic cycle.¹¹⁷

3.1.4 Synthetic Routes to Phosphazide Ligands and Complexes

There are two known preparative routes to phosphazide complexes. Predictably, one method is the coordination of a pre-formed phosphazide to a metal centre (Scheme 3.3, top).^{152,153} Formation of a phosphazide can also occur within a metal's coordination sphere, wherein a metal complex containing a phosphine is reacted with an organic azide, creating a coordinated phosphazide. This process was first reported by Haymore *et al.* (Scheme 3.3, bottom).¹⁵⁴

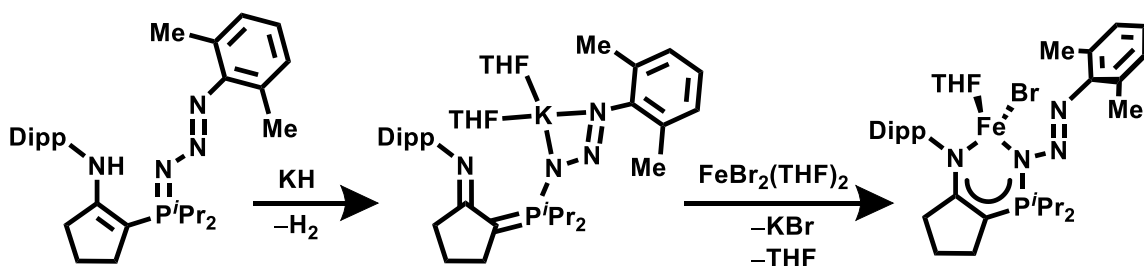


Scheme 3.3 Two synthetic routes to metal phosphazide complexes¹⁵²⁻¹⁵⁴

3.1.5 Synthesis of Phosphazide Ligand Salts

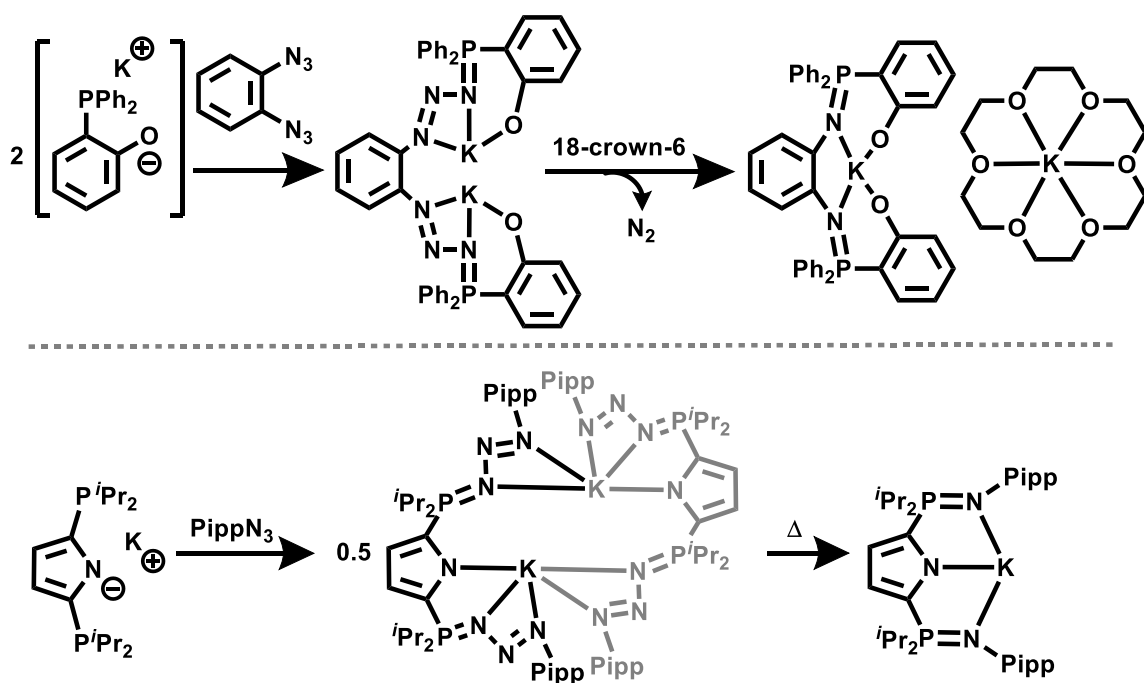
Fryzuk *et al.* reported the first example of a potassium phosphazide complex $\text{K}[(2,6\text{-}^i\text{Pr}_2\text{C}_6\text{H}_4\text{N}=\text{C}_5\text{H}_6)^i\text{Pr}_2\text{PN}_3(2,6\text{-Me}_2\text{C}_6\text{H}_4)]$, formed by reacting the neutral phosphazide $[(2,6\text{-}^i\text{Pr}_2\text{C}_6\text{H}_4\text{NH}-\text{C}_5\text{H}_6)^i\text{Pr}_2\text{PN}_3(2,6\text{-Me}_2\text{C}_6\text{H}_4)]$ with KH (Scheme 3.4).¹⁵⁵ A

salt metathesis reaction of the ligand salt with $\text{FeBr}_2(\text{THF})_2$ generated the complex $\kappa^2\text{-}N,N^\alpha\text{-}[(2,6\text{-}i\text{Pr}_2\text{C}_6\text{H}_4\text{N}=\text{C}_5\text{H}_6)^i\text{Pr}_2\text{PN}_3(2,6\text{-Me}_2\text{C}_6\text{H}_4)]\text{FeBr}\cdot\text{THF}$ (Scheme 3.4) from which further reaction chemistry was explored.¹⁵⁵



Scheme 3.4 Synthesis of the first K-stabilized phosphazide and subsequent salt metathesis reaction to afford $\kappa^2\text{-}N,N^\alpha\text{-}[(2,6\text{-}i\text{Pr}_2\text{C}_6\text{H}_4\text{N}=\text{C}_5\text{H}_6)^i\text{Pr}_2\text{PN}_3(2,6\text{-Me}_2\text{C}_6\text{H}_4)]\text{FeBr}\cdot\text{THF}$ ¹⁵⁵

Hayes *et al.* later published two separate diphosphazide ligand architectures stabilized by K^+ , suggesting potassium is the ideal group 1 metal to prepare phosphazide scaffolds due to the K^+ ion's larger atomic radius relative to Li or Na;^{115,156} however, a few Li phosphazide salts are known.^{127,157} Unlike the work reported by Fryzuk,¹⁵⁵ Hayes *et al.* generated the phosphazide moieties within the coordination sphere of potassium ($\text{K}_2[\text{C}_6\text{H}_4(\text{Ph}_2\text{PN}_3(\textit{ortho}\text{-OC}_6\text{H}_4))_2]$, Scheme 3.5).^{115,156} Subsequent reactions of the phosphasalen-type potassium salt with 18-crown-6 sequestered one of the K^+ ions resulted in rapid N_2 evolution (Scheme 3.5, top right).¹⁵⁶ The other ligand scaffold reported by Hayes *et al.*, a dipotassium diphosphazide pincer-like ligand salt ($\text{K}_2[\text{C}_2\text{NH}_2(^i\text{Pr}_2\text{PN}_3(\textit{para}\text{-}i\text{PrC}_6\text{H}_4))_2]$, Scheme 3.5, bottom),¹¹⁵ has also exhibited loss of N_2 at elevated temperature ($>60\text{ }^\circ\text{C}$) in solution. Both potassium ligand salts were further reacted, *via* salt metathesis reactions, with lanthanide and actinide metals.^{115,156}



Scheme 3.5 Synthesis of phosphazide-containing ligands^{115,156}

3.1.6 Towards Rh^{I} and Ir^{I} Phosphazide complexes

The only known group 9 phosphazide complex, $\text{Br}_2\text{Co}[\text{Cy}_3\text{PN}_3(\text{CO}(\text{C}_4\text{H}_3\text{O}))]\cdot\text{Et}_2\text{O}$ (Figure 3.2), was also one of the first transition metal phosphazide complexes. However, the structure of the complex was not confirmed by X-ray diffraction, and no reaction chemistry of the species was attempted.¹⁵⁸

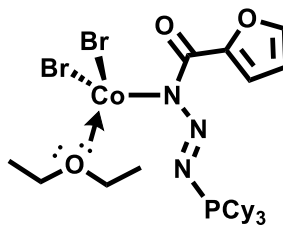


Figure 3.2 Proposed structure of the first transition metal phosphazide complex¹⁵⁸

Given the ubiquity of rhodium, and to a lesser extent iridium, throughout various catalytic processes, it is expected that Rh or Ir phosphazide complexes would be the most likely species to display catalytic activity; however, there is a dearth of reported Rh and Ir phosphazide-containing complexes.¹⁹ A key intermediate in many catalytic cycles is a 14-electron, low-coordinate metal species. For example, in olefin metathesis, alkene dissociation is a crucial step in generating the vital 14-electron intermediate. A square planar Rh^I or Ir^I complex bearing an alkene ligand was therefore targeted as the alkene is likely to be coordinatively labile. The metal dimer [RhCl(COD)]₂ is a commonly used starting material, so it was chosen as an appropriate source of Rh.

It is postulated that a ligand which includes a phosphazide functionality may display increased rates of substrate coordination and product dissociation due to the ability of phosphazides to fluctuate between the $\kappa^2-N^\alpha, N^\gamma$ and κ^1-N^α coordination modes, which can serve to relieve steric strain around the metal centre, as observed by Hayes *et al.*¹¹⁷ A monoanionic phosphazide-containing ligand was targeted to avoid dissociation of the entire phosphazide ligand during chemical transformations.

3.1.7 Literature Precedents for an “Azido”phosponamide

In 2015, the Stasch group was able to co-crystallize two dimers that featured lithium-coordinated “azido”phosponamido ligands [R₂P(N₃R¹)(NR¹)]⁻ (Figure 3.3).¹²⁷ An azidophosponamide is the phosphazide analogue of an iminophosponamide ligand (R₂P(NHR¹)(NR¹)), wherein the phosphazide group (PN₃R¹) is retained from an arrested Staudinger reaction, which would typically extrude N₂ to form the corresponding phosphinimine (P=N).

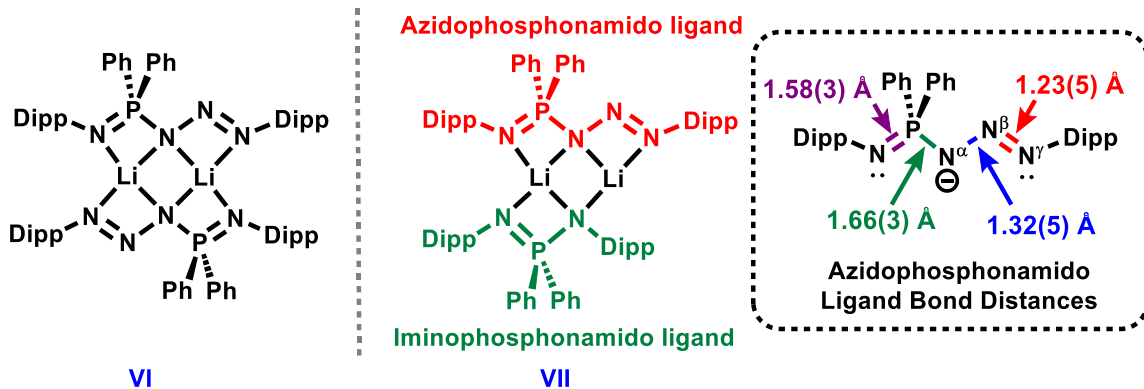
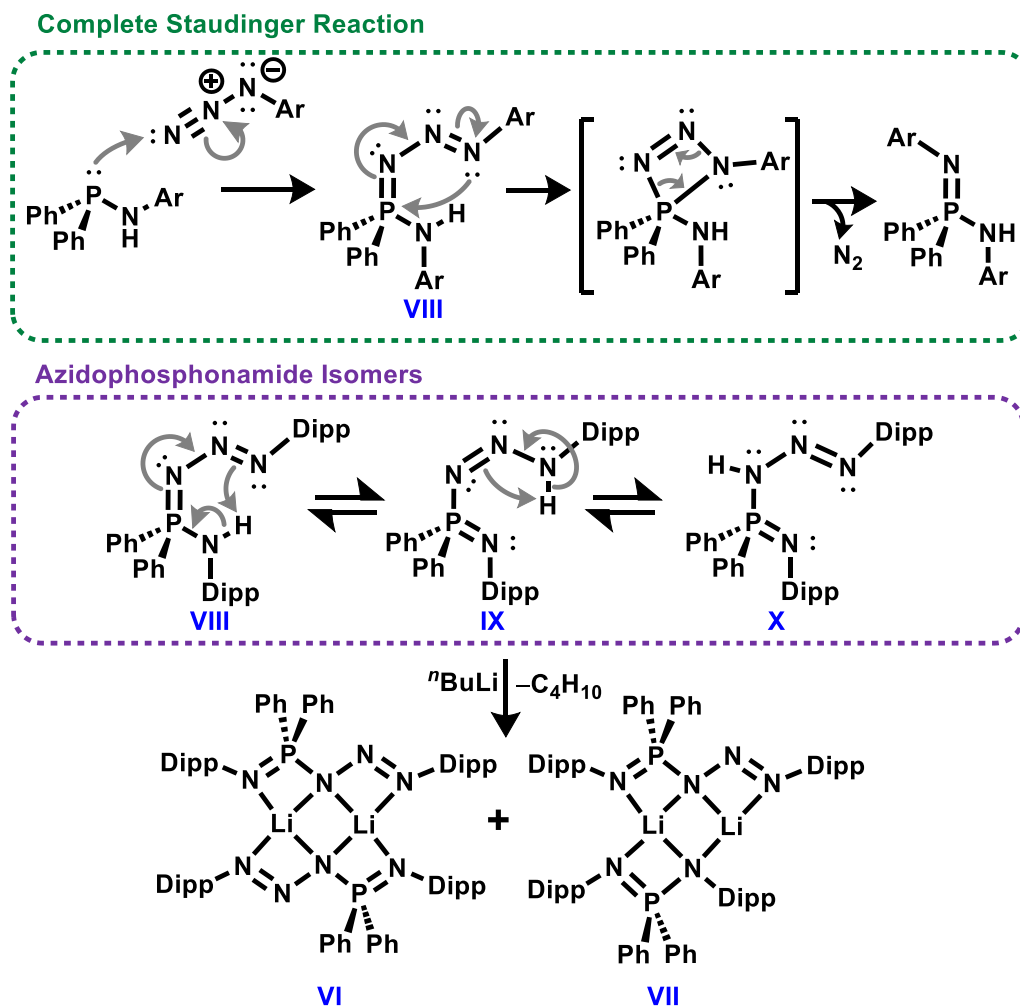


Figure 3.3 Structure of co-crystallized azidophosponamido lithium salts¹²⁷

The azidophosponamido lithium salts $\text{Li}[\text{Ph}_2\text{P}(\text{NDipp})(\text{N}_3\text{Dipp})]_2$ **VI** and $\text{Li}[\text{Ph}_2\text{P}(\text{NDipp})(\text{N}_3\text{Dipp})][\text{Ph}_2\text{P}(\text{NDipp})_2]$ **VII**, were impurities crystallized from the deprotonation of $\text{Ph}_2(\text{NHDipp})(\text{NDipp})$.¹²⁷ Stasch *et al.* concluded that the neutral azidophosponamide, $(\text{Ph}_2(\text{NHDipp})(\text{N}_3\text{Dipp}))$, is a minor impurity formed from an arrested Staudinger reaction (Scheme 3.6).



Scheme 3.6 Complete Staudinger reaction forming an iminophosphonamide (top, green box) and the azidophosphonamide isomers **VIII**, **IX**, and **X** (middle, purple box), which eventually form the azidophosphonamido impurities **VI** and **VII**¹²⁷

The *cisoid* **VIII** isomer is the only tautomer which can readily cyclize to extrude N_2 and form the iminophosphonamide ligand ($Ph_2P(NDipp)(NHDipp)$, Scheme 3.6, top). The two other tautomers, **IX** and **X**, would hinder cyclization of the phosphazide and extrusion of N_2 . Isomer **IX** requires H migration before a $(Dipp)N-PPh_2$ bond can form to eliminate N_2 , and tautomer **X** bears an H atom on the N_2 fragment (which is to be extruded,

Scheme 3.6, middle). Depending on the equilibria between the tautomers in solution, some molecules form **IX** or **X** preferentially, preventing N₂ extrusion and yielding azidophosphonamide species, especially if heating is required to eliminate N₂. In this case, the small amount of azidophosphonamide impurity reacts with ⁿBuLi to form the azidophosphonamidolithium salts **VI** and **VII** (Scheme 3.6, bottom).¹²⁷ Stasch *et al.* found that the ligand adopts the tautomer **X** conformation (Scheme 3.6) before deprotonation, as indicated by the P–N bond distances in the azidophosphonamidolithium salts **VI** and **VII** (Figure 3.3).¹²⁷ Interestingly, the P=N double bond does not formally exist between N^α and phosphorus of the phosphazide moiety. Instead, the P–N^α bond of the phosphazide is elongated to a single bond (1.661(3) Å), suggesting the anionic charge of the ligand is formally resting on N^α (Figure 3.3). A double bond exists between the phosphorus and phosphonamido nitrogen (1.580(3) Å, Figure 3.3).

Stasch *et al.* also reported attempts to isolate a less sterically bulky Mes (2,4,6-MeC₆H₂) substituted azidophosphonamidolithium salt Li[Ph₂P(NMes)(N₃Mes)₂]₂; however, they only reported the non-phosphazide containing *iminophosphonamidolithium* salts Li[Ph₂P(NMes)₂]₂.¹²⁷ Therefore, the equilibria between the tautomers, and consequently the isolation of a stable azidophosphonamide, can be affected by factors such as the steric bulk of the nitrogen substituents.

Alkali metal iminophosphonamide species are useful precursors for salt metathesis reactions, wherein the alkali complex (LiL or KL) is reacted with a metal halide (MX) as a means to attach the desired ligand L to the metal centre M.¹²⁷ This methodology has been employed by Fryzuk *et al.*¹⁵⁵ and Hayes *et al.*^{115,156} as protocols to bind their phosphazide-

containing ligands to transition metals. Despite the ubiquity of salt metathesis as a ligand attachment protocol, no further investigations involving the salts **VI** and **VII**, or isolation of neutral azidophosphonamide ligands, have been reported.

3.2 Synthesis of Azidophosphonamide Ligands

3.2.1 From Iminophosphonamides to Azidophosphonamides

A great advantage of iminophosphonamides $[\text{R}_2\text{P}(\text{NR}^1)_2]^-$, and their carbon analogous, amidinates $[\text{RC}(\text{NR}^1)_2]^-$, is the wide range of steric tunability *via* facile variation of the N-substituents. Exchanging the phosphinimine moiety (in an iminophosphonamide ligand $([\text{R}_2\text{P}(\text{NHR}^1)(\text{NR}^1)])$) with a phosphazide generates a neutral azidophosphonamide $[\text{R}_2\text{P}(\text{NHR}^1)(\text{N}_3\text{R}^1)]$, a compound that has yet to be reported in the literature.¹²⁷

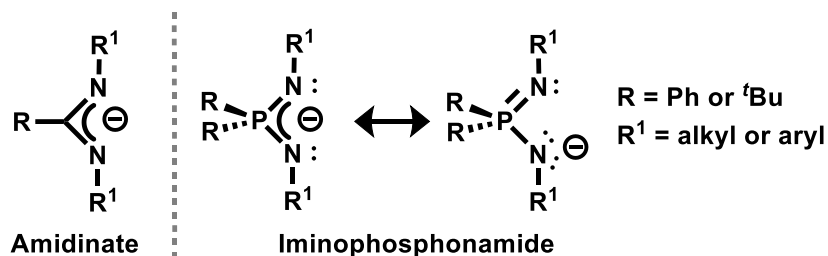


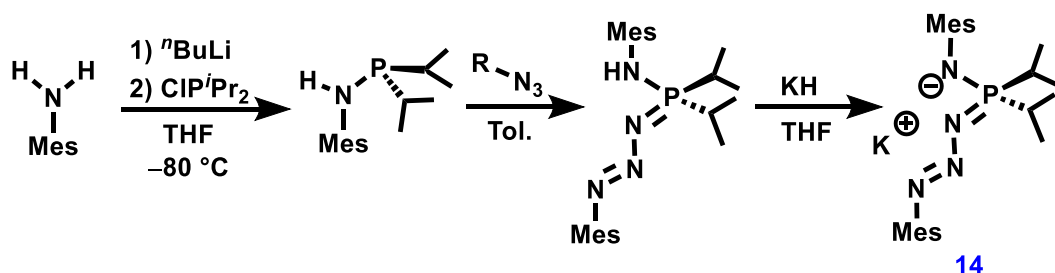
Figure 3.4 Resonance forms of amidinate and iminophosphonamide ligands

The work reported by Stasch *et al.*¹²⁷ suggests that azidophosphonamides, $(\text{R}_2\text{P}(\text{NHR}^1)(\text{N}_3\text{R}^1))$, may not have the same versatility as iminophosphonamides $(\text{R}_2(\text{NHR}^1)(\text{NR}^1))$, instead requiring sterically encumbering groups on nitrogen (such as Dipp) for azidophosphonamide stabilization, as they were not able to isolate the less sterically bulky Mes-substituted azidophosphonamide-containing complex. Aside from

steric factors, namely large groups on both N and P atoms hindering cyclization of the *cis* phosphazide conformer, electronic factors, such as strong electron donors on phosphorus or electron-withdrawing groups on nitrogen, have been shown to stabilize the *trans* phosphazide isomer.¹¹¹ Alkyl phosphorus substituents will not always yield an azidophosphonamide ($R_2P(NHR^1)(N_3R^1)$); for example, the *t*Bu substituted iminophosphonamide *t*Bu₂P(NHSiMe₃)(NSiMe₃) is known,¹⁵⁹⁻¹⁶¹ yet there are no reports of the azidophosphonamide species *t*Bu₂P(NHSiMe₃)(NSiMe₃). Incorporating relatively more electron-donating isopropyl groups on phosphorus in iminophosphonamide ligands has yet to be reported and could potentially lead to an azidophosphonamide.

3.2.2 Synthesis of K[*i*Pr₂P(NMes)(N₃Mes)] (**14**)

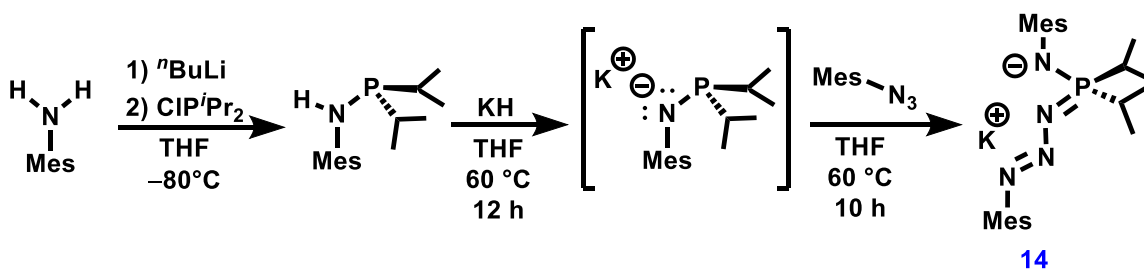
As Statch *et al.* could not isolate a mesityl-substituted azidophosphonamide species,¹²⁷ mesityl groups were selected to demonstrate the isolation of an azidophosphonamide could be attributed to the electronic influence of isopropyl groups on phosphorus rather than the steric bulk on nitrogen. The proposed route to the desired azidophosphonamide *i*Pr₂P(NMes)(N₃Mes) is analogous to the synthesis of iminophosphonamides wherein the Mes-substituted phosphonamide (*i*Pr₂PNHMes) is reacted with an organic azide (MesN₃) (Scheme 3.7). The neutral azidophosphonamide ligand *i*Pr₂P(NMes)(N₃Mes) would be deprotonated with base (KH) to generate the potassium salt **14**, K[*i*Pr₂P(NMes)(N₃Mes)], which can be used for salt metathesis protocols. KH was chosen due to the larger ionic radius of K⁺ compared to Li⁺, which in the literature has been better at stabilizing phosphazides.^{115,155,156}



Scheme 3.7 Attempted synthesis of $\text{K}[\text{Pr}_2\text{P}(\text{NMes})(\text{N}_3\text{Mes})]$, **14**

The reaction between ${}^i\text{Pr}_2\text{PNHMe}$ s and Me_3N_3 yielded a myriad of resonances, ranging from δ 65 to 0 in the ${}^{31}\text{P}\{^1\text{H}\}$ NMR spectrum. Heating the reaction mixture at 60 °C for 48 h reduced the number of ${}^{31}\text{P}\{^1\text{H}\}$ NMR resonances from 12 to 10, but did not yield a single product. Attempts to isolate any of the major products from the mixture proved unsuccessful. Reacting the mixture of products with KH, in an attempt to generate the potassium salt **14**, $\text{K}[\text{Pr}_2\text{P}(\text{NMes})(\text{N}_3\text{Mes})]$, only resulted in the appearance of several additional signals in the ${}^{31}\text{P}\{^1\text{H}\}$ NMR spectrum.

An alternative method to generate phosphazide ligands is to form the PN_3 group within the coordination sphere of the metal. Hayes *et al.* first deprotonated the NH or OH to form the potassium salts $\text{K}[2,5-({}^i\text{Pr}_2\text{P})_2\text{C}_4\text{NH}_2]$ and $\text{K}[\textit{ortho}-(\text{Ph}_2\text{P})(\text{O})\text{C}_6\text{H}_4]$, which were then reacted with an organic azide to form the phosphazide moiety within the K^+ coordination sphere (Scheme 3.4).^{115,156} Therefore, an alternative synthetic route to the azidophosphonamido potassium salt **14** $\text{K}[\text{Pr}_2\text{P}(\text{NMes})(\text{N}_3\text{Mes})]$ was pursued. Specifically, KH was used to deprotonate N–H (of ${}^i\text{Pr}_2\text{PNHMe}$ s) prior to adding the azide (Scheme 3.8).



Scheme 3.8 Synthesis of $\text{K}[\text{}^i\text{Pr}_2\text{P}(\text{NMes})(\text{N}_3\text{Mes})]$, **14**

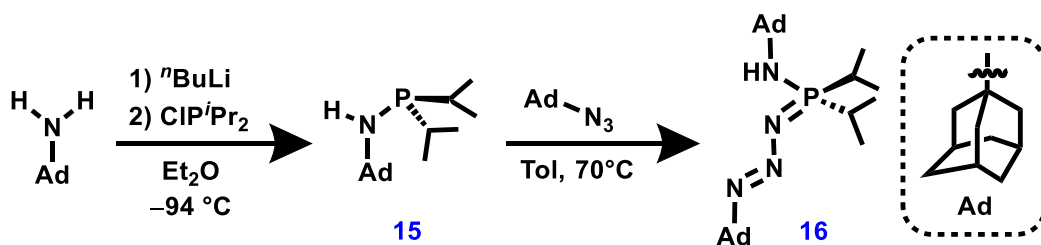
Deprotonation of ${}^i\text{Pr}_2\text{PNHMe}$ s with KH to yield $\text{K}[\text{}^i\text{Pr}_2\text{PNMe}]$ required heating at 60 °C in THF for 12 h. Similarly, the azidophosphonamido salt **14**, $\text{K}[\text{}^i\text{Pr}_2\text{P}(\text{NMes})(\text{N}_3\text{Mes})]$ was generated by heating of the reaction mixture of Me_3N_3 and $\text{K}[\text{}^i\text{Pr}_2\text{PNMe}]$ to 60 °C in THF for 10 h; confirmed through the loss of the ${}^{31}\text{P}\{^1\text{H}\}$ NMR signal attributed to $\text{K}[\text{}^i\text{Pr}_2\text{PNMe}]$ (δ 72.3 in $\text{THF-}d_8$). Heating compound **14** at 60 °C in benzene- d_6 for 2 weeks at 100 °C in toluene- d_8 for 1 week resulted in no observable changes in the ${}^{31}\text{P}\{^1\text{H}\}$ NMR spectrum, indicating the robustness of the phosphazide moiety within **14**.

Two sets of mesityl aromatic and aliphatic resonances ($\text{N}_3\text{-Mes}$ and N-Mes) were observed in the ${}^1\text{H}$ NMR spectrum of **14**. The ${}^{31}\text{P}\{^1\text{H}\}$ NMR spectrum contains one singlet attributed to **14** at δ 19.0 in $\text{THF-}d_8$ and δ 22.9 in benzene- d_6 . Both resonances are upfield shifted from $\text{K}[\text{}^i\text{Pr}_2\text{PNMe}]$ (δ 72.3 in $\text{THF-}d_8$) and ${}^i\text{Pr}_2\text{PNHMe}$ s (δ 57.7 in benzene- d_6). Two separate sets of mesityl aromatic and aliphatic signals in the ${}^1\text{H}$ NMR spectrum and the ${}^{31}\text{P}\{^1\text{H}\}$ NMR chemical shift corroborate that **14**, $\text{K}[\text{}^i\text{Pr}_2\text{P}(\text{NMes})(\text{N}_3\text{Mes})]$, retains the phosphazide moiety. Unfortunately, attempts to obtain a solid-state structure have proven unsuccessful. The percentage of nitrogen (N%) in **14** determined by elemental analysis (11.88%) closely matched the calculated N% of $\text{K}[\text{}^i\text{Pr}_2\text{P}(\text{NMes})(\text{N}_3\text{Mes})]$ **14** (12.01%)

(K[ⁱPr₂P(NMes)₂] N% = 5.75%). Unambiguous confirmation that **14** contains a phosphazide came *via* the X-ray crystal structure of [ⁱPr₂P(N₃Mes)(NMes)]Rh(COD) **20** in section 3.3.

3.2.3 Synthesis of Adamantyl-Substituted Azidophosphonamido Ligands

Alkyl substituents on nitrogen are predicated to subtly change the electronic properties of the azidophosphonamido ligand. However, substitution of the mesityl nitrogen substituents with ubiquitous ^tBu or TMS groups involves the reagents ^tBuN₃ and Me₃SiN₃ to generate the phosphazide moiety.¹⁶² Adamantyl groups were selected as an alternative to ^tBu and SiMe₃ substituents due to the similar steric influence of Ad compared to ^tBu groups,¹³⁷ and the higher C:N ratio of 3.4 of AdN₃ (1 (^tBuN₃) and 1.3 (SiMe₃N₃)). Despite unsuccessful attempts at generating the neutral azidophosphonamide ⁱPr₂(N₃Mes)(NHMes), directly reacting the yet-to-be-reported phosphonamide **15**, ⁱPr₂(NHAd), with AdN₃ to afford the neutral azidophosphonamide **16**, ⁱPr₂(N₃Ad)(NHAd) was proposed (Scheme 3.9).



Scheme 3.9 Synthesis of ⁱPr₂P(NHAd)(N₃Ad), **16**

3.2.4 Synthesis of ${}^i\text{Pr}_2\text{P}(\text{NAd})$ (**15**)

Deprotonation of HNAd by ${}^t\text{BuLi}$ in diethylether at $-94\text{ }^\circ\text{C}$, followed by a subsequent salt metathesis reaction of $\text{Li}[\text{NAd}]$ with ClP^iPr_2 , readily afforded the phosphonamide **15**, ${}^i\text{Pr}_2\text{P}(\text{NHAd})$. The beige liquid **15** solidifies at $-35\text{ }^\circ\text{C}$; however, recrystallization has proven unsuccessful. One set of adamantyl alkyl and isopropyl resonances were observed in the ${}^1\text{H}$ NMR spectrum of **15** ranging from δ 2.0-1.0, and one singular NH signal at δ 0.93 was also identified. In the ${}^{31}\text{P}\{{}^1\text{H}\}$ NMR spectrum, one resonance was observed at δ 38.5.

3.2.5 Synthesis of ${}^i\text{Pr}_2\text{P}(\text{N}_3\text{Ad})(\text{NHAd})$ (**16**)

The adamantyl-substituted azidophosphonamide **16**, ${}^i\text{Pr}_2\text{P}(\text{NHAd})(\text{N}_3\text{Ad})$, was readily generated *via* an arrested Staudinger reaction between phosphonamide **15**, ${}^i\text{Pr}_2\text{PNHAd}$, and AdN_3 in toluene, after heating at $70\text{ }^\circ\text{C}$ for 16 h. The product readily precipitated out of solution upon cooling to ambient temperature. Characterization of **16** was conducted in CDCl_3 due to poor solubility in both benzene- d_6 and THF- d_8 . Extensive heating of **16** at $60\text{ }^\circ\text{C}$ in CDCl_3 for 2 weeks yielded no change in the ${}^{31}\text{P}\{{}^1\text{H}\}$ NMR spectrum, indicating the phosphazide moiety does not easily extrude N_2 . It is originally postulated that hydrogen bonding from the amine nitrogen in **16** stabilized the phosphazide functional group, however the lack of crystallographic evidence seen in section 3.2.5.1. suggests the robust nature of phosphazide is due to the steric and electronic influences of the adamantyl groups on nitrogen.

Two sets of broad adamantyl resonances were observed in the ${}^1\text{H}$ NMR spectrum of **16**, one for each $\text{N}_3\text{-Ad}$ and HN-Ad . The singlet at δ 50.7 (in CDCl_3) in the ${}^{31}\text{P}\{{}^1\text{H}\}$

NMR spectrum is shifted substantially (12 ppm) to a higher frequency compared to the precursor **15**, $^i\text{Pr}_2\text{P}(\text{NAd})$ at δ 38.5 in benzene- d_6 . X-ray diffraction experiments confirmed that **16**, $^i\text{Pr}_2\text{P}(\text{NHAd})(\text{N}_3\text{Ad})$ contained a phosphazide functionality (Figure 3.5).

3.2.5.1 X-ray Crystal Structure of $^i\text{Pr}_2\text{P}(\text{N}_3\text{Ad})(\text{NHAd})$ (**16**)

Light-yellow needles of **16** were grown from a saturated CH_2Cl_2 solution left at ambient temperature for 3 days.

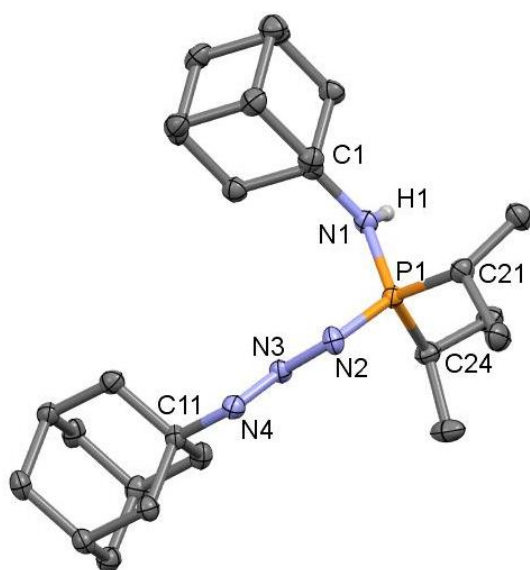


Figure 3.5 X-ray crystal structure of **16** depicted as 50% displacement ellipsoids. Hydrogen atoms (except H1) are omitted for clarity

The $\text{P1}=\text{N2}-\text{N3}=\text{N4}$ torsion angle of the phosphazide within **16**, $^i\text{Pr}_2\text{P}(\text{NHAd})(\text{N}_3\text{Ad})$, $178.7(4)^\circ$ indicated the functional group adopts a *transoid* conformation in the solid state. Interestingly, both $\text{P}-\text{N}^\alpha$ (of the phosphazide) and $\text{P}-\text{N1}$ display single bond character with elongated $\text{P}-\text{N}$ distances of 1.643(5), 1.652(5) Å, respectively, suggesting δ^- on the N atoms and δ^+ on P.

The phosphazide moiety removes some of the steric bulk at phosphorus. As a direct consequence, the C21–P–C24 angle between the phosphorus substituents increased (114.3(3)°) relative to the iminophosphonamido ligand **2**, Ph₂P(NAd)(NHAd) in section 2.2.1 (102.58(9)°). The N1–P–N2 bond angle (118.5(2)°) is also impacted, compared to the iminophosphonamido ligand **2**, which displays a larger N–P–N angle (121.96(9)°, Table 3.1) due to steric crowding around phosphorus (two Ph and two N–Ad substituents).

Table 3.1 Selected bond distances (Å) and angles (°) for compound **16**

Atoms	Distance (Å)	Atoms	Angle (°)
N1–C1	1.477(8)	P–N1–C1	127.7(4)
N4–C11	1.485(7)	C24–P–C21	114.3(3)
P–C21	1.830(6)	N1–P–N2	118.5(2)
P–C24	1.827(6)	P–N2–N3	109.3(4)
P–N1	1.652(5)	N2–N3=N4	113.2(4)
P–N2	1.643(5)	N3=N4–C11	111.9(4)
N2–N3	1.368(6)		
N3=N4	1.256(7)		

3.2.6 Synthesis of Li₂[ⁱPr₂P(N₃Ad)(NAd)]₂ (**17**)

Deprotonation of **16**, ⁱPr₂P(NHAd)(N₃Ad), was attempted using KH in THF; however, no conversion was observed even with heating the reaction to 60 °C for 16 h. Instead, **16**, ⁱPr₂P(NHAd)(N₃Ad) was suspended in THF, and a solution of ^tBuLi in hexanes was added to deprotonate the N–H and generate the lithium salt **17**, Li₂[ⁱPr₂P(NAd)(N₃Ad)]₂. Compound **17** was found to be highly soluble in THF, and thus

the characterization of **17** is reported in THF-*d*₈ (due to the poor solubility of **17** in CDCl₃). Inequivalence of the adamantyl methylene and methine proton signals was observed in the ¹H NMR spectrum. The ³¹P{¹H} NMR chemical shift of **17** is downfield (δ 41.7) compared to the mesityl-substituted potassium salt **14**, K[ⁱPr₂P(NMes)(N₃Mes)], at δ 19.0.

Loss of the N–H resonance in the ¹H NMR spectrum and the appearance of a ⁷Li NMR signal (δ 1.5) confirm the deprotonation of **16**, ⁱPr₂P(NHAd)(N₃Ad). However, the ³¹P{¹H} chemical shift and inequivalence in the ¹H NMR spectrum do not unambiguously indicate retention of the phosphazide moiety, as hydrogen bonding from OH or NH protons can stabilize a phosphazide.¹⁰⁸ It is therefore possible that the azidophosphonamide **17**, ⁱPr₂P(NHAd)(N₃Ad), could have spontaneously extruded N₂ upon loss of the NH to form the iminophosphonamido lithium salt, Li[ⁱPr₂P(NAd)₂].

3.2.6.1 X-ray Crystal Structure of Li₂[ⁱPr₂P(N₃Ad)(NAd)]₂•C₂Cl₂ (**17**)

Light yellow diamonds of **17**•C₂Cl₂ were grown from a 1:1 THF:CH₂Cl₂ solution left at ambient temperature for 1 week. The X-ray crystal structure (Figure 3.6) confirms that the lithium salt **17**, Li₂[ⁱPr₂P(NAd)(N₃Ad)]₂, indeed retained the phosphazide group.

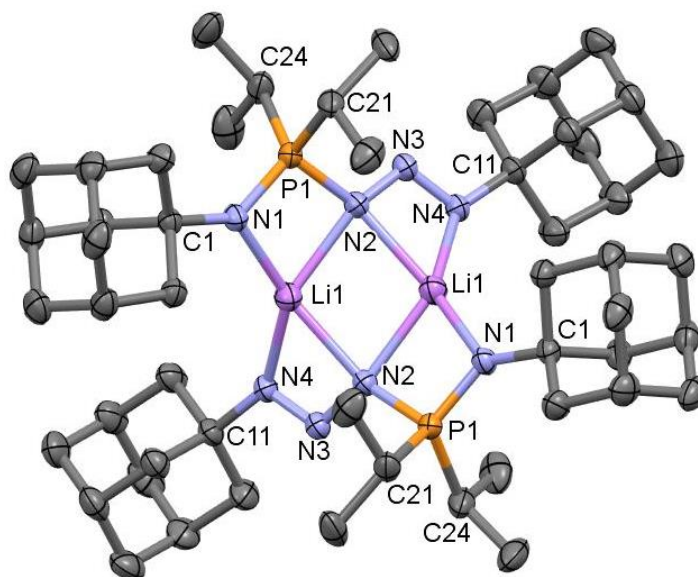


Figure 3.6 X-ray crystal structure of **17**·CH₂Cl₂ depicted as 50% displacement ellipsoids. Hydrogen atoms and the solvent molecule (CH₂Cl₂) are omitted for clarity

Compound **17** was found to crystallize as a dimer (Li₂[ⁱPr₂P(NAd)(N₃Ad)]₂) Figure 3.6), which echoes that reported by Stasch *et al.*¹²⁷ The dimer lies on the Wyckoff special position *a* in the highly symmetric orthorhombic space group *Fdd2*, with the other half of the dimer (not in the asymmetric unit) being generated through the 2-fold rotation axis, hence, why only half an equivalent is observed in the asymmetric unit.

The phosphazide functionality assumes the *transoid*-conformation, akin to its precursor **16**, ⁱPr₂P(NHAd)(N₃Ad), (P1–N2–N3=N4 = 178.7(4)°, albeit with a smaller P1–N2–N3=N4 torsion angle (172.4(2)°, **17**) attributed to coordination of the ligand to lithium. The geometry about lithium is severely distorted $\tau_4 = 0.52$ (with $\tau'_4 = 0.48$) and lies somewhere between tetrahedral and seesaw. The P–N ^{α} bond is close to a typical single bond length (1.669(2) Å, Table 3.2). In contrast, the phosphonamido nitrogen (N1) to

phosphorus bond distance exhibits double bond character (1.573(2) Å), suggesting the ligand's anionic charge primarily resides on N^α (Figure 3.7, left).

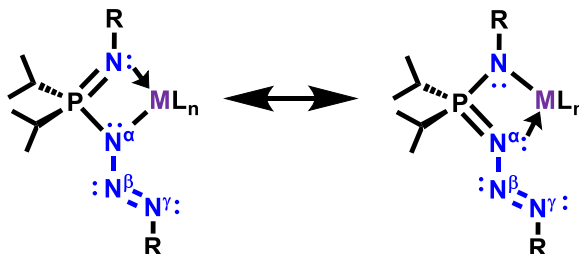


Figure 3.7 Two possible azidophosponamide resonance structures placing the anionic charge of the ligand on the N^α (left) or the phosphonamido nitrogen (right)

Table 3.2 Selected bond distances (Å) and angles (°) for compound **17**

Atoms	Distance (Å)	Atoms	Angle (°)
Li–N1	1.972(5)	N1–Li–N2	75.17(16)
Li–N2	2.104(4)	N2–Li–N2 ¹	101.76(18)
Li ¹ –N2	2.113(5)	N2–Li ¹ –N4 ¹	62.38(14)
Li ¹ –N4	2.048(5)	N4 ¹ –Li–N1	139.1(2)
N2–N3	1.350(3)	P=N1–C1	134.66(16)
N3–N4	1.266(3)	P–N2–N3	115.92(15)
N1–C1	1.481(3)	N2–N3=N4	110.90(18)
N4–C11	1.481(3)	N3=N4–C11	114.13(19)
P–C21	1.836(3)	N1–P–N2	100.26(10)
P–C24	1.835(3)	C21–P–C24	106.29(13)
P–N1	1.573(2)		
P–N2	1.669(2)		

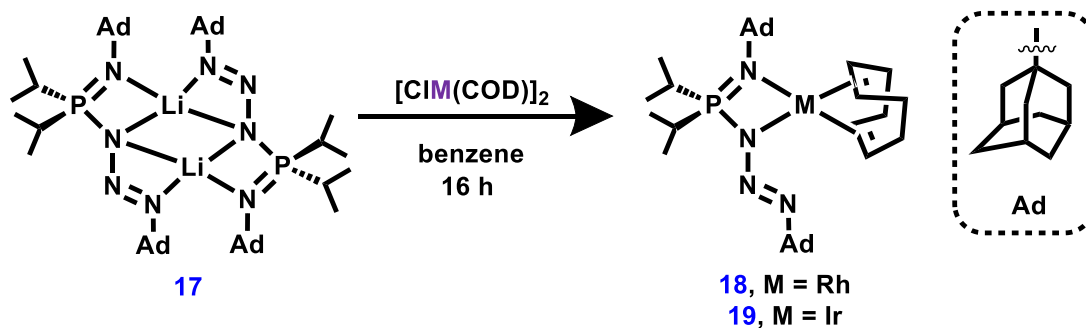
Notes: ¹ = An atom on the monomeric unit of **17** that is generated through symmetry (i.e. does not exist in the asymmetric unit)

3.3 Towards Rh^I and Ir^I Azidophosphonamido Complexes

The readily available starting metal sources $[\text{MCl}(\text{COD})]_2$ ($\text{M} = \text{Rh}, \text{Ir}$) were used to generate Rh and Ir COD complexes. Upon coordination of the ligand to Rh or Ir, it was unknown if the ligand would exhibit a $\kappa^3\text{-}N, N^\alpha, N^\gamma$ coordination mode, where one COD alkene ligand is dissociated, or a $\kappa^2\text{-}N, N^\alpha$ coordination, akin to **17**, $\text{Li}_2[\text{}^i\text{Pr}_2\text{P}(\text{NAd})(\text{N}_3\text{Ad})]_2$ and could later be induced to bind κ^3 .

3.3.1 Synthesis of Rh^I and Ir^I Adamantyl-Substituted Azidophosphonamido Species

In generating the neutral azidophosphonamide **16**, $[\text{}^i\text{Pr}_2\text{P}(\text{N}_3\text{Ad})(\text{NHAd})]$, and the azidophosphonamidolithium salt **17**, $\text{Li}_2[\text{}^i\text{Pr}_2\text{P}(\text{NAd})(\text{N}_3\text{Ad})]_2$, it was expected that the synthesis of **18**, $[\text{}^i\text{Pr}_2\text{P}(\text{N}_3\text{Ad})(\text{NAd})\text{-}\kappa^2\text{-}N, N^\alpha]\text{Rh}(\text{COD})$, and **19**, $[\text{}^i\text{Pr}_2\text{P}(\text{N}_3\text{Ad})(\text{NAd})\text{-}\kappa^2\text{-}N, N^\alpha]\text{Ir}(\text{COD})$ would incur similar solubility problems. Reaction of **17** with half an equivalent of the metal dimers $[\text{MCl}(\text{COD})]_2$ ($\text{M} = \text{Rh}$ or Ir) in benzene readily afforded the Rh^I and Ir^I complexes **18** after 16 h at ambient temperature (Scheme 3.10).



Scheme 3.10 Synthesis of $[\text{}^i\text{Pr}_2\text{P}(\text{N}_3\text{Ad})(\text{NAd})\text{-}\kappa^2\text{-}N, N^\alpha]\text{M}(\text{COD})$, $\text{M} = \text{Rh}$ (**18**) and Ir (**19**)

The $^{31}\text{P}\{^1\text{H}\}$ NMR spectra of **18** and **19** each contain one resonance (δ 24.5 and δ 111.0, respectively). X-ray diffraction experiments confirmed that the phosphazide group was retained (Figure 3.8). Attempts to crystallize the Ir analogue **19** were unsuccessful; however, corroboration that **19** keeps the PN_3 groups and adopts the $\kappa^2\text{-}N,N^\alpha$ coordination mode came *via* the solid-state structure of $[\text{Pr}_2\text{P}(\text{N}_3\text{Ad})(\text{NAd})\text{-}\kappa^2\text{-}N,N^\alpha]\text{Ir}(\text{CO})_2$, **25** (see section 4.3.2).

3.3.1.1 X-ray Crystal structure of $[\text{Pr}_2\text{P}(\text{N}_3\text{Ad})(\text{NAd})\text{-}\kappa^2\text{-}N,N^\alpha]\text{Rh}(\text{COD})$ (**18**)

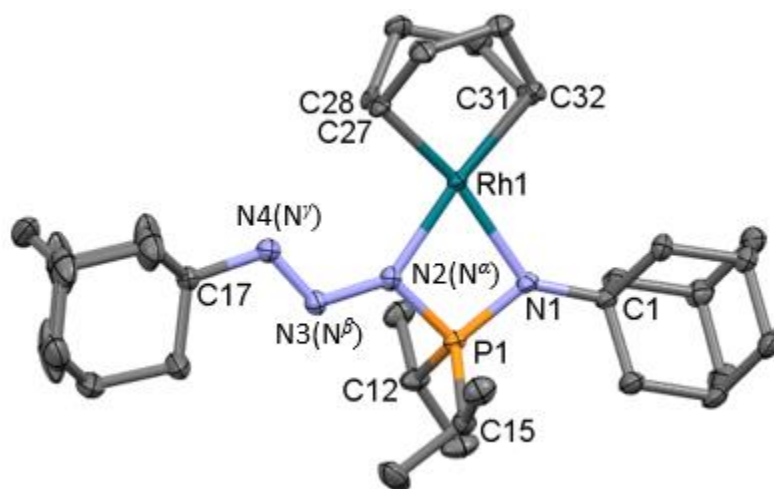


Figure 3.8 X-ray crystal structure of **18** depicted as 50% displacement ellipsoids. Hydrogen atoms are omitted for clarity

The phosphazide functionality in complex **18** adopts the more stable *transoid*-conformation, akin to its precursor **17**, $\text{Li}_2[\text{Pr}_2\text{P}(\text{NAd})(\text{N}_3\text{Ad})]_2$. Complex **18** exhibits a smaller than ideal P-N-N=N torsion angle of $170.8(2)^\circ$, attributed to the steric bulk of the COD ligand. The $\kappa^2\text{-}N,N^\alpha$ bonding mode of the ligand can be explained through examination of the P-N distances, where the ligand's anionic charge is presumed to reside

on the *alpha*-phosphazide nitrogen (N^α), as the P– N^α distance approaches single bond length (1.652(3) Å; Table 3.3); a typical P–N distance ranges from 1.67 to 1.77 Å.¹⁶³ The other phosphonamido nitrogen (N1) exhibits a shorter P=N distance suggestive of double bond character (1.607(3) Å, a typical P=N distance ranges from 1.47 to 1.62 Å.¹⁶³), similar to the two known azidophosphonamidolithium salts.¹²⁷ The geometry about Rh is distorted square planar ($\tau_4 = 0.27$) attributed to the small N–Rh–N bite angle (70.20(10)°) which is similar to the angles observed for the iminophosphonamide species [$\text{Ph}_2(\text{NR})_2\text{M}(\text{COD})$] in chapter 2 ($\tau_4 = 0.2\text{--}0.3$ and N–M–N = 70–80°).

Table 3.3 Selected bond distances (Å) and angles (°) for compound **18**

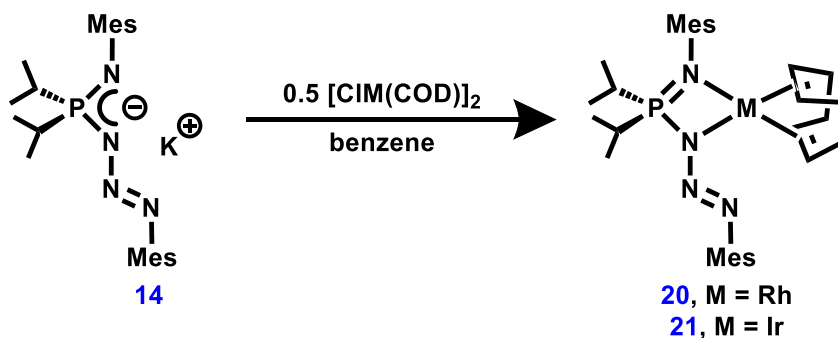
Atoms	Distance (Å)	Atoms	Angle (°)
Rh–N1	2.181(3)	N1–Rh–N2	70.20(10)
Rh–N2	2.053(3)	C31–Rh–N1	99.43(12)
N1–C1	1.475(4)	C32–Rh–N1	106.88(12)
N4–C17	1.480(5)	C27–Rh–N2	96.32(12)
P–C12	1.838(4)	C27–Rh–N2	99.96(13)
P–C15	1.834(3)	C27–Rh–C32	81.77(13)
Rh–C27	2.132(3)	C28–Rh–C31	89.44(14)
Rh–C28	2.126(3)	C12–P–C15	107.21(17)
Rh–C31	2.121(3)	N1=P–N2	96.77(15)
Rh–C32	2.139(3)	P=N1–C1	128.0(2)
P–N1	1.607(3)	P–N2–N3	116.0(2)
P–N2	1.652(3)	N2–N3=N4	114.0(3)
N2–N3	1.362(4)	N3=N4–C17	112.8(3)
N3=N4	1.250(4)		

The broad resonances in the $^{31}\text{P}\{^1\text{H}\}$ NMR spectra for both **18** [$^i\text{Pr}_2\text{P}(\text{N}_3\text{Ad})(\text{NAd})-\kappa^2\text{-N,N}^\alpha\text{Rh}(\text{COD})$], and **19** [$^i\text{Pr}_2\text{P}(\text{N}_3\text{Ad})(\text{NAd})-\kappa^2\text{-N,N}^\alpha\text{Ir}(\text{COD})$], suggest a fluxional process in solution ($\kappa^2\text{-N,N}^\alpha \leftrightarrow \kappa^3\text{-N,N}^\alpha\text{,N}^\beta$), which broadens the peak. A $\kappa^3\text{-N,N}^\alpha\text{,N}^\beta$ coordinated azidophosphonamido complex ($^i\text{Pr}_2\text{P}(\text{N}_3\text{Ad})(\text{NAd})-\kappa^3\text{-N,N}^\alpha\text{,N}^\beta\text{M}(\kappa^1\text{-COD})$) could have only one coordinated and an uncoordinated COD alkene moiety to retain a 16-electron metal center; however, methylene and methine signals attributed to an unbound COD alkene are not observed in both the ^1H and $^{13}\text{C}\{^1\text{H}\}$ NMR spectra. Another possibility could be the formation of an 18-electron, 5 coordinate species ($^i\text{Pr}_2\text{P}(\text{N}_3\text{Ad})(\text{NAd})-\kappa^3\text{-$

N,N^α,N^β] $M(\kappa^2\text{-COD})$), which would possess a COD ligand with two chemically inequivalent alkene moieties; however, a $\kappa^2\text{-}N,N^\alpha$ complex ($[^i\text{Pr}_2\text{P}(\text{N}_3\text{Ad})(\text{NAd})\text{-}\kappa^2\text{-}N,N^\alpha]\text{M}(\kappa^2\text{-COD})$) would also exhibit unsymmetric COD coordination. Two different methine (CH) COD resonances were observed for both **18** and **19** in the ^1H NMR spectra (δ 5.45, 4.64 (**18**) and δ 5.17, 4.49 (**19**)) and corroborated by the $^{13}\text{C}\{^1\text{H}\}$ NMR spectra; thereby, implying non-symmetric coordination of COD ligand. The solid-state structure of **18** exhibits the $\kappa^2\text{-}N,N^\alpha$ coordination mode, although it is unclear if this is the coordination mode observed in the solution-state.

3.3.2 Synthesis of Rh^{I} and Ir^{I} Mesityl-Substituted Azidophosphonamido Complexes

Akin to the synthesis of the adamantyl complexes **18**, $[^i\text{Pr}_2\text{P}(\text{N}_3\text{Ad})(\text{NAd})\text{-}\kappa^2\text{-}N,N^\alpha]\text{Rh}(\text{COD})$ and **19**, $[^i\text{Pr}_2\text{P}(\text{N}_3\text{Ad})(\text{NAd})\text{-}\kappa^2\text{-}N,N^\alpha]\text{Ir}(\text{COD})$, the analogous mesityl complexes, Rh^{I} and Ir^{I} COD complexes **20**, $[^i\text{Pr}_2\text{P}(\text{N}_3\text{Mes})(\text{NMes})\text{-}\kappa^2\text{-}N,N^\alpha]\text{Rh}(\text{COD})$, and **21**, $[^i\text{Pr}_2\text{P}(\text{N}_3\text{Mes})(\text{NMes})\text{-}\kappa^2\text{-}N,N^\alpha]\text{Ir}(\text{COD})$, were prepared *via* a reaction between $[\text{MCl}(\text{COD})]_2$ ($\text{M} = \text{Rh}$ or Ir) and **14**, $\text{Li}[^i\text{Pr}_2\text{P}(\text{N}_3\text{Mes})(\text{NMes})]$, at ambient temperature in benzene- d_6 (Scheme 3.11).



Scheme 3.11 Synthesis of $[^i\text{Pr}_2\text{P}(\text{N}_3\text{Mes})(\text{NMes})\text{-}\kappa^2\text{-}N,N^\alpha]\text{M}(\text{COD})$, where $\text{M} = \text{Rh}$ (**20**), Ir (**21**)

Monitoring the synthesis of the Rh complex **20**, [$^i\text{Pr}_2\text{P}(\text{N}_3\text{Mes})(\text{NMes})-\kappa^2-N,N^\alpha$]Rh(COD), via $^{31}\text{P}\{^1\text{H}\}$ NMR spectroscopy, revealed that complete consumption of the lithium salt **14**, $\text{Li}[^i\text{Pr}_2\text{P}(\text{N}_3\text{Mes})(\text{NMes})]$, occurs within minutes yielding two resonances at δ 84.1 (91%) and 64.9 (9%). The smaller upfield signal (δ 64.9) was initially assigned as the N_2 extrusion product, [$^i\text{Pr}_2\text{P}(\text{NMes})_2$]Rh(COD). Similarly, synthesis of the Ir complex **21**, [$^i\text{Pr}_2\text{P}(\text{N}_3\text{Mes})(\text{NMes})-\kappa^2-N,N^\alpha$]Ir(COD), yielded two resonances in the $^{31}\text{P}\{^1\text{H}\}$ NMR spectrum at δ 105.7 (86%) and 77.0 (14%), where the sharper, upfield signal (δ 77.0) was attributed to [$^i\text{Pr}_2\text{P}(\text{NMes})_2$]Ir(COD). Isolation of the major product in both reactions was achieved by two or more successive recrystallizations. Unambiguous confirmation of the identity of the species as the proposed azidophosphonamido complexes **20**, [$^i\text{Pr}_2\text{P}(\text{N}_3\text{Mes})(\text{NMes})-\kappa^2-N,N^\alpha$]Rh(COD), and **21**, [$^i\text{Pr}_2\text{P}(\text{N}_3\text{Mes})(\text{NMes})-\kappa^2-N,N^\alpha$]Ir(COD), was provided by X-ray diffraction experiments.

3.3.2.1 X-ray Crystal Structure of [$^i\text{Pr}_2\text{P}(\text{N}_3\text{Mes})(\text{NMes})-\kappa^2-N,N^\alpha$]Rh(COD) (**20**)

The phosphazide functionality in complex **20**, [$^i\text{Pr}_2\text{P}(\text{N}_3\text{Mes})(\text{NMes})-\kappa^2-N,N^\alpha$]Rh(COD), adopts the *transoid*-conformation (torsion angle = $(171.6(1)^\circ)$, and an *E* N=N bond configuration ($\text{N}2-\text{N}3=\text{N}4-\text{C}16 = 179.7(2)^\circ$), to minimize steric interaction of the mesityl substituent and the COD ligand.

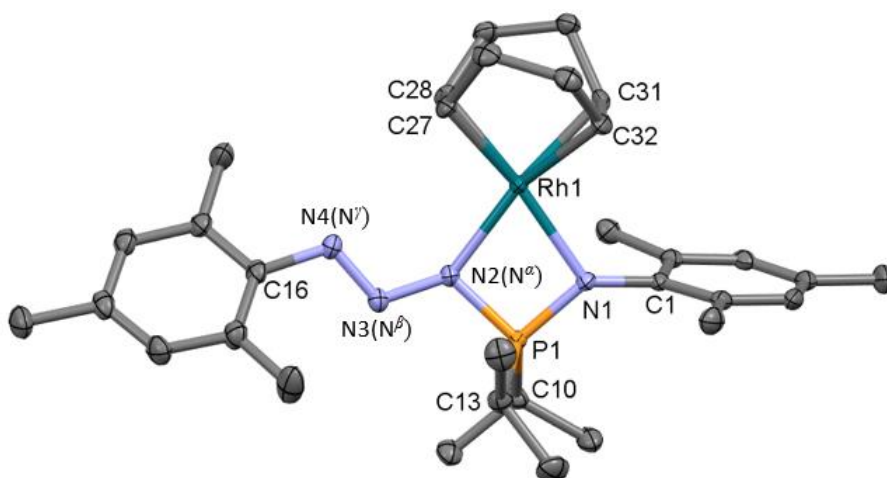


Figure 3.9 X-ray crystal structure of **20** depicted as 50% displacement ellipsoids. Hydrogen atoms are omitted for clarity

The azidophosphonamide ligand in **20** binds to Rh in a κ^2 - N,N^α fashion, akin to that observed in the azidophosphonamido complexes **18** and **19**. The geometry at Rh is distorted square planar, $\tau_4 = 0.28$, and overall, quite similar to the adamantyl-substituted analogue **18**, $[\text{Ph}_2\text{P}(\text{NAd})(\text{NAd})]\text{Rh}(\text{COD})$ ($\tau_4 = 0.27$). The small N–Rh–N bite angle of $70.65(6)^\circ$ (Table 3.4) is similar to the adamantyl-substituted complex **18** ($70.20(10)^\circ$).

Table 3.4 Selected bond distances (Å) and angles (°) for complex **20**

Atoms	Distance (Å)	Atoms	Angle (°)
Rh–N2	2.1217(15)	N1–Rh–N2	70.65(6)
Rh–N2	2.0840(17)	C31–Rh–N1	99.45(7)
N1–C1	1.419(2)	C32–Rh–N1	96.03(7)
N4–C16	1.427(3)	C27–Rh–N2	104.51(7)
P–C10	1.826(2)	C28–Rh–N2	99.89(7)
P–C13	1.820(2)	C10–P–C13	108.02(10)
Rh–C27	2.1253(19)	N1=P–N2	96.13(8)
Rh–C28	2.1125(19)	P=N1–C1	132.10(14)
Rh–C31	2.1263(19)	P–N2–N3	117.59(13)
Rh–C32	2.112(2)	N2–N3=N4	112.94(16)
P–N1	1.6052(17)	N3=N4–C11	113.29(17)
P–N2	1.6635(16)		
N2–N3	1.355(2)		
N3=N4	1.271(2)		

3.3.2.2 X-ray Crystal Structure of [ⁱPr₂P(N₃Mes)(NMes)-κ²-N,N^α]Ir(COD) (**21**)

As in **20**, [ⁱPr₂P(N₃Mes)(NMes)-κ²-N,N^α]Rh(COD)], the phosphazide functionality in **21**, [ⁱPr₂P(N₃Mes)(NMes)-κ²-N,N^α]Ir(COD)], is *transoid*-disposed (P1–N2–N3=N4 = 172.0(2)°), and the *E* configuration was observed about the N=N bond (N2–N3=N4–C16 = 179.7(2)°). The Rh and Ir complexes **20** and **21** crystallize with very similar unit cells (i.e. nearly identical *a*, *b*, *c*, *α*, *β*, and *γ* dimensions, volume (~3050 Å³) and space group (P2₁/c)).

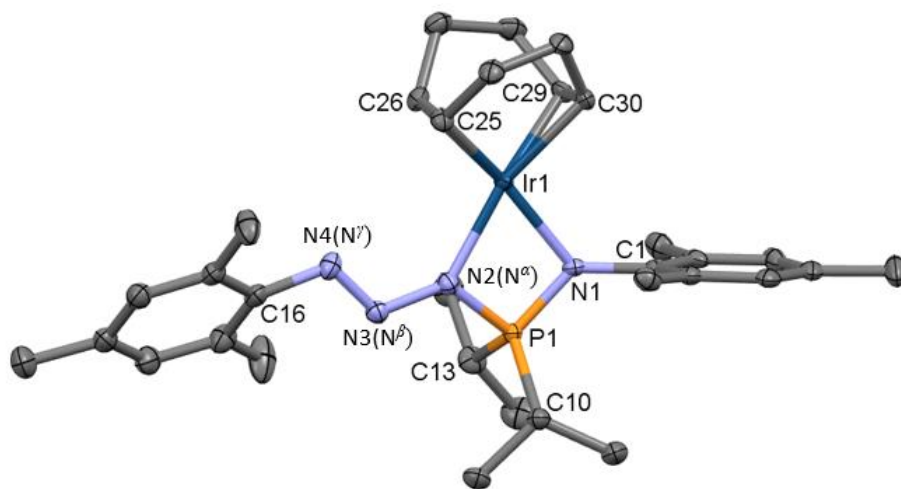


Figure 3.10 X-ray crystal structure of **20** depicted as 50% displacement ellipsoids. Hydrogen atoms are omitted for clarity

Many metrical parameters are statistically indistinguishable between the two complexes **20** [$^i\text{Pr}_2\text{P}(\text{N}_3\text{Mes})(\text{NMe}_s)\text{-}\kappa^2\text{-}N,N^\alpha$] $\text{Rh}(\text{COD})$ (see Table 3.5), and **21** [$^i\text{Pr}_2\text{P}(\text{N}_3\text{Mes})(\text{NMe}_s)\text{-}\kappa^2\text{-}N,N^\alpha$] $\text{Ir}(\text{COD})$ (see Table 3.4). For instance, the N–M–N bite angles (**20** = 69.94(9)°, and **21** = 70.65(6)°) and M–N bond distances (**20** = 2.1217(15) Å, and **21** = 2.110(2) Å) are alike. Similarly, both **20** and **21** display the distorted square planar geometry, $\tau_4 = 0.28$ (**20**) and $\tau_4 = 0.28$ (**21**).

Table 3.5 Selected bond distances (Å) and angles (°) for compound **21**

Atoms	Distance (Å)	Atoms	Angle (°)
Ir–N1	2.110(2)	N1–Ir–N2	69.94(9)
Ir–N2	2.077(2)	C29–Ir–N1	96.36(10)
N1–C1	1.425(3)	C30–Ir–N1	99.74(9)
N4–C11	1.428(4)	C25–Ir–N2	100.87(10)
P–C10	1.817(3)	C26–Ir–N2	105.00(10)
P–C13	1.827(3)	C25–Ir–C30	81.57(11)
Ir–C25	2.097(3)	C26–Ir–C29	81.64(11)
Ir–C26	2.119(3)	C10–P–C13	108.45(13)
Ir–C29	2.101(3)	N1=P–N2	94.29(11)
Ir–C30	2.118(3)	P=N1–C1	132.17(18)
P–N1	1.606(2)	P–N2–N3	117.59(18)
P–N2	1.667(2)	N2–N3=N4	112.6(2)
N2–N3	1.359(3)	N3=N4–C11	112.7(2)
N3=N4	1.267(3)		

The $^{31}\text{P}\{^1\text{H}\}$ NMR resonances for **20** and **21** (δ 84.1 and 105.7) are broad, suggesting a fluxional process on the NMR timescale ($\kappa^2\text{-}N,N^\alpha \leftrightarrow \kappa^3\text{-}N,N^\alpha,N^\beta$), akin to **18**, [$^i\text{Pr}_2\text{P}(\text{N}_3\text{Ad})(\text{NAd})\text{-}\kappa^2\text{-}N,N^\alpha$] $\text{Rh}(\text{COD})$) and **19**, [$^i\text{Pr}_2\text{P}(\text{N}_3\text{Ad})(\text{NAd})\text{-}\kappa^2\text{-}N,N^\alpha$] $\text{Ir}(\text{COD})$. The two distinct methine COD resonances observed in the ^1H NMR spectrum of both **20** (δ 5.42 and 3.36) and **21** (δ 4.74 and 2.22) are suggestive of two chemically inequivalent COD alkene moieties, rather than an uncoordinated COD alkene group (methine signal of δ 5.6). Overall, the X-ray crystal structures of **20** and **21** were confirmed to contain the

azidophosphonamido ligand [$^i\text{Pr}_2\text{P}(\text{N}_3\text{Mes})(\text{NMes})$] $^-$ bound to the metal in the $\kappa^2\text{-N,N}^\alpha$ mode. In solution, the non-symmetric COD ligand could be suggestive of a 4-coordinate, $16e^-$ compound ($\kappa^2\text{-N,N}^\alpha$), a 5-coordinate, $18e^-$ complex ($\kappa^3\text{-N,N}^\alpha\text{,N}'$), or rapid conversion between the two species.

3.4 Concluding Remarks

A new family of azidophosphonamide transition metal complexes has been synthesized and characterized. The COD complexes [$^i\text{Pr}_2\text{P}(\text{N}_3\text{R})(\text{NR})\text{-}\kappa^2\text{-N,N}^\alpha$] $\text{M}(\text{COD})$ ($\text{R} = \text{Mes, Ad}$ and $\text{M} = \text{Rh, Ir}$) were readily generated at ambient or elevated temperatures ($60\text{ }^\circ\text{C}$) within 16 h and purified by crystallization. The reactivity of the azidophosphonamide Rh^{I} and Ir^{I} complexes toward various small molecules to substitute the COD ligand is discussed in Chapter 4.

CHAPTER 4: REACTIVITY OF AZIDOPHOSPHONAMIDE Rh AND Ir COMPLEXES

4.1 Overview

4.1.1 Phosphazides

The phosphazide ($R_3P=N_3-R^1$) is an uncommon species in the literature and often only discussed in the context of the Staudinger reaction (Scheme 3.1), wherein a phosphazide is the intermediate species. Phosphazides are inherently unstable and prone to release N_2 gas when in the *cis* conformation (Scheme 3.1).¹⁰⁸ Many phosphazide stabilization techniques involve favouring the *trans* conformation *via* steric factors, such as bulky groups on both N and P atoms, and electronic factors, including strong electron donors on phosphorus or electron-withdrawing groups on nitrogen.¹¹¹ A more common technique involves coordinating one or more of the phosphazide nitrogen atoms to a metal or Lewis acid;¹¹³ however, a limited number of main group, transition metal, and *f*-block complexes which contain phosphazide ligands are known.¹¹⁴⁻¹¹⁶

4.1.2 Phosphazide Linkage Isomerism

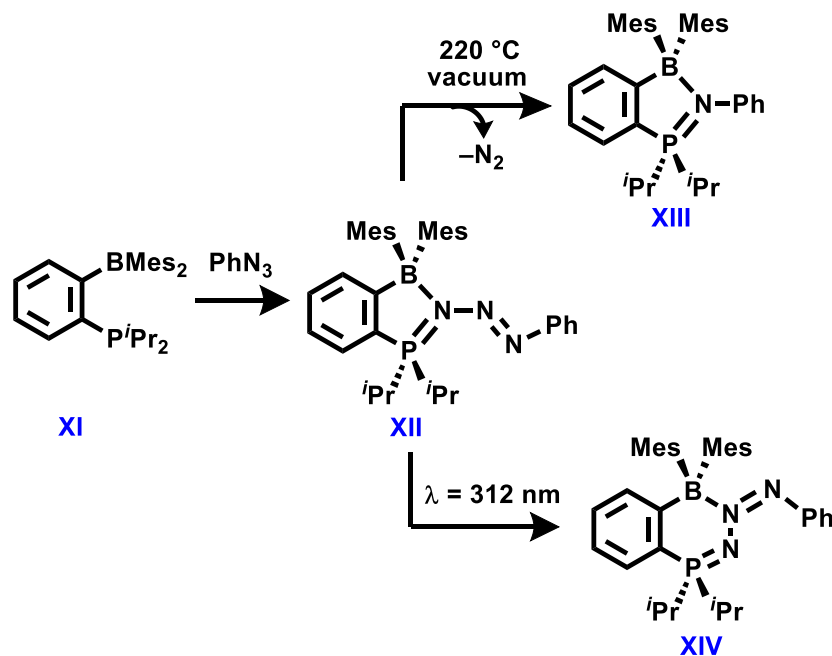
Linkage isomerism is a phenomenon that can occur with ambidentate ligands that are capable of more than one coordination mode. Thiocyanate is a well-known example, as the ligand can coordinate at either the sulfur ($M-S-C\equiv N$) or the nitrogen atom ($M-N=C=S$).

Due to the three possible donor nitrogens present in a phosphazide (N^α , N^β and N^γ), numerous phosphazide coordination modes are known and have been shown to undergo

linkage isomerism (from $\kappa^2\text{-}N^\alpha, N^\gamma$ to $\kappa^1\text{-}N^\alpha$) due to steric crowding.¹¹⁷ More interestingly, frustrated Lewis pairs (FLPs) containing a phosphazide have exhibited thermally or photochemically induced linkage isomerism from the $\kappa^1\text{-}N^\alpha$ to the $\kappa^1\text{-}N^\beta$ coordination mode (see section 4.1.3 and 4.1.4).^{116,164}

4.1.3 Photochemically Induced Phosphazide Linkage Isomerism

Bourissou *et al.* were the first to report phosphazide isomerization using a phosphazide borane FLP (**XII**, *ortho*-[(*i*Pr₂PN₃Ph)C₆H₄(BMes₂)]), which was generated *via* an arrested Staudinger reaction.¹⁶⁴

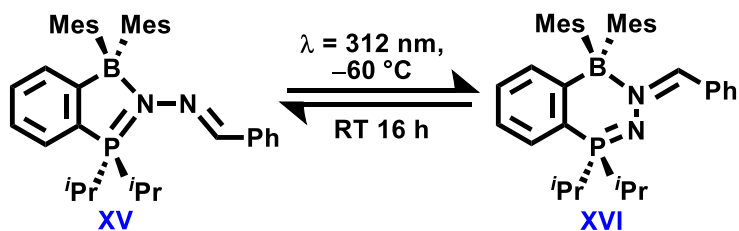


Scheme 4.1 Photochemically induced linkage isomerism of a phosphazidoborane¹⁶⁴

The high thermal stability of **XII**, *ortho*-[(*i*Pr₂PN₃Ph)C₆H₄(BMes₂)] meant that harsh conditions were required to promote N₂ elimination and yield the desired phosphiniminoborane **XIII**, *ortho*-[(*i*Pr₂PNPh)C₆H₄(BMes₂)].¹⁶⁴ Bourissou *et al.*

postulated that photochemical irradiation could induce N₂ extrusion, akin to that observed for azides and diazo-species in the literature,¹⁶⁵ thereby negating the need for high temperature and low pressure. Instead, the phosphazidoborane was found to undergo unprecedented and irreversible photoisomerization wherein the borane (BMes₂) ends up in a κ^1 -N ^{β} →BMes₂ coordination mode (of the *beta*-phosphazide nitrogen), increasing the size of the “chelate ring” to a 6-membered B–N ^{β} –N ^{α} –P–C–C heterocycle (**XII** → **XIV**, Scheme 4.1).¹⁶⁴ The isomerization also changed the phosphazide conformation from *cisoid* (**XII**) to *transoid* (**XIV**) and the N=N bond configuration from *E* (**XII**) to *Z* (**XIV**), which reduces steric crowding around B.¹⁶⁴ Attempts to reverse the linkage isomerization were unsuccessful, yielding complex mixtures.

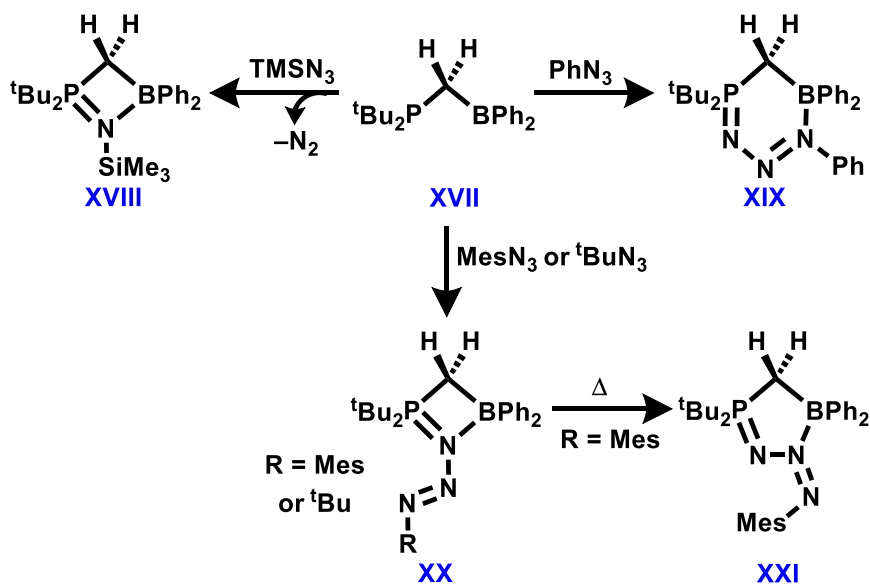
Bourissou *et al.* also reported an analogous phosphazinoborane **XV**, *ortho*-[(*i*Pr₂P=N–N=C–Ph)C₆H₄(BMes₂)], which was found to undergo the same photochemically induced linkage isomerism (N ^{α} →B in **XV** to N ^{β} →Bin **XVI**). However, this process can be reversed if the compound is left in solution at ambient temperature for 16 h (Scheme 4.2).



Scheme 4.2 Photochemically induced linkage isomerism of a phosphazinoborane¹⁶⁴

4.1.4 Thermally-Induced Linkage Isomerism of Phosphazides

In 2019, Slootweg *et al.* reported thermally-induced phosphazide linkage isomerism of another phosphazide-containing FLP.¹¹⁶ The work published by Slootweg *et al.* demonstrated that the ability to isolate a phosphazide without N₂ extrusion partially depends on the phosphazide nitrogen substituent.¹¹⁶ In this case, when Me₃SiN₃ was employed, only the phosphinimine **XVIII**, (tBu₂PNSiMe₃)CH₂BPh₂, was obtained. Conversely, when the same phosphine was allowed to react with PhN₃, the phosphazide species **XIX**, (tBu₂PN₃Ph)CH₂BPh₂, was reported (Scheme 4.3). Phosphazide **XIX** displayed $\kappa^1\text{-N}^\gamma\text{-}\rightarrow\text{B}$ coordination to the borane in the solid state with a six-membered heterocycle (Scheme 4.3). The $\kappa^1\text{-N}^\gamma\text{-}\rightarrow\text{B}$ coordination mode exhibited in **XIX** was computationally determined to be the lowest energy linkage isomer when compared to $\kappa^1\text{-N}^\alpha\text{-}\rightarrow\text{B}$ or $\kappa^1\text{-N}^\beta\text{-}\rightarrow\text{B}$.¹¹⁶



Scheme 4.3 Formation of various phosphazide-containing FLPs¹¹⁶

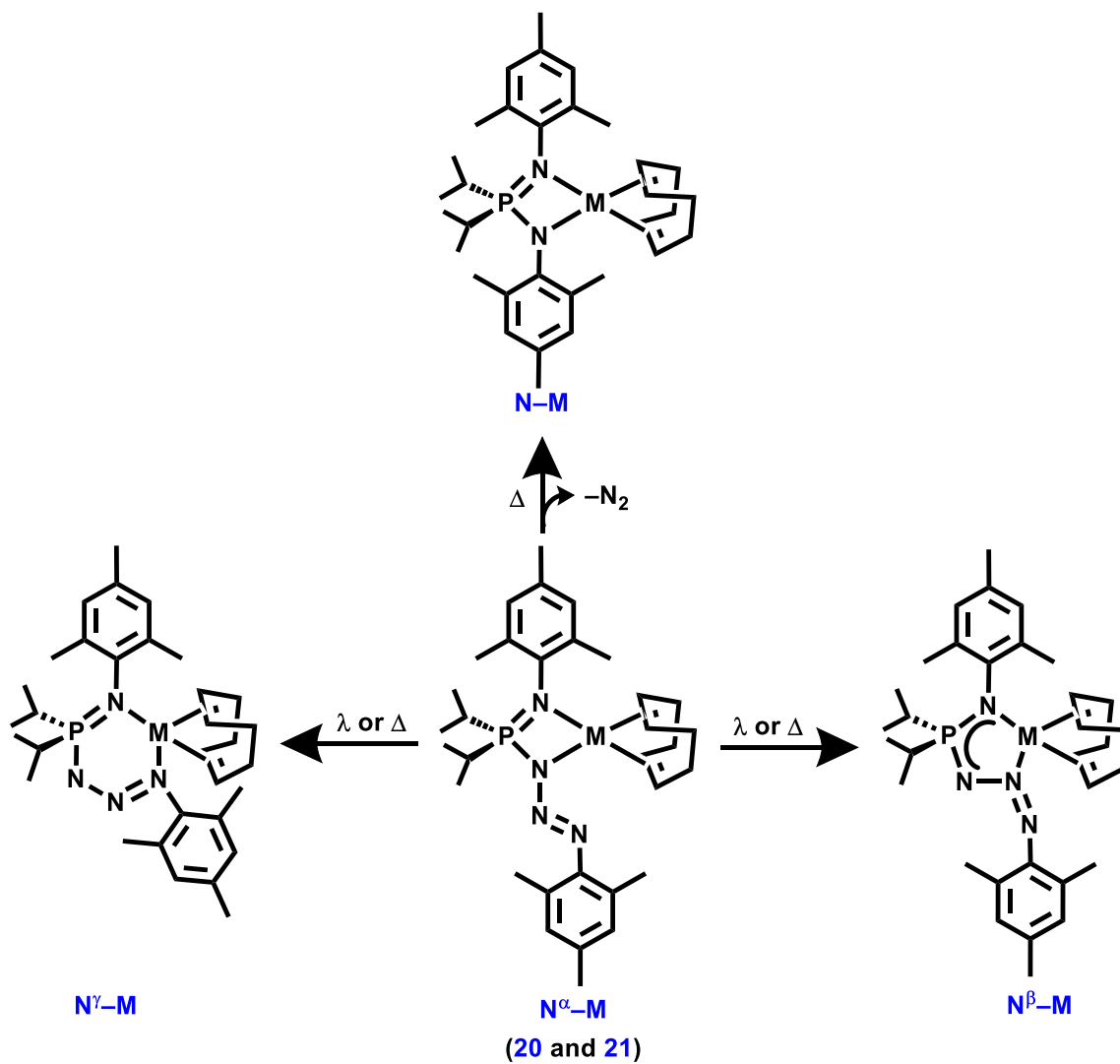
Bulkier nitrogen substituents, namely ^tBu or Mes, yielded $\kappa^1\text{-N}^\alpha\text{-}\rightarrow\text{B}$ species (**XX**, $\kappa^1\text{-N}^\alpha(\text{}^t\text{Bu}_2\text{PN}_3\text{R})\text{CH}_2\text{BPh}_2$, R = ^tBu or Mes) (Scheme 4.3). Slootweg *et al.* proposed that the $\text{N}^\alpha\text{-}\rightarrow\text{B}$ isomer (**XX**) is the kinetic product which can rearrange to the thermodynamically more stable $\kappa^1\text{-N}^\beta\text{-}\rightarrow\text{B}$ isomer. Notably, the ^tBu substituted species exhibited no signs of rearrangement; however, the mesityl-substituted **XX** was found to undergo thermally-induced linkage isomerization. The kinetic $\text{N}^\alpha\text{-}\rightarrow\text{B}$ isomer **XX**, when heated to 75 °C for 3 days, converted into the $\kappa^1\text{-N}^\beta\text{-}\rightarrow\text{B}$ coordination compound **XXI**, $\kappa^1\text{-N}^\beta(\text{}^t\text{Bu}_2\text{PN}_3\text{Mes})\text{CH}_2\text{BPh}_2$. DFT calculations established the five-membered heterocycle in **XXI** to be the thermodynamic product. The phosphazide in **XX** $\kappa^1\text{-N}^\alpha(\text{}^t\text{Bu}_2\text{PN}_3\text{Mes})\text{CH}_2\text{BPh}_2$ adopts a *cisoid*-conformation and *E* N=N bond configuration. In contrast, the $\kappa^1\text{-N}^\beta\text{-}\rightarrow\text{B}$ linkage isomer **XXI**, $\kappa^1\text{-N}^\beta(\text{}^t\text{Bu}_2\text{PN}_3\text{Mes})\text{CH}_2\text{BPh}_2$ exhibits a *transoid* phosphazide conformation (P=N–N=N = 178.4°) and *Z* N=N bond configuration which minimizes the steric impact of the phosphazide mesityl substituent. The work by Bourissou *et al.*¹⁶⁴ and Slootweg *et al.*¹¹⁶ reports the only known examples of both phosphazide linkage isomerization and the $\text{N}^\beta\text{-}\rightarrow\text{B}$ coordination mode.

4.2 Linkage Isomerism of Rh^I and Ir^I Azidophosponamido Complexes

4.2.1 Linkage Isomerism of Mesityl-Substituted Rh^I and Ir^I Complexes (**20** and **21**)

The reaction to generate the complexes **20** [^tPr₂P(N₃Mes)(NMes)- $\kappa^2\text{-N,N}^\alpha$]Rh(COD), and **21** [^tPr₂P(N₃Mes)(NMes)- $\kappa^2\text{-N,N}^\alpha$]Ir(COD), yielded minor impurities observed as sharp singlets in the ³¹P{¹H} NMR spectra at δ 64.9 (impurity in **20**) and δ 77.0 (impurity in **21**) (section 3.3.2). These minor products were first postulated to

correspond to the iminophosphonamido complexes, $[(^i\text{Pr}_2\text{P}(\text{NMe}_s)_2)\text{M}(\text{COD})]$, where N_2 extrusion has occurred. Alternatively, based on the few reports in the literature (*vide infra*),^{164,116} the impurities could be attributed to $\text{N}^\beta\text{-M}$ or $\text{N}^\gamma\text{-M}$ linkage isomers yielding larger metal chelate rings (Scheme 4.4).



Scheme 4.4 Possible structures of the minor impurities observed during the synthesis of complexes **20** and **21**

Nearly complete conversion of **20**, [*i*Pr₂P(N₃Mes)(NMe_s)-κ²-N,N^α]Rh(COD), to the resonance at δ 64.9 in the ³¹P{¹H} NMR spectrum was readily achieved when **20** was heated to 60 °C for 2 days in benzene-*d*₆. Alternatively, irradiating a sample of **20** with a black light (λ = 365 nm) for 16 h also led to the product observed at δ 64.9 in the ³¹P{¹H} spectrum. The lack of obvious gas (N₂) evolution from the reaction vessel suggested that the new compound might be a linkage isomer; however, NMR spectroscopy alone was insufficient to confirm the product's identity. X-ray diffraction experiments unequivocally established the solid-state structure of **22**, [*i*Pr₂P(N₃Mes)(NMe_s)-κ²-N,N^β]Rh(COD), as the N^β-M linkage isomer (Figure 4.1).

4.2.1.1 X-ray Crystal Structure of [*i*Pr₂P(N₃Mes)(NMe_s)-κ²-N,N^β]Rh(COD) (**22**)

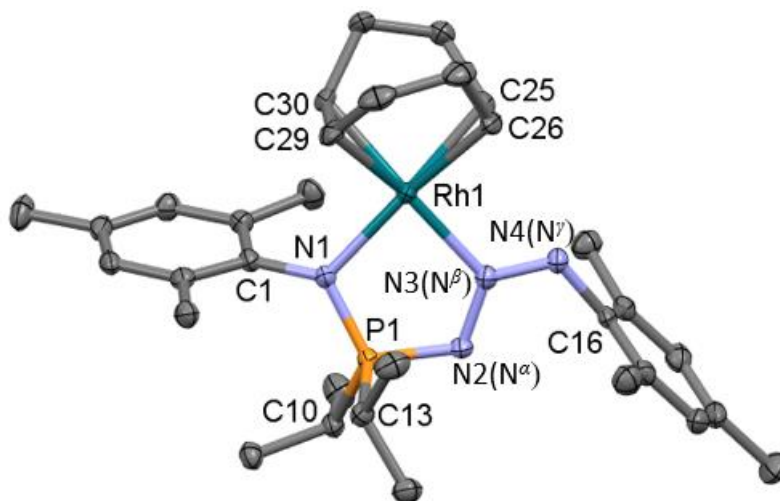
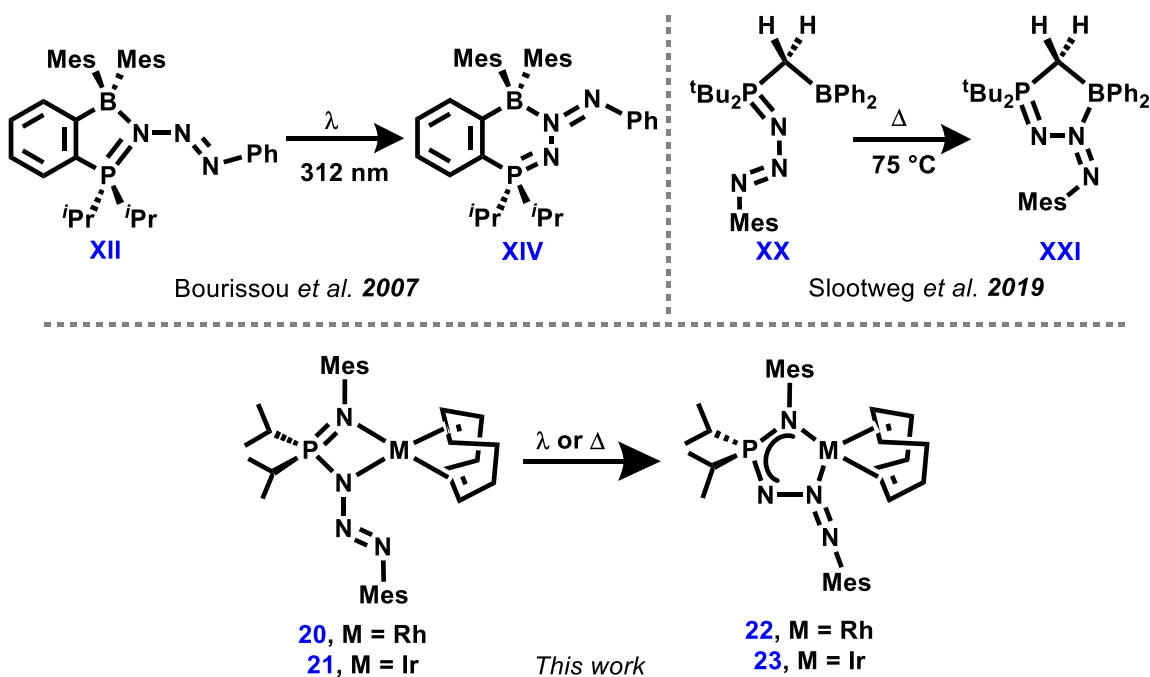


Figure 4.1 X-ray crystal structure of **22** depicted as 50% displacement ellipsoids. Hydrogen atoms are omitted for clarity. Only one of the two independent molecules of **22** in the unit cell is shown

Dark yellow rectangular crystals of **22** were grown from a saturated benzene solution stored in a sealed 20 mL scintillation vial at ambient temperature for 4 days. The square planar geometry ($\tau_4 = 0.20$) is slightly less distorted than the precursor **20**, [$^i\text{Pr}_2\text{P}(\text{N}_3\text{Mes})(\text{NMes})-\kappa^2\text{-N,N}^\alpha$]Rh(COD)], ($\tau_4 = 0.28$), as the 5-membered metallocycle relieves strain at the metal centre *via* increasing the ligand bite angle (N–P–N) from $70.65(6)^\circ$ in **20** to $83.25(7)^\circ$ and $83.11(7)^\circ$ in **22**.

Unlike the linkage isomerization reported by Bourissou¹⁶⁴ and Slootweg *et al.*¹¹⁶, who reported a change of the phosphazide conformation from *cisoid* to *transoid* upon ($\text{N}^\alpha \rightarrow \text{B}$ to $\text{N}^\beta \rightarrow \text{B}$) isomerization, the phosphazide moiety in **22**, [$^i\text{Pr}_2\text{P}(\text{N}_3\text{Mes})(\text{NMes})-\kappa^2\text{-N,N}^\beta$]Rh(COD), retains the *transoid* conformation as evidenced by the P–N–N=N torsion angles of $176.8(2)$ and $178.4(2)^\circ$. However, the linkage isomerization did change the N=N bond configuration from *E* in **20** ($\text{N}2\text{--N}3=\text{N}4\text{--C}16 = 179.7(2)^\circ$) to *Z* in **22** ($\text{N--N=N--C} = 2.7(3)$ and $3.8(3)^\circ$) which minimizes steric interactions between the Mes group and COD ligand, and mimics the same behaviour observed by Bourissou¹⁶⁴ and Slootweg¹¹⁶ (see Scheme 4.5).



Scheme 4.5 Phosphazide linkage isomerism of the $N^{\alpha} \rightarrow B$ to the $N^{\beta} \rightarrow B$ coordination mode; as reported by Bourissou (top left),¹⁶⁴ Slootweg (top right)¹¹⁶ and exhibited by Rh^I and Ir^I azidophosphonamido complexes **20** and **21**

The P– N^{α} distance in **22**, [$iPr_2P(N_3Mes)(NMe_3)-\kappa^2-N,N^{\beta}$]Rh(COD), is reflective of a single bond (1.6578(19), 1.6522(19) Å), while the phosphonamido (N1) nitrogen-to-phosphorus bonds are shorter (1.6132(19), 1.612(2) Å), more akin to a typical P=N bond 1.47–1.62 Å.¹⁶³ Thus, N^{α} in **22**, formally bears the anionic charge, as observed in the pre-isomerized Rh complex **20**, [$iPr_2P(N_3Mes)(NMe_3)-\kappa^2-N,N^{\alpha}$]Rh(COD). The geometry at N^{β} is unaffected by this isomerization and the $N^{\alpha}-N^{\beta}$ and $N^{\beta}=N^{\gamma}$ distances are statistically indistinguishable between the linkage isomers **20** (1.355(2) and 1.272(2) Å) and **22** (1.341(3) and 1.275(3) Å). Most key bond lengths and angles observed in **22** (Table 4.1) (N^{β} –Rh) do not vary substantially from the N^{α} –Rh isomer **20** (Table 3.4).

Table 4.1 Selected bond distances (Å) and angles (°) for compound **22**

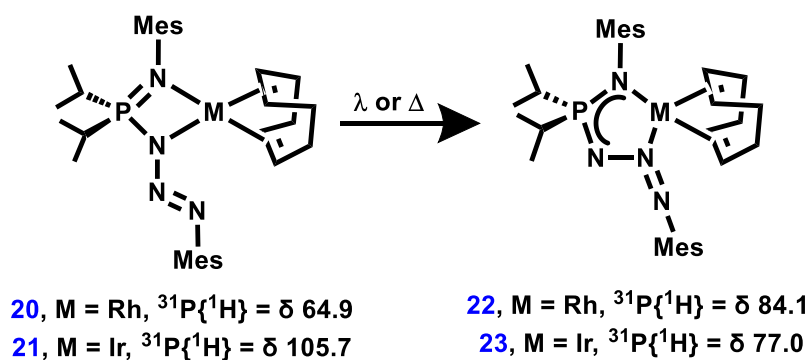
Atoms	Distance (Å)	Atoms	Angle (°)
Rh–N1	2.1006(19)	N1–Rh–N3	83.25(7)
Rh–N3	2.0964(18)	C29–Rh–N1	95.43(9)
N1–C1	1.428(3)	C30–Rh–N1	95.24(8)
N4–C16	1.445(3)	C25–Rh–N3	92.35(8)
P–C10	1.827(2)	C26–Rh–N3	94.42(8)
P–C13	1.832(2)	C29–Rh–C26	81.73(10)
Rh–C25	2.110(2)	C30–Rh–C25	82.43(9)
Rh–C26	2.129(2)	N1–P–N2	110.61(10)
Rh–C29	2.127(2)	N2=N3–Rh	119.92(14)
Rh–C30	2.149(2)	P=N1–Rh	108.86(9)
P=N1	1.6132(19)	P=N1–C1	125.34(16)
P–N2	1.6578(19)	P–N2–N3	111.93(15)
N2–N3	1.341(3)	N2–N3=N4	119.52(19)
N3=N4	1.275(3)	N3=N4–C16	117.79(19)
		C10–P–C13	104.81(11)

The $^{31}\text{P}\{^1\text{H}\}$ NMR signal attributed to **22**, [$^i\text{Pr}_2\text{P}(\text{N}_3\text{Mes})(\text{NMes})-\kappa^2-N,N^\beta$]Rh(COD)), a sharp singlet at δ 64.9, more upfield than its precursor **20**, [$^i\text{Pr}_2\text{P}(\text{N}_3\text{Mes})(\text{NMes})-\kappa^2-N,N^\alpha$]Rh(COD) (δ 84.1). This change agrees well with that reported by Bourissou *et al.* (δ 61 and 35 for $\text{N}^\alpha \rightarrow \text{B}$ and $\text{N}^\beta \rightarrow \text{B}$, respectively).¹⁶⁴ Presumably, no low energy fluxional processes exist for the $\text{N}^\beta\text{-M}$ isomer **22**. In the ^1H

and $^{13}\text{C}\{^1\text{H}\}$ NMR spectra of **22**, two sets of signals were observed for both the Mes substituents and COD ligands.

4.2.2 Linkage Isomerism of [$^i\text{Pr}_2\text{P}(\text{N}_3\text{Mes})(\text{NMes})-\kappa^2\text{-N,N}^\alpha$ Ir(COD)] (**23**)

Given the linkage isomerism displayed by complex **20**, [$^i\text{Pr}_2\text{P}(\text{N}_3\text{Mes})(\text{NMes})-\kappa^2\text{-N,N}^\alpha$]Rh(COD) (“ $\text{N}^\alpha\text{-M}$ ”) similar reactivity was expected with the iridium analogue **21**, [$^i\text{Pr}_2\text{P}(\text{N}_3\text{Mes})(\text{NMes})-\kappa^2\text{-N,N}^\alpha$]Ir(COD). Heating **21** at 60 °C in benzene- d_6 for 72 h did not lead to complete conversion of **21** (δ 105.7) to the putative linkage isomer **23**, [$^i\text{Pr}_2\text{P}(\text{N}_3\text{Mes})(\text{NMes})-\kappa^2\text{-N,N}^\beta$]Ir(COD). However, when **21** was irradiated ($\lambda = 365$ nm) in benzene- d_6 for 30 h, 80% conversion to **23** was observed by $^{31}\text{P}\{^1\text{H}\}$ NMR spectroscopy (**23**: δ 77.0). Isolation of isomer **23** was achieved by two successive recrystallizations from pentane, providing a low but reproducible isolated yield of 48%. The solid-state structure confirmed the identity of **23** as the anticipated linkage isomer, [$^i\text{Pr}_2\text{P}(\text{N}_3\text{Mes})(\text{NMes})-\kappa^2\text{-N,N}^\beta$]Ir(COD) (Figure 4.2). The significant upfield shift of the $^{31}\text{P}\{^1\text{H}\}$ resonance of **23** (δ 77.0) compared to its precursor **21** (δ 105.7) by ~ 29 ppm is similar to the difference between the $\text{N}^\alpha\text{-M}$ and $\text{N}^\beta\text{-M}$ isomers for the analogous Rh complexes **20** ($\text{N}^\alpha\text{-M}$, δ 64.9) to **22** ($\text{N}^\beta\text{-M}$, δ 84.1) and the compounds described by Bourissou *et al.* ($\text{N}^\alpha\text{-B}$ at δ 61, to $\text{N}^\beta\text{-B}$ at δ 35).¹⁶⁴



Scheme 4.6 Thermally or photochemically induced linkage isomerism of complexes **20** and **21**

4.2.2.1 X-ray Crystal Structure of [$\text{Ir}_2\text{P}(\text{N}_3\text{Mes})(\text{NMes})-\kappa^2\text{-N,N}^\beta$] $\text{Ir}(\text{COD})$ (**23**)

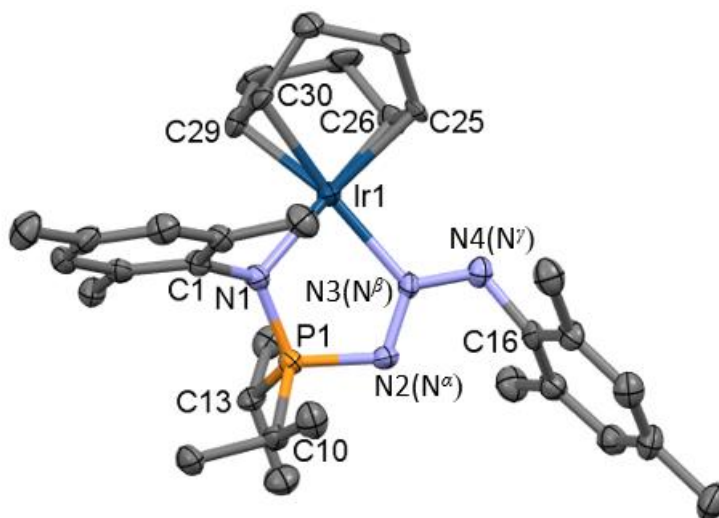


Figure 4.2 X-ray crystal structure of **23** depicted as 50% displacement ellipsoids. Hydrogen atoms are omitted for clarity. Only one of the two independent molecules of **23** in the unit cell is shown

Complexes **22** ($\text{N}^\beta\text{-Rh}$) and **23** ($\text{N}^\beta\text{-Ir}$) are isostructural, exhibiting the same $\kappa^2\text{-N,N}^\beta$ azidophosphonamido coordination mode. The $\text{N}^\beta\text{-M}$ azidophosphonamido ligand bonding mode in **23** increases the N–M–N bite angle to $83.16(17)^\circ$ (Table 4.2) compared

to 69.94(9)° in **21** (Table 3.5). The isomerization expands the metal chelate ring (4 to 5 atoms), thereby relieving strain and improving the square planar geometry about iridium ($\tau_4 = 0.21$ in **23**) compared to $\tau_4 = 0.28$ in **21**. As with **21**, the phosphazide functionality in **23** retains the *transoid* conformation (P–N–N=N = 176.3(4)° and 178.1(4)°); the N=N bond configuration changes from *E* to *Z* upon linkage isomerization (N–N=N–C = 0.4(7)° and 6.1(6)°).

Table 4.2 Selected bond distances (Å) and angles (°) for complex **23**

Atoms	Distance (Å)	Atoms	Angle (°)
Ir–N1	2.079(4)	N1–Ir–N3	83.16(17)
Ir–N3	2.104(4)	C29–Ir–N1	94.52(19)
N1–C1	1.429(6)	C30–Ir–N1	95.42(19)
N4–C16	1.447(7)	C25–Ir–N3	92.8(2)
P–C10	1.828(5)	C26–Ir–N3	95.4(2)
P–C13	1.825(5)	C25–Ir–C30	81.6(2)
Ir–C25	2.102(5)	C26–Ir–C29	81.5(2)
Ir–C26	2.121(5)	N1–P–N2	110.1(3)
Ir–C29	2.120(5)	N2=N3–Ir	119.5(3)
Ir–C30	2.146(5)	P–N1–Ir	108.9(2)
P=N1	1.621(5)	P=N1–C1	125.2(3)
P–N2	1.648(4)	P–N2–N3	111.6(3)
N2–N3	1.355(6)	N2–N3=N4	119.8(4)
N3=N4	1.274(6)	N3=N4–C16	116.7(4)
		C10–P–C13	105.9(3)

Complexes **22**, $[\text{}^i\text{Pr}_2\text{P}(\text{N}_3\text{Mes})(\text{NMes})-\kappa^2\text{-}N,N^\beta]\text{Rh}(\text{COD})$, and **23** $[\text{}^i\text{Pr}_2\text{P}(\text{N}_3\text{Mes})(\text{NMes})-\kappa^2\text{-}N,N^\beta]\text{Ir}(\text{COD})$, are the first transition metal species produced by thermally or photochemically induced phosphazide linkage isomerization. Both **22** and **23** are also the first transition metal complexes crystallographically confirmed to exhibit the $\text{N}^\beta\rightarrow\text{M}$ phosphazide coordination mode, albeit, in 1996, Bertrand *et al.* reported an intermediate Zr complex that purportedly adopted the $\text{N}^\beta\rightarrow\text{M}$ bonding mode; however, the compound in question was not isolated.¹⁶⁶

4.2.3 Lack of Thermally- or Photochemically-Induced Coordinative Isomerism

Given the thermally and photochemically induced linkage isomerism between $\text{N}^\alpha\text{-M}$ and $\text{N}^\beta\text{-M}$ observed in complexes **20**, $[\text{}^i\text{Pr}_2\text{P}(\text{N}_3\text{Mes})(\text{NMes})-\kappa^2\text{-}N,N^\alpha]\text{Rh}(\text{COD})$, and **21** $[\text{}^i\text{Pr}_2\text{P}(\text{N}_3\text{Mes})(\text{NMes})-\kappa^2\text{-}N,N^\alpha]\text{Ir}(\text{COD})$, it seemed apparent to attempt to induce such isomerism in the adamantyl complexes **18**, $[\text{}^i\text{Pr}_2\text{P}(\text{N}_3\text{Ad})(\text{NAd})-\kappa^2\text{-}N,N^\alpha]\text{Rh}(\text{COD})$, and **19** $[\text{}^i\text{Pr}_2\text{P}(\text{N}_3\text{Ad})(\text{NAd})-\kappa^2\text{-}N,N^\alpha]\text{Ir}(\text{COD})$. Efforts to promote linkage isomerization in either **18** or **19** *via* heating the complexes in benzene-*d*₆ at 60 °C for 72 h, or irradiation at 365 nm in benzene-*d*₆ for 72 h, yielded no changes in the $^{31}\text{P}\{^1\text{H}\}$ NMR spectra suggesting these $\kappa^2\text{-}N,N^\alpha$ complexes are both the kinetic and thermodynamic products, similar to the work reported by Slootweg *et al.*¹¹⁶ The Slootweg group found that only the mesityl substituted phosphazide-containing FLP **XX**, $(\text{}^t\text{Bu}_2\text{PN}_3\text{Mes})\text{CH}_2\text{BPh}_2$, forms an initial kinetic product ($\text{N}^\alpha\rightarrow\text{B}$) that undergoes thermally-induced linkage isomerism to the $\text{N}^\beta\rightarrow\text{B}$ borane **XXI** (Scheme 4.3).¹¹⁶ Slootweg also reported a *tert*-butyl substituted phosphazide FLP which remained in the $\text{N}^\alpha\rightarrow\text{B}$ mode, as said conformation is purportedly both the kinetic and thermodynamic product (Scheme 4.5).¹¹⁶ The adamantyl complexes **18** and **19**

mimic the *tert*-butyl substituted borane (**XX**, Scheme 4.3),¹¹⁶ wherein the $N^{\alpha} \rightarrow M$ species initially formed is the thermodynamic product and does not rearrange to another linkage isomer ($N^{\gamma} \rightarrow B$ or $N^{\beta} \rightarrow B$).

4.3 Reaction Chemistry of Rh^I and Ir^I Azidophosphonamido Complexes

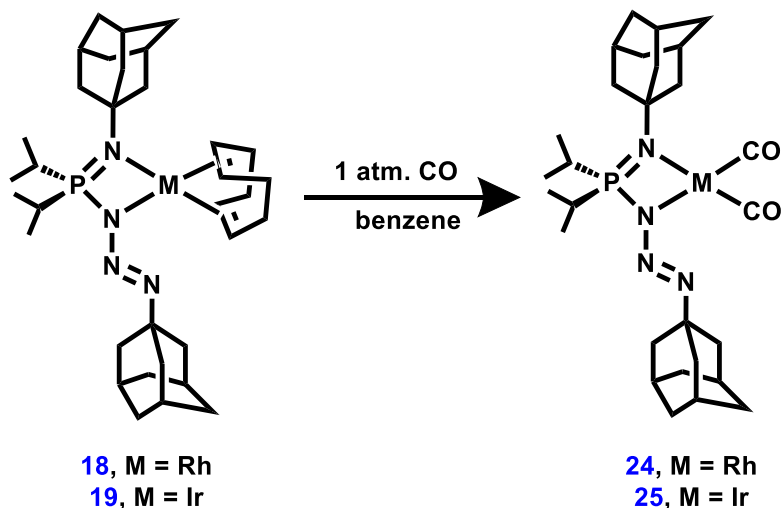
The azidophosphonamide COD complexes **18**, [^{*i*}Pr₂P(N₃Ad)(NAd)- κ^2 -*N,N* ^{α}]Rh(COD)], **19** [^{*i*}Pr₂P(N₃Ad)(NAd)- κ^2 -*N,N* ^{α}]Ir(COD)], **20**, [^{*i*}Pr₂P(N₃Mes)(NMes)- κ^2 -*N,N* ^{α}]Rh(COD)], and **21** [^{*i*}Pr₂P(N₃Mes)(NMes)- κ^2 -*N,N* ^{α}]Ir(COD)], have demonstrated great stability of the phosphazide moiety; however, it was uncertain if stoichiometric reactions of said complexes would promote N₂ loss. Given the ubiquity of Rh and Ir complexes throughout various hydrofunctionalization (E–H) reactions, probing the reactivity of compounds **18–21** towards hydrosilylation and hydrogenation (two types of H–E activation) was of interest.¹⁸

4.3.1 Reactions of [^{*i*}Pr₂P(N₃Ad)(NAd)- κ^2 -*N,N* ^{α}]M(COD)], M = Rh (**18**), Ir (**19**), with CO

Carbon monoxide was chosen as a potent σ -donor, and π -accepting ligand that would readily displace COD in complexes **18–21**, thereby demonstrating that substitution of the COD ligand is possible without N₂ elimination from the azidophosphonamido ligand. The decrease in the IR ν_{CO} stretching frequency of the CO ligand in the resultant azidophosphonamido mono-, di- or tri- carbonyl complexes (^{*i*}Pr₂P(N₃R)(NR)]M(CO)₁₋₃, R = Ad, Mes; M = Rh, Ir) can help gauge the electronic impact that the N-substituents have on the metal centre, otherwise known as the Tolman electronic parameter (TEP). The ν_{CO} for N^{α} –M and N^{β} –M carbonyl complexes could be used to gauge the isomerization impact

via the electron richness of the metal. The TEP, however, is designed for neutral monodentate ligands (L) in the model system, *cis*-[RhCl(CO)₂(L)],⁴⁴ thus it is more appropriate to compare any isolated mono-, di- or tri- carbonyl complexes ([ⁱPr₂P(N₃R)(NR)]M(CO)₁₋₃ to with analogous [LRh(CO)₂] literature complexes featuring other bidentate monoanionic ligands.

Upon exposure to an excess of CO at ambient temperature, the COD ligand in the adamantyl complexes **18**, [ⁱPr₂P(N₃Ad)(NAd)-κ²-N,N^α]Rh(COD)], and **19** [ⁱPr₂P(N₃Ad)(NAd)-κ²-N,N^α]Ir(COD), was readily displaced without rapid N₂ extrusion, affording the carbonyl-containing species **24**, [ⁱPr₂P(N₃Ad)(NAd)-κ²-N,N^α]Rh(CO)₂) and **25**, [ⁱPr₂P(N₃Ad)(NAd)-κ²-N,N^α]Ir(CO)₂ (Scheme 4.7).



Scheme 4.7 Synthesis of [ⁱPr₂P(N₃Ad)(NAd)-κ²-N,N^α]M(CO)₂, M = Rh (**24**), Ir (**25**)

Loss of the COD methine and methylene resonances in the ¹H NMR spectrum of **24** and **25**, and the appearance of two CO signals in the ¹³C{¹H} NMR spectrum (**24** = δ

191.20 and 188.87 ($^1J_{\text{RhC}} = 69.7$ Hz and $^1J_{\text{RhC}} = 70.2$ Hz), and **25** = δ 180.03 and 175.71), corroborate the displacement of COD by CO. The $^{31}\text{P}\{^1\text{H}\}$ NMR resonance of the rhodium carbonyl complex **24** (δ 99.7) is largely shifted downfield from the Rh–COD precursor **18** (δ 24.5). In contrast, the Ir-carbonyl species **25** (δ 108.1) is minimally shifted upfield from the Ir–COD analogue **19** (δ 111.0), suggesting that **25** may have lost N_2 to generate a more-upfield, phosphinimine-analogue $[\text{Ir}_2\text{P}(\text{NAd})_2]\text{Ir}(\text{COD})$. However, the solid-state structure of both complexes **24** (Figure 4.3) and **25** (Figure 4.4) confirm retention of the phosphazide functionality and the $\kappa^2\text{-N,N}'$ coordination mode of the azidophosponamido ligand. Thus, it is unknown why the $^{31}\text{P}\{^1\text{H}\}$ NMR signals for the Ir-carbonyl complex **25** (δ 108.1) is shifted upfield relative to **19** (δ 111.0). The carbonyl species **24** and **25** are also highly robust, showing no signs of N_2 extrusion or linkage isomerism when heated (60 °C in benzene- d_6 or 100 °C in toluene- d_8 for 1 week) or upon irradiation with UV light ($\lambda = 365$ nm in benzene- d_6) for 1 week.

4.3.1.1 X-ray Crystal structure of $[\text{Ir}_2\text{P}(\text{N}_3\text{Ad})(\text{NAd})\text{-}\kappa^2\text{-N,N}^\alpha]\text{Rh}(\text{CO})_2$ (**24**)

The adamantyl carbonyl complexes **24** and **25** readily crystallized from saturated pentane solutions to afford yellow plates.

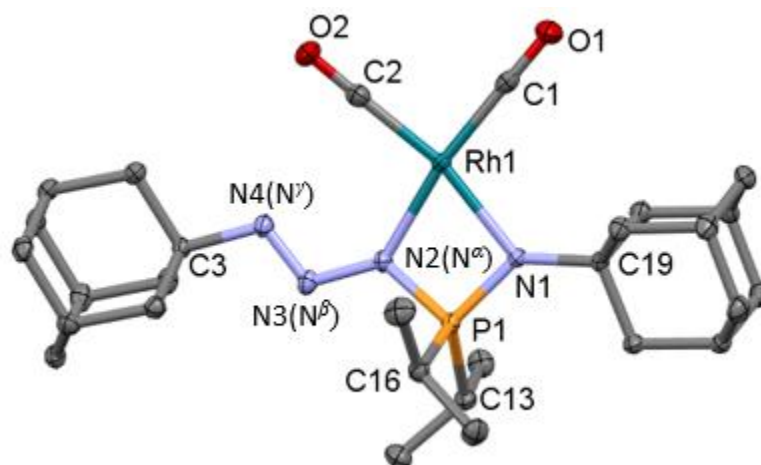


Figure 4.3 X-ray crystal structure of **24** depicted as 50% displacement ellipsoids. Hydrogen atoms are omitted for clarity

Complex **24** retains the κ^2-N,N^α binding of the azidophosponamide ligand with minimal distortion from square planar geometry ($\tau_4 = 0.14$). The phosphazide P–N–N=N torsion angle of $168.8(2)^\circ$ indicates retention of the *transoid*-conformation. Two distinctly different P–N bond distances, where the P–N $^\alpha$ bond ($1.633(18) \text{ \AA}$) is the longer of the two (N1=P of $1.6515(18) \text{ \AA}$, Table 4.3), suggesting localization of the ligand's anionic charge on N $^\alpha$.

Table 4.3 Selected bond distances (Å) and angles (°) for compound **24**

Atoms	Distance (Å)	Atoms	Angle (°)
Rh–N1	2.1067(17)	N1–Rh–N2	70.02(7)
Rh–N2	2.0456(18)	C1–Rh–N1	101.77(8)
N1–C19	1.470(3)	C2–Rh–N2	98.46(9)
N4–C3	1.491(3)	C1–Rh–C2	89.94(10)
P–C13	1.825(2)	C13–P–C16	106.31(10)
P–C16	1.824(2)	N1=P–N2	93.73(9)
Rh–C1	1.850(2)	P=N1–C19	132.91(15)
Rh–C2	1.863(2)	P–N2–N3	121.81(14)
C1=O1	1.147(3)	N2–N3=N4	112.46(18)
C2=O2	1.140(3)	N3=N4–C3	113.14(18)
P–N1	1.6133(18)		
P–N2	1.6516(18)		
N2–N3	1.366(3)		
N3=N4	1.248(3)		

4.3.2 X-ray Crystal structure of [ⁱPr₂P(N₃Ad)(NAd)-κ²-N,N^α]Ir(CO)₂ (**25**)

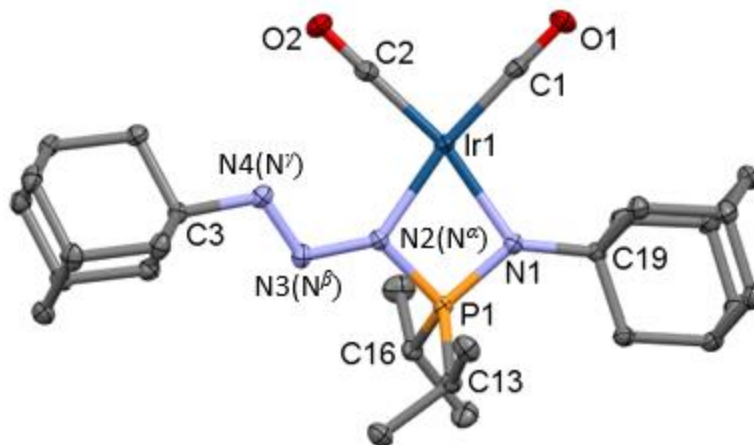


Figure 4.4 X-ray crystal structure of **25** depicted as 50% displacement ellipsoids. Hydrogen atoms are omitted for clarity

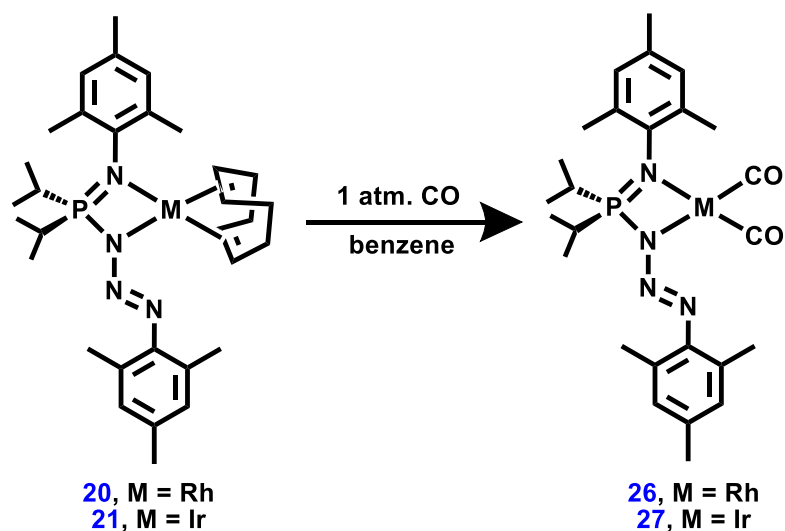
Like **24**, the solid-state structure of **25** also confirms retention of the κ^2 -N,N^α azidophosphonamido binding mode and ($\tau_4 = 0.14$), and the *transoid* phosphazide conformation (P–N–N=N = 170.5(1)°). The short carbonyl bond distances (1.149(3) and 1.144(3) Å) are diagnostic for a triple bond C≡O, while the two different P=N and P–N^α bond lengths (1.6515(18) and 1.6220(18) Å, respectively), echo that observed in all of the κ^2 -N,N^α azidophosphonamide structures reported thus far. Overall, the bond distances and angles do not vary substantially between **25** (Table 4.4) and the Rh analogue **24**, [ⁱPr₂P(N₃Ad)(NAd)-κ²-N,N^α]Rh(CO)₂ (Table 4.3).

Table 4.4 Selected bond distances (Å) and angles (°) for compound **25**

Atoms	Distance (Å)	Atoms	Angle (°)
Ir–N1	2.1047(17)	N1–Ir–N2	69.51(7)
Ir–N2	2.0529(17)	C1–Ir–N1	101.79(8)
N1–C19	1.468(3)	C2–Ir–N2	99.01(8)
N4–C3	1.498(3)	C1–Rh–C2	89.83(9)
P–C13	1.822(2)	C13–P–C16	106.72(9)
P–C16	1.817(2)	N1=P–N2	92.81(9)
Ir–C1	1.848(2)	P=N1–C19	132.57(14)
Ir–C2	1.859(2)	P–N2–N3	121.74(14)
C1=O1	1.149(3)	N2–N3=N4	112.06(17)
C2=O2	1.144(3)	N3=N4–C3	113.11(17)
P–N1	1.6220(18)		
P–N2	1.6512(17)		
N2–N3	1.371(2)		
N3=N4	1.251(2)		

4.3.3 Reactions of [*i*Pr₂P(N₃Mes)(NMe_s)-κ²-N,N^α]M(COD)], M = Rh (**20**), Ir (**21**), with CO

The mesityl-substituted complexes **26**, [*i*Pr₂P(N₃Mes)(NMe_s)-κ²-N,N^α]Rh(CO)₂, and **27**, [*i*Pr₂P(N₃Mes)(NMe_s)-κ²-N,N^α]Ir(CO)₂, were generated *via* the addition of CO (1 atm.) to a J. Young NMR tube containing the appropriate COD precursor (**20** or **21**), (Scheme 4.8).



Scheme 4.8 Synthesis of $[^i\text{Pr}_2\text{P}(\text{N}_3\text{Mes})(\text{NMes})-\kappa^2-N,N^\alpha]\text{M}(\text{CO})_2$, M = Rh (**26**), Ir (**27**)

The rhodium complex **26** formed quantitatively in 5 minutes, while the iridium complex **27** required 20 minutes for complete conversion. The $^{31}\text{P}\{^1\text{H}\}$ NMR signals attributed to carbonyl complexes **26** (δ 95.2) and **27** (δ 104.1) are shifted slightly from their precursors **20** (δ 84.1) and **21** (δ 105.7). In both the ^1H and $^{13}\text{C}\{^1\text{H}\}$ NMR spectra of **26** and **27**, two separate sets of mesityl resonances were observed. Attempts at crystallizing **26** and **27** to obtain a solid-state structure to confirm preservation of the phosphazide moiety have proven unsuccessful. Elemental analysis was instead utilized to support that **26** and **27** indeed contain the phosphazide group, as N% found in both species **26** (9.06% and **27** (7.82%) closely matched the calculated N% values **26** \rightarrow 8.83% and **27** \rightarrow 7.74% (c.f. $[^i\text{Pr}_2\text{P}(\text{NMes})_2-\kappa^2-N,N^\alpha]\text{M}(\text{CO})_2$, where M = Rh \rightarrow 4.62%) and M = Ir \rightarrow 4.03%). Whether or not **26** and **27** adopt $\text{N}^\alpha\text{-M}$ coordination (as depicted in Scheme 4.8) or an alternate bonding mode (e.g. $\text{N}^\beta\text{-M}$ or $\text{N}^\gamma\text{-M}$) has not been determined.

The disappearance of the COD resonances in both the ^1H and $^{13}\text{C}\{^1\text{H}\}$ NMR spectra of **26** [$^i\text{Pr}_2\text{P}(\text{N}_3\text{Mes})(\text{NMes})-\kappa^2\text{-N,N}^\alpha$] $\text{Rh}(\text{CO})_2$, and **27**, [$^i\text{Pr}_2\text{P}(\text{N}_3\text{Mes})(\text{NMes})-\kappa^2\text{-N,N}^\alpha$] $\text{Ir}(\text{CO})_2$, indicate loss of the COD ligand. In addition, the CO signals observed in the $^{13}\text{C}\{^1\text{H}\}$ NMR spectrum of **26** (δ 188.48 and 188.34) exhibit diagnostic coupling to ^{103}Rh ($^1J_{\text{RhC}} = 69.5$ and 70.7 Hz). The $\text{C}\equiv\text{O}$ resonances from **27** (δ 177.22 and 175.06), as expected, are singlets.

The linkage isomers $\text{N}^\beta\text{-M}$ **22** [$^i\text{Pr}_2\text{P}(\text{N}_3\text{Mes})(\text{NMes})-\kappa^2\text{-N,N}^\beta$] $\text{Rh}(\text{COD})$ and **23** [$^i\text{Pr}_2\text{P}(\text{N}_3\text{Mes})(\text{NMes})-\kappa^2\text{-N,N}^\beta$] $\text{Ir}(\text{COD})$ are unreactive towards CO both at ambient and elevated temperatures (60°C) in benzene- d_6 . Complexes **26** and **27** are also highly robust, showing no signs of N_2 extrusion or linkage isomerism in solution (benzene- d_6) when heated to 60°C or irradiated at 365 nm.

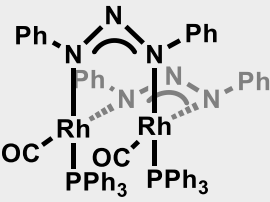
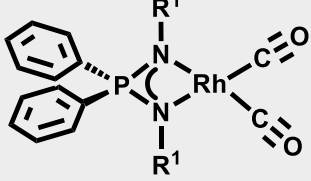
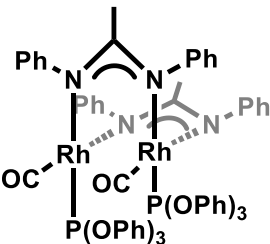
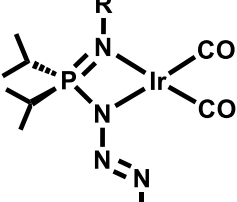
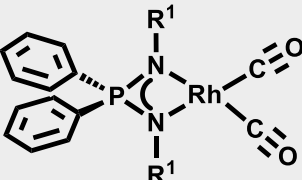
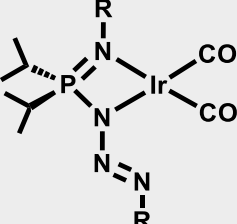
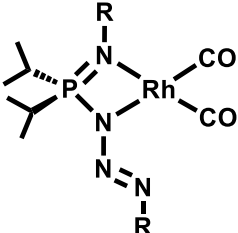
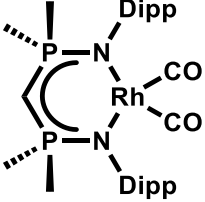
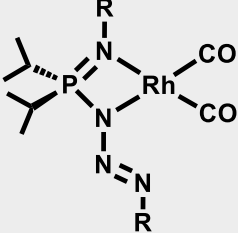
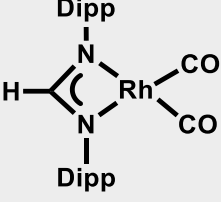
4.3.4 Comparison of Carbonyl-Azidophosphonamido complexes (24-27)

All four carbonyl complexes **24**, [$^i\text{Pr}_2\text{P}(\text{N}_3\text{Ad})(\text{NAd})-\kappa^2\text{-N,N}^\alpha$] $\text{Rh}(\text{CO})_2$, **25** [$^i\text{Pr}_2\text{P}(\text{N}_3\text{Ad})(\text{NAd})-\kappa^2\text{-N,N}^\alpha$] $\text{Ir}(\text{CO})_2$, **26** [$^i\text{Pr}_2\text{P}(\text{N}_3\text{Mes})(\text{NMes})-\kappa^2\text{-N,N}^\alpha$] $\text{Rh}(\text{CO})_2$, and **27** [$^i\text{Pr}_2\text{P}(\text{N}_3\text{Mes})(\text{NMes})-\kappa^2\text{-N,N}^\alpha$] $\text{Ir}(\text{CO})_2$, exhibit two ν_{CO} stretches in their respective IR spectra (Table 4.5). In 2003, Crabtree *et al.* first employed the model iridium complex to measure the TEP of NHC ligands. They proposed an interconversion equation between Ir^{I} and Rh^{I} values: $\text{TEP}_{\text{Rh}} = 0.8475[\nu_{\text{av}}(\text{Ir})] + 336.2 \text{ cm}^{-1}$.¹⁴⁸ Thus, the TEP_{Ir} values for **25** [$^i\text{Pr}_2\text{P}(\text{N}_3\text{Ad})(\text{NAd})-\kappa^2\text{-N,N}^\alpha$] $\text{Ir}(\text{CO})_2$, and **27** [$^i\text{Pr}_2\text{P}(\text{N}_3\text{Mes})(\text{NMes})-\kappa^2\text{-N,N}^\alpha$] $\text{Ir}(\text{CO})_2$ have been converted into TEP_{Rh} values and are listed in Table 2.6. There is some discrepancy between the measured TEP_{Rh} value for the rhodium species **24** (2012 cm^{-1}) and **26** (2021 cm^{-1}) compared to the calculated TEP_{Rh} values for the iridium complexes **25**

(2028 cm⁻¹) and **27** (2028 cm⁻¹), suggesting that the TEP_{Ir} to TEP_{Rh} conversion provided by Crabtree, originally intended for neutral monodentate ligands, is not applicable to monoanionic bidentate ligands.

Comparing the TEP of like structures would give the best indicator of the ligand's electronic influence, yet there is a lack of analogous azidophosphonamide-carbonyl complexes in the literature. Instead, several known rhodium dicarbonyl compounds are supported by bidentate monoanionic ligands, namely bridging diaryltriazenido (Table 4.5, 1st row, left),¹⁴² including bridging amidinate (Table 4.5, 2nd row, left) ligands,¹⁴³ which have reported TEP values for comparison. There are also a few calculated TEP values for ligands similar to azidophosphonamides [R₂P(NR¹)(N₃R¹)], such as bis(phosphinimine)methanides (Table 4.5, 4th row, right) and a single amidinate ligand (Table 4.5, 5th row, right).¹⁴⁴ Most relevant are the Rh dicarbonyl iminophosphonamido complexes reported in chapter 3; **5**, [Ph₂P(NMes)₂]Rh(CO)₂ (Table 4.5, 1st row, right), and **6**, [Ph₂P(NAd)₂]Rh(CO)₂ (Table 4.5, 3rd row, left); as the impact of the phosphazide group on the electronic richness of the metal center can be gauged by the difference in TEP between **5-6** and **24-27**.

Table 4.5 TEP_{Rh} values (cm^{-1}) for known $\kappa^2\text{-}N,N'$ monoanionic complexes and complexes **5**, **6**, and **24-27**

Complex	TEP (cm^{-1})	Complex	TEP (cm^{-1})
	1973 ¹⁴²		2025
5 R = Mes			
	1993 ¹⁴³		2028 (TEP_{Ir} 1996)
25 , R = Ad			
	1995		2028 (TEP_{Ir} 1996)
6 R = Ad		27 , R = Mes	
	2012		*2097 ¹⁴⁴
24 , R = Ad			
	2021		*2109 ¹⁴⁴
26 , R = Mes			

* Indicates calculated CO stretching frequencies of L bound to a $\text{Rh}(\text{CO})_2$ fragment at the b3-lyp/def-TZVP level of theory¹⁴⁴

The adamantyl-substituted azidophosphonamido complex **24**, [$^i\text{Pr}_2\text{P}(\text{N}_3\text{Ad})(\text{NAd})-\kappa^2\text{-N,N}^\alpha$] $\text{Rh}(\text{CO})_2$, exhibits a TEP value (2012 cm^{-1}) 17 cm^{-1} higher than the iminophosphonamide Rh complex **6** ($[\text{Ph}_2\text{P}(\text{NAd})_2]\text{Rh}(\text{CO})_2$, TEP = 1995 cm^{-1}). A higher TEP value exhibited by **24** suggests that the azidophosphonamide ligand ($^i\text{Pr}_2\text{P}(\text{N}_3\text{Ad})(\text{NAd})-\kappa^2\text{-N,N}^\alpha$) is less electron-donating than the iminophosphonamide analogue ($\text{Ph}_2\text{P}(\text{NAd})_2$). The mesityl-substituted azidophosphonamido species **26**, [$^i\text{Pr}_2\text{P}(\text{N}_3\text{Mes})(\text{NMes})-\kappa^2\text{-N,N}^\alpha$] $\text{Rh}(\text{CO})_2$ displays a TEP value (2021 cm^{-1}) similar to the phosphinimine-containing **5** ($[\text{Ph}_2\text{P}(\text{NMes})_2]\text{Rh}(\text{CO})_2$, TEP = 2025 cm^{-1}); thereby, indicating that the mesityl-substituted azidophosphonamide and iminophosphonamide ligands have similar donor properties. Direct comparison of the rhodium mesityl **24** (2012 cm^{-1}) and adamantyl **26** (2021 cm^{-1}) substituted complexes demonstrates the minimal impact (9 cm^{-1}) the nitrogen substituents have on the overall donor capacity of the ligand. Similarly, the adamantyl iminophosphonamide ligand in complex **6**, $[\text{Ph}_2\text{P}(\text{NAd})_2]\text{Rh}(\text{CO})_2$, in section 2.4.1 was found to be more-electron donating (TEP = 1995 cm^{-1}) than its mesityl analogue **5** $[\text{Ph}_2\text{P}(\text{NMes})_2]\text{Rh}(\text{CO})_2$, 2025 cm^{-1}) as evidenced by lower ν_{CO} stretching frequencies of 30 cm^{-1} .

Notably, using an azidophosphonamide ligand, in the Ir species **25** and **27** aids in the stabilization of an iridium carbonyl species, as attempts to generate an iminophosphonamide iridium dicarbonyl complex in section 2.6.1 were unsuccessful. Complexes **25** [$^i\text{Pr}_2\text{P}(\text{N}_3\text{Ad})(\text{NAd})-\kappa^2\text{-N,N}^\alpha$] $\text{Ir}(\text{CO})_2$, and **27** [$^i\text{Pr}_2\text{P}(\text{N}_3\text{Mes})(\text{NMes})-\kappa^2\text{-N,N}^\alpha$] $\text{Ir}(\text{CO})_2$, exhibit the same TEP_{Ir} value (1996 cm^{-1}), and consequently the TEP_{Rh} value (2028 cm^{-1}); as calculated using the formula proposed by Crabtree *et al.* (TEP_{Rh} =

$0.8475[\nu_{\text{av}}(\text{Ir})] + 336.2 \text{ cm}^{-1}$).¹⁴⁸ The caveat of TEP_{Ir} to TEP_{Rh} interconversion, as it provides additional mathematical uncertainties,¹⁴⁸ is exhibited through the discrepancies in the calculated TEP_{Rh} values of **25** (2028 cm^{-1}) and **27** (2028 cm^{-1}), compared to the measured TEP_{Rh} values of **24** (2012 cm^{-1}) and **26** (2021 cm^{-1}). However, a more accurate explanation is that conversion provided by Crabtree was originally intended for neutral monodentate ligands and therefore is not applicable to monoanionic bidentate ligands.

4.3.5 Reactivity of Rh^{I} and Ir^{I} Azidophosphonamido Complexes Toward Small Molecules

The catalytic processes of hydrosilylation and hydrogenation of alkenes are mechanistically similar and commercially relevant, as they produce valuable silanes and alkanes, both of which are important in organic synthesis. Given the prevalence of group 9 species as hydrogenation¹⁶⁷ and hydrosilylation catalysts,¹⁴⁵ the ability of the described Rh^{I} and Ir^{I} azidophosphonamido complexes **18**, [$^i\text{Pr}_2\text{P}(\text{N}_3\text{Ad})(\text{NAd})-\kappa^2\text{-N},\text{N}^\alpha$] $\text{Rh}(\text{COD})$, **19** [$^i\text{Pr}_2\text{P}(\text{N}_3\text{Ad})(\text{NAd})-\kappa^2\text{-N},\text{N}^\alpha$] $\text{Ir}(\text{COD})$, **20** [$^i\text{Pr}_2\text{P}(\text{N}_3\text{Mes})(\text{NMes})-\kappa^2\text{-N},\text{N}^\alpha$] $\text{Rh}(\text{COD})$, **21** [$^i\text{Pr}_2\text{P}(\text{N}_3\text{Mes})(\text{NMes})-\kappa^2\text{-N},\text{N}^\alpha$] $\text{Ir}(\text{COD})$, **22** [$^i\text{Pr}_2\text{P}(\text{N}_3\text{Mes})(\text{NMes})-\kappa^2\text{-N},\text{N}^\beta$] $\text{Rh}(\text{COD})$, and **23** [$^i\text{Pr}_2\text{P}(\text{N}_3\text{Mes})(\text{NMes})-\kappa^2\text{-N},\text{N}^\beta$] $\text{Ir}(\text{COD})$, to mediate hydrosilylation and hydrogenation was probed.

4.3.5.1 Reactions of Rh^{I} and Ir^{I} Azidophosphonamido COD Complexes with Silanes

One stoichiometric equivalent of the described complex, **18–23**, was reacted with one equivalent of a silane (*e.g.* H_3SiPh , H_2SiPh_2 , and HSiEt_3) in benzene- d_6 in an attempt to isolate a silyl complex [$^i\text{Pr}_2\text{P}(\text{N}_3\text{R})(\text{NR})$] $\text{M}(\text{H})(\text{SiR}_3)$ (an intermediate of most

hydrosilylation processes). No reactions were observed at ambient temperature, and systematic variation of reaction conditions, namely elevated temperatures (to 70 °C), and different solvents (benzene, THF-*d*₈), yielded similar results. Catalytic scoping reactions, wherein an equivalent of the COD complexes **18-23** was added to a vessel containing 10 equivalents of primary silane (H₃SiPh) and 10 equivalents of 2-butyne, also afforded no reaction.

4.3.5.2 Reactions of Rh^I and Ir^I Azidophosphonamido COD Complexes with H₂

In an attempt to generate dihydride species [ⁱPr₂P(N₃R)(NR)]M(H)₂ (an intermediate in catalytic hydrogenation), the complexes **18-23** were introduced to an atmosphere of H₂ in an NMR tube equipped with a J-Young valve. No reaction was observed at ambient temperature in aromatic solvent (benzene-*d*₆). Elevating the temperature of the reaction to 70 °C or replacing benzene-*d*₆ with the more polar solvent THF-*d*₈ elicited no change. Similarly, adding 10 equivalents of 2-butyne to the J-Young NMR tube prior to exposure of an atmosphere of H₂ afforded no reaction.

4.3.5.3 Reactions of Rh^I and Ir^I Azidophosphonamido CO Complexes with Small Molecules

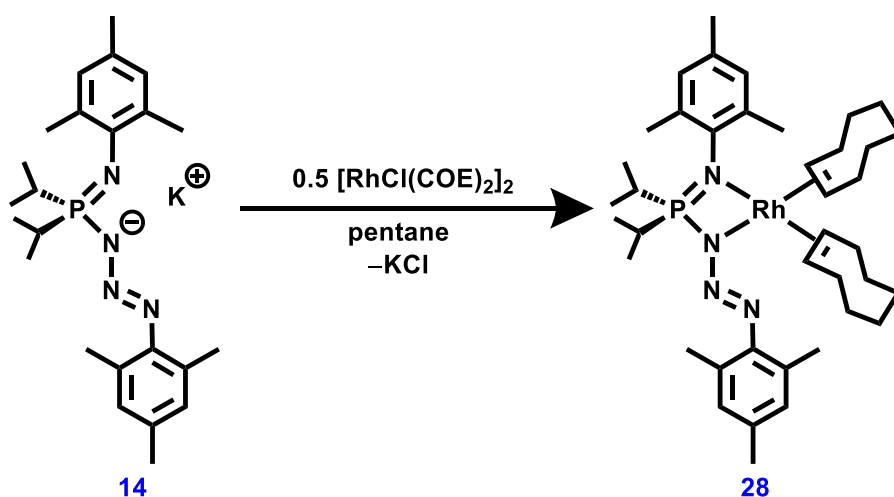
Unsurprisingly, the carbonyl complexes **24**, [ⁱPr₂P(N₃Ad)(NAd)-κ²-*N,N*^α]Rh(CO)₂, **25** [ⁱPr₂P(N₃Ad)(NAd)-κ²-*N,N*^α]Ir(CO)₂, **26** [ⁱPr₂P(N₃Mes)(NMes)-κ²-*N,N*^α]Rh(CO)₂, and **27** [ⁱPr₂P(N₃Mes)(NMes)-κ²-*N,N*^α]Ir(CO)₂ were also unreactive towards H₂ and silanes (H₃SiPh, H₂SiPh₂, and HSiEt₃) in benzene-*d*₆. Presumably, dissociation of either a CO or

COD ligand is a high-energy process. Irradiation ($\lambda = 365$ nm) of the aforementioned dicarbonyl and COD complexes in the presence of silanes or H_2 at 365 nm for 1 week did not afford any changes.

4.4 Towards a More Reactive Azidophosphonamido Rh^{I} Complex

4.4.1 Substituting COD with COE

The azidophosphonamide COD complexes **18-23** are limited in terms of their reactivity, as they appear to be inert to substitution. Accordingly, it was decided to target species that contain two cyclooctene (COE) ligands instead of the chelating COD, which was anticipated to render the resultant complexes more reactive. Substitution of $[\text{RhCl}(\text{COD})]_2$ by the COE dimer $[\text{RhCl}(\text{COE}_2)]_2$, in the salt-metathesis reaction with **14**, $\text{K}[\text{iPr}_2\text{P}(\text{N}_3\text{Mes})(\text{NMes})]$, generated the corresponding Rh^{I} COE complex **28**, $[\text{iPr}_2\text{P}(\text{N}_3\text{Mes})(\text{NMes})]\text{Rh}(\text{COE})_2$ (Scheme 4.9).



Scheme 4.9 Synthesis of $[\text{iPr}_2\text{P}(\text{N}_3\text{Mes})(\text{NMes})]\text{Rh}(\text{COE})_2$ **28**

4.4.1.1 X-ray Crystal Structure of $[\text{Pr}_2\text{P}(\text{N}_3\text{Ad})(\text{NAd})-\kappa^2\text{-N,N}^\alpha]\text{Rh}(\text{COE})_2$, (**28**)

Crystals of **28** were grown from a pentane solution of $[\text{RhCl}(\text{COE}_2)_2]$ and **14**, $\text{K}[\text{Pr}_2\text{P}(\text{N}_3\text{Mes})(\text{NMes})]$, stored at $-35\text{ }^\circ\text{C}$ for 4 days. The identity of **28** was confirmed via X-ray diffraction experiments.

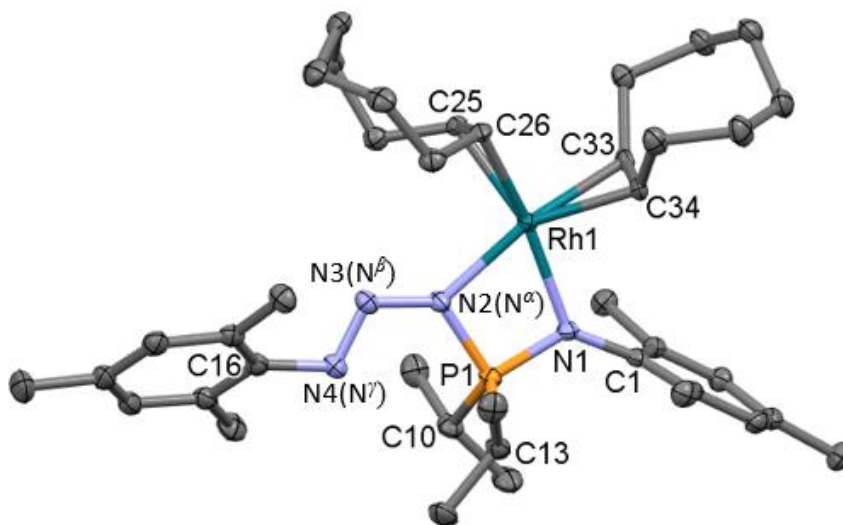


Figure 4.5 X-ray crystal structure of **28** depicted as 50% displacement ellipsoids. Hydrogen atoms are omitted for clarity

Intriguingly, the phosphazide functionality assumes a *cisoid* conformation, $\text{P-N-N}=\text{N} = 3.0(2)^\circ$. Complex **28** is the first azidophosponamide species to adopt the less stable conformation in the solid state, suggesting this species may be more susceptible to N_2 extrusion. The $\text{N}=\text{N}$ bond is a nearly ideal *E* configuration, with an N2-N3=N4-C16 torsion angle of $179.3(1)^\circ$, to position the steric bulk of the mesityl substituent far from the isopropyl groups on P. As with the other azidophosponamido complexes, the P-N bonds show distinct localization ($1.6736(16)$ and $1.6167(16)$ Å). Additional bond lengths and

angles in **28** (Table 4.6) are largely unchanged compared with the analogous COD complex **20**, [ⁱPr₂P(N₃Mes)(NMe_s)]Rh(COD) (Table 3.4).

Table 4.6 Selected bond distances (Å) and angles (°) for compound **28**

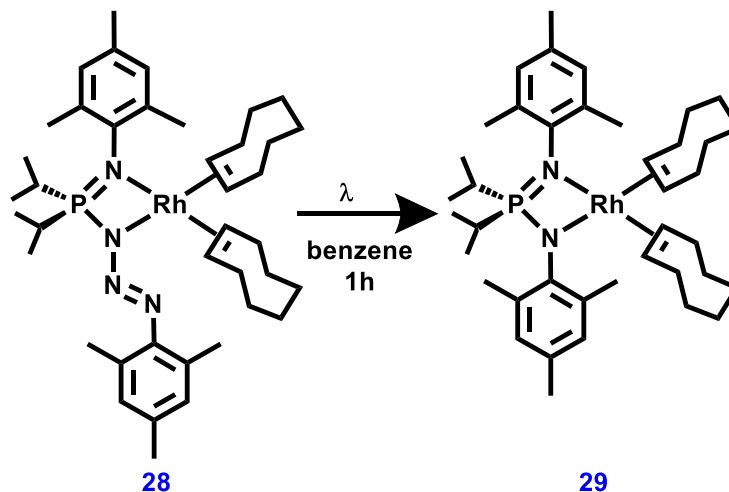
Atoms	Distance (Å)	Atoms	Angle (°)
Rh–N1	2.1142(15)	N1–Rh–N2	69.94(6)
Rh–N2	2.0921(15)	C33–Rh–N1	96.37(6)
N1–C1	1.428(2)	C34–Rh–N1	90.38(7)
N4–C16	1.437(2)	C25–Rh–N2	96.50(7)
P–C10	1.8272(19)	C26–Rh–N2	100.42(7)
P–C13	1.838(2)	C25–Rh–C33	90.67(7)
Rh–C25	2.1342(18)	C26–Rh–C34	91.47(7)
Rh–C26	2.1317(17)	C10–P–C13	106.60(9)
Rh–C33	2.1753(18)	N1=P–N2	94.22(8)
Rh–C34	2.1344(18)	P=N1–C1	127.85(12)
P–N1	1.6167(16)	P–N2–N3	125.01(12)
P–N2	1.6736(16)	N2–N3=N4	114.87(15)
N2–N3	1.338(2)	N3=N4–C16	112.80(15)
N3=N4	1.275(2)		

The crystals of **28** were found to be stable under reduced pressure for short periods (e.g., 5 minutes). However, decomposition in solution occurs at ambient temperature to give another product that gives rise to a ³¹P{¹H} NMR signal at 64.0. This new compound is suspected to be the iminophosphonamide species [ⁱPr₂P(NMe_s)₂]Rh(COE)₂, wherein N₂

extrusion from the phosphazide functionality has occurred. Alternatively, perhaps linkage isomerization to an N^β -M or N^γ -M conformation occurs. Similarly to most of the azidophosphonamide species reported thus far, the $^{31}\text{P}\{^1\text{H}\}$ resonance is quite downfield, (δ 99.55, br s) (c.f. **20**, [$^i\text{Pr}_2\text{P}(\text{N}_3\text{Mes})(\text{NMes})$] $\text{Rh}(\text{COD})$, δ 84.1). In both the ^1H and $^{13}\text{C}\{^1\text{H}\}$ NMR spectra of **28**, two sets of COE resonances were observed, as the two ligands are not chemically equivalent. The two sets of methine and methylene COE signals (δ 3.28, 2.97 and 1.64, 1.09) were found far from free COE, suggesting both COE ligands are coordinated to the metal in solution; however, a small amount of free COE is observed and attributed to the slow degradation of **28** in solution. The azidophosphonamide likely exhibits the κ^2 - N,N^α binding mode in solution, as no evidence for κ^3 - N,N^α,N' coordination (such as a broad $^{31}\text{P}\{^1\text{H}\}$ resonance) was observed in solution.

In an attempt to quantitatively convert complex **28** into the unknown compound that resonates at δ 64.0 in the $^{31}\text{P}\{^1\text{H}\}$ spectrum, a benzene- d_6 solution of **28** was heated to 70 °C. Under these conditions, 18% conversion to a product that resonates at δ 64.0 in its $^{31}\text{P}\{^1\text{H}\}$ NMR spectrum was observed after 16 h. Upon irradiating a separate solution of **28** at 365 nm for 1 h, complete loss of the $^{31}\text{P}\{^1\text{H}\}$ NMR resonance attributed to **28** was observed. During this period, several new signals appeared at δ 64.0 (s, 29%), 61.1 (s, 28%), 51.7 (s, 26%), and 11.8 (s, 16%); the percent conversions are relative to each other (a total of 100%). Yellow/orange plates of **29** [$^i\text{Pr}_2\text{P}(\text{NMes})_2$] $\text{Rh}(\text{COE})_2$ (δ 64.0) grew from this mixture over one week at ambient temperature. X-ray diffraction experiments confirmed the identity of **29** as the iminophosphonamide species [$^i\text{Pr}_2\text{P}(\text{NMes})_2$] $\text{Rh}(\text{COE})_2$

(Scheme 4.10). The identity of the other products in the $^{31}\text{P}\{^1\text{H}\}$ NMR spectrum (δ 61.1, 51.7, and 11.8) has not been established.



Scheme 4.10 Synthesis of $[\text{Pr}_2\text{P}(\text{NMe}_s)_2]\text{Rh}(\text{COE})_2$ **29**

4.4.1.2 X-ray Crystal Structure of $(\text{Ph}_2\text{P}(\text{NAd})_2)\text{Rh}(\text{COE})_2$, (**29**)

Complex **29**, $[\text{Pr}_2\text{P}(\text{NMe}_s)_2]\text{Rh}(\text{COE})_2$, crystallizes in the tetragonal space group $I4_1/a$, as one independent molecule contained within the unit cell (Figure 4.6). The P–N distances in **29**, $[\text{Pr}_2\text{P}(\text{NMe}_s)_2]\text{Rh}(\text{COE})_2$, are different compared to the Rh azidophosphonamide precursor **28**, $[\text{Pr}_2\text{P}(\text{N}_3\text{Me}_s)(\text{NMe}_s)]\text{Rh}(\text{COE})_2$. Specifically, both the P–N lengths in **29** are similar (1.615(3) and 1.624(3) Å), indicating delocalization within the iminophosphonamide ligand, echoing the iminophosphonamido Rh and Ir complexes reported through chapter 2. Key bond angles and distances observed in **29** (Table 4.7) are similar to those in **28** (Table 4.6), such as the N–M–N bond angles, $70.36(11)^\circ$ (**29**), and $69.94(6)^\circ$ (**28**), and square planar geometric distortion, $\tau_4 = 0.26$ (**29**),

and $\tau_4 = 0.25$ for **(28)**, suggesting that loss of N_2 does not dramatically affect geometry at the metal centre.

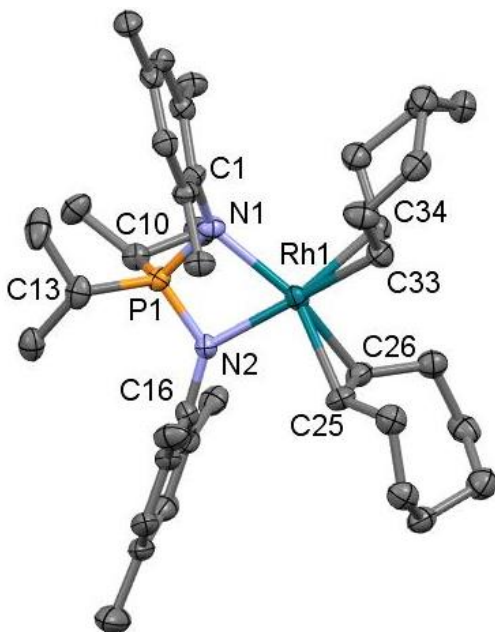


Figure 4.6 X-ray crystal structure of **29** depicted as 50% displacement ellipsoids. Hydrogen atoms are omitted for clarity

Table 4.7 Selected bond distances (Å) and angles (°) for compound **29**

Atoms	Distance (Å)	Atoms	Angle (°)
Rh–N1	2.106(3)	N1–Rh–N2	70.36(11)
Rh–N2	2.193(3)	C33–Rh–N1	106.06(14)
N1–C1	1.426(5)	C34–Rh–N1	99.40(14)
N2–C16	1.406(5)	C25–Rh–N2	87.35(14)
P–C10	1.841(4)	C26–Rh–N2	91.64(14)
P–C13	1.844(4)	C25–Rh–C33	90.65(17)
P–N1	1.615(3)	C26–Rh–C34	89.36(16)
P–N2	1.624(3)	N1=P–N2	99.83(16)
Rh–C25	2.164(4)	C10–P–C13	106.70(18)
Rh–C26	2.199(4)	P–N1–C1	125.3(3)
Rh–C33	2.151(4)	P–N2–C16	128.7(2)
Rh–C34	2.138(4)		

The crystals of **29** were found to be unstable under vacuum; thus, argon was blown over the crystals to remove any volatiles such as pentane. $^{31}\text{P}\{^1\text{H}\}$ NMR spectroscopy confirmed the identity of the crystals as the resonance previously observed at δ 64.0. Despite the flowing argon, the sample contained a large quantity of pentane, rendering it impossible to identify the resonances correlating to **29** in the ^1H NMR spectrum. $^{31}\text{P}\{^1\text{H}\}$ NMR spectroscopy was used to monitor the decomposition of **29** to a resonance observed at δ 11.8, tentatively attributed to the neutral iminophosphonamide ligand $^i\text{Pr}_2\text{P}(\text{NMes})(\text{NHMe})$, as the chemical shift is similar to the decomposition product

(Ph₂P(NMes)(NHMes), ³¹P{¹H} δ 15.4) observed from **13**, [Ph₂P(NMes)₂]Rh(COE)₂ (³¹P{¹H} δ 27.5).

4.4.2 Synthetic Challenges that Arise from COE Groups

Replacement of the COD ligand by two COE moieties generated complex **28**, [ⁱPr₂P(N₃Mes)(NMes)]Rh(COE)₂, which was less stable in solution compared to its COD analogue **13**, [ⁱPr₂P(N₃Mes)(NMes)]Rh(COD), as **28** slowly eliminates N₂ at ambient temperature, (a process that is expedited by UV irradiation) to form the iminophosphonamide COE complex **29**, [ⁱPr₂P(NMes)₂]Rh(COE)₂. Complex **29** itself decomposes in solution, presumably releasing neutral ligand ⁱPr₂P(NMes)(NHMes), which makes isolation of the compound difficult. Due to time constraints, scoping of the reactivity of complexes **28** and **29** was not undertaken.

4.5 Concluding Remarks

The mesityl-substituted azidophosphonamido complexes **20**, [ⁱPr₂P(N₃Mes)(NMes)-κ²-N,N^α]Rh(COD), and **21**, [ⁱPr₂P(N₃Mes)(NMes)-κ²-N,N^α]Ir(COD), are the first transition metal complexes to undergo thermally or photochemically induced linkage isomerism of a phosphazide. The resultant “N^β-M” species **22**, [ⁱPr₂P(N₃Mes)(NMes)-κ²-N,N^β]Rh(COD), and **23**, [ⁱPr₂P(N₃Mes)(NMes)-κ²-N,N^β]Ir(COD), were highly thermally stable. The adamantyl analogous **18**, [ⁱPr₂P(N₃Ad)(NAd)-κ²-N,N^α]Rh(COD), and **19**, [ⁱPr₂P(N₃Ad)(NAd)-κ²-N,N^α]Ir(COD), however, did not undergo similar linkage isomerism.

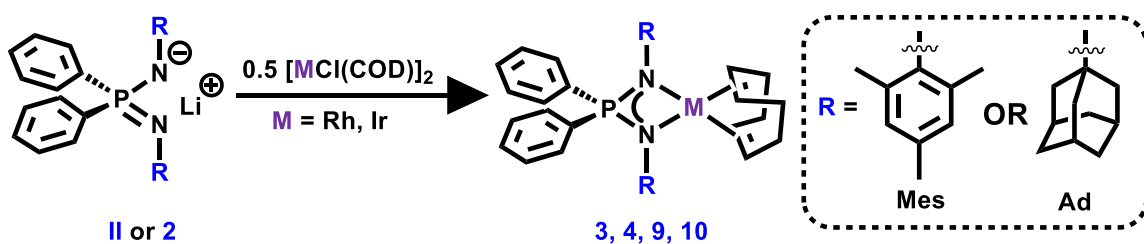
The COD complexes **18-21** were inert to H₂ and silanes; however, the COD ligand can be displaced with CO. Preliminary work substituting COE for COD has afforded **28**, [ⁱPr₂P(N₃Mes)(NMe_s)]Rh(COE)₂, which retains the phosphazide functionality. Complex **28** represents the first azidophosphonamide species to exhibit N₂ extrusion upon exposure to UV light (365 nm), giving the isopropyl-substituted iminophosphonamido complex **29**, [ⁱPr₂P(NMe_s)₂]Rh(COE)₂. The rapid decomposition of **29** in solution is considered a promising sign that the COE ligands can be readily substituted. Future work investigating *in situ* generation of the COE species **28** and **29** could lead to various applications not possible with the COD complexes **18-21**.

CHAPTER 5: SUMMARY, CONCLUSION AND FUTURE

WORK AVENUES

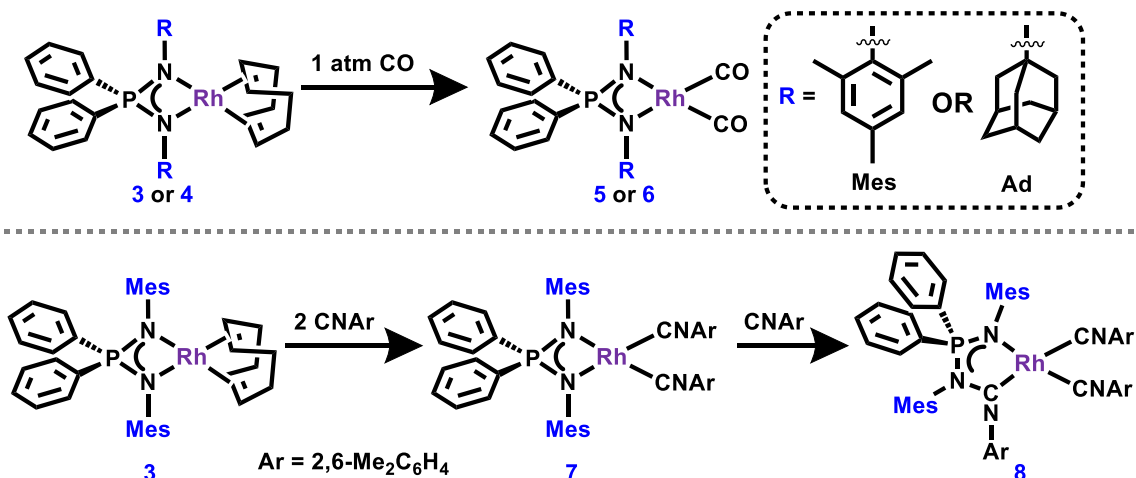
5.1 Summary of Chapter 2

The second chapter of this thesis describes the development of a new family of Rh^I and Ir^I iminophosponamido complexes (Scheme 5.1).



Scheme 5.1 General synthetic route to generate Rh^I and Ir^I imino- and azidophosponamido complexes **3**, **4**, **9**, and **10**

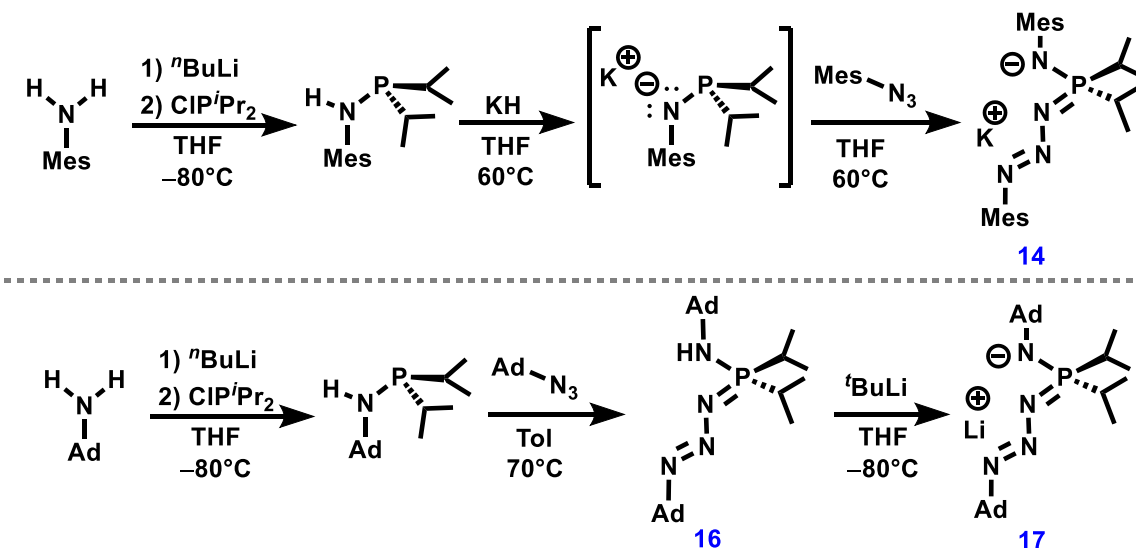
Only strong π -accepting ligands, namely CO and isocyanides, have been shown to displace the COD ligand (Scheme 5.2).



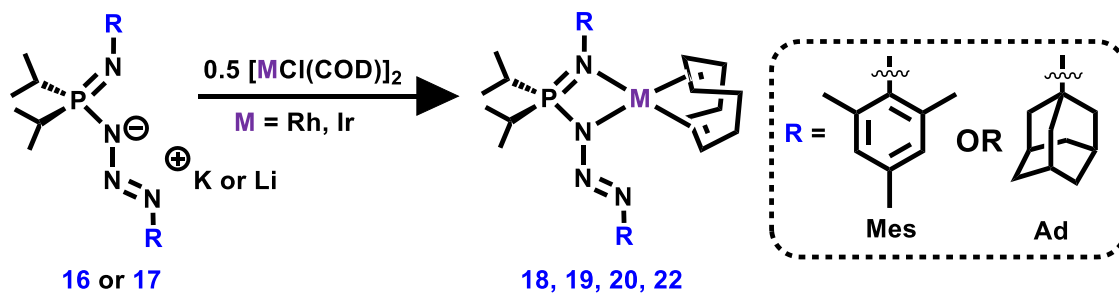
Scheme 5.2 Reaction of Rh^I iminophosphonamido complexes **3** and **4** towards strong π -accepting ligands

5.2 Summary of Chapter 3

A neutral azidophosphonamido ligand and an azidophosphonamido potassium ligand salt were isolated (Scheme 5.3), from which a new family of Rh^I and Ir^I azidophosphonamido complexes was readily generated (Scheme 5.4).



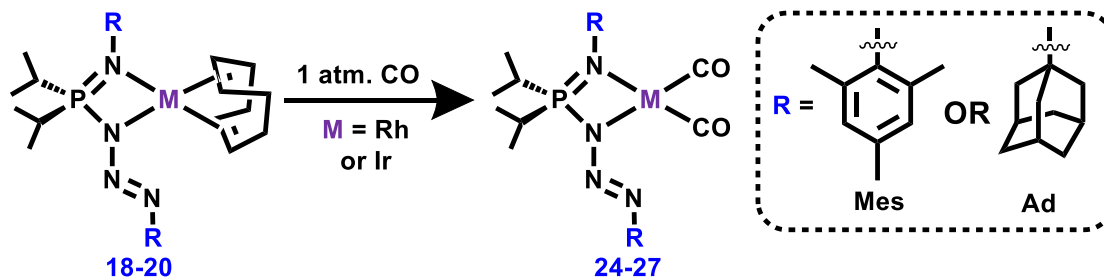
Scheme 5.3 Synthetic route to azidophosphonamido ligand salts **14**, **17**



Scheme 5.4 General synthetic route to generate Rh^I and Ir^I azidophosphonamido complexes **18-22**

5.3 Summary of Chapter 4

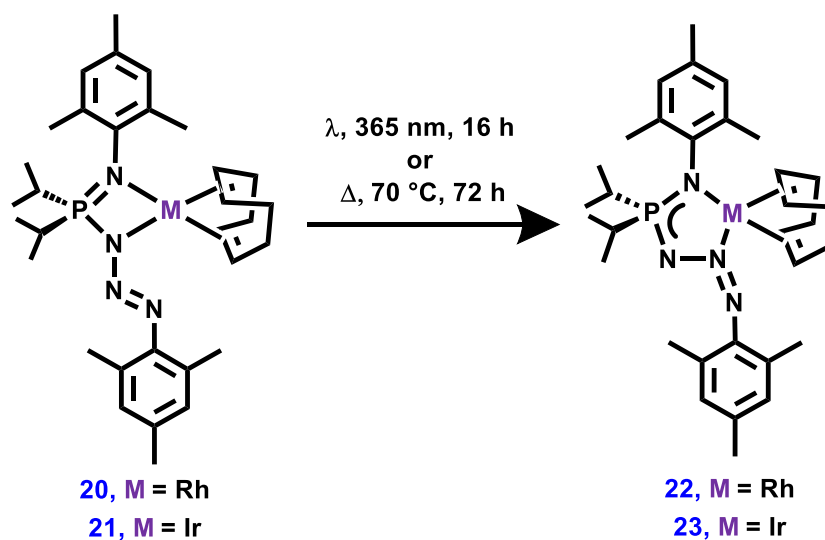
Only a strong π -accepting ligand, namely CO, was shown to displace the COD ligand in the azidophosphonamido complexes **18-20** (Scheme 5.5).



Scheme 5.5 Reaction of Rh^I iminophosphonamido complexes **18-20** towards CO

Thermally and photochemically induced phosphazide linkage isomerism of the N^α -M azidophosphonamide species **20** [$^iPr_2P(N_3Mes)(NMe_3)-\kappa^2-N,N^\alpha$]Rh(COD), and **21** [$^iPr_2P(N_3Mes)(NMe_3)-\kappa^2-N,N^\alpha$]Ir(COD), formed the “ N^β -M” complexes **22** [$^iPr_2P(N_3Mes)(NMe_3)-\kappa^2-N,N^\beta$]Rh(COD), and **23** [$^iPr_2P(N_3Mes)(NMe_3)-\kappa^2-$

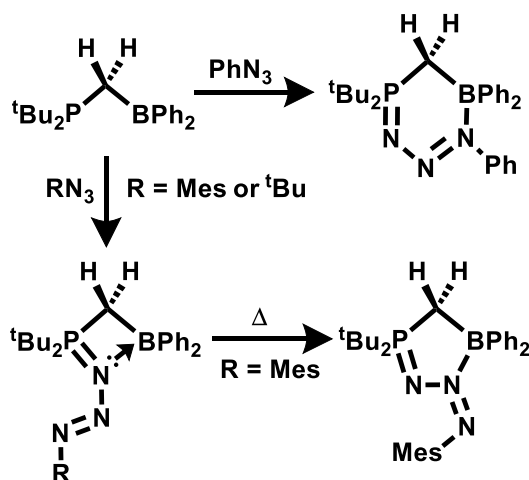
N,N^β]Ir(COD). The “ N^β -M” complexes **22** and **23** contain a 5-membered metallacycle (Scheme 5.6), which exhibits a larger ligand bite angles (N-M-N) $70^\circ \rightarrow 83^\circ$. Both **22** and **23** are postulated to be the thermodynamic product for the mesityl-substituted complexes; as the adamantyl analogous **18** [$^i\text{Pr}_2\text{P}(\text{N}_3\text{Ad})(\text{NAd})-\kappa^2-N,N^\alpha$]Rh(COD)], and **19** [$^i\text{Pr}_2\text{P}(\text{N}_3\text{Ad})(\text{NAd})-\kappa^2-N,N^\alpha$]Ir(COD)], do not undergo similar linkage isomerism.



Scheme 5.6 Linkage isomerism of mesityl-substituted azidophosponamido complexes **20** and **21** to **22** and **23**

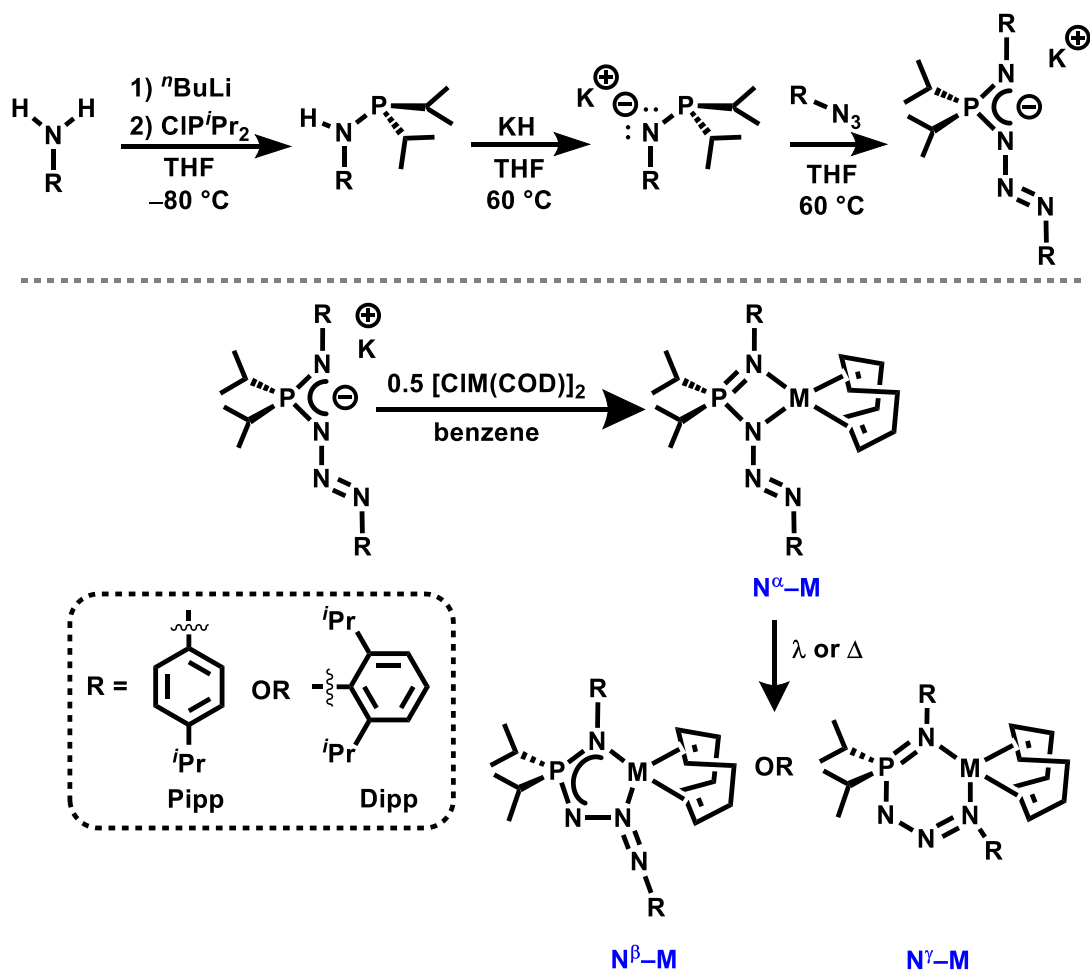
5.4 Future Work Stemming from Chapter 4: Azidophosponamide Isomerization

Slootweg *et al.* demonstrated that the phosphazide adopts one of three different coordination modes ($N^\alpha \rightarrow B$, $N^\beta \rightarrow B$, and $N^\gamma \rightarrow B$) depending on the nitrogen substituent, mesityl, phenyl or *tert*-butyl (Scheme 5.7). Akin to the work of Slootweg *et al.*, the induced phosphazide linkage isomerism exhibited within this thesis (N^α -M to the N^β -M) only employed the mesityl-substituted azidophosponamide species [$^i\text{Pr}_2\text{P}(\text{N}_3\text{Mes})(\text{NMes})-\kappa^2-N,N^\alpha$]M(COD) M = Rh (**20**), Ir (**21**) (Scheme 5.6).



Scheme 5.7 Phosphazide-containing FLP linkage isomers reported by Slootweg *et al.*¹¹⁶

A continuation of the work contained within this thesis would be to explore the steric impact of nitrogen substituents on induced phosphazide linkage isomerism and which conformation (N^α -M, N^β -M or N^γ -M) is favoured. The mesityl groups in complexes **20** and **21** could easily be exchanged for different aromatic substituents, as the aliphatic adamantyl complexes [i Pr₂P(N₃Ad)(NAd)- κ^2 - N,N^α]M(COD) M = Rh (**22**), Ir (**23**) solely favoured the N^α -M conformation. It is predicted that using a group with more bulk in the *ortho* position, such as Dipp, could favour the N^α -M or N^β -M coordination mode, while using a Pipp-substituent may yield a N^γ -M complex. As both PippN₃ and DippN₃ are easily synthesized following literature procedures,^{168,169} generating the azidophosponamido ligand salts (Scheme 5.8, top) and metal complexes should be facile (Scheme 5.8, bottom).

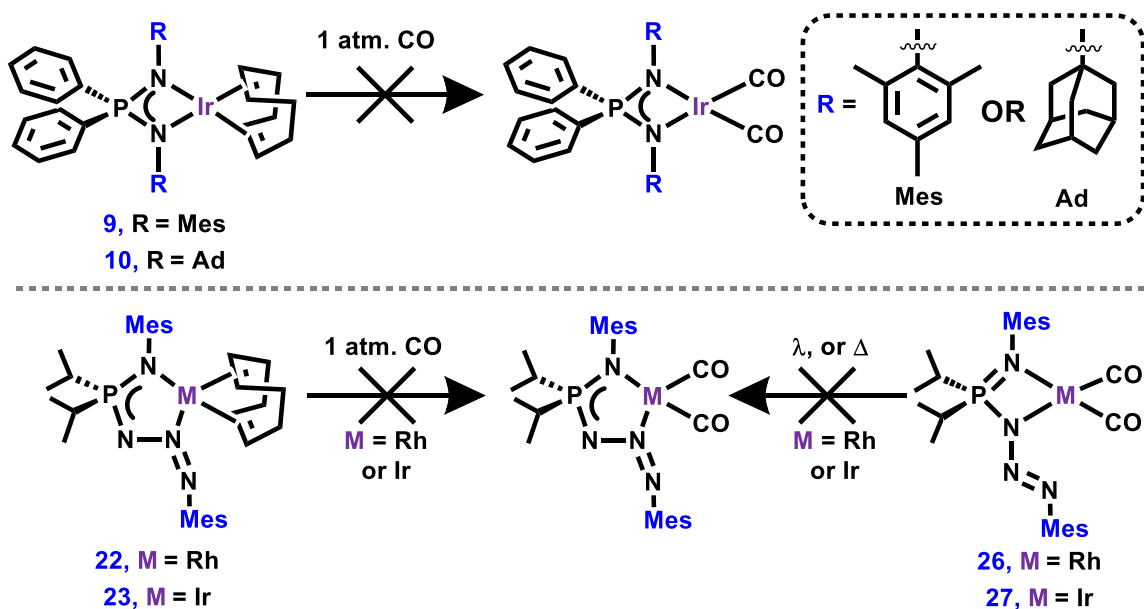


Scheme 5.8 Proposed synthesis and linkage isomerism of Pipp and Dipp substituted azidophosphonamido complexes

5.5 Conclusions from Chapters 2 and 4

The COD ligand on the metal centre in both the imino- and azidophosphonamide families has proven convenient for facile generation, isolation, and characterization. Examining the influence of phosphazide functional groups upon the reactivity of a metal complex, a major goal of this work, was not achieved as both the imino- and azidophosphonamido COD complexes were shown to be substitutionally inert towards H₂

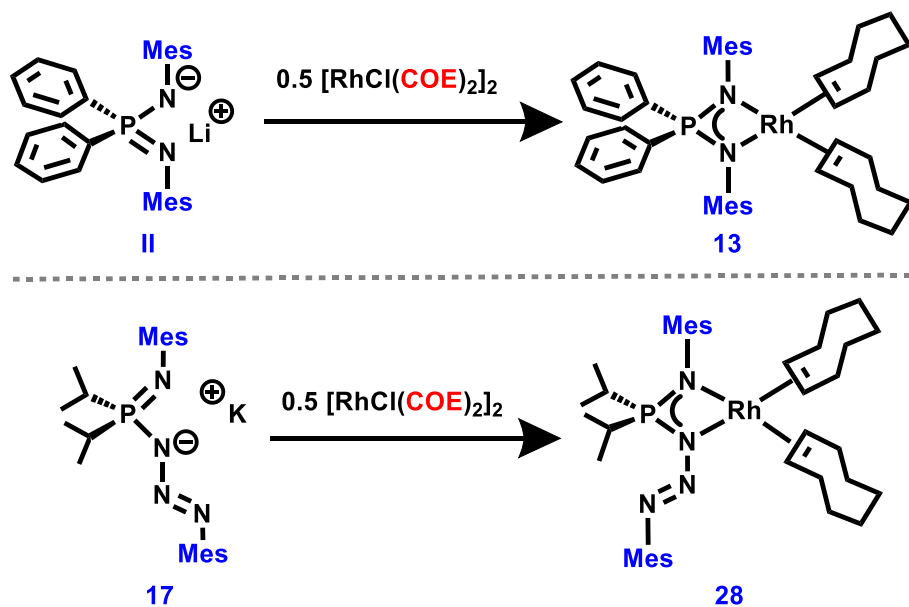
or silanes. Only strong π -accepting ligands, namely CO and isocyanides, were demonstrated to displace the COD ligand, with a few exceptions (Scheme 5.9). The chelate effect of the COD ligand, coupled with strong π -backdonation from either Rh or Ir are attributed as the main causes for the lack of reactivity of the imino- and azidophosphonamido COD complexes with small molecules (other than CO or CNR). Preliminary work substituting COD with two COE ligands was attempted in order to mitigate the chelate effect that COD possesses.



Scheme 5.9 Complexes that are inert to an atmosphere of CO

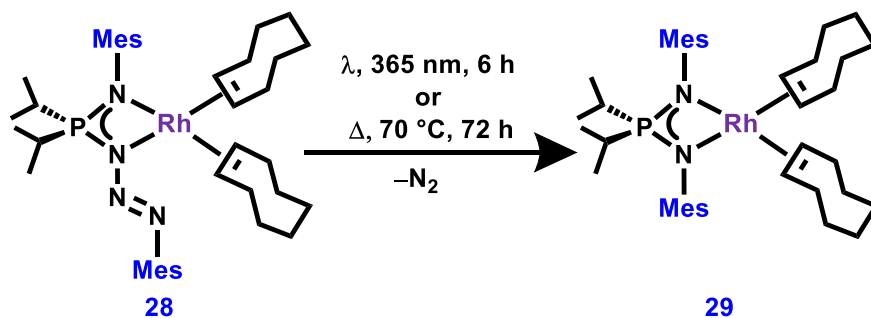
5.6 Towards Substituting COD for COE Chapters 2 and 4

The bis(cyclooctene) complexes **13**, $[\text{Ph}_2\text{P}(\text{NMe}_s)_2]\text{Rh}(\text{COE})_2$, and **28**, $[\text{Pr}_2\text{P}(\text{N}_3\text{Me}_s)(\text{NMe}_s)]\text{Rh}(\text{COE})_2$ were readily generated (Scheme 5.10).



Scheme 5.10 Synthesis of $[\text{Ph}_2\text{P}(\text{NMe}_s)_2]\text{Rh}(\text{COE})_2$ **13**, and $[\textit{i}\text{Pr}_2\text{P}(\text{N}_3\text{Me}_s)(\text{NMe}_s)]\text{Rh}(\text{COE})_2$ **28**

Complex **28**, $[\textit{i}\text{Pr}_2\text{P}(\text{N}_3\text{Me}_s)(\text{NMe}_s)]\text{Rh}(\text{COE})_2$, is unusual, as it is the first azidophosphonamido complex to exhibit *cisoid*-conformation of the phosphazide moiety. Extrusion of N_2 from complex **28** can be induced under either photochemical or thermal conditions, affording the isopropyl-substituted iminophosphonamido complex **29**, $[\textit{i}\text{Pr}_2\text{P}(\text{NMe}_s)_2]\text{Rh}(\text{COE})_2$ (Scheme 5.11).



Scheme 5.11 Synthesis of [*i*Pr₂P(NMes)₂]Rh(COE)₂ **29**

5.7 Conclusions from Preliminary Work Substituting COD with Two COE Ligands in Chapter 4

Both **29**, [*i*Pr₂P(NMes)₂]Rh(COE)₂, and the phenyl-substituted analogue **13**, [Ph₂P(NMes)₂]Rh(COE)₂, were found to rapidly decompose to neutral iminophosphonamide ligand R₂P(NMes)(NHMs), R = *i*Pr or Ph, and Rh black when at ambient temperature in solution, or when placed under vacuum. The instability of the COE complexes is thought to be a good indicator of facile substitution of the COE groups, wherein the COE complexes could be generated *in situ* and further reacted with small molecules such as H₂ or various silanes. However, *in situ* generation and subsequent reaction chemistry of both **13** and **29** was not examined due to time constraints.

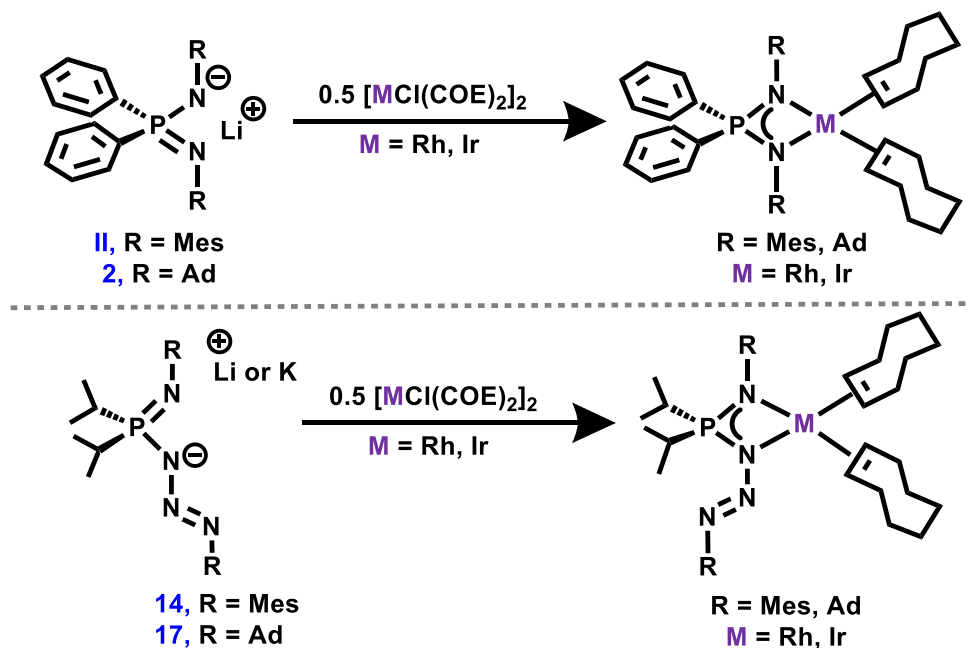
5.8 Future Work Stemming from Chapters 2 and 4: COE Complexes and Catalysis

Future avenues for this project include generation of a family of COE imino- and azidophosphonamido species [R₂P(NR¹)₂]M(COE)₂ (R = Ph, *i*Pr; R¹ = Mes, Ad; M = Rh, Ir) and [*i*Pr₂P(N₃R)(NR)]M(COE)₂ (R = Mes, Ad; M = Rh, Ir) as only the mesityl-

substituted Rh COE complexes **13**, $[\text{Ph}_2\text{P}(\text{NMes})_2]\text{Rh}(\text{COE})_2$, **28**

$[\text{}^i\text{Pr}_2\text{P}(\text{N}_3\text{Mes})(\text{NMes})]\text{Rh}(\text{COE})_2$, and **29** $[\text{}^i\text{Pr}_2\text{P}(\text{NMes})_2]\text{Rh}(\text{COE})_2$ were isolated.

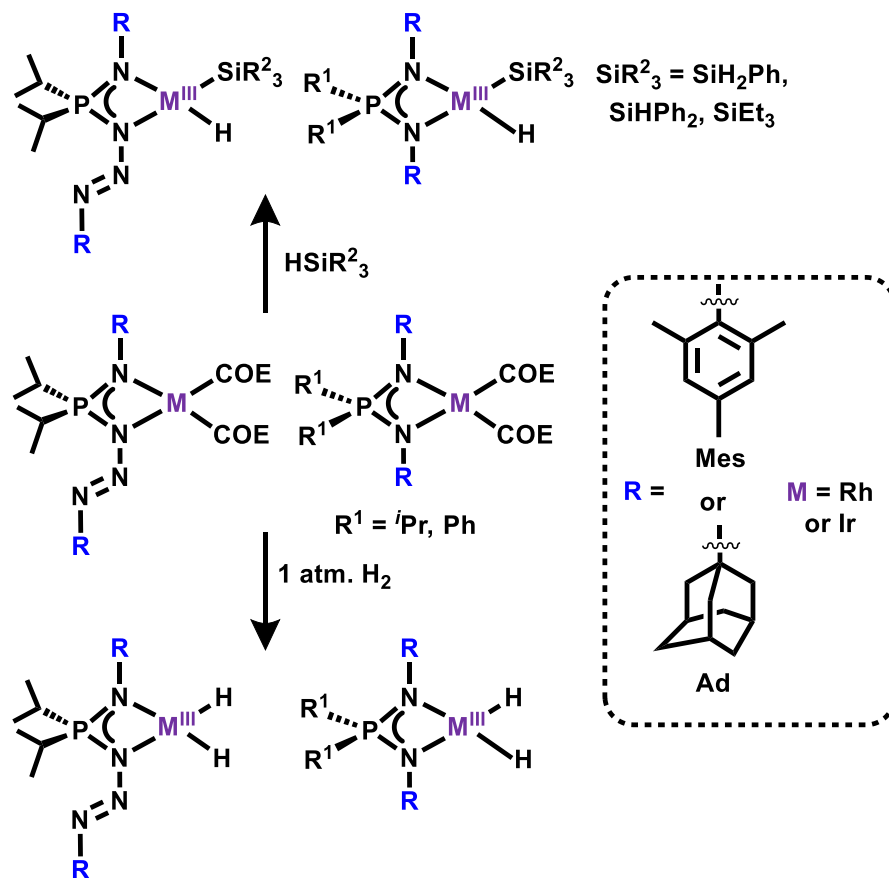
The various COE complexes $[\text{R}_2\text{P}(\text{NR}^1)_2]\text{M}(\text{COE})_2$ ($\text{R} = \text{Ph}, \text{}^i\text{Pr}$; $\text{R}^1 = \text{Mes}, \text{Ad}$; $\text{M} = \text{Rh}, \text{Ir}$) and $[\text{}^i\text{Pr}_2\text{P}(\text{N}_3\text{R})(\text{NR})]\text{M}(\text{COE})_2$ ($\text{R} = \text{Mes}, \text{Ad}$; $\text{M} = \text{Rh}, \text{Ir}$) could be readily synthesized *via* a salt metathesis reaction between the various imido and azidophosphonamido ligand salts (**II** $\text{Li}[\text{Ph}_2\text{P}(\text{NMes})_2]$, **2** $[\text{Ph}_2\text{P}(\text{NAd})_2]$, **14** $\text{K}[\text{}^i\text{Pr}_2\text{P}(\text{N}_3\text{Mes})(\text{NMes})]$ and **17** $\text{Li}[\text{}^i\text{Pr}_2\text{P}(\text{N}_3\text{Ad})(\text{NAd})]$) and the COE metal dimers $[\text{MCl}(\text{COE})_2]_2$, $\text{M} = \text{Rh}, \text{Ir}$ (Scheme 5.12).



Scheme 5.12 Proposed synthetic route to COE imino- and azidophosphonamido species

Given the inherent instability of the COE complexes in solution, *in situ* synthesis may be the best option to generate the COE species for immediate reaction of the COE ligands with H_2 or a variety of silanes to isolate a dihydride, or silyl complex (intermediates

of hydrogenation and hydrosilylation respectively), expanding the family of known Rh^I and Ir^I imino and azidophosponamido complexes (Scheme 5.13).



Scheme 5.13 Example of proposed substitution reactions, replacing COD to generate dihydride and silyl complexes, expanding the family of imino- and azidophosponamido complexes

If substitution of the COE ligand proves viable, said complexes, $[\textit{i}\text{Pr}_2\text{P}(\text{N}_3\text{R})(\text{NR})]\text{M}(\text{COE})_2$ and $[\text{Ph}_2\text{P}(\text{NR})_2]\text{M}(\text{COE})_2$, could be scoped for their activity towards hydrogenation and hydrosilylation. Similarly, a variety of other hydrofunctionalization catalytic reactions could be scoped, such as hydroformylation

(activation of CO₂), hydroboration (activation of boranes), and hydroamination (reaction with amines).

The N₂ extrusion observed for the azidophosponamido complex **28**, [ⁱPr₂P(N₃Mes)(NMe_s)]Rh(COE)₂, to form **29**, [ⁱPr₂P(NMe_s)₂]Rh(COE)₂ could be exploited to generate iminophosponamido species with isopropyl groups on phosphorus purposely. Isopropyl substituents on phosphorus in iminophosponamide ligands have yet to be reported in the literature. The effect this modification has on the electron donation capacity of the ligand is unknown and could yield more stable dihydride or silyl complexes or generate a catalytically active isopropyl-substituted iminophosponamido complex.

CHAPTER 6: EXPERIMENTAL METHODS

6.1 General Laboratory Equipment

The manipulation of all oxygen and moisture-sensitive materials and reagents was conducted in the absence of moisture and air using either a double manifold vacuum line and with corresponding techniques,¹⁷⁰ or in an argon-filled MBraun Labmaster 130 glove box, unless otherwise specified. An Edwards RV12 pump was used to evacuate the vacuum lines and glove box antechambers. Speciality thick-walled (5 mm) glass bombs with Kontes® Teflon valves and swivel frit glassware apparatus were employed in this work. All glassware used was stored in an oven at 115 °C for a minimum of 16 h. The glass was either placed in the glove box antechamber, evacuated while hot and assembled in a glove box, or assembled on a vacuum line and evacuated for 1 h.

6.2 Solvents

All solvents used were obtained from either Millipore Sigma or an MBraun Solvent Purification System (SPS). Non-halogenated solvents (benzene, toluene, pentane, heptane, THF, and diethylether) were further dried over molecular sieves (3 Å) and degassed, then transferred to 500 mL glass bombs charged with Na/benzophenone for storage.² Halogenated solvents (chloroform and dichloromethane) were dried, degassed and stored over CaH₂ in 500 mL bombs. When needed, solvents were transferred to the reaction vessel under reduced pressure and temperature (−94 °C, liquid nitrogen/acetone, unless otherwise stated). Solvents used for NMR spectroscopy were prepared as follows: benzene-*d*₆ (C₆D₆)

was dried over Na/benzophenone, THF-*d*₈ was dried over Na, while chloroform-*d* (CDCl₃) was dried over CaH₂. Deuterated solvents were degassed *via* three freeze-pump-thaw cycles, distilled into a glass bomb under reduced pressure and temperature (−78 °C), and stored under static vacuum over molecular sieves (3 Å).

6.3 Chemical Materials

The reagents: ⁿBuLi (2.5 M in hexanes), ^tBuLi (1.7 M in hexanes), trichlorosilane, Li[HMDS], K[HMDS], KH, 1-adamantylamine, 1-mesitylamine chlorodiphenylphosphine and chlorodiisopropylphosphine were purchased from Sigma Aldrich and used without further purification. The following compounds: Ph₂P(NHMes)(NMe_s),¹²⁶ MesNHPⁱPr₂,¹⁷¹ MesN₃,¹⁶⁹ Li[Ph₂P(NMe_s)₂],¹²⁷ AdNHPPPh₂,¹⁷² AdN₃,¹⁷³ [Rh(Cl)(COD)]₂,¹⁷⁴ [IrCl(COD)]₂¹⁷⁵ and [RhCl(COE)₂]₂¹⁴⁹ were prepared using literature procedures. All solid reagents used in air- and moisture-sensitive reactions were dried under vacuum for 48 h at ambient temperature and kept under an inert atmosphere before use. All liquid reagents were transferred *via* cannula to a glass bomb for storage and degassed *via* two freeze-pump-thaw cycles.

Chemical warning – Caution! The stability of an organic azide depends upon its chemical structure, mainly the carbon-to-nitrogen ratio (C:N). A C:N ratio between 1 and 3 generally indicates that the material can be explosive.^{135,136} Organic azides should be handled in a fume hood behind a protective blast shield. Any reactions involving organic azides should not be conducted in a closed system as the reaction of azides to phosphines can rapidly eliminate N₂ gas. Extra care should be taken involving reactions where the

organic azide is heated. The azides MesN₃ and AdN₃, C:N ratios of 3 and 3.4, make them less flammable and prone to combustion; nonetheless, care should be taken when handling these materials. MesN₃, an orange liquid, is stored in a freezer (−35 °C), while AdN₃ is a beige solid stored at ambient conditions; both azides are stable under ambient conditions for long periods.

6.4 Instrumentation Details for NMR Experiments

All NMR spectra (¹H, ¹H{³¹P}, ⁷Li, ⁷Li{¹H}, ¹³C{¹H}, ¹³C APT, ¹³C DEPT 135 ²⁹Si, ²⁹Si{¹H}, ³¹P{¹H}, ¹H–¹H COSY, ¹H–³¹C HSQC, ¹H–¹³C HMBC) were recorded using a Bruker Avance II 300 MHz spectrometer (300.13 MHz for ¹H, 75.47 MHz for ¹³C, 121.48 MHz for ³¹P, and 59.63 MHz for ²⁹Si) or a Bruker Avance III HD 700 MHz spectrometer (700.13 MHz for ¹H, 272.10 MHz for ⁷Li, 176.05 MHz for ¹³C, 283.54 MHz for ³¹P, and 139.09 MHz for ²⁹Si) NMR spectrometer. Experiments were performed at ambient temperature unless otherwise stated. NMR spectroscopic data is reported in parts per million (ppm). The ¹H and ¹³C{¹H} shifts are referenced to SiMe₄ through internal ¹H and ¹³C{¹H} resonance(s) of the employed solvent; benzene-*d*₆ (7.16 and 128.0), THF-*d*₈ (1.73, 3.58 and 25.4, 67.6), or CDCl₃ (7.27 and 77.4). ⁷Li NMR spectra were referenced to an external 1 M LiCl sample in D₂O (δ 0.0). ³¹P{¹H} spectra were referenced to an external 85% H₃PO₄ sample in D₂O (δ 0.0). The ¹H NMR data for all compounds are reported as follows: chemical shift, multiplicity (s = singlet, d = doublet, t = triplet, q = quartet, sp = septet, dsp = doublet of septets, br = broad, m = multiplet, ov = overlapping), coupling constant (Hz), integration, assignment. The assignment of ¹H and ¹³C{¹H} resonances was

supported by ^1H - ^1H COSY, $^{13}\text{C}\{^1\text{H}\}$ APT, $^{13}\text{C}\{^1\text{H}\}$ DEPT 135, ^1H - ^{13}C HSQC and ^1H - ^{13}C HMBC experiments.

6.5 X-ray Crystallographic Details

All crystallographic data was collected on a Rigaku SuperNova diffractometer. The diffractometer was equipped with an Oxford 800 cryo stream-cooling device,¹⁷⁶ a Dectris Pilatus 3R 200K-A hybrid-pixel-array detector, and two sealed graphite-monochromated X-ray sources [molybdenum (NOVA) ($K_{\alpha} = 0.71073 \text{ \AA}$) and copper (MOVA) ($K_{\alpha} = 1.54178 \text{ \AA}$)]. Crystals suitable for X-ray diffraction were coated in Paratone oil in a glove box, removed from the inert atmosphere and visually inspected by a polarizing light and a standard microscope on a glass slide under ambient conditions. The crystal selected for analysis was placed on a MiTeGen Dual Thickness MicroMount attached to a four-circle κ goniometer head. CrysAlisPro software¹⁷⁷ was used to determine unit cell parameters. The structures were solved using Intrinsic Phasing methods and refined using the least-squares methods of the SHELXL-2014^{178,179} in Olex2-1.5 software.¹⁸⁰ Molecular graphics were generated using Mercury 2020.2.0 software.¹⁸¹

6.6 Elemental Analysis Details

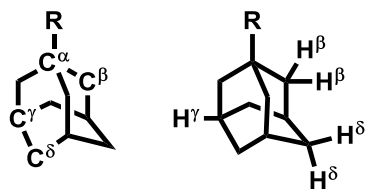
CHNS elemental analyses were performed at the University of Lethbridge by Dr. Dylan J. Webb using an Elementar America's Vario. Vanadium oxide was used as a combustion agent in cases when only the carbon percentages were low (3% deviation from predicted values).

6.7 Additional Instrumentation

Infrared spectroscopic analysis was conducted on bulk recrystallized compounds employing a Thermo-Nicolet iS10 FT-IR spectrometer under ambient atmospheric conditions. The remaining sample was then placed under vacuum, brought into a glove box, dissolved in the appropriate NMR solvent and then analyzed for decomposition due to the brief exposure to air.

6.8 Naming Conventions of Adamantyl Groups

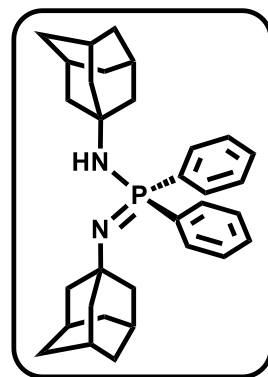
Naming conventions for Adamantyl substituents:



6.9 Synthetic Experimental Procedures Pertaining to Chapter 2

Synthesis of $\text{Ph}_2\text{P}(\text{NC}_{10}\text{H}_{15})(\text{NHC}_{10}\text{H}_{15})$ (**1**)

AdNHPPH_2 (556 mg, 1.66 mmol) and AdN_3 (294 mg, 1.66 mmol) were weighed into a two-necked round bottom flask. Toluene (~40 mL) was transferred under reduced pressure to the flask. The yellow solution was heated to 70 °C for 16 h. The solvent was removed *in vacuo*, yielding a light brown solid. The solid was

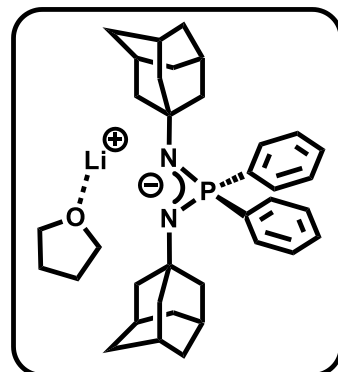


brought into a glove box and washed with pentane (4×2 mL). The remaining solvent was removed from the beige solid under vacuum. Light-yellow needles of **1** were grown from

a saturated solution of benzene stored at ambient temperature for 3 days. Yield: 714 mg, 89%. ^1H NMR (300 MHz, C_6D_6): δ 7.97 (ddd, $^3J_{\text{PH}} = 12.0$, $^2J_{\text{HH}} = 7.7$, $^4J_{\text{HH}} = 1.7$ Hz, 4H, *ortho*-Ph), 7.22–7.11 (m, 4H, *meta*-Ph), 7.10–6.91 (m, 2H, *para*-Ph), 2.57 (d, $^2J_{\text{PH}} = 8.4$ Hz, 1H, NH), 2.16 (ov s, 6H, P=N-Ad- H^β), 2.12 (ov s, 3H, P=N-Ad- H^γ), 1.93 (ov s, 6H, HN-Ad- H^β), 1.86 (s, 3H, HN-Ad- H^γ), 1.75 (ov t, $^3J_{\text{HH}} = 11.7$ Hz, 3H, P=N-Ad- H^δ), 1.67 (ov t, $^3J_{\text{HH}} = 11.7$ Hz, 3H, P=N-Ad- H^δ), 1.45 (br s, 6H, HN-Ad- H^δ). $^1\text{H}\{^{31}\text{P}\}$ NMR (300 MHz, C_6D_6): δ 8.03 (dd, $^2J_{\text{HH}} = 7.7$, $^4J_{\text{HH}} = 1.7$ Hz, 4H, *ortho*-Ph), 7.28–7.17 (m, 4H, *meta*-Ph), 7.15–6.97 (m, 2H, *para*-Ph), 2.63 (s, 1H, NH), 2.22 (ov s, 6H, P=N-Ad- H^β), 2.18 (ov s, 3H, P=N-Ad- H^γ), 1.99 (ov s, 6H, HN-Ad- H^β), 1.92 (ov s, 3H, HN-Ad- H^γ), 1.75 (ov t, $^3J_{\text{HH}} = 11.7$ Hz, 3H, P=N-Ad- H^δ), 1.67 (ov t, $^3J_{\text{HH}} = 11.7$ Hz, 3H, P=N-Ad- H^δ), 1.52 (br s, 6H, HN-Ad- H^δ). $^{13}\text{C}\{^1\text{H}\}$ NMR (75 MHz, C_6D_6): δ 140.59 (d, $^1J_{\text{HP}} = 125.0$ Hz, *ipso*-Ph), 132.86 (d, $^2J_{\text{HP}} = 9.5$ Hz, *ortho*-Ph), 130.27 (d, $^3J_{\text{HP}} = 2.8$ Hz, *meta*-Ph), 128.17 (s, *para*-Ph), 53.11 (d, $^2J_{\text{PC}} = 2.0$ Hz, HN-Ad- C^α), 52.56 (d, $^3J_{\text{PC}} = 4.1$ Hz, P=N-Ad- C^α), 49.88 (d, $^3J_{\text{PC}} = 11.0$ Hz, P=N-Ad- C^β), 46.10 (d, $^3J_{\text{PC}} = 3.0$ Hz, HN-Ad- C^β), 37.75 (s, P=N-Ad- C^δ), 36.79 (s, HN-Ad- C^δ), 31.51 (s, P=N-Ad- C^γ), 30.58 (s, HN-Ad- C^γ). $^{31}\text{P}\{^1\text{H}\}$ NMR (122 MHz, C_6D_6): δ -22.4 (s). Anal. Calcd. for $\text{C}_{32}\text{H}_{41}\text{N}_2\text{P}$: C: 79.30 H: 8.53 N: 5.78%; found: C: 78.92 H: 7.66 N: 5.70%.

Synthesis of Li [Ph₂P(NC₁₀H₁₅)₂]⁺·THF (2)

Complex **2** (211 mg, 0.435 mmol) was weighed into a two-necked round bottom flask. The flask was cooled to -94 °C (liquid nitrogen/acetone), and THF (~30 mL) was transferred to the flask *in vacuo*. ^tBuLi (0.282 mL, 0.478 mmol, 1.7 M)

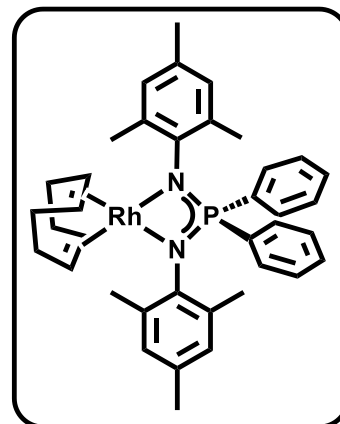


was injected dropwise over 10 min. The yellow opaque solution was left in the cold bath to slowly warm to ambient temperature. After 12 h, the THF was removed under vacuum, resulting in a yellow solid. The solid was washed in a glove box with pentane (4 × 2 mL), and residual solvent was removed *in vacuo*, yielding a white solid. Yield: 224 mg, 84%. ¹H NMR (700 MHz, THF-*d*₈): δ 7.94 (t, ³J_{PH} = 8.2 Hz, 4H, *ortho*-Ph), 7.25–7.16 (m, 6H, *meta*- and *para*-Ph), 3.54 (s, 4H, coord. THF-CH₂ (2,5)), 1.69 (s, 3H, coord. THF-CH₂ (3,4)), 1.64 (s, 6H, Ad-*H*^β), 1.36 (s, 3H, Ad-*H*^γ), 1.35 (s, 6H, Ad-*H*^β), 1.32 (s, 12H, Ad-*H*^δ), 1.29 (s, 3H, Ad-*H*^γ). ¹H{³¹P} NMR (700 MHz, THF-*d*₈): δ 7.94 (br s, 4H, *ortho*-Ph), 7.24–7.15 (m, 6H, *meta*- and *para*-Ph), 3.54 (s, 4H, coord. THF-CH₂ (2,5)), 1.69 (s, 4H, coord. THF-CH₂ (3,4)), 1.64 (br s, 6H, Ad-*H*^β), 1.36 (s, 3H, Ad-*H*^γ), 1.35 (s, 6H, Ad-*H*^β), 1.32 (s, 12H, Ad-*H*^δ), 1.30 (s, 3H, Ad-*H*^γ). ⁷Li NMR (272 MHz, THF-*d*₈): δ 0.9 (d, ²J_{LiP} = 4.7 Hz). ⁷Li{¹H} NMR (272 MHz, THF-*d*₈): δ 0.9 (d, ²J_{LiP} = 4.7 Hz). ¹³C{¹H} NMR (176 MHz, THF-*d*₈) δ 145.85 (d, ¹J_{HP} = 75.4 Hz, *ipso*-Ph), 133.21 (d, ²J_{HP} = 9.1 Hz, *ortho*-Ph), 128.36 (d, ⁴J_{HP} = 2.7 Hz, *para*-Ph), 127.10 (d, ³J_{HP} = 9.7 Hz, *meta*-Ph), 68.03 (s, coord. THF-CH₂ (2,5)), 50.93 (s, Ad-C^β), 49.76 (d, ²J_{PC} = 9.9 Hz, Ad-C^α), 37.77 (s, Ad-C^δ), 31.52 (s, Ad-

C^{ν}), 26.19 (s, coord. THF-CH₂ (3,4)). $^{31}\text{P}\{^1\text{H}\}$ NMR (284 MHz, THF- d_8): δ -2.3 (s). Anal. Calcd. for C₃₆H₄₈LiN₂OP: C: 76.84 H: 8.60 N: 4.98%; found: C: 76.29 H: 8.60 N: 5.00%.

Synthesis of [Ph₂P(N(2,4,6-Me₃C₆H₂))₂]Rh(COD) (**3**)

Li[Ph₂P(NMes)₂] (98.7 mg, 0.208 mmol) and [RhCl(COD)]₂ (51.3 mg, 0.104 mmol) were weighed into a two-necked round bottom flask attached to a swivel frit apparatus. The flask was cooled to 0 °C (ice/sodium chloride), and benzene (~20 mL) was transferred to the flask

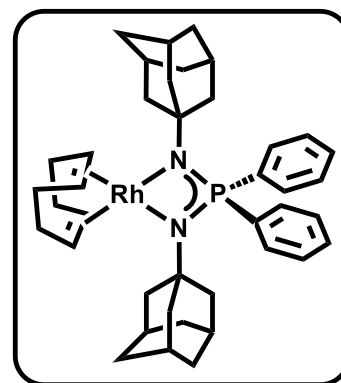


under reduced pressure. The yellow solution was left to stir at ambient temperature under a positive Ar atmosphere. After 16 h, the solution was filtered through the frit, resulting in a transparent yellow solution. The solvent was removed under vacuum, yielding a yellow powder. Yellow plate-shaped crystals of **3** were grown from a saturated pentane solution stored at -30 °C for 3 days. Yield: 133 mg, 90%. ^1H NMR (300 MHz, C₆D₆): δ 7.73–7.60 (m, 4H, *ortho*-Ph), 7.02–6.87 (m, 6H, *meta*- and *para*-Ph), 6.85 (s, 4H, Mes-CH), 3.52 (s, 4H, COD-CH), 2.53 (s, 12H, *ortho*-Mes-CH₃), 2.38 (br s, 4H, COD-CH₂), 2.17 (s, 6H, *para*-Mes-CH₃), 1.63 (d, $^3J_{\text{HH}} = 8.0$ Hz, 4H, COD-CH₂). ^1H NMR (300 MHz, C₆D₆): δ 7.67 (d, $^3J_{\text{HH}} = 6.8$ Hz, 4H, *ortho*-Ph), 7.02–6.88 (m, 6H, *meta*- and *para*-Ph), 6.85 (s, 4H, Mes-CH), 3.52 (s, 4H, COD-CH), 2.53 (s, 12H, *ortho*-Mes-CH₃), 2.38 (br s, 4H, COD-CH₂), 2.17 (s, 6H, *para*-Mes-CH₃), 1.63 (d, $^3J_{\text{HH}} = 8.0$ Hz, 4H, COD-CH₂). $^{13}\text{C}\{^1\text{H}\}$ NMR (75 MHz, C₆D₆): δ 141.82 (d, $^2J_{\text{PC}} = 3.5$ Hz, *ipso*-Mes-C-P), 139.03 (d, $^1J_{\text{PC}} = 89.8$ Hz, *ipso*-Ph), 136.35 (d, $^3J_{\text{PC}} = 5.0$ Hz, *ortho-*ipso**-Mes-C-CH₃), 131.97 (d, $^5J_{\text{PC}} = 2.9$ Hz, *para*-

ipso-Mes-C-CH₃), 131.28 (ov d, ³J_{PC} = 2.4 Hz, *meta*-Ph), 131.20 (ov d, ²J_{PC} = 9.2 Hz, *ortho*-Ph), 130.13 (d, ⁴J_{PC} = 1.9 Hz, *para*-Ph), 128.18 (d, ⁴J_{PC} = 11.2, Mes-CH, partially obscured by solvent resonance), 76.81 (d, ¹J_{CRh} = 13.3 Hz, COD-CH), 31.73 (s, COD-CH₂), 22.36 (d, ⁴J_{PC} = 0.8 Hz, *ortho*-Mes-CH₃), 21.22 (s, *para*-Mes-CH₃). ³¹P{¹H} NMR (122 MHz, C₆D₆): δ 24.5 (d, ²J_{RhP} = 13.8 Hz). Anal. Calcd. for C₃₉H₄₈PN₂Rh: C: 69.02 H: 7.13 N: 4.13%; found: C: 68.65 H: 6.88 N: 4.33%.

Synthesis of [Ph₂P(NC₁₀H₁₅)₂]Rh(COD) (4)

To a two-necked round bottom flask containing **2** (53.8 mg, 0.0956 mmol) and [RhCl(COD)]₂ (23.6 mg, 0.0478 mmol), benzene (~20 mL) was transferred to the flask *in vacuo* resulting in a yellow solution. The flask was then warmed to 60 °C for 1 h under a positive Ar atmosphere. The

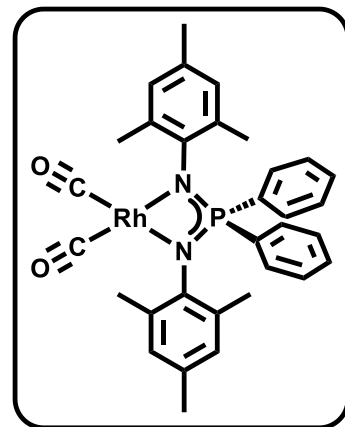


solvent was removed *in vacuo*, resulting in a yellow/brown solid. The solid was brought into a glove box, dissolved in benzene (10 mL) and filtered through a Kimwipe (packed into pipette to act as a filter). The benzene was removed under vacuum, yielding a yellow solid. Complex **4** was crystallized as yellow rectangular crystals from a saturated 1:1 benzene pentane solution stored in a sealed 20 mL scintillation vial at ambient temperature for 1 week. Yield: 45.2 mg, 61%. ¹H NMR (300 MHz, C₆D₆): δ 8.64–8.44 (m, 4H, *ortho*-Ph), 7.23–7.11 (m, 6H, *meta*- and *para*-Ph), 4.95 (br s, 4H, COD-CH), 2.59–2.40 (br m, 4H, COD-CH₂), 1.76 (s, 6H, Ad-*H*^α), 1.73–1.67 (ov m, 4H, COD-CH₂), 1.62 (s, 12H, Ad-*H*^β), 1.36 (s, 12H, Ad-*H*^δ). ¹H{³¹P} NMR (300 MHz, C₆D₆): δ 8.53 (d, ³J_{HH} = 6.9 Hz, 4H,

ortho-Ph), 7.24–7.12 (m, 6H, *meta*- and *para*-Ph), 4.94 (br s, 4H, COD-CH), 2.64–2.38 (br m, 4H, COD-CH₂), 1.75 (s, 6H, Ad-H^α), 1.73–1.65 (m, 4H, COD-CH₂), 1.61 (s, 12H, Ad-H^β), 1.35 (s, 12H, Ad-H^δ). ¹³C{¹H} NMR (75 MHz, C₆D₆): δ 140.30 (d, ¹J_{PC} = 76.6 Hz, *ipso*-Ph), 132.97 (d, ²J_{PC} = 9.0 Hz, *ortho*-Ph), 130.26 (d, ³J_{PC} = 2.7 Hz, *meta*-Ph), 127.58 (s, *para*-Ph), 70.66 (d, ²J_{RhC} = 12.7 Hz, COD-CH), 55.67 (d, ²J_{PC} = 8.7 Hz, Ad-C^α), 46.14 (d, ³J_{PC} = 2.0 Hz, Ad-C^β), 36.34 (s, Ad-C^δ), 31.09 (s, COD-CH₂), 30.41 (s, Ad-C^γ). ³¹P{¹H} NMR (122 MHz, C₆D₆): δ 50.0 (d, ²J_{RhP} = 11.8 Hz). Attempts to obtain high-quality elemental analyses (within 3% of computed values) for this compound have been unsuccessful.

Synthesis of [Ph₂P(N(2,4,6-Me₃C₆H₂))₂]Rh(CO)₂ (**5**)

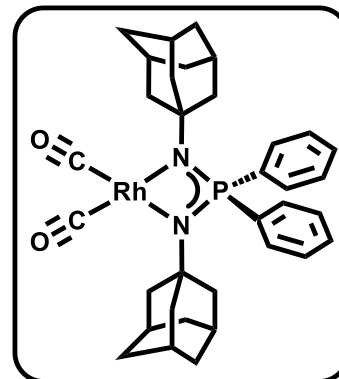
Complex **3** (31.2 mg, 0.0413 mmol) was added to a J. Young NMR tube and dissolved in 0.5 mL of benzene-*d*₆. The NMR tube was attached to a double manifold vacuum line and degassed by two freeze-pump-thaw cycles. An atmosphere of CO (1 atm) was applied to the tube, and the reaction was monitored by ³¹P{¹H} NMR spectroscopy. The yellow solution turned brown and complete conversion of **3** to **5** occurred within 2 min at ambient temperature. The CO atmosphere and benzene-*d*₆ were removed under vacuum. The brown solid was brought into a glove box, dissolved in pentane (~5 mL) and filtered through a Kimwipe (packed into pipette to act as a filter) (to remove any Rh black particles). The solvent was removed *in vacuo*, yielding a light brown powder. Light yellow rectangular crystals of **5** were grown



from a saturated benzene solution stored in a sealed 20 mL scintillation vial at ambient temperature for 3 days. Yield: 23.3 mg, 91%. ^1H NMR (300 MHz, C_6D_6): δ 7.47 (dd, $^3J_{\text{PH}} = 11.6$, $^3J_{\text{HH}} = 7.3$ Hz, 4H, *ortho*-Ph), 6.93 (t, $^3J_{\text{HH}} = 7.3$ Hz, 2H, *para*-Ph), 6.83 (ov dt, $^3J_{\text{HH}} = 7.7$, $^3J_{\text{PH}} = 2.6$ Hz, 4H, *meta*-Ph), 6.80 (s, 4H, Mes-CH), 2.44 (s, 12H, *ortho*-Mes- CH_3), 2.13 (s, 6H, *para*-Mes- CH_3). ^1H NMR (300 MHz, C_6D_6): δ 7.47 (d, $^3J_{\text{HH}} = 7.4$ Hz, 4H, *ortho*-Ph), 6.93 (t, $^3J_{\text{HH}} = 7.3$ Hz, 2H, *para*-Ph), 6.83 (d, $^3J_{\text{HH}} = 7.6$ Hz, 4H, *meta*-Ph), 6.80 (s, 4H, Mes-CH), 2.44 (s, 12H, *ortho*-Mes- CH_3), 2.13 (s, 6H, *para*-Mes- CH_3). $^{13}\text{C}\{^1\text{H}\}$ NMR (75 MHz, C_6D_6): δ 187.21 (d, $^1J_{\text{RhC}} = 69.8$ Hz, $\text{C}\equiv\text{O}$), 143.87 (s, *ipso*-Mes-C-P), 136.98 (d, $^1J_{\text{PC}} = 90.6$ Hz, *ipso*-Ph), 135.97 (d, $^3J_{\text{PC}} = 4.9$ Hz, *ortho-*ipso**-Mes-C- CH_3), 133.21 (d, $^5J_{\text{PC}} = 2.9$ Hz, *para-*ipso**-Mes-C- CH_3), 132.01 (d, $^4J_{\text{PC}} = 2.7$ Hz, *meta*-Ph), 131.47 (d, $^3J_{\text{PC}} = 9.5$ Hz, *ortho*-Ph), 130.26 (d, $^5J_{\text{PC}} = 1.9$ Hz, *para*-Ph), 128.39 (d, $^4J_{\text{PC}} = 11.6$ Hz, Mes-CH, partially obscured by solvent resonance), 22.43 (s, *ortho*-Mes- CH_3), 21.15 (s, *para*-Mes- CH_3). $^{31}\text{P}\{^1\text{H}\}$ NMR (122 MHz, C_6D_6): δ 39.8 (d, $^2J_{\text{RhP}} = 15.1$ Hz). IR ν_{CO} (cm^{-1}): 2053, 1996. Anal. Calcd. for $\text{C}_{33}\text{H}_{26}\text{PN}_2\text{O}_2\text{Rh}$: C: 63.26 H: 5.76 N: 4.47%; found: C: 66.83 H: 5.53 N: 4.72%.

Synthesis of $[\text{Ph}_2\text{P}(\text{NC}_{10}\text{H}_{15})_2]\text{Rh}(\text{CO})_2$ (**6**)

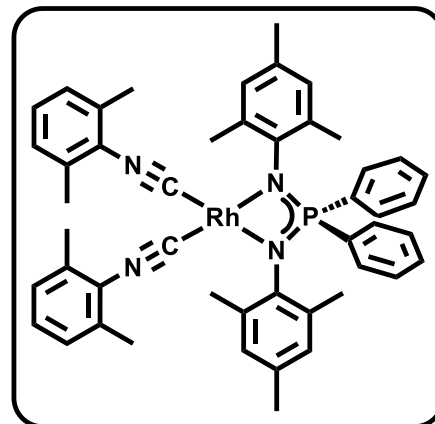
Complex **4** (44.7 mg, 0.0573 mmol) was added to a J. Young NMR tube and dissolved in 0.5 mL of benzene- d_6 . The NMR tube was attached to a double manifold vacuum line and degassed by two freeze-pump-thaw cycles. An atmosphere of CO (1 atm) was applied to the tube and



monitored by $^{31}\text{P}\{^1\text{H}\}$ NMR spectroscopy. The solution turned dark brown and reached complete conversion within 20 min at ambient temperature. The atmosphere of CO and benzene- d_6 were removed under vacuum. The brown solid was brought into a glove box, dissolved in pentane (~5 mL) and filtered through a Kimwipe (packed into pipette to act as a filter) (to remove any Rh black particles). The pentane was removed under vacuum resulting in a brown powder. Complex **6** was crystallized as yellow rectangular crystals grown from a saturated benzene solution stored in a sealed 20 mL scintillation vial at ambient temperature for 1 week. Yield: 36.5 mg, 87%. ^1H NMR (700 MHz, C_6D_6): δ 8.26 (dd, $^3J_{\text{PH}} = 9.8$, $^3J_{\text{HH}} = 8.5$ Hz, 4H, *ortho*-Ph), 7.15–7.10 (m, 6H, *meta*- and *para*-Ph), 1.80 (s, 6H, Ad- H^α), 1.71 (s, 12H, Ad- H^β), 1.34 (s, 12H, Ad- H^δ). $^1\text{H}\{^{31}\text{P}\}$ NMR (700 MHz, C_6D_6): δ 8.26 (t, $^3J_{\text{HH}} = 6.8$ Hz, 4H, *ortho*-Ph), 7.16–7.10 (m, 6H, *meta*- and *para*-Ph), 1.80 (s, 6H, Ad- H^α), 1.71 (s, 12H, Ad- H^β), 1.35 (s, 12H, Ad- H^δ). ^{13}C NMR (176 MHz, C_6D_6): δ 189.05 (d, $^1J_{\text{RhC}} = 67.4$ Hz, $\text{C}\equiv\text{O}$), 137.54 (d, $^1J_{\text{PC}} = 83.3$ Hz, *ipso*-Ph), 132.98 (d, $^2J_{\text{PC}} = 9.5$ Hz, *ortho*-Ph), 131.14 (d, $^3J_{\text{PC}} = 3.3$ Hz, *meta*-Ph), 127.98 (s, *para*-Ph), 52.15 (s, Ad- C^ω), 47.30 (d, $^3J_{\text{PC}} = 7.3$ Hz, Ad- C^β), 36.06 (s, Ad- C^δ), 30.28 (s, Ad- C^γ). $^{31}\text{P}\{^1\text{H}\}$ NMR (122 MHz, C_6D_6): δ 49.8 (d, $^2J_{\text{RhP}} = 10.0$ Hz). IR ν_{CO} (cm^{-1}): 2033, 1957. Anal. Calcd. for $\text{C}_{35}\text{H}_{44}\text{PN}_2\text{O}_2\text{Rh}$: C: 63.83 H: 6.73 N: 4.25%; found: C: 63.47 H: 6.60 N: 4.48%.

Synthesis of $[\text{Ph}_2\text{P}(\text{N}(2,4,6\text{-Me}_3\text{C}_6\text{H}_2))_2]\text{Rh}(\text{CNAr})_2$ (**7**)

Complex **3** (57.1 mg, 0.0754 mmol) was added to a 20 mL scintillation vial containing 2,6-dimethylphenylisocyanide (20.8 mg, 0.0158 mmol). The vial was then placed in the freezer ($-35\text{ }^\circ\text{C}$), cold pentane (5 mL) was added and placed back into the freezer. An orange solution with an orange precipitate

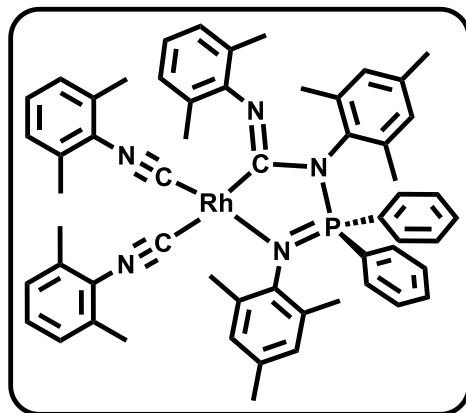


was observed after 16 h. Benzene (5 mL) was added, and the mixture was filtered through a Kimwipe (packed into pipette to act as a filter) to yield an orange solution. The solvent was removed under vacuum, resulting in a yellow solid. The solid was washed with cold pentane (4×2 mL), and residual solvent was removed *in vacuo*. Complex **7** was crystallized as yellow cubes from a saturated (1:1) benzene:pentane solution stored in a sealed 20 mL scintillation vial at ambient temperature for 3 days. Yield: 50.0 mg, 75%. ^1H NMR (700 MHz, C_6D_6): δ 7.81–7.71 (m, 4H, *ortho*-Ph), 6.97 (t, $^3J_{\text{HH}} = 7.4$ Hz, 2H, *para*-Ph), 6.92 (td, $^3J_{\text{HH}} = 7.5$, $^4J_{\text{PH}} = 2.5$ Hz, 4H, *meta*-Ph), 6.83 (s, 4H, Mes-CH), 6.68 (t, $^3J_{\text{HH}} = 7.6$ Hz, 2H, *para*-CH Ar-N \equiv C), 6.59 (d, $^3J_{\text{HH}} = 7.5$ Hz, 4H, *meta*-CH Ar-N \equiv C), 2.68 (s, 12H, *ortho*-Mes-CH $_3$), 2.18 (s, 6H, *para*-Mes-CH $_3$), 1.93 (s, 12H, *ortho*-CH $_3$ Ar-N \equiv C). $^1\text{H}\{^{31}\text{P}\}$ NMR (700 MHz, C_6D_6): δ 7.81–7.73 (m, 4H, *ortho*-Ph), 6.97 (t, $^3J_{\text{HH}} = 7.4$ Hz, 2H, *para*-Ph), 6.92 (t, $^3J_{\text{HH}} = 7.6$ Hz, 4H, *meta*-Ph), 6.83 (s, 4H, Mes-CH), 6.68 (t, $^3J_{\text{HH}} = 7.6$ Hz, 2H, *para*-CH Ar-N \equiv C), 6.59 (d, $^3J_{\text{HH}} = 7.5$ Hz, 4H, *meta*-CH Ar-N \equiv C), 2.68 (s, 12H, *ortho*-Mes-CH $_3$), 2.18 (s, 6H, *para*-Mes-CH $_3$), 1.93 (s, 12H, *ortho*-CH $_3$ Ar-N \equiv C). $^{13}\text{C}\{^1\text{H}\}$ NMR (176 MHz, C_6D_6): δ 161.97 (d, $^1J_{\text{RhC}} = 71.3$ Hz, Ar-N \equiv C), 145.75 (d, $^2J_{\text{PC}}$

= 2.1 Hz, *ipso*-Mes-C-P), 139.45 (d, $^1J_{PC}$ = 89.5 Hz, *ipso*-Ph), 136.67 (d, $^3J_{PC}$ = 5.0 Hz, *ortho-ipso*-Mes-C-CH₃), 134.44 (s, *ortho-ipso*-C-CH₃ Ar-N≡C), 131.51 (d, $^3J_{PC}$ = 9.2 Hz, *ortho*-Ph), 131.35 (d, $^5J_{PC}$ = 2.9 Hz, *para-ipso*-Mes-C-CH₃), 131.05 (d, $^2J_{PC}$ = 2.5 Hz, *para*-Ph), 130.77 (s, *ipso*-C-N≡C), 129.82 (d, $^4J_{PC}$ = 1.8 Hz, Mes-CH), 128.68 (s, *meta*-Ph, partially obscured by solvent resonance), 127.98 (s, *para*-CH Ar-N≡C), 126.56 (s, *meta*-CH Ar-N≡C), 22.86 (s, *ortho*-Mes-CH₃), 21.20 (s, *para*-Mes-CH₃), 18.86 (s, *ortho*-CH₃ Ar-N≡C). $^{31}\text{P}\{^1\text{H}\}$ NMR (284 MHz, C₆D₆): δ 25.1 (d, $^2J_{\text{RhP}}$ = 13.7 Hz). IR ν_{CN} (cm⁻¹): 2035 1964. Attempts to obtain high-quality elemental analyses (within 3% of computed values) for this compound have been unsuccessful.

Synthesis of [Ph₂P(N(2,4,6-Me₃C₆H₂))₂]Rh(CNAr)₃ (**8**)

Complex **3** (41.2 mg, 0.0607 mmol) and 2,6-dimethylphenylisocyanide (15.9 mg, 0.121 mmol) were added to a J. Young NMR tube and dissolved in 0.5 mL of benzene-*d*₆. The reaction was monitored by $^{31}\text{P}\{^1\text{H}\}$ NMR spectroscopy, and consumption of (**23**) was observed within 1 h.

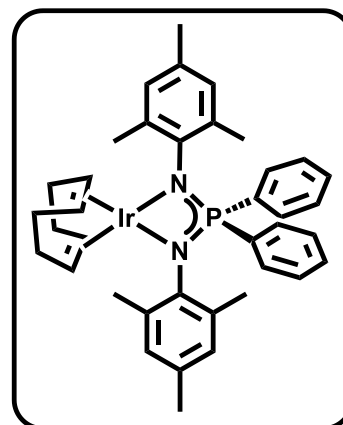


Another equivalent of 2,6-dimethylphenylisocyanide (20.8 mg, 0.0158 mmol) was added, and complete consumption of **3** and **8** was observed within 15 min. The tube was placed under vacuum for 1 h, resulting in a yellow solid. Yellow rectangular crystals of **8** were grown from a saturated benzene solution stored in a sealed 20 mL scintillation vial at ambient temperature for 3 days. Yield: 39.8 mg, 69%. ^1H NMR (700 MHz, C₆D₆): δ 8.21–

8.11 (m, 4H, *ortho*-Ph), 6.97 (t, $^3J_{\text{HH}} = 6.9$ Hz, 2H, *para*-Ph), 6.91 (td, $^3J_{\text{HH}} = 7.6$, $^4J_{\text{HP}} = 2.9$ Hz, 4H), 6.88–6.84 (m, 2H, *meta*-CH Ar–N≡C), 6.83 (s, 1H, *para*-CH Ar–N≡C), 6.82–6.73 (m, 3H, *meta*- and *para*-CH Ar–N≡C), 6.72 (s, 2H, Mes-CH), 6.60 (s, 2H, Mes-CH), 6.52–6.47 (m, 2H, *meta*-CH Ar–N≡C), 6.44–6.40 (m, 1H, *para*-CH Ar–N≡C), 2.76 (s, 6H, *ortho*-CH₃ Ar–N≡C), 2.57 (s, 6H, *ortho*-Mes-CH₃), 2.39 (s, 6H, *ortho*-CH₃ Ar–N≡C), 2.15 (s, 6H, *ortho*-Mes-CH₃), 2.08 (s, 3H, *para*-Mes-CH₃), 2.03 (s, 3H, *para*-Mes-CH₃), 1.81 (s, 6H, *ortho*-CH₃ Ar–N≡C). $^{13}\text{C}\{^1\text{H}\}$ NMR (176 MHz, C₆D₆): δ 153.99 (s, Ar–N≡C), 147.99 (s, *ortho*-*ipso*-Mes-C–CH₃), 145.06 (s, *ipso*-Mes-C–P), 138.95 (s, *ipso*-Ph), 136.66 (s, *ortho*-*ipso*-C–CH₃ Ar–N≡C), 135.97 (s, *para*-*ipso*-Mes-C–CH₃), 135.80 (s), 134.37 (s, *ortho*-*ipso*-C–CH₃ Ar–N≡C), 134.17 (s, *ortho*-*ipso*-C–CH₃ Ar–N≡C), 133.70 (d, $^2J_{\text{PC}} = 9.2$ Hz, *ortho*-Ph), 131.40 (s, *para*-*ipso*-Mes-C–CH₃), 131.10 (d, $^3J_{\text{PC}} = 2.1$ Hz, *meta*-Ph), 130.80 (s, *ipso*-C–N≡C), 130.65 (s, *ipso*-C–N≡C), 130.07 (s, *ipso*-C–N≡C), 129.15 (s, *para*-Ph), 128.91 (s, Mes-CH), 128.23 (s, *para*-CH Ar–N≡C), 127.98 (s, *meta*-CH Ar–N≡C), 127.29 (s, *meta*-CH Ar–N≡C), 127.05 (s, Mes-CH), 126.98 (s, *meta*-CH Ar–N≡C), 126.62 (s, *para*-CH Ar–N≡C), 120.42 (s, *para*-CH Ar–N≡C), 22.58 (s, *ortho*-Mes-CH₃), 21.02 (s, *ortho*-CH₃ Ar–N≡C), 20.63 (s, *para*-Mes-CH₃), 20.27 (s, *para*-Mes-CH₃), 20.20 (s, *ortho*-Mes-CH₃), 19.02 (br s, *ortho*-CH₃ Ar–N≡C), 18.36 (br s, *ortho*-CH₃ Ar–N≡C), 18.16 (s, *ortho*-CH₃ Ar–N≡C). The resonance for Rh–C=N was not found or confirmed in the $^{13}\text{C}\{^1\text{H}\}$ NMR spectrum. $^{31}\text{P}\{^1\text{H}\}$ NMR (122 MHz, C₆D₆): δ 15.2 (s). IR ν_{CN} (cm⁻¹): 2106, 2044, 1566. Anal. Calcd. for C₅₇H₅₉PN₅Rh: C: 72.22 H: 6.72 N: 7.39%; found: C: 72.49 H: 6.47 N: 7.43%.

Synthesis of [Ph₂P(N(2,4,6-Me₃C₆H₂))₂]Ir(COD) (**9**)

Li[Ph₂P(NMes)₂] (73.9 mg, 0.167 mmol) and [IrCl(COD)]₂ (56.1 mg, 0.0840 mmol) were weighed into a two-necked round bottom flask attached to a swivel frit apparatus. Benzene (~20 mL) was transferred under reduced pressure to the vessel. The bright orange solution was left to



stir at ambient temperature under a positive Ar atmosphere. After 16 h, the mixture was filtered through the frit, and the solvent was removed from the transparent orange solution.

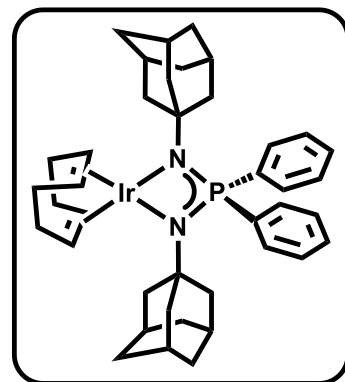
Yellow plate-shaped crystals of **9** were grown from a saturated pentane solution stored in a sealed 20 mL scintillation vial at ambient temperature for 3 days. Yield: 123 mg, 90%.

¹H NMR (700 MHz, C₆D₆): δ 7.66–7.58 (m, 4H, *ortho*-Ph), 6.94 (td, ³J_{HH} = 7.4, ⁶J_{PH} = 1.2 Hz, 2H, *para*-Ph), 6.86 (ov td, ³J_{HH} = 7.8, ⁵J_{PH} 2.8 Hz, 4H, *meta*-Ph), 6.84 (ov s, 4H, Mes-CH), 3.41–3.31 (br m, 4H, COD-CH), 2.50 (s, 12H, *ortho*-Mes-CH₃), 2.39–2.31 (br m, 4H, COD-CH₂), 2.19 (s, 6H, *para*-Mes-CH₃), 1.60–1.49 (m, 4H, COD-CH₂). ¹H NMR (700 MHz, C₆D₆): δ 7.63 (t, ³J_{HH} = 8.1 Hz, 4H, *ortho*-Ph), 6.94 (ov dd, ³J_{HH} = 7.4 Hz, 2H, *para*-Ph), 6.87 (ov t, ³J_{HH} = 7.3 Hz, 4H, *meta*-Ph), 6.85 (ov s, 4H, Mes-CH), 3.41–3.31 (br m, 4H, COD-CH), 2.50 (s, 12H, *ortho*-Mes-CH₃), 2.39–2.29 (br m, 4H, COD-CH₂), 2.19 (s, 6H, *para*-Mes-CH₃), 1.60–1.49 (m, 4H, COD-CH₂). ¹³C{¹H} NMR (176 MHz, C₆D₆): δ 139.71 (d, ²J_{PC} = 4.4 Hz, *ipso*-Mes-C-P), 137.79 (d, ¹J_{PC} = 88.4 Hz, *ipso*-Ph), 136.12 (d, ³J_{PC} = 4.6 Hz, *ortho-ipso*-Mes-C-CH₃), 132.42 (d, ⁵J_{PC} = 2.8 Hz, *para-ipso*-Mes-C-CH₃), 131.12 (d, ⁴J_{PC} = 2.6 Hz, *para*-Ph), 130.55 (d, ²J_{PC} = 9.3 Hz, *ortho*-Ph), 129.41 (d, ⁵J_{PC} = 1.6 Hz, *meta*-Ph), 128.32 (d, ⁴J_{PC} = 10.5 Hz, Mes-CH, partially obscured by solvent

resonance), 58.24 (s, COD-CH), 32.12 (s, COD-CH₂), 21.39 (d, ⁴J_{PC} = 1.0 Hz, *ortho*-Mes-CH₃), 20.45 (s, *para*-Mes-CH₃). ³¹P{¹H} NMR (284 MHz, C₆D₆): δ 40.9 (s). Anal. Calcd. for C₃₉H₄₈PN₂Ir: C: 60.99 H: 6.30 N: 3.65%; found: C: 60.82 H: 6.17 N: 3.85%.

Synthesis of [Ph₂P(NC₁₀H₁₅)₂]Ir(COD) (**10**)

Compound **2** (97.1 mg, 0.198 mmol), and [IrCl(COD)]₂ (66.3 mg, 0.099 mmol) were added to a 20 mL scintillation vial. Pentane (8 mL) was added, and the vial was placed in the freezer (−35 °C). After 16 h, the reddish-orange mixture was filtered through a Kimwipe (packed into pipette

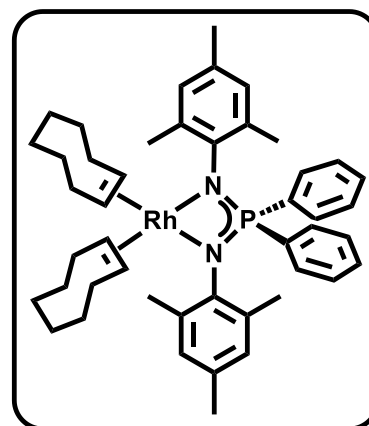


to act as a filter), removing the precipitate from the orange solution. Complex **10** was crystallized as colourless block crystals from a saturated benzene solution stored in a sealed 20 mL scintillation vial at ambient temperature for 3 days. Yield: 136 mg, 78%. ¹H NMR (300 MHz, C₆D₆): δ 8.50 (ov dt, ³J_{PH} = 10.0, ³J_{HH} = 6.7 Hz, 4H, *ortho*-Ph), 7.15–7.08 (m, 6H, *meta*- and *para*-Ph), 4.72 (s, 4H, COD-CH), 2.53–2.38 (br m, 4H, COD-CH₂), 1.76 (s, 6H, Ad-*H*^α), 1.67 (s, 12H, Ad-*H*^β), 1.64–1.52 (ov m, 4H, COD-CH₂), 1.34 (s, 12H, Ad-*H*^δ). ¹H{³¹P} NMR (300 MHz, C₆D₆): δ 8.63–8.37 (m, 4H, *ortho*-Ph), 7.16–7.06 (m, 6H, *meta*- and *para*-Ph), 4.72 (s, 4H, COD-CH), 2.57–2.35 (br m, 4H, COD-CH₂), 1.76 (s, 6H, Ad-*H*^α), 1.67 (s, 12H, Ad-*H*^β), 1.64–1.51 (ov m, 4H, COD-CH₂), 1.34 (s, 12H, Ad-*H*^δ). ¹³C{¹H} NMR (75 MHz, C₆D₆): δ 140.26 (d, ¹J_{PC} = 77.8 Hz, *ipso*-Ph), 133.62 (d, ²J_{PC} = 9.3 Hz, *ortho*-Ph), 131.53 (d, ³J_{PC} = 2.8 Hz, *meta*-Ph), 128.73 (s, *para*-Ph, partially obscured by solvent resonance), 57.75 (d, ²J_{PC} = 3.7 Hz, Ad-*C*^α), 53.45 (s, COD-CH), 46.63 (d, ³J_{PC} =

2.0 Hz, Ad- C^{β}), 36.90 (s, Ad- C^{δ}), 32.86 (s, COD- CH_2), 30.98 (s, Ad- C^{γ}). $^{31}P\{^1H\}$ NMR (122 MHz, C_6D_6): δ 66.7 (s). Anal. Calcd. for $C_{41}H_{56}PN_2Ir$: C: 61.55 H: 7.06 N: 3.50%; found: C: 61.55 H: 6.98 N: 3.26%.

Synthesis of $[Ph_2P(N(2,4,6-Me_3C_6H_2))_2Rh(COE)_2]$ (13)

A 20 mL scintillation vial containing $Li[Ph_2P(NMes)_2]$ (108.2 mg, 0.236 mmol), and $[RhCl(COE)_2]_2$ (84.7 mg, 0.118 mmol) was placed in a freezer ($-35\text{ }^{\circ}C$). A cold 1:1 solution of pentane and THF (8 mL) was added, and the vial was left in the freezer. After



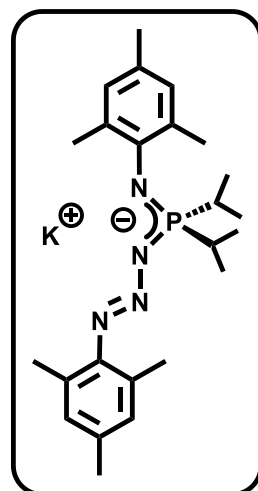
1 h, the dark brown solution was filtered through a Kimwipe (packed into pipette to act as a filter) (to remove any solid particles). Yellow-orange crystalline blocks were seen forming on the sides of the vial within one week at $-35\text{ }^{\circ}C$. The crystals were vacuum sensitive and quickly decomposed to the neutral ligand $[Ph_2P(NMes)(NHMe)]$. Argon was flowed over the crystals in an attempt to remove any volatile solvents. Yield: 35.1 mg, 19%. 1H NMR (700 MHz, C_6D_6): δ 7.74–7.65 (m, 4H, *ortho*-Ph), 6.98–6.93 (m, 2H, *para*-Ph), 6.92–6.89 (m, 4H, *para*-Ph), 6.86 (s, 4H, Mes-*CH*), 5.65 (m, 1H, non-coordinated COE), 3.58 (s, 4H, THF-*CH_2*), 3.28 (br s, 2H, COE-*CH*), 2.97 (br s, 2H, COE-*CH*), 2.64 (br s, 6H, *ortho*-Mes- CH_3), 2.59 (br s, 3H, *para*-Mes- CH_3), 2.39 (s, 6H, *ortho*-Mes- CH_3), 2.16 (br s, 3H, *para*-Mes- CH_3), 2.13 (s, 4H, non-coordinated COE), 2.10–1.97 (m, 2H, non-coordinated COE), 1.64 (br s, 4H, COE-*CH_2*), 1.53–1.44 (m, 4H, non-coordinated COE), 1.41 (s, 4H, THF- CH_3), 1.40–1.27 (m, 4H, COE-*CH_2*), 1.29–1.22 (m, 1H, pentane),

1.17 (br s, 8H, COE-CH₂), 1.00 (br s, 4H, COE-CH₂), 0.88 (t, *J* = 7.2 Hz, 1H, pentane). ³¹P{¹H} NMR (284 MHz, C₆D₆): δ 27.5 (d, ²*J*_{RHP} = 9.6 Hz). ³¹C{¹H} characterization of (13) is not reported as the complex is not stable in solution at ambient temperature, decomposing entirely to neutral ligand within 6 h. Attempts to obtain high-quality elemental analyses (within 3% of computed values) for this compound have been unsuccessful.

6.10 Synthetic Experimental Procedures Pertaining to Chapter 3

Synthesis of K[ⁱPr₂P(N(2,4,6-Me₃C₆H₂))₂] (14)

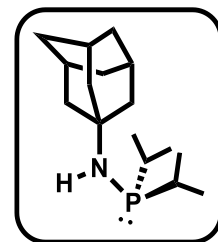
Tetrahydrofuran (~40 mL) was transferred *in vacuo* to a two-necked round bottom flask containing MesNHP^{*i*}Pr₂ (686 mg, 2.73 mmol), an off-white solid and KH (110 mL, 2.73 mmol), resulting in a light yellow solution and solid KH powder. The flask was then heated to 60 °C under a positive argon atmosphere for 16 h with constant stirring. Afterwards, MesN₃ (440 mg, 2.73 mmol), an orange liquid, was injected into the flask rapidly within 2 min. The orange solution was then left stirring at 60 °C while remaining under an argon atmosphere for 16 h. THF was removed *in vacuo*, resulting in a light brown solid. The brown solid was washed with pentane (4 × 2 mL) in a glove box and dried *in vacuo*, yielding a beige powder. Yield: 1.06 g, 86%. ¹H NMR (300 MHz, C₆D₆): δ 6.87 (s, 2H, N-Mes-CH), 6.80 (s, 2H, N₃-Mes-CH), 2.30 (ov s, 3H, N₃-*para*-Mes-CH₃), 2.29 (ov s, 3H, N-*para*-Mes-CH₃), 2.20 (s, 6H, N₃-*ortho*-Mes-CH₃), 1.98 (s, 6H, N-*ortho*-Mes-CH₃), 1.90 (ov sp, ³*J*_{HH} = 7.1 Hz, 2H), 0.99



(ov dd, $^2J_{\text{PH}} = 14.0$, $^3J = 7.1$ Hz, 12H, $\text{CH}(\text{CH}_3)_2$). $^{13}\text{C}\{^1\text{H}\}$ NMR (75 MHz, C_6D_6): δ 149.43 (s, N_3 -*ipso*-Mes-C-P), 147.80 (d, $^3J_{\text{PC}} = 4.1$ Hz, N-*ortho-ipso*-Mes-C- CH_3), 133.25 (s, N_3 -*ortho-ipso*-Mes-C- CH_3), 131.67 (d, $^2J_{\text{PC}} = 7.0$ Hz, N-*ipso*-Mes-C-P), 130.55 (s, N_3 -*para-ipso*-Mes-C- CH_3), 129.92 (s, N_3 -Mes-CH), 129.74 (s, N-Mes-CH), 126.70 (d, $^3J_{\text{PC}} = 2.2$ Hz, N-*para-ipso*-Mes-C- CH_3), 28.67 (d, $^1J_{\text{PC}} = 81.0$ Hz, $\text{CH}(\text{CH}_3)_2$), 21.93 (s, N_3 -*ortho*-Mes- CH_3), 21.93 (s, N_3 -*para*-Mes- CH_3), 21.44 (s, N-*para*-Mes- CH_3), 19.07 (s, N-*ortho*-Mes- CH_3), 17.90 (d, $^2J_{\text{PC}} = 3.4$ Hz, $\text{CH}(\text{CH}_3)_2$), 17.50 (d, $^2J_{\text{PC}} = 2.7$ Hz, $\text{CH}(\text{CH}_3)_2$). $^{31}\text{P}\{^1\text{H}\}$ NMR (122 MHz, C_6D_6): δ 22.9 (s). Anal. Calcd. for $\text{C}_{27}\text{H}_{48}\text{KN}_4\text{P}$: C: 64.34 H: 8.64 N: 12.01%; found: C: 64.89 H: 8.98 N: 11.88%.

Synthesis of $^i\text{Pr}_2\text{PNHC}_{10}\text{H}_{15}$ (15)

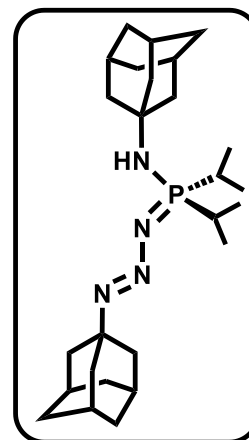
AdNH₂ (315 mg, 2.09 mmol) was weighed into a two-necked round bottom flask attached to a swivel frit apparatus. The flask was cooled to -94 °C (liquid nitrogen/acetone), diethylether (~60 mL) was transferred to the flask under reduced pressure, and $^n\text{BuLi}$ (0.92 mL, 2.23 mmol, 2.5M in hexanes) was injected dropwise over ~10 min. The opaque white mixture was then left in the cold bath to slowly warm to ambient temperature. After 1 h, the vessel was cooled to -94 °C and chlorodiisopropylphosphine (0.33 mL, 2.09 mmol, 0.959 g/mL) was injected dropwise into the flask over two min. The solution was left to slowly warm to ambient temperature while remaining in the cold bath. After 16 h, the Et₂O was removed *in vacuo* from the yellow opaque mixture resulting in a beige oily solid. Toluene (~20 mL) was then transferred to the flask under reduced pressure, resulting in a yellow solution with a white



precipitate. The mixture was filtered through the frit, yielding a transparent yellow solution. Residual solvent was removed under vacuum, resulting in a beige liquid; the liquid was found to solidify at $-35\text{ }^{\circ}\text{C}$. Yield: 494 mg, 89%. ^1H NMR (300 MHz, C_6D_6): δ 1.98 (br s, 3H, (Ad- H^{α})), 1.70 (d, $^4J_{\text{HH}} = 2.3\text{ Hz}$, 6H, Ad- H^{β}), 1.56 (d, $^4J_{\text{HH}} = 2.7\text{ Hz}$, 6H, (Ad- H^{δ})), 1.40 (dsp, $^3J_{\text{HH}} = 7.0$, $^2J_{\text{HP}} = 2.0\text{ Hz}$, 2H, $\text{CH}(\text{CH}_3)_2$), 1.13–0.97 (m, 12H, $\text{CH}(\text{CH}_3)_2$), 0.93 (d, $J = 11.2\text{ Hz}$, 1H, NH). $^1\text{H}\{^3\text{P}\}$ NMR (300 MHz, C_6D_6): δ 1.98 (br s, 3H, Ad- H^{α}), 1.70 (d, $^4J_{\text{HH}} = 2.8\text{ Hz}$, 6H, Ad- H^{β}), 1.56 (d, $^4J_{\text{HH}} = 2.7\text{ Hz}$, 6H, Ad- H^{δ}), 1.40 (sp, $^3J_{\text{HH}} = 7.0\text{ Hz}$, 2H, $\text{CH}(\text{CH}_3)_2$), 1.07 (d, $^3J_{\text{HH}} = 7.1\text{ Hz}$, 6H, $\text{CH}(\text{CH}_3)_2$), 1.01 (d, $^3J_{\text{HH}} = 6.9\text{ Hz}$, 6H, $\text{CH}(\text{CH}_3)_2$), 0.93 (s, 1H, NH). $^{13}\text{C}\{^1\text{H}\}$ NMR (75 MHz, C_6D_6): δ 49.73 (d, $^2J_{\text{PC}} = 16.8\text{ Hz}$, Ad- C^{α}), 47.34 (d, $^3J_{\text{PC}} = 7.5\text{ Hz}$, Ad- C^{β}), 37.14 (s, Ad- C^{δ}), 30.89 (d, $^4J_{\text{PC}} = 0.9\text{ Hz}$, Ad- C^{γ}), 26.78 (d, $^1J_{\text{PC}} = 12.4\text{ Hz}$, $\text{CH}(\text{CH}_3)_2$), 20.20 (d, $^2J_{\text{PC}} = 21.6\text{ Hz}$, $\text{CH}(\text{CH}_3)_2$), 17.81 (d, $^2J_{\text{PC}} = 7.9\text{ Hz}$, $\text{CH}(\text{CH}_3)_2$). $^{31}\text{P}\{^1\text{H}\}$ NMR (122 MHz, C_6D_6): δ 38.5 (s). Anal. Calcd. for $\text{C}_{16}\text{H}_{30}\text{NP}$: C: 71.87 H: 11.31 N: 5.24%; found: C: 71.94 H: 11.21 N: 5.04%.

Synthesis of $^i\text{Pr}_2\text{P}(\text{N}_3\text{C}_{10}\text{H}_{15})(\text{NHC}_{10}\text{H}_{15})$ (**16**)

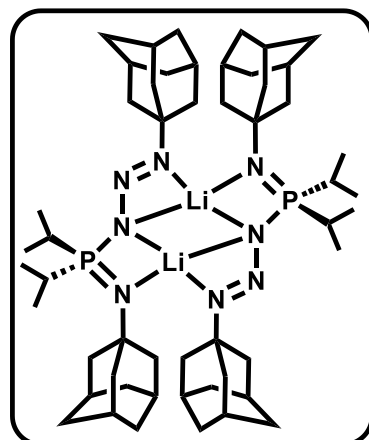
AdN_3 (408 mg, 2.30 mmol) and **15** (617 mg, 2.30 mmol) were weighed into a two-necked round bottom flask. Toluene ($\sim 20\text{ mL}$) was added to the vessel under reduced pressure, yielding a transparent yellow solution and heated to $80\text{ }^{\circ}\text{C}$. After 16 h, the vessel was cooled to ambient temperature, and the solvent was removed *in vacuo* from the cloudy mixture, resulting in a beige solid. The solid was brought into a glove box, washed with pentane ($4 \times 2\text{ mL}$), and any residual solvent



was removed under vacuum. The resultant off-white solid was insoluble in aromatic and aliphatic solvents. Compound **16** crystallized as yellow needles from a saturated CH₂Cl₂ solution. Yield: 914 mg, 89%. ¹H NMR (700 MHz, CDCl₃): δ 2.33 (dsp, ²J_{PH} = 14.4, ³J_{HH} = 7.2 Hz, 2H, CH(CH₃)₂), 2.09 (br s, 3H, N₃-Ad-H^γ), 2.03 (br s, 3H, NH-Ad-H^γ), 1.85 (d, ³J_{HH} = 2.4 Hz, 6H, NH-Ad-H^β), 1.83 (d, ³J_{HH} = 2.4 Hz, 3H, N₃-Ad-H^β), 1.69 (ov t, ³J_{HH} = 12.2 Hz, 6H, N₃-Ad-H^δ), 1.64–1.56 (m, 3H, NH-Ad-H^δ), 1.29 (dd, ³J_{HH} = 7.2, ³J_{PH} = 2.2 Hz, 12H, CH(CH₃)₂), 1.27 (dd, ³J_{HH} = 7.2, ³J_{PH} = 2.5 Hz, 6H, CH(CH₃)₂). NH resonance is not found in the spectrum. ¹H{³¹P} NMR (700 MHz, CDCl₃): δ 2.39–2.30 (m, 2H, CH(CH₃)₂), 2.09 (br s, 3H, N₃-Ad-H^γ), 2.04 (br s, 3H, NH-Ad-H^γ), 1.85 (d, ³J_{HH} = 1.8 Hz, 6H, NH-Ad-H^β), 1.83 (d, ³J_{HH} = 2.0 Hz, 3H, N₃-Ad-H^β), 1.69 (ov t, ³J_{HH} = 12.2 Hz, 6H, N₃-Ad-H^δ), 1.65–1.54 (m, 6H, NH-Ad-H^δ), 1.33–1.20 (m, 12H, CH(CH₃)₂). NH resonance is not found in the spectrum. ¹³C{¹H} NMR (176 MHz, CDCl₃): δ 60.61 (s, N₃-Ad-C^α), 52.63 (s, NH-Ad-C^α), 45.69 (d, ³J_{PC} = 2.3 Hz, NH-Ad-C^β), 42.64 (s, N₃-Ad-C^β), 37.18 (s, N₃-Ad-C^δ), 36.21 (s, N₃-Ad-C^δ), 30.06 (s, ⁴J_{PC} = 18.1 Hz, NH-Ad-C^γ), 29.95 (s, N₃-Ad-C^γ), 26.60 (d, ¹J_{PC} = 76.9 Hz, CH(CH₃)₂), 17.73 (d, ³J_{PC} = 2.8 Hz, CH(CH₃)₂), 17.15 (d, ²J_{PC} = 2.5 Hz, CH(CH₃)₂). ³¹P{¹H} NMR (284 MHz, CDCl₃): δ 50.7 (s). Anal. Calcd. for C₂₆H₄₅N₄P: C: 70.23 H: 10.20 N: 12.60%; found: C: 69.95 H: 10.38 N: 12.64%.

Synthesis of $\text{Li}_2[\text{Pr}_2\text{P}(\text{N}_3\text{C}_{10}\text{H}_{15})(\text{NC}_{10}\text{H}_{15})_2]$ (**17**)

THF (~50 mL) was transferred *in vacuo* to a two-necked round bottom flask containing **16** (553 mg, 1.24 mmol), resulting in a suspension. The flask was cooled to $-94\text{ }^\circ\text{C}$ (liquid nitrogen/acetone), $n\text{BuLi}$ (0.17 mL, 1.24 mmol, 2.5M in hexanes) was injected dropwise over ~5 min, and the mixture was left to slowly warm to ambient

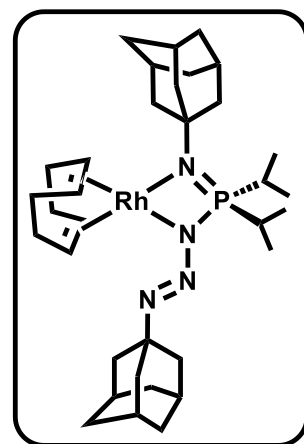


temperature while remaining in the cold. After 16 h, the THF was removed under vacuum, resulting in a beige solid, brought into a glove box, washed with pentane ($4 \times 2\text{ mL}$), and removed any residual solvent under vacuum. The white solid was sparingly soluble in CDCl_3 ; hence characterization is done in $\text{THF-}d_8$. Slightly yellow diamond-like crystals of **15** were grown from a 1:1 THF:DCM solution. Yield: 521 mg, 93%. ^1H NMR (300 MHz, $\text{THF-}d_8$): δ 2.40 (dsp, $^2J_{\text{PH}} = 14.5$, $^3J_{\text{HH}} 7.2\text{ Hz}$, 6H, $\text{CH}(\text{CH}_3)_2$), 2.05 (br s, 3H, $\text{N}_3\text{-Ad-}H'$), 1.99 (s, 3H, $\text{N-Ad-}H'$), 1.78 (s, 12H, $\text{N}_3\text{-Ad-}H^\delta$ and $\text{N-Ad-}H^\delta$), 1.64–1.55 (m, 6H, $\text{N}_3\text{-Ad-}H^\beta$, partially obscured by solvent resonance), 1.62 (s, 6H, $\text{N-Ad-}H^\beta$), 1.22 (dd, $^3J_{\text{PH}} = 14.4$, $^3J_{\text{HH}} 7.2\text{ Hz}$, 6H, $\text{CH}(\text{CH}_3)_2$), 1.04 (dd, $^3J_{\text{PH}} = 13.9$, $^3J_{\text{HH}} 6.9\text{ Hz}$, 6H, $\text{CH}(\text{CH}_3)_2$). $^1\text{H}\{^{31}\text{P}\}$ NMR (300 MHz, $\text{THF-}d_8$): δ 2.40 (sp, $^3J_{\text{HH}} = 7.0\text{ Hz}$, 6H, $\text{CH}(\text{CH}_3)_2$), 2.05 (s, 3H, $\text{N}_3\text{-Ad-}H'$), 1.99 (s, 3H, $\text{N-Ad-}H'$), 1.78 (s, 12H, $\text{N}_3\text{-Ad-}H^\delta$ and $\text{N-Ad-}H^\delta$), 1.64–1.55 (m, 6H, $\text{N}_3\text{-Ad-}H^\beta$, partially obscured by solvent resonance), 1.62 (s, 3H, $\text{N-Ad-}H^\beta$), 1.22 (d, $^3J_{\text{HH}} = 7.2\text{ Hz}$, 6H, $\text{CH}(\text{CH}_3)_2$), 1.04 (d, $^3J_{\text{HH}} = 6.9\text{ Hz}$, 6H, $\text{CH}(\text{CH}_3)_2$). ^7Li NMR (272 MHz, $\text{THF-}d_8$): δ 1.47 (s). $^7\text{Li}\{^1\text{H}\}$ NMR (272 MHz, $\text{THF-}d_8$): δ 1.47 (s). $^{13}\text{C}\{^1\text{H}\}$ NMR (75 MHz, $\text{THF-}d_8$): δ 58.79 (s, $\text{N-Ad-}C^\alpha$), 50.76 (d, $^3J_{\text{PC}} = 7.4\text{ Hz}$, $\text{N-Ad-}C^\beta$), 50.41 (s,

N₃-Ad-C^α), 43.89 (s, N₃-Ad-C^β), 37.93 (s, N₃-Ad-C^δ), 37.82 (s, N-Ad-C^δ), 31.86 (s, N₃-Ad-C^γ), 31.00 (s, N-Ad-C^γ), 27.19 (d, ¹J_{PC} = 54.8 Hz, CH(CH₃)₂), 17.11 (s, CH(CH₃)₂), 16.84 (d, ²J_{PC} = 2.8 Hz, CH(CH₃)₂). ³¹P{¹H} NMR (122 MHz, THF-*d*₈): δ 41.7 (s). Anal. Calcd. for C₅₄H₉₆Li₂N₈P₂: C: 69.50 H: 10.37 N: 12.01%; found: C: 69.98 H: 10.18 N: 11.91%.

Synthesis of [ⁱPr₂P(N-C₁₀H₁₅)(N₃-C₁₀H₁₅)-κ²-N,N^α]Rh(COD) (**18**)

Compound **17** (88.4 mg, 0.189 mmol) and [RhCl(COD)]₂ (46.7 mg, 0.0947 mmol) were weighed into a 20 mL scintillation vial. Benzene (~10 mL) was added to the vial, and the reaction was left stirring at ambient temperature. After 16 h, the opaque yellow mixture was filtered through a Kimwipe (packed into pipette to act as a filter) yielding a yellow solution. Residual

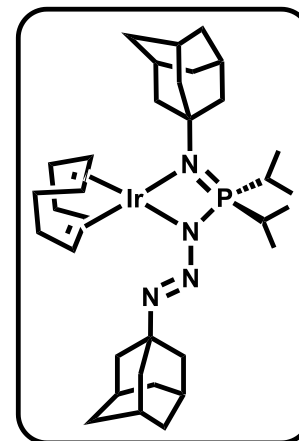


solvent was removed from the solution *in vacuo*, resulting in a yellow powder. Yellow crystalline blocks of **16** were grown from a saturated 1:1 benzene : pentane solution stored in a sealed 20 mL scintillation vial at ambient temperature for 1 week. Yield: 112 mg, 85%. ¹H NMR (300 MHz, C₆D₆): δ 5.45 (s, 2H, COD-CH), 4.64 (s 2H, COD-CH), 2.47–2.26 (m, 4H, COD-CH₂), 2.25–2.11 (m, 2H, CH(CH₃)₂), 2.06 (br s, 3H, N₃-Ad-H^γ), 1.98 (s, 3H, N-Ad-H^γ), 1.90 (s, 6H, N-Ad-H^β), 1.85–1.71 (m, 2H, COD-CH₂), 1.65 (br s, 14H, COD-CH₂, N₃-Ad-H^δ and N-Ad-H^δ), 1.54 (s, 6H, N₃-Ad-H^β), 1.49–1.32 (dd, ³J_{PH} = 14.3, ³J_{HH} 7.0 Hz, 6H, CH(CH₃)₂), 1.23 (dd, ³J_{PH} = 14.7, ³J_{HH} = 7.3 Hz, 6H, CH(CH₃)₂). ¹H{³¹P} NMR (300 MHz, C₆D₆): δ 5.45 (s, 2H, COD-CH), 4.63 (s, 2H, COD-CH), 2.47–2.25 (m,

4H, COD-CH₂), 2.18 (sp, ³J_{HH} = 7.4 Hz, 2H, CH(CH₃)₂), 2.06 (br s, 3H, N₃-Ad-H^γ), 1.98 (s, 3H, N-Ad-H^γ), 1.89 (s, 6H, N-Ad-H^β), 1.76–1.69 (m, 2H, COD-CH₂), 1.65 (br s, 14H, COD-CH₂, N₃-Ad-H^δ and N-Ad-H^δ), 1.54 (s, 6H, N₃-Ad-H^β), 1.32 (d, ³J_{HH} = 7.0 Hz, 6H, CH(CH₃)₂), 1.24 (d, ³J_{HH} = 7.2 Hz, 6H, CH(CH₃)₂). ¹³C{¹H} NMR (75 MHz, C₆D₆): δ 74.74 (d, ¹J_{RhC} = 12.2 Hz, COD-CH), 72.41 (d, ¹J_{RhC} = 13.1 Hz, COD-CH), 61.22 (s, N₃-Ad-C^α), 53.27 (d, ²J_{PC} = 2.2 Hz, N-Ad-C^α), 47.96 (d, ³J_{PC} = 7.3 Hz, N-Ad-C^β), 43.22 (s, N₃-Ad-C^β), 37.52 (s, N-Ad-C^β), 37.03 (s, N₃-Ad-C^δ), 31.12 (s, N-Ad-C^δ), 30.48 (s, COD-CH₂) 31.12 (s, COD-CH₂), 30.48 (s, N₃-Ad-C^γ), 29.30 (d, ¹J_{PC} = 46.1 Hz, CH(CH₃)₂), 17.40 (d, ²J_{PC} = 2.7 Hz, CH(CH₃)₂), 17.25 (d, ²J_{PC} = 1.8 Hz, CH(CH₃)₂). ³¹P{¹H} NMR (112 MHz, C₆D₆): δ 24.5 (d, ²J_{RhP} = 13.8 Hz). Anal. Calcd. for C₃₅H₆₀N₄PRh: C: 62.67 H: 9.02 N: 8.35%; found: C: 62.17 H: 8.92 N: 8.26%

Synthesis of [Pr₂P(N-C₁₀H₁₅)(N₃-C₁₀H₁₅)-κ²-N,N^α][Ir(COD)] (19)

Compound **17** (60.3 mg, 0.129 mmol) and [RhCl(COD)]₂ (43.4 mg, 0.0646 mmol) were weighed into a 20 mL scintillation vial, after which benzene (~10 mL) was added. The solution was vigorously stirred at ambient temperature for 16 h. The opaque orange mixture was filtered through a Kimwipe (packed into pipette to act as a filter), resulting in a bright orange solution. The

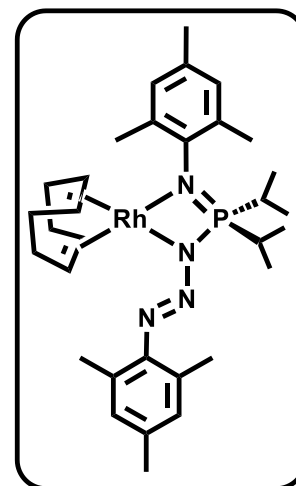


solvent was removed from the solution *in vacuo*, yielding **19** as an orange solid. Yield: 82.3 mg, 80%. ¹H NMR (300 MHz, C₆D₆): δ 5.17 (s, 2H, COD-CH), 4.49 (s, 2H, COD-CH), 2.40–2.24 (m, 4H, COD-CH₂), 2.19–2.08 (m, 2H, CH(CH₃)₂), 2.04 (s, 3H, N₃-Ad-H^γ),

1.98 (s, 3H, N-Ad- H^{γ}), 1.89 (s, 6H, N₃-Ad- H^{β}), 1.70 (s, 6H, N-Ad- H^{β}), 1.66–1.57 (m, 10H, N₃-Ad- H^{δ} , COD- CH_2), 1.53 (s, 6H, N₃-Ad- H^{δ}), 1.31–1.08 (m, 12H, CH(CH₃)₂). ¹H{³¹P} NMR (300 MHz, C₆D₆): δ 5.17 (s, 2H, COD- H), 4.48 (s, 2H, COD- CH), 2.46–2.22 (m, 4H, COD- CH_2), 2.09 (ov sp, ³J_{HH} = 7.2 Hz, 2H, CH(CH₃)₂), 2.05 (s, 3H, N₃-Ad- H^{γ}), 1.97 (s, 3H, N-Ad- H^{γ}), 1.89 (s, 6H, N₃-Ad- H^{β}), 1.70 (s, 6H, N-Ad- H^{β}), 1.68–1.56 (m, 10H, N₃-Ad- H^{δ} , COD- CH_2), 1.53 (s, 6H, N-Ad- H^{δ}), 1.23 (d, ³J_{HH} = 7.2 Hz, 6H, CH(CH₃)₂), 1.18 (d, ³J_{HH} = 6.6 Hz, 6H, CH(CH₃)₂). ¹³C{¹H} NMR (75 MHz, C₆D₆): δ 61.00 (s, N₃-Ad- C^{α}), 56.49 (s, COD- CH), 54.55 (s, COD- CH), 54.20 (d, ²J_{PC} = 4.1 Hz, N-Ad- C^{α}), 46.91 (d, ³J_{PC} = 6.7 Hz, N-Ad- C^{β}), 42.34 (s, N₃-Ad- C^{β}), 36.74 (s, N-Ad- C^{δ}), 36.23 (s, N₃-Ad- C^{δ}), 32.38 (s, COD- CH_2), 32.23 (s, COD- CH_2), 30.37 (s, N-Ad- C^{γ}), 29.74 (s, N₃-Ad- C^{γ}), 29.42 (d, ¹J_{PC} = 47.0 Hz, CH(CH₃)₂), 16.40 (d, ²J_{PC} = 2.4 Hz, CH(CH₃)₂), 16.33 (d, ²J_{PC} = 1.8 Hz, CH(CH₃)₂). ³¹P NMR (112 MHz, C₆D₆): δ 111.0 (s).

Synthesis of [¹Pr₂P(N-2,4,6-Me₃C₆H₂)(N₃-2,4,6-Me₃C₆H₂)-κ²-N,N^α]Rh(COD) (20)

Complex **14** (92.8 mg, 0.181 mmol) and [RhCl(COD)]₂ (44.5 mg, 0.0903 mmol) were weighed into a 20 mL scintillation vial, and pentane (~10 mL) was added. The vial was then placed in a dark place (closed freezer at -35 °C) in the glove box. After 16 h, the opaque yellow mixture was filtered through a Kimwipe (packed into pipette to act as a filter). Yellow crystalline blocks were grown from a pentane solution stored in a sealed 20 mL scintillation vial at ambient temperature for 5 days. Yield: 110 mg, 85%. ¹H NMR (300

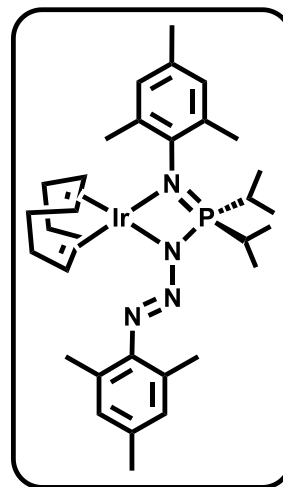


MHz, C₆D₆): δ 6.84 (s, 4H, Mes-CH), 5.42 (br dd, $^2J_{\text{RHH}} = 5.2$, $^3J_{\text{HH}} = 2.4$ Hz, 2H, COD-CH), 3.36 (br dd, $^2J_{\text{RHH}} = 5.1$, $^3J_{\text{HH}} = 2.3$ Hz, 2H, COD-CH), 2.72 (s, 6H, N-*ortho*-Mes-CH₃), 2.52–2.40 (m, 2H, COD-CH₂), 2.38 (s, 6H, N₃-*ortho*-Mes-CH₃), 2.34–2.26 (m, 2H, CH(CH₃)₂), 2.26–2.20 (m, 2H, COD-CH₂), 2.18 (s, 3H, N₃-*para*-Mes-CH₃), 2.17 (s, 3H, N-*para*-Mes-CH₃), 1.86–1.70 (m, 2H, COD-H₂), 1.62–1.48 (m, 2H, COD-CH₂), 1.18 (dd, $^2J_{\text{PH}} = 15.1$, $^3J_{\text{HH}} = 7.2$ Hz, 6H, CH(CH₃)₂), 1.08 (dd, $^3J_{\text{PH}} = 15.3$, $^3J_{\text{HH}} = 7.2$ Hz, 6H, CH(CH₃)₂). $^1\text{H}\{^{31}\text{P}\}$ NMR (300 MHz, C₆D₆): δ 6.85 (s, 4H, Mes-CH), 5.42 (br dd, $^2J_{\text{RHH}} = 5.2$, $^3J_{\text{HH}} = 2.4$ Hz, 2H, COD-CH), 3.36 (br dd, $^2J_{\text{RHH}} = 5.1$, $^3J_{\text{HH}} = 2.3$ Hz, 2H, COD-CH), 2.72 (s, 6H, N-*ortho*-Mes-CH₃), 2.51–2.41 (m, 2H, COD-CH), 2.38 (s, 6H, N₃-*ortho*-Mes-CH₃), 2.30 (ov sp, $^3J_{\text{HH}} = 7.3$ Hz, 2H, CH(CH₃)₂), 2.27–2.20 (m, 2H, COD-CH₂), 2.18 (s, 3H, N₃-*para*-Mes-CH₃), 2.17 (s, 3H, N-*para*-Mes-CH₃), 1.86–1.67 (m, 2H, COD-CH), 1.62–1.47 (m, 2H, COD-CH), 1.18 (d, $^3J_{\text{HH}} = 7.2$ Hz, 6H, CH(CH₃)₂), 1.09 (d, $^3J_{\text{HH}} = 7.2$ Hz, 6H, CH(CH₃)₂). $^{13}\text{C}\{^1\text{H}\}$ NMR (75 MHz, C₆D₆): δ 148.55 (s, N₃-*ipso*-Mes-C-P), 141.57 (d, $^2J_{\text{PC}} = 2.1$ Hz, N-*ortho-ipso*-Mes-C-CH₃), 134.99 (d, $^3J_{\text{PC}} = 4.7$ Hz, N-*ipso*-Mes-C-P), 134.30 (s, N₃-*ortho-ipso*-Mes-C-CH₃), 131.89 (d, $^5J_{\text{PC}} = 3.0$ Hz, N-*para-ipso*-Mes-C-CH₃), 130.43 (s, N₃-*para-ipso*-Mes-C-CH₃), 130.09 (s, N-Mes-CH), 130.04 (s, N₃-Mes-CH), 78.53 (d, $^1J_{\text{CRh}} = 13.0$ Hz, COD-CH), 74.24 (d, $^1J_{\text{CRh}} = 12.9$ Hz, COD-CH), 32.59 (s, COD-CH₂), 30.79 (s, COD-CH₂), 30.54 (d, $^1J_{\text{PC}} = 48.1$ Hz, CH(CH₃)₂), 21.63 (d, $^4J = 0.8$ Hz, N-*ortho*-Mes-CH₃), 21.29 (s, N₃-*para*-Mes-CH₃), 21.16 (s, N-*para*-Mes-CH₃), 20.10 (s, N₃-*ortho*-Mes-CH₃), 16.87 (d, $^2J_{\text{PC}} = 2.5$ Hz, CH(CH₃)₂), 16.61 (d, $^2J_{\text{PC}} = 2.7$ Hz, CH(CH₃)₂). $^{31}\text{P}\{^1\text{H}\}$ NMR (122 MHz, C₆D₆): δ 84.1 (br s, 95.2%, **20**), 64.9 (s,

4.8%, **22**). Anal. Calcd. for C₃₆H₆₄RhN₄P: C: 62.96 H: 9.39 N: 8.16%; found: C: 62.61 H: 8.33 N: 8.79%

Synthesis of [ⁱPr₂P(N-2,4,6-Me₃C₆H₂)(N₃-2,4,6-Me₃C₆H₂)-κ²-N,N^αIr(COD) (**21**)

Compound **14** (96.8 mg, 0.194 mmol) and [IrCl(COD)]₂ (65.2 mg, 0.0970 mmol) were weighed into a 20 mL scintillation vial. Pentane (~10 mL) was added to the vial. The vial was left in a dark place (closed freezer at -35 °C) within the glove box at ambient temperature. After 16 h, the dark yellow mixture was filtered through a Kimwipe (packed into pipette to act as a filter) twice. Yellow needles were grown from a pentane solution stored



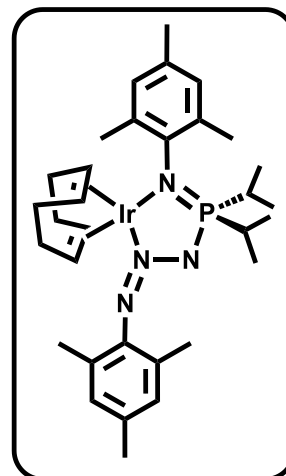
in a sealed 20 mL scintillation vial at ambient temperature in a dark location (closed freezer at -35 °C) for 3 days and contained mostly **21** with trace amounts of **23**. Three consecutive recrystallizations from pentane were required to isolate pure **21** as yellow blocks. Yield: 122 mg, 78%. ¹H NMR (300 MHz, C₆D₆): δ 6.84 (s, 2H, N-Mes-CH), 6.83 (s, 2H, N₃-Mes-CH), 5.10–4.97 (m, 2H, COD-CH), 3.25–3.16 (m, 2H, COD-CH), 2.66 (s, 6H N-ortho-Mes-CH₃), 2.48–2.39 (m, 2H, COD-CH₂), 2.37 (s, 6H, N₃-ortho-Mes-CH₃), 2.34–2.29 (m, 2H, COD-CH₂), 2.30–2.21 (m, 2H, CH(CH₃)₂), 2.19 (s, 3H, N₃-para-Mes-CH₃), 2.17 (s, 3H, N₃-para-Mes-CH₃), 1.75–1.61 (m, 2H, COD-CH₂), 1.56–1.43 (s, 2H, COD-CH₂), 1.07 (dd, ³J_{PH} = 15.5, ³J_{HH} 7.2 Hz, 6H, CH(CH₃)₂), 1.06 (dd, ³J_{PH} = 15.7, ³J_{HH} = 7.2 Hz, 6H, CH(CH₃)₂). ¹H{³¹P} NMR (300 MHz, C₆D₆): δ 6.84 (s, 2H, N-Mes-CH), 6.83 (s, 2H, N₃-Mes-CH), 5.08–4.96 (m, 2H, COD-CH), 3.25–3.16 (m, 2H, COD-CH), 2.66 (s,

6H, N-*ortho*-Mes-CH₃), 2.47–2.38 (m, 2H, COD-CH₂), 2.37 (s, 6H, N₃-*ortho*-Mes-CH₃), 2.35–2.27 (m, 2H, COD-CH₂), 2.23 (ov sp, $J = 7.2$ Hz, 2H, CH(CH₃)₂), 2.19 (s, 3H, N₃-*para*-Mes-CH₃), 2.17 (s, 3H, N-*para*-Mes-CH₃), 1.77–1.60 (m, 2H, COD-CH₂), 1.56–1.43 (m, 2H, COD-CH₂), 1.07 (d, $^3J_{\text{HH}} = 7.2$ Hz, 6H, CH(CH₃)₂), 1.07 (d, $^3J_{\text{HH}} = 7.1$ Hz, 6H, CH(CH₃)₂). ¹³C{¹H} NMR (75 MHz, C₆D₆): δ 147.65 (s, N₃-*ipso*-Mes-C-P), 139.87 (d, $^3J_{\text{PC}} = 3.5$ Hz, N-*ortho-ipso*-Mes-C-CH₃), 135.46 (d, $^2J_{\text{PC}} = 4.2$ Hz, N-*ipso*-Mes-C-P), 134.82 (s, N₃-*ortho-ipso*-Mes-C-CH₃), 133.10 (d, $^5J_{\text{PC}} = 2.7$ Hz, N-*para-ipso*-Mes-C-CH₃), 130.60 (s, N₃-*para-ipso*-Mes-C-CH₃), 130.16 (s, N₃-Mes-CH), 130.08 (d, $^4J_{\text{PC}} = 1.8$ Hz, N-Mes-CH), 61.66 (s, COD-CH), 56.73 (s, COD-CH), 33.71 (s, COD-CH₂), 31.94 (s, COD-CH₂), 31.15 (d, $^1J_{\text{PC}} = 45.1$ Hz, CH(CH₃)₂), 21.36 (s, N-*ortho*-Mes-CH₃), 21.27 (s, N₃-*para*-Mes-CH₃), 21.07 (s, N-*para*-Mes-CH₃), 20.17 (s, N₃-*ortho*-Mes-CH₃), 16.65 (d, $^2J_{\text{PC}} = 2.3$ Hz, CH(CH₃)₂), 16.21 (d, $^2J_{\text{PC}} = 2.6$ Hz, CH(CH₃)₂). ³¹P{¹H} NMR (122 MHz, C₆D₆): δ 105.7 (br s, 96.1%, **21**), 77.0 (s, 3.9%, **23**). Anal. Calcd. for C₃₆H₆₄IrN₄P: C: 55.71 H: 8.31 N: 7.22%; found: C: 55.60 H: 8.47 N: 7.44%

2.2 Hz, 2H, COD-CH), 2.68 (s, 6H, N-*ortho*-Mes-CH₃), 2.43–2.36 (m, 2H, COD-CH₂), 2.36 (s, 6H, N₃-*ortho*-Mes-CH₃), 2.24–2.15 (m, 2H, COD-CH₂), 2.14 (s, 3H, N₃-*para*-Mes-CH₃), 2.11 (s, 3H, N-*para*-Mes-CH₃), 2.00–1.87 (m, 2H, COD-CH₂), 1.71 (sp, ³J_{HH} = 7.2 Hz, 2H, CH(CH₃)₂), 1.64–1.54 (m, 2H, COD-CH₂), 1.29 (d, ³J_{HH} = 7.3 Hz, 6H, CH(CH₃)₂), 0.78 (d, ³J_{HH} 7.0 Hz, 6H, CH(CH₃)₂). ¹³C{¹H} NMR (176 MHz, C₆D₆): δ 149.18 (s, N₃-*ipso*-Mes-C-P), 144.08 (d, ²J_{PH} = 4.8 Hz, N-*ipso*-Mes-C-P), 135.79 (d, ³J_{PC} = 4.0 Hz, N-*ortho-ipso*-Mes-C-CH₃), 133.57 (s, N₃-*ortho-ipso*-Mes-C-CH₃), 132.20 (d, ⁵J_{PC} = 2.4 Hz, N-*para-ipso*-Mes-C-CH₃), 130.11 (d, ⁴J_{PC} = 1.7 Hz, N-Mes-CH), 128.93 (s, N₃-Mes-CH), 128.68 (s, N₃-Mes-CH), 127.98 (s, N₃-*para-ipso*-Mes-C-CH₃), 83.82 (d, ¹J_{RhC} = 12.0 Hz, COD-CH), 80.65 (d, ¹J_{RhC} = 12.9 Hz, COD-CH), 31.32 (s, COD-CH₂), 30.96 (s, COD-CH₂), 26.16 (d, ¹J_{PC} = 68.9 Hz, CH(CH₃)₂), 21.73 (s, N-*ortho*-Mes-CH₃), 21.35 (s, N₃-*para*-Mes-CH₃), 21.21 (s, N-*para*-Mes-CH₃), 18.36 (s, N₃-*ortho*-Mes-CH₃), 17.32 (d, ²J_{PC} = 3.3 Hz, CH(CH₃)₂), 16.72 (d, ²J_{PC} = 2.7 Hz, CH(CH₃)₂). ³¹P{¹H} NMR (122 MHz, C₆D₆): δ 64.9 (s). Attempts to obtain high-quality elemental analyses (within 3% of computed values) for this compound have been unsuccessful.

Synthesis of [¹Pr₂P(N-2,4,6-Me₃C₆H₂)(N₃-2,4,6-Me₃C₆H₂)-κ²-N,N^β]Ir(COD) (**23**)

Compound **21** (62.3 mg, 0.0802 mmol) was added to a J. Young valve NMR tube, followed by benzene (0.5 mL). The vessel was irradiated with a black light ($\lambda = 365$ nm). After 30 h, the solvent was removed, and the tube was brought into a glove box. The yellow solid was dissolved in pentane (~10 mL) filtered through a Kimwipe (packed into pipette to act as a filter) (to remove any Ir black particles), and residual solvent was removed



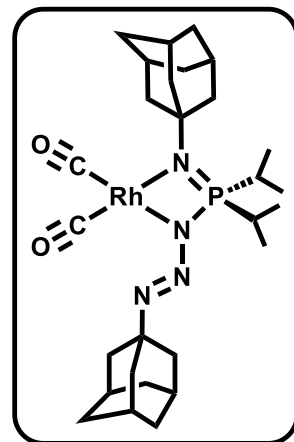
in vacuo. ³¹P{¹H} NMR analysis revealed that the powered product contained 25% **21**.

Three consecutive recrystallizations from pentane were required to isolate pure **23** as yellow-orange blocks. Yield: 29.8 mg, 49%. ¹H NMR (300 MHz, C₆D₆): δ 6.86 (s, 2H, N-Mes-CH), 6.84 (s, 2H, N₃-Mes-CH), 4.58–4.35 (m, 2H, COD-H), 3.58–3.36 (m, 2H, COD-CH), 2.61 (s, 6H, N-ortho-Mes-CH₃), 2.34 (s, 6H, N₃-ortho-Mes-CH₃), 2.23–2.06 (m, 10H, para-Mes-CH₃ and COD-H₂), 2.06–1.84 (m, 2H, CH(CH₃)₂), 1.78–1.44 (m, 4H, COD-CH₂), 1.16 (dd, ³J_{PH} = 14.6, ³J_{HH} = 7.2 Hz, 6H, CH(CH₃)₂), 0.73 (dd, ³J_{PH} = 15.4, ³J_{HH} = 7.0 Hz, 6H, CH(CH₃)₂). ¹H{³¹P} NMR (300 MHz, C₆D₆): δ 6.86 (s, 2H, N-Mes-CH), 6.83 (s, 2H, N₃-Mes-CH), 4.58–4.30 (m, 2H, COD-CH), 3.59–3.34 (m, 2H, COD-CH), 2.61 (s, 6H, N-ortho-Mes-CH₃), 2.36–2.26 (m, 6H, N₃-ortho-Mes-CH₃), 2.23–2.07 (m, 10H, para-Mes-CH₃ and COD-H₂), 2.02–1.81 (m, 2H, CH(CH₃)₂), 1.60 (s, 4H, COD-CH₂), 1.16 (d, ³J_{HH} = 7.0 Hz, 6H, CH(CH₃)₂), 0.73 (d, ³J_{HH} = 6.7 Hz, 6H, CH(CH₃)₂). ¹³C{¹H} NMR (75 MHz, C₆D₆): δ 150.09 (s, N₃-ipso-Mes-C-P), 143.79 (d, ³J_{PC} = 3.4 Hz, N-ortho-ipso-Mes-C-CH₃), 137.09 (d, ²J_{PC} = 4.0 Hz, N-ipso-Mes-C-P), 134.86 (s, N₃-

ortho-ipso-Mes-C-CH₃), 134.25 (d, $^5J_{PC} = 2.6$ Hz, *N-para-ipso-Mes-C-CH₃*), 131.60 (s, *N_{3-para-ipso-Mes-C-CH₃}*), 131.14 (d, $^4J_{PC} = 2.3$ Hz, *N-Mes-CH*), 130.00 (s, *N_{3-Mes-CH}*), 69.48 (s, COD-CH), 63.92 (s, COD-CH), 34.71 (s, COD-CH₂), 32.60 (s, COD-CH₂), 26.07 (d, $^1J_{PC} = 59.3$ Hz, CH(CH₃)₂), 22.75 (s, *N_{3-ortho-Mes-CH₃}*), 22.37 (s, *N_{3-para-Mes-CH₃}*), 21.18 (s, *N-para-Mes-CH₃*), 19.27 (s, *N_{3-ortho-Mes-CH₃}*), 18.17 (d, $^2J_{PC} = 3.3$ Hz, CH(CH₃)₂), 17.86 (d, $^2J_{PC} = 3.4$ Hz, CH(CH₃)₂). $^{31}\text{P}\{^1\text{H}\}$ NMR (122 MHz, C₆D₆): δ 77.0 (s). Anal. Calcd. for C₃₆H₆₄N₄PIr: C: 55.71 H: 8.31 N: 7.22%; found: C: 55.35 H: 8.18 N: 7.38%.

Synthesis of [*i*Pr₂P(N-C₁₀H₁₅)(N_{3-C₁₀H₁₅)- κ^2 -N,N^{*a*}]Rh(CO)₂ (**24**)}

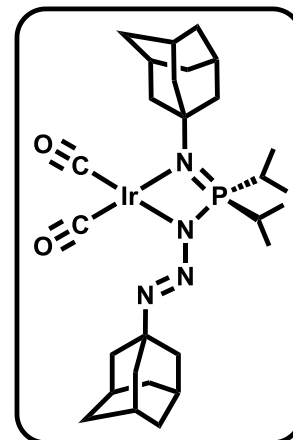
Complex **18** (45.9 mg, 0.0655 mmol) was added to a J. Young NMR tube and dissolved in 0.5 mL of benzene-*d*₆. The NMR tube was attached to a double manifold vacuum line, and the solution was degassed by two freeze-pump-thaw cycles. A carbon monoxide atmosphere (1 atm) was applied to the tube using a vacuum line to J. Young NMR tube adaptor, and the reaction was monitored by $^{31}\text{P}\{^1\text{H}\}$ NMR spectroscopy. After 20 min at ambient temperature, complete conversion was observed, and the yellow solution turned brown. The atmosphere of CO and benzene-*d*₆ were removed *in vacuo*, yielding a brown solid. The solid was brought into a glove box, dissolved in pentane (~10 mL), filtered through a Kimwipe (packed into pipette to act as a filter) (to remove any Rh black particles) and residual solvent was removed under vacuum resulting in a brown solid. Yellow plates of



21 were grown from a saturated pentane solution stored in a sealed 20 mL scintillation vial at ambient temperature for 5 days. Yield: 30.8 mg, 72%. ^1H NMR (300 MHz, C_6D_6): δ 2.16–2.02 (m, 5H, $\text{N}_3\text{-Ad-}H^{\alpha}$ and $\text{CH}(\text{CH}_3)_2$), 1.99 (ov s, 3H, $\text{N-Ad-}H^{\alpha}$), 1.98 (ov s, 6H, $\text{N}_3\text{-Ad-}H^{\beta}$), 1.69 (ov s, 3H, $\text{N-Ad-}H^{\beta}$), 1.68 (ov s, 3H, $\text{N-Ad-}H^{\beta}$), 1.67–1.58 (m, 6H, $\text{N}_3\text{-Ad-}H^{\delta}$), 1.55–1.45 (m, 6H, $\text{N-Ad-}H^{\delta}$), 1.14 (dd, $^3J_{\text{PH}}=15.2$, $^3J_{\text{HH}}=7.0$ Hz, 6H, $\text{CH}(\text{CH}_3)_2$), 1.05 (dd, $^3J_{\text{PH}}=15.6$, $^3J_{\text{HH}}=7.2$ Hz, 6H, $\text{CH}(\text{CH}_3)_2$). $^1\text{H}\{^{31}\text{P}\}$ NMR (300 MHz, C_6D_6): δ 2.13–2.01 (m, 5H, $\text{N}_3\text{-Ad-}H^{\alpha}$ and $\text{CH}(\text{CH}_3)_2$), 1.99 (ov s, 3H, $\text{N-Ad-}H^{\alpha}$), 1.98 (ov s, 6H, $\text{N}_3\text{-Ad-}H^{\beta}$), 1.69 (ov s, 3H, $\text{N-Ad-}H^{\beta}$), 1.68 (ov s, 3H, $\text{N-Ad-}H^{\beta}$), 1.66–1.58 (m, 6H, $\text{N}_3\text{-Ad-}H^{\delta}$), 1.55–1.45 (m, 6H, $\text{N-Ad-}H^{\delta}$), 1.13 (ov d, $^3J_{\text{HH}}=7.0$ Hz, 3H, $\text{CH}(\text{CH}_3)_2$), 1.13 (ov d, $^3J_{\text{HH}}=7.1$ Hz, 3H, $\text{CH}(\text{CH}_3)_2$), 1.04 (ov d, $^3J_{\text{HH}}=7.2$ Hz, 3H, $\text{CH}(\text{CH}_3)_2$), 1.04 (ov d, $^3J_{\text{HH}}=7.3$ Hz, 3H, $\text{CH}(\text{CH}_3)_2$). $^{13}\text{C}\{^1\text{H}\}$ NMR (75 MHz, C_6D_6): δ 191.20 (d, $^1J_{\text{RhC}}=69.7$ Hz, $\text{C}\equiv\text{O}$), 188.87 (d, $^1J_{\text{RhC}}=70.2$ Hz, $\text{C}\equiv\text{O}$), 61.04 (s, $\text{N}_3\text{-Ad-}C^{\alpha}$), 50.59 (d, $^2J_{\text{PC}}=1.2$ Hz, $\text{N-Ad-}C^{\alpha}$), 48.76 (d, $^3J_{\text{PC}}=6.2$ Hz, $\text{N-Ad-}C^{\beta}$), 43.05 (s, $\text{N}_3\text{-Ad-}C^{\beta}$), 37.39 (s, $\text{N}_3\text{-Ad-}C^{\delta}$), 36.73 (s, $\text{N-Ad-}C^{\delta}$), 30.98 (s, $\text{N-Ad-}C^{\gamma}$), 30.39 (s, $\text{N}_3\text{-Ad-}C^{\gamma}$), 28.99 (d, $^1J_{\text{PC}}=48.2$ Hz, $\text{CH}(\text{CH}_3)_2$), 17.33 (d, $^2J_{\text{PC}}=2.7$ Hz, $\text{CH}(\text{CH}_3)_2$), 16.58 (d, $^2J_{\text{PC}}=2.0$ Hz, $\text{CH}(\text{CH}_3)_2$). $^{31}\text{P}\{^1\text{H}\}$ NMR (112 MHz, C_6D_6): δ 99.7 (d, $^2J_{\text{RhP}}=6.4$ Hz). IR ν_{CO} (cm^{-1}): 2050, 1974. Attempts to obtain high-quality elemental analyses (within 3% of computed values) for this compound have been unsuccessful.

Synthesis of [¹Pr₂P(N-C₁₀H₁₅)(N₃-C₁₀H₁₅)-κ²-N,N^α]Ir(CO)₂ (**25**)

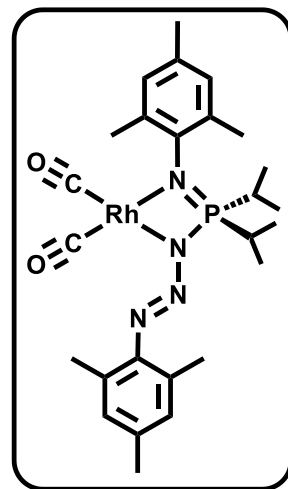
Complex **19** (42.4 mg, 0.0537 mmol) was added to a J. Young NMR tube and dissolved in 0.5 mL of benzene-*d*₆. The NMR tube was attached to a double manifold vacuum line, and the solution was degassed by two freeze-pump-thaw cycles. A carbon monoxide atmosphere (1 atm) was applied to the tube using a vacuum line to J. Young NMR tube adaptor, and the reaction was monitored by ³¹P{¹H} NMR spectroscopy. After 20 min at ambient temperature, complete conversion was observed, and the yellow solution turned brown. The atmosphere of CO and benzene-*d*₆ were removed under vacuum, resulting in a reddish-brown solid. The solid was brought into a glove box, dissolved in pentane (~10 mL), filtered through a Kimwipe (packed into pipette to act as a filter) (to remove any Ir black particles), and residual solvent was removed *in vacuo*, yielding a deep reddish-brown solid. Slightly reddish plates of **25** were grown from a saturated pentane solution stored in a sealed 20 mL scintillation vial at ambient temperature for 4 days. Yield: 34.0 mg, 86%. ¹H NMR (700 MHz, C₆D₆): δ 2.04 (br s, 3H, N₃-Ad-*H*^γ), 1.98 (ov s, 3H, N₃-Ad-*H*^β), 1.96 (ov s, 3H, N₃-Ad-*H*^β), 1.96–1.93 (m, 5H, N-Ad-*H*^γ and CH(CH₃)₂), 1.70 (m, 3H, N-Ad-*H*^β), 1.68 (ov s, 3H, N-Ad-*H*^β), 1.63 (br s, 6H, N₃-Ad-*H*^δ), 1.49 (br s, 6H, N-Ad-*H*^δ), 1.08 (dd, ³J_{PH} = 15.7, ³J_{HH} = 7.0 Hz, 6H, CH(CH₃)₂), 0.99 (dd, ³J_{PH} = 16.0, ³J_{HH} = 7.2 Hz, 6H, CH(CH₃)₂). ¹H{³¹P} NMR (700 MHz, C₆D₆): δ 2.04 (br s, 3H, N₃-Ad-*H*^γ), 1.98 (ov s, 3H, N₃-Ad-*H*^β), 1.97 (ov s, 3H, N₃-Ad-*H*^β), 1.96–1.91 (m, 5H, N-Ad-*H*^γ and CH(CH₃)₂), 1.69 (ov s, 3H, N-Ad-*H*^β), 1.67 (ov s, 3H, N-Ad-*H*^β), 1.63 (br s, 6H, N₃-Ad-



H^{δ}), 1.49 (br s, 6H, N-Ad- H^{δ}), 1.12–1.05 (m, 6H, CH(CH₃)₂), 1.03–0.95 (m, 6H, CH(CH₃)₂). ¹³C{¹H} NMR (176 MHz, C₆D₆): δ 180.03 (s, C≡O), 175.71 (s, C≡O), 61.24 (s, N₃-Ad-C^α), 51.85 (d, ²J_{PC} = 2.0 Hz, N-Ad-C^α), 48.23 (d, ³J_{PC} = 5.7 Hz, N-Ad-C^β), 42.86 (s, N₃-Ad-C^β), 37.31 (s, N-Ad-C^β), 36.62 (s, N₃-Ad-C^β), 30.91 (s, N₃-Ad-C^γ), 30.34 (s, N-Ad-C^γ), 29.20 (d, ¹J_{PC} = 48.2 Hz, CH(CH₃)₂), 17.09 (d, ²J_{PC} = 2.6 Hz, CH(CH₃)₂), 16.28 (d, ²J_{PC} = 2.1 Hz, CH(CH₃)₂). ³¹P{¹H} NMR (284 MHz, C₆D₆): δ 108.1 (s). IR ν_{CO} (cm⁻¹): 2037, 1955. Anal. Calcd. for C₃₁H₅₆N₄O₂PIr: C: 50.32 H: 7.63 N: 7.57%; found: C: 50.39 H: 7.57 N: 7.35%

Synthesis of [ⁱPr₂P(N-2,4,6-Me₃C₆H₂)(N₃-2,4,6-Me₃C₆H₂)-κ²-N,N^α]Rh(CO)₂ (26)

Complex **20** (55.6 mg, 0.0776 mmol) was added to a J. Young NMR tube and dissolved in 0.5 mL of benzene-*d*₆. The NMR tube was attached to a double manifold vacuum line, and the solution was degassed by two freeze-pump-thaw cycles. A carbon monoxide atmosphere (1 atm) was applied to the tube using a vacuum line to J. Young NMR tube adaptor, and the reaction was monitored by ³¹P{¹H} NMR spectroscopy. After 5

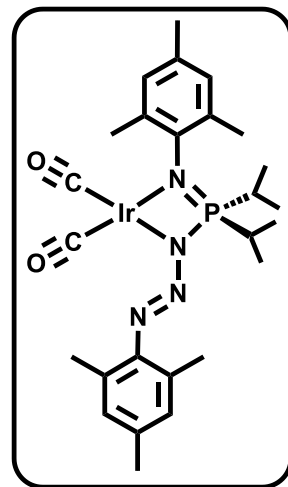


min at ambient temperature, complete conversion was observed, and the yellow solution turned brown. The atmosphere of CO and benzene-*d*₆ were removed *in vacuo*, yielding a brown solid. The tube was brought into a glove box, the solid dissolved in pentane (~10 mL), filtered through a Kimwipe (packed into pipette to act as a filter) (to remove any Rh black particles) and residual solvent was removed under vacuum yielding a brown powder.

Yield: 39.6 mg, 80%. ^1H NMR (300 MHz, C_6D_6): δ 6.83 (s, 2H, N-Mes-CH), 6.80 (s, 2H, N_3 -Mes-CH), 2.57 (s, 6H, N-ortho-Mes-CH₃), 2.39 (s, 6H, N_3 -ortho-Mes-CH₃), 2.23 (sp, $J = 7.1$ Hz, 2H, CH(CH₃)₂), 2.17 (s, 2H, N_3 -para-Mes-CH₃), 2.14 (s, 2H, N-para-Mes-CH₃), 1.01 (dd, $^3J_{\text{Ph}} = 15.5$, $^3J_{\text{HH}} = 7.2$ Hz, 6H, CH(CH₃)₂), 0.90 (dd, $^3J_{\text{PH}} = 15.9$, $^3J_{\text{HH}} = 7.2$ Hz, 6H, CH(CH₃)₂). $^1\text{H}\{^{31}\text{P}\}$ NMR (300 MHz, C_6D_6): δ 6.83 (s, 2H, N-Mes-CH), 6.80 (s, 2H, N_3 -Mes-CH), 2.57 (s, 6H, N-ortho-Mes-CH₃), 2.39 (s, 6H, N_3 -ortho-Mes-CH₃), 2.23 (sp, $^3J_{\text{HH}} = 7.1$ Hz, 2H, CH(CH₃)₂), 2.17 (s, 3H, N_3 -para-Mes-CH₃), 2.14 (s, 3H, N-para-Mes-CH₃), 1.01 (d, $^3J_{\text{HH}} = 7.2$ Hz, 6H, CH(CH₃)₂), 0.90 (d, $^3J_{\text{HH}} = 7.2$ Hz, 6H, CH(CH₃)₂). $^{13}\text{C}\{^1\text{H}\}$ NMR (75 MHz, C_6D_6): δ 188.48 (d, $^1J_{\text{RhC}} = 69.5$, C \equiv O), 188.34 (d, $^1J_{\text{RhC}} = 70.7$ Hz, C \equiv O), 146.73 (s, N_3 -ipso-Mes-C-P), 143.70 (s, N-ipso-Mes-C-P), 135.23 (s, N-ortho-ipso-Mes-C-CH₃), 134.55 (d, $^3J_{\text{PC}} = 4.5$ Hz, N_3 -ortho-ipso-Mes-C-CH₃), 133.05 (d, $^5J_{\text{PC}} = 2.9$ Hz, N-para-ipso-Mes-C-CH₃), 130.84 (s, N_3 -para-ipso-Mes-C-CH₃), 130.23 (d, $^4J_{\text{PH}} = 2.2$ Hz, N_3 -Mes-CH), 130.10 (s, N-Mes-CH), 30.53 (d, $^1J_{\text{PC}} = 48.7$ Hz, CH(CH₃)₂), 21.84 (s, N-ortho-Mes-CH₃), 21.29 (s, N_3 -para-Mes-CH₃), 21.10 (s, N-para-Mes-CH₃), 19.69 (s, N_3 -ortho-Mes-CH₃), 16.50 (d, $^2J_{\text{PC}} = 2.3$ Hz, CH(CH₃)₂), 16.33 (d, $^2J_{\text{PC}} = 2.8$ Hz, CH(CH₃)₂). $^{31}\text{P}\{^1\text{H}\}$ NMR (122 MHz, C_6D_6): δ 95.2 (d, $^2J_{\text{Rhp}} = 8.5$ Hz, 97.0%, **26**), 64.9 (s, 3.0%, **20**). IR ν_{CO} (cm^{-1}): 2054, 1987. Anal. Calcd. for $\text{C}_{30}\text{H}_{52}\text{N}_4\text{O}_2\text{PRh}$: C: 56.78 H: 8.26 N: 8.83%; found: C: 56.68 H: 8.02 N: 9.06%

Synthesis of $[\text{Pr}_2\text{P}(\text{N}-2,4,6\text{-Me}_3\text{C}_6\text{H}_2)(\text{N}_3-2,4,6\text{-Me}_3\text{C}_6\text{H}_2)-\kappa^2\text{-N},\text{N}^a]\text{Ir}(\text{CO})_2$ (**27**)

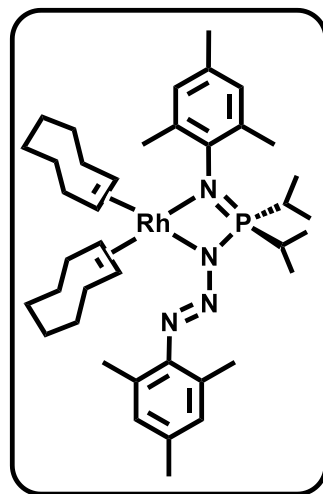
Complex **21** (48.3 mg, 0.0599 mmol) was added to a J. Young NMR tube and dissolved in 0.5 mL of benzene- d_6 . The NMR tube was attached to a double manifold vacuum line, and the solution was degassed by two freeze-pump-thaw cycles. A carbon monoxide atmosphere (1 atm) was applied to the tube using a vacuum line to J. Young NMR tube adaptor, and the reaction was monitored by $^{31}\text{P}\{^1\text{H}\}$ NMR spectroscopy. After 20 min at ambient temperature, the yellow solution turned brown, and complete conversion was observed. The atmosphere of CO and benzene- d_6 were removed under vacuum, resulting in a brown solid. The tube was brought into a glove box. The solid was dissolved in pentane (~10 mL), filtered through a Kimwipe (packed into pipette to act as a filter) (to remove any Ir black particles) and the remaining solvent was removed *in vacuo* resulting in a brown solid. Yield: 39.2 mg, 83%. ^1H NMR (300 MHz, C_6D_6): δ 6.82 (s, 2H, N-Mes-CH), 6.78 (s, 2H, N_3 -Mes-CH), 2.57 (s, 6H, N-ortho-Mes- CH_3), 2.40 (s, 6H, N_3 -ortho-Mes- CH_3), 2.16 (s, 3H, N-para-Mes- CH_3), 2.22–2.02 (m, 2H, $\text{CH}(\text{CH}_3)_2$), 2.14 (s, 3H, N_3 -para-Mes- CH_3), 0.94 (dd, $^3J_{\text{PH}} = 16.1$, $^3J_{\text{HH}} = 7.2$ Hz, 6H, $\text{CH}(\text{CH}_3)_2$), 0.86 (d, $^3J_{\text{PH}} = 16.2$, $^3J_{\text{HH}} = 7.2$ Hz, 6H, $\text{CH}(\text{CH}_3)_2$). ^1H NMR (300 MHz, C_6D_6): δ 6.82 (s, 2H, N-Mes-CH), 6.78 (s, 2H, N_3 -Mes-CH), 2.57 (s, 6H, N-ortho-Mes- CH_3), 2.40 (s, 6H, N_3 -ortho-Mes- CH_3), 2.16 (s, 3H, N_3 -para-Mes- CH_3), 2.25–2.04 (m, 2H, $\text{CH}(\text{CH}_3)_2$), 2.14 (s, 2H, N_3 -para-Mes- CH_3), 0.94 (d, $^3J_{\text{HH}} = 7.2$ Hz, 6H, $\text{CH}(\text{CH}_3)_2$), 0.86 (d, $^3J_{\text{HH}} = 7.2$ Hz, 6H, $\text{CH}(\text{CH}_3)_2$). $^{13}\text{C}\{^1\text{H}\}$ NMR (75 MHz, C_6D_6): δ 177.22 (s, $\text{C}\equiv\text{O}$), 175.06 (s, $\text{C}\equiv\text{O}$), 146.05



(s, N₃-*ipso*-Mes-C-P), 142.37 (s, N-*ipso*-Mes-C-P), 135.66 (s, N₃-*ortho-ipso*-Mes-C-CH₃), 135.05 (d, ³J_{PC} = 4.2 Hz, N-*ortho-ipso*-Mes-C-CH₃), 134.12 (d, ⁵J_{PC} = 2.7 Hz, N-*para-ipso*-Mes-C-CH₃), 130.97 (s, N₃-*para-ipso*-Mes-C-CH₃), 130.25 (d, ⁴J_{PC} = 2.1 Hz, N-Mes-CH), 130.17 (s, N₃-Mes-CH), 30.87 (d, ¹J_{PC} = 47.9 Hz, CH(CH₃)₂), 21.60 (s), 21.28 (s), 21.02 (s), 19.74 (s), 16.14 (d, ²J_{PC} = 1.8 Hz, CH(CH₃)₂). ³¹P{¹H} NMR (122 MHz, C₆D₆): δ 104.1 (br s, 96.1%, **27**), 76.95 (s, 3.9%, **21**). IR ν_{CO} (cm⁻¹): 2033, 1959. Anal. Calcd. for C₃₀H₅₂N₄O₂Pr: C: 49.77 H: 7.24 N: 7.74%; found: C: 49.41 H: 7.24 N: 7.82%

Synthesis of [ⁱPr₂P(N-2,4,6-Me₃C₆H₂)(N₃-2,4,6-Me₃C₆H₂)-κ²-N,N^α]Rh(COE)₂ (**28**)

Compound **14** (73.9 mg, 0.167 mmol) and [RhCl(COE)₂]₂ (56.1 mg, 0.0840 mmol) were weighed into a 20 mL scintillation vial and placed in a freezer (-35 °C) for 1 h. Pre-chilled pentane (~10 mL) was added to the mixture, stirred for 30 seconds. The vial was then placed back into the freezer. After 16 h, the bright orange mixture was filtered through a Kimwipe (packed into pipette to act as a filter) twice

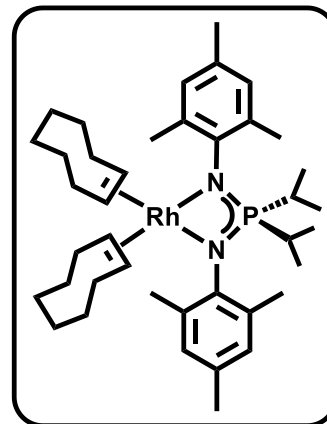


(to remove KCl and undissolved particles). The orange solution was placed back in the freezer. After 4 days, orange-reddish plates of **28** were observed. Using X-ray diffraction experiments, the crystals were identified as complex **28**. Complex **28** was found to be vacuum stable for short periods; however, when dissolved in C₆D₆, the crystals partially decomposed (14%) to ⁱPr₂P(N-2,4,6-Me₃C₆H₂)₂Rh(COE)₂, **29**, ³¹P{¹H} NMR 64.0, at

ambient temperature within 72 h. Yield: 92.9 mg, 67%. ^1H NMR (700 MHz, C_6D_6): δ 6.85 (s, 2H, N-Mes-CH), 6.82 (s, 2H, N_3 -Mes-CH), 3.11 (br m, 2H, COE-CH), 2.90 (br s, 4H, COE-CH and COE-CH₂), 2.75 (s, 6H, N-ortho-Mes-CH₃), 2.55 (br m, 2H, COE-CH₂), 2.46 (br s, 2H, CH(CH₃)₂), 2.39 (s, 6H, N_3 -ortho-Mes-CH₃), 2.17 (s, 3H, N-para-Mes-CH₃), 2.11 (s, 3H, N_3 -para-Mes-CH₃), 1.96 (br m, 2H, COE-CH₂), 1.70 (br s, 2H, COE-CH₂), 1.59 (br s, 2H, COE-CH₂), 1.50 (br s, 2H, COE-CH₂), 1.44 (br s, 4H, COE-CH₂), 1.28 (dd, $^3J_{\text{PH}} = 15.8$, $^3J_{\text{HH}} = 7.0$ Hz, 6H, CH(CH₃)₂), 1.24–1.18 (m, 4H, COE-CH₂), 1.17 (dd, $^3J_{\text{PH}} = 15.3$, $^3J_{\text{HH}} = 7.1$ Hz, 6H, CH(CH₃)₂), 1.09 (br s, 2H, COE-CH₂), 0.99 (br s, 2H, COE-CH₂). ^{13}C NMR (176 MHz, C_6D_6): δ 147.64 (s, N_3 -ipso-Mes-C-P), 139.61 (s, N-ortho-ipso-Mes-C-CH₃), 136.13 (s, N-ipso-Mes-C-P), 134.28 (s, N_3 -ortho-ipso-Mes-C-CH₃), 132.35 (s, N-para-ipso-Mes-C-CH₃), 130.64 (s, N_3 -para-ipso-Mes-C-CH₃), 130.41 (s, N_3 -Mes-CH), 130.19 (s, N-Mes-CH), 73.07 (d, $^1J_{\text{RhC}} = 12.0$ Hz, COE-CH), 71.70 (d, $^1J_{\text{RhC}} = 11.9$ Hz, COE-CH), 31.64 (br s, COE-CH₂), 30.75 (br s, COE-CH₂), 30.43 (br s, COE-CH₂), 29.87 (s, COE-CH₂), 29.60 (br d, $^1J_{\text{PC}} = 44.7$ Hz, CH(CH₃)₂), 27.74 (br s, COE-CH₂), 27.46 (br s, COE-CH₂), 26.80 (br s, COE-CH₂), 26.76 (s, COE-CH₂), 26.13 (s, COE-CH₂), 21.80 (s, N_3 -ortho-Mes-CH₃), 21.20 (s, N_3 -para-Mes-CH₃), 21.16 (s, N-para-Mes-CH₃), 20.50 (s, N_3 -ortho-Mes-CH₃), 17.63 (s, CH(CH₃)₂), 16.13 (s, CH(CH₃)₂). $^{31}\text{P}\{^1\text{H}\}$ NMR (284 MHz, C_6D_6): δ 99.6 (br s). Attempts to obtain high-quality elemental analyses (within 3% of computed values) for this compound have been unsuccessful.

Method to acquire crystals of $^i\text{Pr}_2\text{P}(\text{N}(2,4,6\text{-Me}_3\text{C}_6\text{H}_2))_2\text{Rh}(\text{COE})_2$ (**29**)

Complex **29** (32.2 mg, 0.0388 mmol) was added to a J. Young valve NMR tube, followed by benzene (0.5 mL), yielding an orange solution. The vessel was irradiated with a black light ($\lambda = 365$ nm) for 1 h. Afterwards several resonances were observed in the ^{31}P NMR spectrum ($^{31}\text{P}\{^1\text{H}\}$ NMR (284 MHz, C_6D_6) δ 64.0 (s, **29**, 29.4%), 61.1 (s, 27.9%), 51.7 (s, 26.4%), 11.8 (s, 16.3%). The tube was brought into a glove box. The solution was then filtered through a Kimwipe (packed into pipette to act as a filter) (to remove any Rh black particles). A few yellow/orange plates of **29** were grown from the solution when left at ambient temperature for 1 week. The few crystals were “dried” by flowing argon over them through a pipette to evaporate residual pentane. $^{31}\text{P}\{^1\text{H}\}$ NMR analysis of the crystals revealed one resonance at δ 64.0 attributed to **29**. The sample of **29** contained a large amount of residual pentane and was too dilute to observe any key resonances corresponding to **29** in the ^1H NMR spectrum.



CHAPTER 7: References

1. Sierra, M. A.; de La Torre, M. C. *Angew. Chem. Int. Ed.* **2000**, *39*, 1538-1559.
2. Zhang, M.; Huang, X.; Shen, L.; Qin, Y. *J. Am. Chem. Soc.* **2009**, *131*, 6013-6020.
3. Zi, W.; Xie, W.; Ma, D. *J. Am. Chem. Soc.* **2012**, *134* (22), 9126-9129.
4. Liu, X.-Y.; Qin, Y. *Green Synth. Catal.* **2022**, *3* (1), 25-39.
5. Hartwig, J. F. Structure and Bonding. In *Organotransition Metal Chemistry: From Bonding to Catalysis*, 1 ed.; University Science Books, 2010; pp 1-120.
6. Hartwig, J. F.; Walsh, P. J. Principles of Catalysis. In *Organotransition Metal Chemistry: From Bonding to Catalysis*, 1 ed.; University Science Books, 2010; pp 539-575.
7. Trnka, T. M.; Grubbs, R. H. *Acc. Chem. Res.* **2001**, *34*, 18-29.
8. Etayo, P.; Vidal-Ferran, A. *Chem. Soc. Rev.* **2013**, *42*, 728-754.
9. Ruiz-Castillo, P.; Buchwald, S. L. *Chem. Rev.* **2016**, *116*, 12564-12649.
10. Crabtree, R. H. Cationic Rhodium and Iridium Complexes in Catalysis. In *Homogeneous Catalysis with Metal Phosphine Complexes*, Springer US, 1983; pp 297-316.
11. Osborn, J. A.; Jardine, F. H.; Young, J. F.; Wilkinson, G. *J. Chem. Soc.* **1966**, 1711-1732.
12. Duckett, S. B.; Newell, C. L.; Eisenberg, R. *J. Am. Chem. Soc.* **1994**, *116*, 10548-10556.
13. Vaska, L.; DiLuzio, J. W. *J. Am. Chem. Soc.* **1961**, *83*, 2784-2785.
14. Crabtree, R. *Acc. Chem. Res.* **1979**, *12*, 331-337.
15. Chen, Z.; Dong, V. M. Rhodium(I)-Catalyzed Hydroformylation and Hydroamination. In *Rhodium Catalysis in Organic Synthesis*, 2019; pp 49-62.

16. Endo, K. Rhodium(I)-Catalyzed Hydroboration and Diboration. In *Rhodium Catalysis in Organic Synthesis*, 2019; pp 39-48.
17. Corey, J. Y. *Chem. Rev.* **2016**, *116*, 11291-11435.
18. Medici, S.; Peana, M.; Pelucelli, A.; Zoroddu, M. A. *Molecules* **2021**, *26*, 2553.
19. Evans, A. P. *Modern rhodium-catalyzed organic reactions*; Wiley-VCH: Weinheim, 2005.
- 20.
21. Alisha, M.; Philip, R. M.; Anilkumar, G. *J. Organomet. Chem.* **2022**, *959*, 122207.
22. Ishiyama, T.; Hartwig, J. *J. Am. Chem. Soc.* **2000**, *122*, 12043-12044.
23. Peng, Q.; Yan, H.; Zhang, X.; Wu, Y.-D. *J. Org. Chem.* **2012**, *77*, 7487-7496.
24. Qi, X.; Li, Y.; Bai, R.; Lan, Y. *Acc. Chem. Res.* **2017**, *50*, 2799-2808.
25. Cotton, F. A.; Wilkinson, G.; Murillo, C. A.; Bochmann, M. *Advanced inorganic chemistry*. 6 ed.; John Wiley and Sons, Inc., 1999.
26. Mond, L.; Langer, C.; Quincke, F., *Chemiker-Ztg.* Bd: 1890.
27. Herrmann, W. A. *J. Organomet. Chem.* **1990**, *383*, 21-44.
28. Sen, A. *Acc. Chem. Res.* **1993**, *26*, 303-310.
29. Henrici-Olivé, G.; Olivé, S. *The chemistry of the catalyzed hydrogenation of carbon monoxide*. Springer Science & Business Media, 2012.
30. Stahl, G. E. *Georgii Ernesti Stahl, Experimenta, Observationes, Animadversiones, CCC Numero, Chymicae Et Physicae*. Haude, **1731**.
31. Constable, E. C. *Chemistry* **2019**, *1*, 126-163.
32. Finlay, V. *The brilliant history of color in art*. Getty Publications, **2014**.
33. Zeise, W. C. *Ann. Phys.* **1831**, *97*, 497-541.
34. Black, M.; Mais, R.; Owston, P. *Acta Crystallogr. B: Struct. Sci. Cryst. Eng. Mater.* **1969**, *25*, 1753-1759.
35. Ellis, J. E.; Beck, W. *Angew. Chem. Int. Ed.* **1995**, *34*, 2489-2491.

36. Beck, W. *Angew. Chem. Int. Ed.* **1991**, *30*, 168-169.
37. Brennan, J. G.; Andersen, R. A.; Robbins, J. L. *J. Am. Chem. Soc.* **1986**, *108*, 335-336.
38. Selg, P.; Brintzinger, H. H.; Andersen, R. A.; Horváth, I. T. *Angew. Chem. Int. Ed.* **1995**, *34*, 791-793.
39. Tacke, M.; Klein, C.; Stufkens, D.; Oskam, A.; Jutzi, P.; Bunte, E. *Z. Anorg. Allg. Chem.* **1993**, *619*, 865-868.
40. Cotton, F. A.; Wilkinson, G.; Gaus, P. L. *Basic Inorganic Chemistry*. Wiley, 1995.
41. Meißner, A.; Alberico, E.; Drexler, H.-J.; Baumann, W.; Heller, D. *Catal. Sci. Technol.* **2014**, *4*, 3409-3425.
42. Van der Boom, M. E.; Milstein, D. *Chem. Rev.* **2003**, *103*, 1759-1792.
43. Eilbracht, P.; Dahler, P. *Chem. Ber.* **1980**, *113*, 542-554.
44. Crabtree, R. H. *J. Organomet. Chem.* **2005**, *690*, 5451-5457.
45. Tolman, C. A. *Chem. Rev.* **1977**, *77*, 313-348.
46. Hopkinson, M. N.; Richter, C.; Schedler, M.; Glorius, F. *Nature* **2014**, *510*, 485-496.
47. Ni, H.; Chan, W.-L.; Lu, Y. *Chem. Rev.* **2018**, *118*, 9344-9411.
48. Atkins, P.; Overton, T. *Shriver and Atkins' inorganic chemistry*. Oxford University Press, USA, 2010.
49. Dierkes, P.; van Leeuwen, P. W. *J. Chem. Soc.* **1999**, 1519-1530.
50. Barber, T.; Argent, S. P.; Ball, L. T. *ACS Catal.* **2020**, *10*, 5454-5461.
51. Kealy, T.; Pauson, P. *Nature* **1951**, *168*, 1039-1040.
52. Miller, S. A.; Tebboth, J. A.; Tremaine, J. F. *J. Chem. Soc.* **1952**, 632-635.
53. Pauson, P. L. *J. Organomet. Chem.* **2001**, *637*, 3-6.
54. Werner, H. *Angew. Chem. Int. Ed.* **2012**, *51*, 6052-6058.

55. Wilkinson, G.; Birmingham, J. *J. Am. Chem. Soc.* **1954**, *76*, 4281-4284.
56. Cossee, P. *J. Catal.* **1964**, *3*, 80-88.
57. Claverie, J. P.; Schaper, F. *MRS Bulletin* **2013**, *38*, 213-218.
58. Grimmer, N. E.; Coville, N. J. *S. Afr. J. Chem.* **2001**, *54*.
59. Brintzinger, H.; Bercaw, J. E. *J. Am. Chem. Soc.* **1971**, *93*, 2045-2046.
60. Trost, B. M.; Ryan, M. C. *Angew. Chem. Int. Ed.* **2017**, *56*, 2862-2879.
61. Werner, H. *Landmarks in organo-transition metal chemistry: a personal view*. Springer, 2009.
62. Shapiro, P. J. *Coord. Chem. Rev.* **2002**, *1*, 67-81.
63. Bryliakov, K. P. *Russ. Chem. Rev.* **2007**, *76*, 253.
64. Hönicke, D.; Födisch, R.; Claus, P.; Olson, M. *Ullmann's encycl. ind. chem.* **2000**.
65. Britovsek, G. J. P.; Gibson, V. C.; Wass, D. F. *Angew. Chem. Int. Ed.* **1999**, *38*, 428-447.
66. Kempe, R. *Eur. J. Inorg. Chem.* **2003**, *2003*, 791-803.
67. Gade, L. H. *J. Organomet. Chem.* **2002**, *661*, 85-94.
68. Vidyaratne, I.; Gambarotta, S.; Korobkov, I.; Budzelaar, P. H. *Inorg. Chem.* **2005**, *44*, 1187-1189.
69. Bourget-Merle, L.; Lappert, M. F.; Severn, J. R. *Chem. Rev.* **2002**, *102*, 3031-3066.
70. Camp, C.; Arnold, J. *Dalton Trans.* **2016**, *45*, 14462-14498.
71. Chen, C.; Bellows, S. M.; Holland, P. L. *Dalton Trans.* **2015**, *44*, 16654-16670.
72. Carey, D. T.; Cope-Eatough, E. K.; Vilaplana-Mafé, E.; Mair, F. S.; Pritchard, R. G.; Warren, J. E.; Woods, R. J. *Dalton Trans.* **2003**, 1083-1093.
73. Romero-Fernández, M. P.; Ávalos, M.; Babiano, R.; Cintas, P.; Jiménez, J. L.; Light, M. E.; Palacios, J. C. *Org. Biomol. Chem.* **2014**, *12*, 8997-9010.

74. Do, D. C. H.; Keyser, A.; Protchenko, A. V.; Maitland, B.; Pernik, I.; Niu, H.; Kolychev, E. L.; Rit, A.; Vidovic, D.; Stasch, A. *Chem. Eur. J.* **2017**, *23*, 5830-5841.
75. Webster, R. L. *Dalton Trans.* **2017**, *46*, 4483-4498.
76. Coles, M. P. *Chem. Commun.* **2009**, 3659-3676.
77. Patmore, N. J. Recent developments in the chemistry of metal-metal multiply bonded paddlewheel compounds. In *Organometallic Chemistry*, 2010; pp 77-92.
78. Chlupatý, T.; Růžička, A. *Coord. Chem. Rev.* **2016**, *314*, 103-113.
79. Kazeminejad, N.; Munzel, D.; Gamer, M. T.; Roesky, P. W. *Chem. Commun.* **2017**, *53*, 1060-1063.
80. Bambirra, S.; Bouwkamp, M. W.; Meetsma, A.; Hessen, B. *J. Am. Chem. Soc.* **2004**, *126*, 9182-9183.
81. Collins, S. *Coord. Chem. Rev.* **2011**, *255*, 118-138.
82. Flores, J. C.; Chien, J. C.; Rausch, M. D. *Organometallics* **1995**, *14*, 1827-1833.
83. Tacke, R.; Ribbeck, T. *Dalton Trans.* **2017**, *46*, 13628-13659.
84. Peris, E.; Crabtree, R. H. *Chem. Soc. Rev.* **2018**, *47*, 1959-1968.
85. Lawrence, M. A. W.; Green, K.-A.; Nelson, P. N.; Lorraine, S. C. *Polyhedron* **2018**, *143*, 11-27.
86. Piccirilli, L.; Lobo Justo Pinheiro, D.; Nielsen, M. *J. Catal.* **2020**, *10*, 773.
87. Morales-Morales, D. *Rev. Soc. Quím.* **2004**, *48*, 338-346.
88. Heinemann, C.; Müller, T.; Apeloig, Y.; Schwarz, H. *J. Am. Chem. Soc.* **1996**, *118*, 2023-2038.
89. Jalal, M.; Hammouti, B.; Touzani, R.; Aouniti, A.; Ozdemir, I. *Mater Today Proc* **2020**, *31*, S122-S129.
90. Kempe, R. *Angew. Chem. Int. Ed.* **2000**, *39*, 468-493.
91. Roesky, P. W. *Chem. Soc. Rev.* **2000**, *29*, 335-345.

92. Webb, D. J.; Hayes, P. G. 1.07 - On the Coordination Chemistry of Bis- and Trisphosphinimine Containing Ligands. In *Comprehensive Coordination Chemistry III*, Elsevier, 2021; pp 131-157.
93. Dehnicke, K.; Weller, F. *Coord. Chem. Rev.* **1997**, *158*, 103-169.
94. Ly, T. Q.; Woollins, J. *Coord. Chem. Rev.* **1998**, *176*, 451-481.
95. Panda, T. K.; Roesky, P. W. *Chem. Soc. Rev.* **2009**, *38*, 2782-2804.
96. Li, S.; Miao, W.; Tang, T.; Dong, W.; Zhang, X.; Cui, D. *Organometallics* **2008**, *27*, 718-725.
97. Hanson, S. S.; Doni, E.; Traboulsee, K. T.; Coulthard, G.; Murphy, J. A.; Dyker, C. A. *Angew. Chem. Int. Ed.* **2015**, *54*, 11236-11239.
98. Abel, E. W.; Mucklejohn, S. A. *Phosphorus Sulfur Silicon Relat. Elem.* **1981**, *9*, 235-266.
99. Eguchi, S.; Matsushita, Y.; Yamashita, K. *Org. Prep. Proced. Int.* **1992**, *24*, 209-243.
100. Staudinger, H.; Meyer, J. *Helv. Chim. Acta* **1919**, *2*, 635-646.
101. Gololobov, Y. G.; Zhmurova, I. N.; Kasukhin, L. F. *Tetrahedron* **1981**, *37*, 437-472.
102. Gololobov, Y. G.; Kasukhin, L. F. *Tetrahedron* **1992**, *48*, 1353-1406.
103. Panda, T. K.; Zulys, A.; Gamer, M. T.; Roesky, P. W. *J. Organomet. Chem.* **2005**, *690*, 5078-5089.
104. Liddle, S. T.; Mills, D. P.; Wooles, A. J. *Chem. Soc. Rev.* **2011**, *40*, 2164-2176.
105. Panda, T. K.; Roesky, P. W. *Chem. Soc. Rev.* **2009**, *38*, 2782-2804.
106. Gregson, M.; Wooles, A. J.; Cooper, O. J.; Liddle, S. T. *Comments Inorg.* **2015**, *35*, 262-294.
107. MacNeil, C. S.; Hayes, P. G. *Chem. Eur. J.* **2019**, *25*, 8203-8207.
108. MacNeil, C. S.; Hsiang, S.-J.; Hayes, P. G. *Chem. Commun.* **2020**, *56*, 12323-12326.

109. Bebbington, M. W.; Bourissou, D. *Coord. Chem. Rev.* **2009**, *253*, 1248-1261.
110. Tian, W. Q.; Wang, Y. A. *J. Org. Chem.* **2004**, *69*, 4299-308.
111. Fianchini, M.; Maseras, F. *Tetrahedron* **2019**, *75*, 1852-1859.
112. Alajarin, M.; Conesa, C.; Rzepa, H. S. *J. Chem. Soc., Perkin Trans. 2* **1999**, 1811-1814.
113. Widauer, C.; Grützmacher, H.; Shevchenko, I.; Gramlich, V. *Eur. J. Inorg. Chem.* **1999**, *1999*, 1659-1664.
114. Bebbington, M. W. P.; Bourissou, D. *Coord. Chem. Rev.* **2009**, *253*, 1248-1261.
115. Steiner, M. R.; Hlina, J. A.; Uher, J. M.; Fischer, R. C.; Neshchadin, D.; Wilfling, T. *Dalton Trans.* **2022**.
116. Dickie, T. K.; Aborawi, A. A.; Hayes, P. G. *Organometallics* **2020**, *39*, 2047-2052.
117. Boom, D. H.; Jupp, A. R.; Nieger, M.; Ehlers, A. W.; Slootweg, J. C. *Chem. Eur. J.* **2019**, *25*, 13299-13308.
118. Dickie, T. K. K.; Hayes, P. G. *Organometallics* **2022**, *41*, 278-283.
119. Goswami, B. *Enantiopure Iminophosphonamido complexes: Synthesis, Photoluminescence and Catalysis*. 1 ed.; Cuvillier Verlag, 2020; p 222.
120. Tat'yana, A. P.; Sinopalnikova, I. S.; Peregudov, A. S.; Fedyanin, I. V.; Demonceau, A.; Ustynyuk, N. A.; Kalsin, A. M. *Dalton Trans.* **2016**, *45*, 17030-17041.
121. Li, S.; Cui, D.; Li, D.; Hou, Z. *Organometallics* **2009**, *28*, 4814-4822.
122. Albahily, K.; Fomitcheva, V.; Gambarotta, S.; Korobkov, I.; Murugesu, M.; Gorelsky, S. I. *J. Am. Chem. Soc.* **2011**, *133*, 6380-6387.
123. Stapleton, R. L.; Chai, J.; Taylor, N. J.; Collins, S. *Organometallics* **2006**, *25*, 2514-2524.
124. Straub, B. F.; Gruber, I.; Rominger, F.; Hofmann, P. *J. Organomet. Chem.* **2003**, *684*, 124-143.

125. Tomaszewski, R.; Vollmerhaus, R.; Al-Humydi, A.; Wang, Q.; Taylor, N. J.; Collins, S. *Can. J. Chem.* **2006**, *84*, 214-224.
126. Sinopalnikova, I.; Peganova, T.; Belkova, N.; Deydier, E.; Daran, J.-C.; Shubina, E.; Kalsin, A.; Poli, R. *Eur. J. Inorg. Chem.* **2018**, 2285-2299.
127. Prashanth, B.; Singh, S. *Chem. Sci. J.* **2015**, *127*, 315-325.
128. Hawley, A. L.; Stasch, A. *Eur. J. Inorg. Chem.* **2015**, *2015*, 258-270.
129. Barry, S. T. *Coord. Chem. Rev.* **2013**, *257*, 3192-3201.
130. Fryzuk, M. D.; Yu, P.; Patrick, B. O. *Can. J. Chem.* **2001**, *79*, 1194-1200.
131. Hawley, A. L.; Ohlin, C. A.; Fohlmeister, L.; Stasch, A. *Chem. Eur. J.* **2017**, *23*, 447-455.
132. Goswami, B.; Feuerstein, T. J.; Yadav, R.; Köppe, R.; Lebedkin, S.; Kappes, M. M.; Roesky, P. W. *Chem. Eur. J.* **2021**, *27*, 4401-4411.
133. Peganova, T. y. A.; Filippov, O. A.; Belkova, N. V.; Fedyanin, I. V.; Kalsin, A. M. *Eur. J. Inorg. Chem.* **2018**, *2018*, 5098-5107.
134. Peganova, T. A.; Kalsin, A. M.; Ustynyuk, N. A.; Vasil'ev, A. A. *Russ. Chem. Bull.* **2014**, *63*, 2305-2308.
135. Kalsin, A. M.; Peganova, T. A.; Sinopalnikova, I. S.; Fedyanin, I. V.; Belkova, N. V.; Deydier, E.; Poli, R. *Dalton Trans.* **2020**, *49*, 1473-1484.
136. Scriven, E. F. V.; Turnbull, K. *Chem. Rev.* **1988**, *88*, 297-368.
137. Treitler, D. S.; Leung, S. *J. Org. Chem.* **2022**, *87*, 11293-11295.
138. Chen, L.; Ren, P.; Carrow, B. P. *J. Am. Chem. Soc.* **2016**, *138*, 6392-6395.
139. Nonnenmacher, M.; Buck, D. M.; Kunz, D. *Beilstein J Org Chem* **2016**, *12*, 1884-1896.
140. Huynh, H. V. *Chem. Rev.* **2018**, *118*, 9457-9492.
141. Lu, W. Y.; Cavell, K. J.; Wixey, J. S.; Kariuki, B. *Organometallics* **2011**, *30*, 5649-5655.

142. Bonati, F.; Wilkinson, G. *J. Chem. Soc.* **1964**, 3156-3160.
143. Connelly, N. G.; Davis, P. R.; Harry, E. E.; Klangsinrikul, P.; Venter, M. *J. Chem. Soc.* **2000**, 2273-2277.
144. Boyd, D. C.; Connelly, N. G.; Herbosa, G. G.; Hill, M. G.; Mann, K. R.; Mealli, C.; Orpen, A. G.; Richardson, K. E.; Rieger, P. H. *Inorg. Chem.* **1994**, *33*, 960-971.
145. Zhu, D.; Budzelaar, P. H. *Dalton Trans.* **2013**, *42*, 11343-11354.
146. Nakajima, Y.; Shimada, S. *RSC Adv.* **2015**, *5*, 20603-20616.
147. Crabtree, R. H. Introduction and History. In *Iridium Catalysis*, Springer Berlin Heidelberg, 2011; pp 1-10.
148. Shannon, R. D. *Acta Crystallogr. A: Found. Crystallogr.* **1976**, *32*, 751-767.
149. Chianese, A. R.; Li, X.; Janzen, M. C.; Faller, J.; Crabtree, R. H. *Organometallics* **2003**, *22*, 1663-1667.
150. van der Ent, A.; Onderdelinden, A. L.; Schunn, R. A. Chlorobis(cyclooctene)rhodium(I) and -Iridium(I) Complexes. In *Inorg. Synth.*, 1973; pp 92-95.
151. Meguro, T.; Yoshida, S.; Igawa, K.; Tomooka, K.; Hosoya, T. *Org. Lett.* **2018**, *20*, 4126-4130.
152. Dickie, T. K. K. Lethbridge, Alta.: University of Lethbridge, Dept. of Chemistry and Biochemistry, 2022.
153. Tejada, J.; Reau, R.; Dahan, F.; Bertrand, G. *J. Am. Chem. Soc.* **1993**, *115*, 7880-7881.
154. Bieger, K.; Tejada, J.; Reau, R.; Dahan, F.; Bertrand, G. *J. Am. Chem. Soc.* **1994**, *116*, 8087-8094.
155. Hillhouse, G. L.; Goeden, G. V.; Haymore, B. L. *Inorg. Chem.* **1982**, *21*, 2064-2071.
156. Ogawa, T.; Suzuki, T.; Hein, N. M.; Pick, F. S.; Fryzuk, M. D. *Dalton Trans.* **2015**, *44*, 54-7.
157. Dickie, T. K.; MacNeil, C. S.; Hayes, P. G. *Dalton Trans.* **2020**, *49*, 578-582.

158. Fajardo, J.; Chan, A. L.; Tham, F. S.; Lavallo, V. *Inorganica Chim. Acta* **2014**, *422*, 206-208.
159. Beck, W.; Rieber, W.; Kirmaier, H. *Z. fur Naturforsch. B: J. Chem. Sci.* **1977**, *32*, 528-532.
160. Boese, R.; Düppmann, M.; Kuchen, W.; Peters, W. *Z. Anorg. Allg. Chem.* **1998**, *624*, 837-845.
161. Hofmann, P.; Shishkov, I. V.; Rominger, F. *Inorg. Chem.* **2008**, *47*, 11755-11762.
162. Shishkov, I. V.; Rominger, F.; Hofmann, P. *Organometallics* **2009**, *28*, 1049-1059.
163. Cristau, H.-J.; Jouanin, I.; Taillefer, M. *J. Organomet. Chem.* **1999**, *584*, 68-72.
164. Allcock, H. *Phosphorus-nitrogen compounds: cyclic, linear, and high polymeric systems*. Elsevier, 2012.
165. Bebbington, M. W.; Bontemps, S.; Bouhadir, G.; Bourissou, D. *Angew. Chem. Int. Ed.* **2007**, *119*, 3397-3400.
166. Bräse, S.; Banert, K. *Organic azides: syntheses and applications*. John Wiley & Sons, 2010.
167. Bieger, K.; Bouhadir, G.; Réau, R.; Dahan, F.; Bertrand, G. *J. Am. Chem. Soc.* **1996**, *118*, 1038-1044.
168. Crabtree, R.; Chodosh, D.; Quirk, J.; Felkin, H.; Fillebeen-Khan, T.; Morris, G. Iridium Compounds in Homogeneous Hydrogenation. In *Fundamental Research in Homogeneous Catalysis*, Springer, 1979; pp 475-485.
169. Johnson, K. R.; Hayes, P. G. *Organometallics* **2009**, *28*, 6352-6361.
170. Barral, K.; Moorhouse, A. D.; Moses, J. E. *Org. Lett.* **2007**, *9*, 1809-1811.
171. Burger, B. J.; Bercaw, J. E. Vacuum Line Techniques for Handling Air-Sensitive Organometallic Compounds. In *Experimental Organometallic Chemistry*, J. Am. Chem. Soc., 1987; Vol. 357, pp 79-115.
172. Greenwood, B. P.; Forman, S. I.; Rowe, G. T.; Chen, C.-H.; Foxman, B. M.; Thomas, C. M. *Inorg. Chem.* **2009**, *48*, 6251-6260.

173. Bîrzoï, R. M.; Lungu, D.; Jones, P. G.; Bartsch, R.; du Mont, W.-W. *Z. Anorg. Allg. Chem.* **2018**, *644*, 381-390.
174. Sebest, F.; Lachhani, K.; Pimpasri, C.; Casarrubios, L.; White, A. J. P.; Rzepa, H. S.; Díez-González, S. *Adv. Synth. Catal.* **2020**, *362*, 1877-1886.
175. McCleverty, J. A.; Wilkinson, G.; Lipson, L. G.; Maddox, M. L.; Kaesz, H. D. *Inorg. Synth.* **1966**, *8*, 211-214.
176. Cotton, F. A.; Lahuerta, P.; Sanau, M.; Schwotzer, W. *Inorganica Chim. Acta* **1986**, *120*, 153-157.
177. Cosier, J.; Glazer, A. M. *J. Appl. Crystallogr.* **1986**, *19*, 105-107.
178. *CrysAlisPRO*, CrysAlisPRO, Oxford Diffraction / Agilent Technologies UK Ltd, Yarnton, England, 2010.
179. Sheldrick, G. M. *Acta Crystallogr. A: Found. Crystallogr.* **2015**, *71*, 3-8.
180. Sheldrick, G. M. *Acta Crystallogr. C: Struct. Chem.* **2015**, *71*, 3-8.
181. Dolomanov, O. V.; Bourhis, L. J.; Gildea, R. J.; Howard, J. A. K.; Puschmann, H. *J. Appl. Crystallogr.* **2009**, *42*, 339-341.
182. Macrae, C. F.; Sovago, I.; Cottrell, S. J.; Galek, P. T. A.; McCabe, P.; Pidcock, E.; Platings, M.; Shields, G. P.; Stevens, J. S.; Towler, M.; Wood, P. A. *J. Appl. Crystallogr.* **2020**, *53*, 226-235.

APPENDIX 1– CRYSTALLOGRAPHIC DATA TABLES

Table A1.1 X-ray crystallography data of compounds (Ph₂P(NAd)(NHAd) (**2**) and Ph₂P(NMes)₂Rh(COD) (**3**)

	2	3
Identification code	PH21021_Refinalized	PH21032
Empirical formula	C ₃₂ H ₄₁ N ₂ P	C ₃₈ H ₄₄ N ₂ PRh
Formula weight	484.67	662.63
Temperature/K	101(1)	103.2(9)
Crystal system	triclinic	Triclinic
Space group	P-1	P-1
<i>a</i> /Å	6.4858(2)	9.1183(2)
<i>b</i> /Å	12.7888(4)	9.6326(2)
<i>c</i> /Å	16.1089(5)	19.8829(3)
<i>α</i> /°	82.095(3)	95.4090(10)
<i>β</i> /°	81.942(3)	98.877(2)
<i>γ</i> /°	76.216(2)	108.400(2)
Volume/Å ³	1277.31(7)	1618.09(6)
Z	2	2
ρ _{calc} /cm ³	1.2601	1.360
μ/mm ⁻¹	1.116	4.941
F(000)	525.9	692.0
Crystal size/mm ³	0.2 × 0.07 × 0.06	0.24 × 0.18 × 0.03
Radiation	Cu Kα (λ = 1.54184)	Cu Kα (λ = 1.54184)
2θ range for data collection/°	7.16 to 150.1	4.552 to 150.738
Index ranges	-8 ≤ <i>h</i> ≤ 8, -15 ≤ <i>k</i> ≤ 16, -19 ≤ <i>l</i> ≤ 18	-11 ≤ <i>h</i> ≤ 11, -12 ≤ <i>k</i> ≤ 12, -24 ≤ <i>l</i> ≤ 24
Reflections collected	24756	31451
Independent reflections	5142 [R _{int} = 0.0379, R _{sigma} = 0.0270]	6562 [R _{int} = 0.0548, R _{sigma} = 0.0383]
Data/restraints/parameters	5142/0/316	6562/0/385
Goodness-of-fit on F ²	1.029	1.083
Final R indexes [I ≥ 2σ (I)]	R ₁ = 0.0490, wR ₂ = 0.1067	R ₁ = 0.0352, wR ₂ = 0.0920
Final R indexes [all data]	R ₁ = 0.0516, wR ₂ = 0.1079	R ₁ = 0.0378, wR ₂ = 0.0935
Largest diff. peak/hole / e Å ⁻³	0.38/-0.50	1.43/-1.24

Table A1.2 X-ray crystallography data of compounds $\text{Ph}_2\text{P}(\text{NAd})_2\text{Rh}(\text{COD})\cdot 1.5\text{C}_6\text{H}_6$ (**4**) and $\text{Ph}_2\text{P}(\text{NMe})_2\text{Rh}(\text{CO})_2$ (**5**)

	4^a	5
Identification code	PH21038b	PH21047
Empirical formula	$\text{C}_{49}\text{H}_{61}\text{N}_2\text{PRh}$	$\text{C}_{32}\text{H}_{32}\text{N}_2\text{O}_2\text{PRh}$
Formula weight	811.92	610.47
Temperature/K	100.02(10)	100.1(3)
Crystal system	triclinic	triclinic
Space group	P-1	P-1
a/Å	10.3047(1)	12.4860(2)
b/Å	10.6941(1)	15.0637(2)
c/Å	20.0564(1)	16.6788(2)
$\alpha/^\circ$	98.612(1)	103.0550(10)
$\beta/^\circ$	97.210(1)	107.6730(10)
$\gamma/^\circ$	112.369(1)	94.9090(10)
Volume/Å ³	1980.18(4)	2871.29(7)
Z	2	4
$\rho_{\text{calc}}/\text{cm}^3$	1.3616	1.412
μ/mm^{-1}	4.138	5.577
F(000)	860.8	1256.0
Crystal size/mm ³	0.41 × 0.1 × 0.09	0.32 × 0.16 × 0.1
Radiation	Cu K α ($\lambda = 1.54184$)	Cu K α ($\lambda = 1.54184$)
2 Θ range for data collection/ $^\circ$	4.54 to 150.2	5.768 to 150.162
Index ranges	-12 ≤ h ≤ 10, -13 ≤ k ≤ 13, -25 ≤ l ≤ 25	-15 ≤ h ≤ 13, -18 ≤ k ≤ 18, -20 ≤ l ≤ 20
Reflections collected	62066	76974
Independent reflections	8080 [$R_{\text{int}} = 0.0296$, $R_{\text{sigma}} = 0.0162$]	11603 [$R_{\text{int}} = 0.0502$, $R_{\text{sigma}} = 0.0282$]
Data/restraints/parameters	8080/0/478	11603/0/697
Goodness-of-fit on F ²	1.086	1.060
Final R indexes [$I \geq 2\sigma(I)$]	$R_1 = 0.0239$, $wR_2 = 0.0591$	$R_1 = 0.0354$, $wR_2 = 0.0895$
Final R indexes [all data]	$R_1 = 0.0253$, $wR_2 = 0.0596$	$R_1 = 0.0396$, $wR_2 = 0.0932$
Largest diff. peak/hole / e Å ⁻³	0.44/-0.58	1.19/-1.05

Notes: ^a Crystallized with one and a half molecules of benzene in the asymmetric unit.

Table A1.3 X-ray crystallography data of compounds Ph₂P(NAd)₂Rh(CO)₂ (**6**) and Ph₂P(NMes)₂Rh(CN(2,6-Me₂C₆H₃))₂ (**7**)

	6	7
Identification code	PH2022002_1	PH2022002_1
Empirical formula	C ₃₄ H ₄₀ N ₂ O ₂ PRh	C ₃₄ H ₄₀ N ₂ O ₂ PRh
Formula weight	642.56	642.56
Temperature/K	100.02(10)	100.02(10)
Crystal system	orthorhombic	orthorhombic
Space group	Pbca	Pbca
a/Å	12.6612(2)	12.6612(2)
b/Å	20.7651(3)	20.7651(3)
c/Å	22.2704(3)	22.2704(3)
α/°	90	90
β/°	90	90
γ/°	90	90
Volume/Å ³	5855.14(15)	5855.14(15)
Z	8	8
ρ _{calc} /cm ³	1.458	1.458
μ/mm ⁻¹	5.495	5.495
F(000)	2672.0	2672.0
Crystal size/mm ³	0.67 × 0.18 × 0.12	0.67 × 0.18 × 0.12
Radiation	Cu Kα (λ = 1.54184)	Cu Kα (λ = 1.54184)
2θ range for data collection/°	7.94 to 150.346	7.94 to 150.346
Index ranges	-14 ≤ h ≤ 15, -26 ≤ k ≤ 25, -27 ≤ l ≤ 26	-14 ≤ h ≤ 15, -26 ≤ k ≤ 25, -27 ≤ l ≤ 26
Reflections collected	30145	30145
Independent reflections	5896 [R _{int} = 0.0334, R _{sigma} = 0.0231]	5896 [R _{int} = 0.0334, R _{sigma} = 0.0231]
Data/restraints/parameters	5896/0/361	5896/0/361
Goodness-of-fit on F ²	1.087	1.087
Final R indexes [I ≥ 2σ (I)]	R ₁ = 0.0280, wR ₂ = 0.0748	R ₁ = 0.0280, wR ₂ = 0.0748
Final R indexes [all data]	R ₁ = 0.0309, wR ₂ = 0.0763	R ₁ = 0.0309, wR ₂ = 0.0763
Largest diff. peak/hole / e Å ⁻³	0.74/-0.60	0.74/-0.60

Table A1.4 X-ray crystallography data of compounds and $\text{Ph}_2\text{P}(\text{NMe}_3)_2\text{Rh}(\text{CN}(2,6\text{-Me}_2\text{C}_6\text{H}_3))_3$ (**8**) and $\text{Ph}_2\text{P}(\text{NMe}_3)_2\text{Ir}(\text{COD})$ (**9**)

	8	9
Identification code	PH21040b_1	PH21045
Empirical formula	$\text{C}_{63}\text{H}_{65}\text{N}_5\text{PRh}$	$\text{C}_{38}\text{H}_{44}\text{IrN}_2\text{P}$
Formula weight	1026.08	751.98
Temperature/K	100.00(13)	120(20)
Crystal system	triclinic	triclinic
Space group	P-1	P-1
a/Å	11.83260(10)	9.0929(1)
b/Å	14.32790(10)	9.6410(1)
c/Å	15.89910(10)	19.9481(1)
$\alpha/^\circ$	94.3780(10)	95.844(1)
$\beta/^\circ$	93.3060(10)	98.856(1)
$\gamma/^\circ$	90.2760(10)	108.397(1)
Volume/Å ³	2683.02(3)	1618.35(3)
Z	2	2
$\rho_{\text{calc}}/\text{cm}^3$	1.270	1.5431
μ/mm^{-1}	3.187	8.660
F(000)	1076.0	749.4
Crystal size/mm ³	0.17 × 0.13 × 0.09	0.36 × 0.16 × 0.06
Radiation	Cu K α ($\lambda = 1.54184$)	Cu K α ($\lambda = 1.54184$)
2 θ range for data collection/ $^\circ$	5.584 to 150.566	4.54 to 150.06
Index ranges	-14 ≤ h ≤ 14, -17 ≤ k ≤ 17, -19 ≤ l ≤ 19	-11 ≤ h ≤ 10, -12 ≤ k ≤ 12, -24 ≤ l ≤ 24
Reflections collected	83528	48926
Independent reflections	10909 [$R_{\text{int}} = 0.0378$, $R_{\text{sigma}} =$ 0.0211]	6543 [$R_{\text{int}} = 0.0553$, $R_{\text{sigma}} =$ 0.0249]
Data/restraints/parameters	10909/0/643	6543/0/385
Goodness-of-fit on F ²	1.059	1.033
Final R indexes [$I \geq 2\sigma(I)$]	$R_1 = 0.0252$, $wR_2 = 0.0616$	$R_1 = 0.0233$, $wR_2 = 0.0594$
Final R indexes [all data]	$R_1 = 0.0271$, $wR_2 = 0.0623$	$R_1 = 0.0253$, $wR_2 = 0.0602$
Largest diff. peak/hole / e Å ⁻³	0.44/-0.38	1.15/-1.67

Table A1.5 X-ray crystallography data of compounds $\text{Ph}_2\text{P}(\text{NAd})_2\text{Ir}(\text{COD})\cdot 1.5\text{C}_6\text{H}_6$ (**10**)
and $\text{Ph}_2\text{P}(\text{NMes})_2\text{Rh}(\text{COE})_2\cdot 0.5\text{C}_6\text{H}_6$ (**13**)

	10^a	13^b
Identification code	PH22008	PH22008
Empirical formula	$\text{C}_{49}\text{H}_{61}\text{IrN}_2\text{P}$	$\text{C}_{49}\text{H}_{61}\text{IrN}_2\text{P}$
Formula weight	901.16	901.16
Temperature/K	100.00(10)	100.00(10)
Crystal system	triclinic	triclinic
Space group	P-1	P-1
a/Å	10.32870(10)	10.32870(10)
b/Å	10.70080(10)	10.70080(10)
c/Å	19.9937(2)	19.9937(2)
$\alpha/^\circ$	98.5250(10)	98.5250(10)
$\beta/^\circ$	96.9650(10)	96.9650(10)
$\gamma/^\circ$	112.6530(10)	112.6530(10)
Volume/Å ³	1977.91(4)	1977.91(4)
Z	2	2
$\rho_{\text{calc}}/\text{cm}^3$	1.513	1.513
μ/mm^{-1}	7.186	7.186
F(000)	922.0	922.0
Crystal size/mm ³	0.11 × 0.08 × 0.05	0.11 × 0.08 × 0.05
Radiation	Cu K α ($\lambda = 1.54184$)	Cu K α ($\lambda = 1.54184$)
2 Θ range for data collection/ $^\circ$	4.556 to 150.664	4.556 to 150.664
Index ranges	-12 ≤ h ≤ 12, -13 ≤ k ≤ 13, -24 ≤ l ≤ 25	-12 ≤ h ≤ 12, -13 ≤ k ≤ 13, -24 ≤ l ≤ 25
Reflections collected	78381	78381
Independent reflections	8041 [$R_{\text{int}} = 0.0441$, $R_{\text{sigma}} = 0.0222$]	8041 [$R_{\text{int}} = 0.0441$, $R_{\text{sigma}} = 0.0222$]
Data/restraints/parameters	8041/0/478	8041/0/478
Goodness-of-fit on F ²	1.045	1.045
Final R indexes [$I \geq 2\sigma(I)$]	$R_1 = 0.0199$, $wR_2 = 0.0466$	$R_1 = 0.0199$, $wR_2 = 0.0466$
Final R indexes [all data]	$R_1 = 0.0208$, $wR_2 = 0.0471$	$R_1 = 0.0208$, $wR_2 = 0.0471$
Largest diff. peak/hole / e Å ⁻³	1.10/-0.93	1.10/-0.93

Notes: ^a Crystallized with one and a half molecules of benzene in the asymmetric unit.

^b Crystallized with a half molecule of benzene in the asymmetric unit.

Table A1.6 X-ray crystallography data of compounds $i\text{-Pr}_2\text{P}(\text{N}_3\text{Ad})(\text{NHAd})$ (**15**) and $[\text{i-Pr}_2\text{P}(\text{N}_3\text{Ad})(\text{NAd})]\text{Li}\cdot 0.5\text{CH}_2\text{Cl}_2$ (**16**)

	15	16^a
Identification code	PH21025	PH21026
Empirical formula	$\text{C}_{26}\text{H}_{45}\text{N}_4\text{P}$	$\text{C}_{53}\text{H}_{90}\text{Cl}_2\text{Li}_2\text{N}_8\text{P}_2$
Formula weight	444.63	986.04
Temperature/K	101.4(10)	102.0(9)
Crystal system	monoclinic	orthorhombic
Space group	P2_1	Fdd2
a/Å	6.38450(10)	39.1886(5)
b/Å	10.1846(2)	25.6868(4)
c/Å	18.9425(3)	11.18700(10)
$\alpha/^\circ$	90	90
$\beta/^\circ$	95.269(2)	90
$\gamma/^\circ$	90	90
Volume/Å ³	1226.50(4)	11261.2(2)
Z	2	8
$\rho_{\text{calc}}/\text{cm}^3$	1.204	1.163
μ/mm^{-1}	1.131	1.880
F(000)	488.0	4272.0
Crystal size/mm ³	$0.52 \times 0.08 \times 0.06$	$0.45 \times 0.31 \times 0.18$
Radiation	$\text{Cu K}\alpha$ ($\lambda = 1.54184$)	$\text{Cu K}\alpha$ ($\lambda = 1.54184$)
2 Θ range for data collection/ $^\circ$	4.684 to 150.046	8.232 to 149.898
Index ranges	$-6 \leq h \leq 7, -12 \leq k \leq 12,$ $-23 \leq l \leq 23$	$-48 \leq h \leq 48, -31 \leq k \leq 24,$ $-13 \leq l \leq 13$
Reflections collected	28554	24402
Independent reflections	4950 [$R_{\text{int}} = 0.0549, R_{\text{sigma}} =$ 0.0329]	5481 [$R_{\text{int}} = 0.0384, R_{\text{sigma}} =$ 0.0256]
Data/restraints/parameters	4950/1/284	5481/1/307
Goodness-of-fit on F^2	1.166	1.035
Final R indexes [$I \geq 2\sigma(I)$]	$R_1 = 0.0643, wR_2 = 0.1835$	$R_1 = 0.0401, wR_2 = 0.1068$
Final R indexes [all data]	$R_1 = 0.0653, wR_2 = 0.1841$	$R_1 = 0.0411, wR_2 = 0.1078$
Largest diff. peak/hole / $e \text{ \AA}^{-3}$	1.06/-0.38	0.42/-0.35
Flack parameter	0.361(10)	-0.021(8)

Notes: ^a Crystallized with a half molecules of dichloromethane in the asymmetric unit.

Table A1.7 X-ray crystallography data of compounds [ⁱPr₂P(N₃Ad)(NAd)-κ²-*N,N*^α]Rh(COD) (**18**) and [ⁱPr₂P(N₃Mes)(NMes)-κ²-*N,N*^α]Rh(COD) (**20**)

	18	20
Identification code	PH22004	PH21042_1
Empirical formula	C ₂₈ H ₄₄ N ₄ O ₂ PRh	C ₃₂ H ₄₈ N ₄ PRh
Formula weight	602.57	622.62
Temperature/K	100.01(10)	100.00(10)
Crystal system	monoclinic	monoclinic
Space group	P2 ₁ /c	P2 ₁ /c
<i>a</i> /Å	20.3871(3)	16.6189(2)
<i>b</i> /Å	10.2202(1)	9.52490(10)
<i>c</i> /Å	13.3986(2)	20.2559(2)
α/°	90	90
β/°	102.800(1)	108.0110(10)
γ/°	90	90
Volume/Å ³	2722.36(6)	3049.25(6)
Z	4	4
ρ _{calc} /cm ³	1.4701	1.356
μ/mm ⁻¹	5.881	5.218
F(000)	1268.7	1312.0
Crystal size/mm ³	0.12 × 0.07 × 0.04	0.55 × 0.29 × 0.23
Radiation	Cu Kα (λ = 1.54184)	Cu Kα (λ = 1.54184)
2θ range for data collection/°	4.44 to 150.34	5.592 to 150.092
Index ranges	-21 ≤ <i>h</i> ≤ 25, -12 ≤ <i>k</i> ≤ 12, -16 ≤ <i>l</i> ≤ 15	-20 ≤ <i>h</i> ≤ 20, -11 ≤ <i>k</i> ≤ 9, -25 ≤ <i>l</i> ≤ 25
Reflections collected	27137	36471
Independent reflections	5505 [R _{int} = 0.0381, R _{sigma} = 0.0266]	6181 [R _{int} = 0.0282, R _{sigma} = 0.0150]
Data/restraints/parameters	5505/0/329	6181/0/353
Goodness-of-fit on F ²	1.020	1.129
Final R indexes [<i>I</i> ≥ 2σ(<i>I</i>)]	R ₁ = 0.0265, wR ₂ = 0.0685	R ₁ = 0.0261, wR ₂ = 0.0606
Final R indexes [all data]	R ₁ = 0.0290, wR ₂ = 0.0697	R ₁ = 0.0270, wR ₂ = 0.0609
Largest diff. peak/hole / e Å ⁻³	1.02/-0.64	0.34/-0.78

Table A1.8 X-ray crystallography data of compounds [ⁱPr₂P(N₃Mes)(NMe_s)-κ²-*N,N^α*]Ir(COD) (**21**) and [ⁱPr₂P(N₃Mes)(NMe_s)-κ²-*N,N^β*]Rh(COD) (**22**)

	21	22
Identification code	PH21049	PH21050
Empirical formula	C ₃₂ H ₄₈ IrN ₄ P	C ₃₂ H ₄₈ N ₄ PRh
Formula weight	711.91	622.62
Temperature/K	100.0(2)	100.01(10)
Crystal system	monoclinic	monoclinic
Space group	P2 ₁ /c	P2 ₁ /c
a/Å	16.6265(2)	18.4528(2)
b/Å	9.54030(10)	15.92790(10)
c/Å	20.2554(3)	21.1815(2)
α/°	90	90
β/°	108.204(2)	92.7750(10)
γ/°	90	90
Volume/Å ³	3052.14(7)	6218.25(10)
Z	4	8
ρ _{calc} /cm ³	1.549	1.330
μ/mm ⁻¹	9.158	5.118
F(000)	1440.0	2624.0
Crystal size/mm ³	0.52 × 0.12 × 0.08	0.24 × 0.16 × 0.1
Radiation	Cu Kα (λ = 1.54184)	Cu Kα (λ = 1.54184)
2θ range for data collection/°	5.596 to 149.95	4.794 to 150.15
Index ranges	-20 ≤ h ≤ 20, -11 ≤ k ≤ 8, -24 ≤ l ≤ 25	-22 ≤ h ≤ 17, -19 ≤ k ≤ 19, -26 ≤ l ≤ 26
Reflections collected	30115	61570
Independent reflections	6140 [R _{int} = 0.0335, R _{sigma} = 0.0229]	12542 [R _{int} = 0.0328, R _{sigma} = 0.0242]
Data/restraints/parameters	6140/0/353	12542/0/705
Goodness-of-fit on F ²	1.073	1.041
Final R indexes [I ≥ 2σ (I)]	R ₁ = 0.0221, wR ₂ = 0.0518	R ₁ = 0.0330, wR ₂ = 0.0839
Final R indexes [all data]	R ₁ = 0.0250, wR ₂ = 0.0530	R ₁ = 0.0374, wR ₂ = 0.0872
Largest diff. peak/hole / e Å ⁻³	0.71/-0.91	1.70/-0.77

Table A1.9 X-ray crystallography data of compounds [$^i\text{Pr}_2\text{P}(\text{N}_3\text{Mes})(\text{NMes})-\kappa^2-N, N^\beta$]Ir(COD) (**23**) and [$^i\text{Pr}_2\text{P}(\text{N}_3\text{Ad})(\text{NAd})-\kappa^2-N, N^\alpha$]Rh(CO)₂ (**24**)

	23	24
Identification code	wit_PH21053	PH22004
Empirical formula	C ₃₂ H ₄₈ IrN ₄ P	C ₂₈ H ₄₄ N ₄ O ₂ PRh
Formula weight	711.91	602.57
Temperature/K	100.00(10)	100.01(10)
Crystal system	triclinic	monoclinic
Space group	P-1	P2 ₁ /c
a/Å	8.22470(10)	20.3871(3)
b/Å	18.4134(5)	10.2202(1)
c/Å	20.6924(4)	13.3986(2)
α /°	89.781(2)	90
β /°	81.953(2)	102.800(1)
γ /°	80.652(2)	90
Volume/Å ³	3061.12(11)	2722.36(6)
Z	4	4
$\rho_{\text{calc}}/\text{g}/\text{cm}^3$	1.545	1.4701
μ/mm^{-1}	9.131	5.881
F(000)	1440.0	1268.7
Crystal size/mm ³	0.12 × 0.07 × 0.05	0.12 × 0.07 × 0.04
Radiation	Cu K α (λ = 1.54184)	Cu K α (λ = 1.54184)
2 Θ range for data collection/°	4.314 to 150.482	4.44 to 150.34
Index ranges	-10 ≤ h ≤ 10, -21 ≤ k ≤ 22, -25 ≤ l ≤ 25	-21 ≤ h ≤ 25, -12 ≤ k ≤ 12, -16 ≤ l ≤ 15
Reflections collected	41171	27137
Independent reflections	11996 [R _{int} = 0.0577, R _{sigma} = 0.0555]	5505 [R _{int} = 0.0381, R _{sigma} = 0.0266]
Data/restraints/parameters	11996/5/725	5505/0/329
Goodness-of-fit on F ²	1.065	1.020
Final R indexes [I ≥ 2 σ (I)]	R ₁ = 0.0428, wR ₂ = 0.1070	R ₁ = 0.0265, wR ₂ = 0.0685
Final R indexes [all data]	R ₁ = 0.0558, wR ₂ = 0.1143	R ₁ = 0.0290, wR ₂ = 0.0697
Largest diff. peak/hole / e Å ⁻³	1.66/-1.99	1.02/-0.64

Table A1.10 X-ray crystallography data of compounds ${}^i\text{Pr}_2\text{P}(\text{N}_3\text{Ad})(\text{NAd})\text{-}\kappa^2\text{-}$
 $N,N^\alpha\text{]Ir}(\text{CO})_2$ (**25**) and ${}^i\text{Pr}_2\text{P}(\text{NMes})(\text{N}_3\text{Mes})\text{-}\kappa^2\text{-}N,N^\alpha\text{]Rh}(\text{COE})_2$ (**28**)

	25	28
Identification code	PH22009	PH21052a
Empirical formula	$\text{C}_{28}\text{H}_{44}\text{IrN}_4\text{O}_2\text{P}$	$\text{C}_{40}\text{H}_{64}\text{N}_4\text{PRh}$
Formula weight	691.88	734.83
Temperature/K	112(17)	100.00(10)
Crystal system	monoclinic	monoclinic
Space group	$\text{P2}_1/\text{c}$	$\text{P2}_1/\text{c}$
a/Å	20.3459(2)	11.1367(2)
b/Å	10.2319(1)	31.9151(5)
c/Å	13.4483(1)	10.88390(10)
$\alpha/^\circ$	90	90
$\beta/^\circ$	102.991(1)	99.0400(10)
$\gamma/^\circ$	90	90
Volume/Å ³	2727.97(4)	3820.40(10)
Z	4	4
$\rho_{\text{calc}}/\text{g}/\text{cm}^3$	1.6845	1.278
μ/mm^{-1}	10.283	4.241
F(000)	1378.7	1568.0
Crystal size/mm ³	0.14 × 0.12 × 0.05	0.29 × 0.17 × 0.07
Radiation	Cu K α ($\lambda = 1.54184$)	Cu K α ($\lambda = 1.54184$)
2 Θ range for data collection/ $^\circ$	4.46 to 150.06	5.538 to 150.43
Index ranges	-25 ≤ h ≤ 25, -11 ≤ k ≤ 12, -16 ≤ l ≤ 16	-13 ≤ h ≤ 13, -33 ≤ k ≤ 39, -13 ≤ l ≤ 13
Reflections collected	54872	37489
Independent reflections	5587 [$R_{\text{int}} = 0.0367$, $R_{\text{sigma}} =$ 0.0171]	7695 [$R_{\text{int}} = 0.0350$, $R_{\text{sigma}} =$ 0.0263]
Data/restraints/parameters	5587/0/329	7695/0/425
Goodness-of-fit on F ²	1.035	1.063
Final R indexes [$I \geq 2\sigma(I)$]	$R_1 = 0.0173$, $wR_2 = 0.0423$	$R_1 = 0.0262$, $wR_2 = 0.0637$
Final R indexes [all data]	$R_1 = 0.0183$, $wR_2 = 0.0428$	$R_1 = 0.0295$, $wR_2 = 0.0650$
Largest diff. peak/hole / e Å ⁻³	0.83/-0.66	0.48/-0.38

Table A1.11 X-ray crystallography data of compounds ${}^i\text{Pr}_2\text{P}(\text{NMes})_2\text{Rh}(\text{COE})_2$ (**29**)

29	
Identification code	PH22013
Empirical formula	$\text{C}_{40}\text{H}_{64}\text{N}_2\text{PRh}$
Formula weight	706.81
Temperature/K	100.01(10)
Crystal system	tetragonal
Space group	$I4_1/a$
$a/\text{\AA}$	35.2607(3)
$b/\text{\AA}$	35.2607(3)
$c/\text{\AA}$	11.7947(2)
$\alpha/^\circ$	90
$\beta/^\circ$	90
$\gamma/^\circ$	90
Volume/ \AA^3	14664.6(4)
Z	16
$\rho_{\text{calc}}/\text{g/cm}^3$	1.281
μ/mm^{-1}	4.382
F(000)	6048.0
Crystal size/ mm^3	$0.15 \times 0.11 \times 0.05$
Radiation	$\text{Cu K}\alpha$ ($\lambda = 1.54184$)
2Θ range for data collection/ $^\circ$	5.012 to 150.204
Index ranges	$-43 \leq h \leq 42, -43 \leq k \leq 43,$ $-11 \leq l \leq 14$
Reflections collected	59794
Independent reflections	7480 [$R_{\text{int}} = 0.0697, R_{\text{sigma}} = 0.0363$]
Data/restraints/parameters	7480/0/407
Goodness-of-fit on F^2	1.039
Final R indexes [$I \geq 2\sigma(I)$]	$R_1 = 0.0502, wR_2 = 0.1202$
Final R indexes [all data]	$R_1 = 0.0597, wR_2 = 0.1255$
Largest diff. peak/hole / $e \text{\AA}^{-3}$	2.28/-1.66